Optical Properties of ZnO-based Nanostructured Materials

A thesis
submitted for the degree of

Doctor of Philosophy

in Jadavpur University

by

Manoranjan Ghosh

Department of Material Sciences
S. N. Bose National Centre for Basic Sciences
Block - JD, Sector - III, Salt Lake, Kolkata - 98
India

December 2008

CERTIFICATE FROM THE SUPERVISOR(S)

This is to certify that the thesis entitled "**Optical Properties of ZnO-based Nanostructured Materials**" submitted by **Sri/Smt. Manoranjan Ghosh** got his/her name registered on 9th November, 2006 for the award of **Ph.D.(Science) degree of Jadavpur University,** is absolutely based upon his own work under the supervision of Prof. A. K. Raychaudhuri and that neither this thesis not any part of its has been submitted for any degree/diploma or any other academic award anywhere before.

....
....
(Signature of the Supervisor(s) date with official seal)

To my wife Karabi...

Acknowledgment

I would like to thank all my friends who were always a source of happiness and fun in my life irrespective of my failure or success. I can not name all of them in this limited space but few of my batchmates like Prabodh, Bisu, Som, Samrat, Sandy, Buddha, Kanchan, Suman, Sajal, Manoj, Sourav, Kunal, Anjan, Kartick, Badiur, Rupa, Tuhin,..... seniors like Manirulda, Anujda, Monoda, Biplabda, Nupurdi...... and juniors like Samir, Santu, Ajay, Bipul, Debu ..... have always given me enough boost in my personal life as well as in research.

Last but not the least, Karabi has always remained inseparably associated with all the stages of my research work namely discussing new ideas and plans, sample preparation, data collection and analysis, sharing exciting results and finally preparing the report.

I apologize to all those whose names I could not mention in this limited space but were always supportive in my research work.

List of publications and patent applications

Publications in peer-reviewed journal:

1. Ionic environment control of visible photo-luminescence from ZnO nanoparticles 2008 Manoranjan Ghosh and A K Raychaudhuri *Applied Physics Letter* **93** 123113.

2. Shape transition in ZnO nanostructures and its effect on blue-green photoluminescence 2008 Manoranjan Ghosh and A K Raychaudhuri *Nanotechnology* **19** 445704.

3. Growth of compact arrays of optical quality single crystalline ZnO nanorods by low temperature method 2008 Manoranjan Ghosh, Ritwik Bhattacharyya and A. K. Raychaudhuri *Bulletin of Material Science* **31** 283.

4. Band gap variation in Mg- and Cd doped ZnO nanostructures and moleculer cluster 2007 Manoj K Yadav, Manoranjan Ghosh, Ranjit Biswas, Arup K Raychaudhuri and Abhijit Mookerjee *Physical Review B* **76** 195450.

5. Structure and optical properties of Cd-substituted ZnO ($Zn_{1-x}Cd_xO$) nanostructures synthesized by the high-pressure solution route 2007 Manoranjan Ghosh and A K Raychaudhuri *Nanotechnology* **18** 115618.

6. Structural and optical properties of $Zn_{1-x}Mg_xO$ nanocrystals obtained by low temperature method 2006 Manoranjan Ghosh and A. K. Raychaudhuri *Journal of Applied Physics* **100** 034315.

7. Ultrafast photoinduced deligation and ligation dynamics: DCM in micelle and micelle-enzyme complex 2006 Rupa Sarkar, Ajay Kumar Shaw, Manoranjan Ghosh and Samir Kumar Pal *Journal of Photochemistry and Photobiology B: Biology* **83** 213.

8. Ultrafast surface solvation dynamics and functionality of an enzyme α-chymotrypsin upon interfacial binding to a cationic micelle 2005 Rupa Sarkar, Manoranjan Ghosh, Ajay Kumar Shaw and Samir Kumar Pal *Journal of Photochemistry and Photobiology B: Biology* **79** 67.

9. Ultrafast relaxation dynamics of a biologically relevant probe dansyl at the micellar surface 2005 Rupa Sarkar, Manoranjan Ghosh and Samir Kumar Pal *Journal of Photochemistry and Photobiology B: Biology* **78** 93.

Conference proceeding:

1. Optical properties of $Zn_{1-x}Mg_xO$ nano-particles obtained by low temperature method 2006 Manoranjan Ghosh and A. K. Raychaudhuri *Emerging Technologies - Nanoelectronics, 2006 IEEE Conference on Volume Issue,* **10-13 Jan.** 263.

List of patent applications (Indian):

1. Electric field controlled visible photoluminescence in ZnO nanostructures 2008 Manoranjan Ghosh and A K Raychaudhuri, Application No.-**1089/KOL/2008**, Date 24/06/2008.

2. Control of visible photoluminescence from ZnO nanoparticles by control of ionic environment 2008 Manoranjan Ghosh and A K Raychaudhuri, Application No.-**1090/KOL/2008**, Date: 24/06/2008.

Contents

List of Figures

List of Tables

Chapter 1

Introduction

1.1 Motivation

Zinc oxide is a wide band gap ($\sim$3.3 eV) semiconductor having Wurtzite structure. Recently it has attracted enormous attention because of its unique optical properties ([1], [5]). Fundamental absorption even at room temperature shows excitonic contribution due to its large excitonic binding energy ($\sim$60 meV). Therefore it is a promising lasing material due to the sharp UV emission as it is stable well above the room temperature ([3], [4]). It is cheap, human friendly and also widely available. ZnO has promising applications in many optoelectronic and sensing devices such as UV lasing [19], transparent conduction electrodes [20] and gas sensors [21]. With a large exciton binding energy and high melting temperature, ZnO nanowires has been studied as field emission source ([28], [29] and [30]). These application prospects depend on the successful fabrication of a variety of ZnO microstructures/nanostructures for specific purposes. In this thesis, as we will elaborate later on, some specific issues related to optical properties of ZnO nanostructures will be addressed to.

ZnO can be synthesized easily. Broadly the synthesis methods can be classified into two categories: the physical vapour deposition method and the low temperature chemical methods. Synthesis of ZnO for optoelectronic applications are generally done through vapor phase deposition with or without catalyst. Routes that have been used to prepare ZnO based materials are Molecular Beam Epitaxy (MBE) [145], Vapor liquid solid phase growth (VLS) [159], Pulsed Laser Deposition (PLD) [146] and Metallo-organic Vapor Phase Epitaxial growth (MOVPE) [147]. Materials obtained are mostly films or rods. ZnO can also be synthesized by a variety of wet chemical routes due to its broad chemistry ([165]-[169]). Because of the same reason, very fine etching can be achieved by the wet chemical routes for fabrication of nanodevices ([64]-[66]). In this work we mainly focus on the ZnO based materials synthesized by wet chemical route. The advantage of the solution route is that it can produce high quality crystalline materials through an energy efficient route that allows wide area growth. One of the principal motivations is to explore whether such a low temperature route will allow us to grow well-characterized nanocrystals of ZnO based optical materials.

Below we give a small review of nanostructures synthesized by chemical methods (see table 1.1). One of the smallest forms of the ZnO based nanomaterials are the nearly spherical particles. By the wet chemical route, one can synthesize the single crystals of ZnO nanospheres of size as low as 1-2 nm ([75], [151]). These nanostructures remain suspended in a liquid medium and

Table 1.1: Nanostructures synthesized by chemical method

Ref.	Types of nanostructures	Typical size
ref. [39]	needle	$\sim 1~\mu m$
	disk	$\sim 2~\mu m$
ref. [37]	tubular	outer dia$\sim$ 40 nm
		wall thickness$\sim$ 15 nm
ref. [38]	spherical	$\sim$10 nm
	pyramid	$\sim$20 nm
ref. [151]	spherical	$>$ 3 nm
ref. [40]	rod	dia$\sim$2 nm
		length$\sim$40-50 nm
ref. [75]	not shown	$\sim$1 nm

can be deposited in the form of an array on any substrate. Also the shapes and sizes can be controlled by changing the growth parameters of the wet chemical method [38]. Limited studies are available on the ZnO nanostructures of different shapes and sizes suspended in a liquid medium ([75], [80]). One dimensional (1D) nanorods are another very important and widely studied physical form of ZnO nanostructures. These nanorods can be obtained in colloidal form in a solution as well as can be grown on a substrate in the form of 2D array. Periodic array of nanorods can be grown by vapour phase methods (([46], [47])) but the low cost solution growth methods have been proven advantageous in many respects like wide area growth and larger sample quantity([22], [23]). Study of the structural and optical properties of 1D nanorods is important in the viewpoint of academic as well as technological interest and find applications in the optimum generation of green oxidizer H_2O_2 by photocatalytic reaction after tuning the crystal faces [27] and optimized field emission by controlling the density of the ZnO nanowire arrays through vapour-solid-liquid (VLS) growth process [31].

1.2   Basic properties of ZnO

Structural properties: ZnO is commonly observed in wurtzite phase (space group P63mc). This is a hexagonal lattice and is characterized by two interconnecting sublattices of Zn^{2+} and O^{2-}, so that a Zn ion is surrounded by tetrahedra of O ions and vice versa [figure 1.1 (a)]. Each of the sublattices consist of one type of atom displaced w.r.t. each other along the threshold c axis by an amount 3/8=0.375 (in ideal wurtzite structure). The wurtzite structure has a hexagonal unit cell with two lattice parameters a and c in the ratio of c/a=1.633 [figure 1.1 (b)]. The lattice parameters of the hexagonal unit cell are a= 3.2495Å and c= 5.2069Å while its density is 5.605 gm/cc. In a real ZnO crystal, the wurtzite structure deviates from its ideal arrangement by changing the c/a ratio. This ratio has strong correlation with the microstrain which in turn depends on the method of synthesis of the sample. The tetrahedral coordination of O ions gives rise to polar symmetry along the hexagonal axis. This polar behaviour is responsible for a number of properties in ZnO including its piezoelectricity and spontaneous polarization, crystal growth, etching and defect generation. The four most common face terminations of wurtzite ZnO are the polar Zn terminated (0001) and O terminated (000$\bar{1}$) faces (c-axis) and the nonpolar

$(11\bar{2}0)$ and $(10\bar{1}0)$ (a-axis) faces which contains equal number of Zn and O atoms. The polar faces are known to possess different physical and chemical properties, and the oxygen terminated face possesses slightly different electronic structure from the other three faces. Aditionally, the
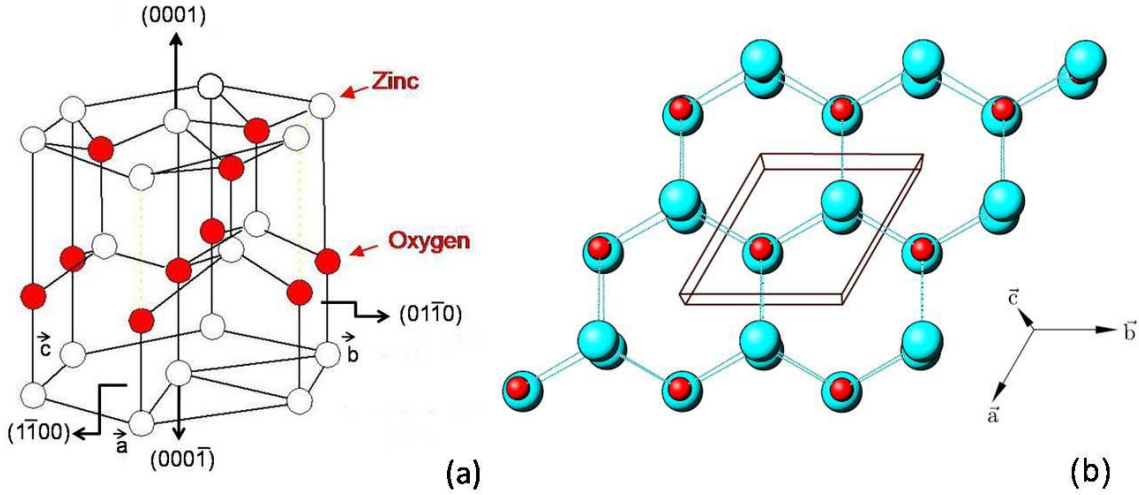
Figure 1.1: The wurtzite ZnO. (a) Hexagonal lattice of ZnO, characterized by two interconnecting sublattices of Zn^{2+} and O^{2-}, so that a Zn ion is surrounded by tetrahedra of O ions and vice versa. (b) Unit cell of wurtzite ZnO and neighbouring atoms, viewing direction approx. parallel to [0001)] direction. Small, red spheres: O^{2-}, big blue spheres: Zn^{2+}.

polar surfaces and the (1010) surfaces are found to be stable, however the $(11\bar{2}0)$ face is less stable and generally has a higher level of surface roughness compared to the other faces. The sp^3 covalent bonding leads to tetrahedral coordination of this compound. However the Zn-O bond also possesses very strong ionic character and thus ZnO lies on the border line between being classed as a covalent and ionic compound with an ionicity of f =0.616 [53] on the Philips ionicity scale [54].

Optical properties: The most interesting and widely studied aspects of ZnO lie in its optical properties ([5], [1]). Bulk ZnO shows band gap ~ 3.3 eV which can be easily determined by optical absorption measurement. Energy corresponding to the onset of the absorption spectra gives the value of the band gap energy. Due to its wide band gap ($\sim$3.3 eV), ZnO is transparent in the visible region and an excellent absorber and emitter of UV light. In figure 1.2, absorption spectra of few ZnO based materials as indicated in the graph has been shown. Onset of the absorption spectrum shifts to higher energy as the size decreases due to quantum confinement effect. Also the band gap of the pure ZnO nanostructures can be enhanced or reduced by incorporating impurities like Mg and Cd respectively. There is a distinct peak arising from the high excitonic binding energy ($\sim$60 meV) at the onset of the absorption spectrum. The excitonic binding energy has to be taken into account for accurate determination of the band gap from the absorption spectra.

Photoluminescence spectra of bulk ZnO shows a number of peaks in the the UV region ($\sim$380 nm) of the spectrum when excited well above the band gap. Low temperature PL spectra shows sharp and intense excitonic lines which makes ZnO a promising lasing material [179]. Whereas
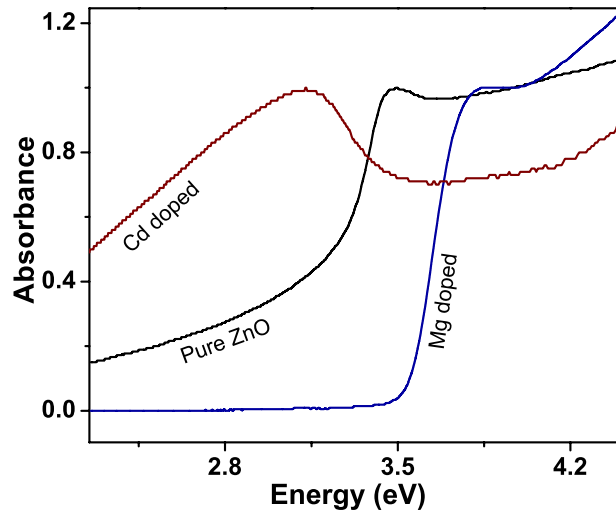
Figure 1.2: Absorption spectra of undoped ZnO nanostructures (size~15 nm) as well as those doped with Mg and Cd (size~15-20 nm).
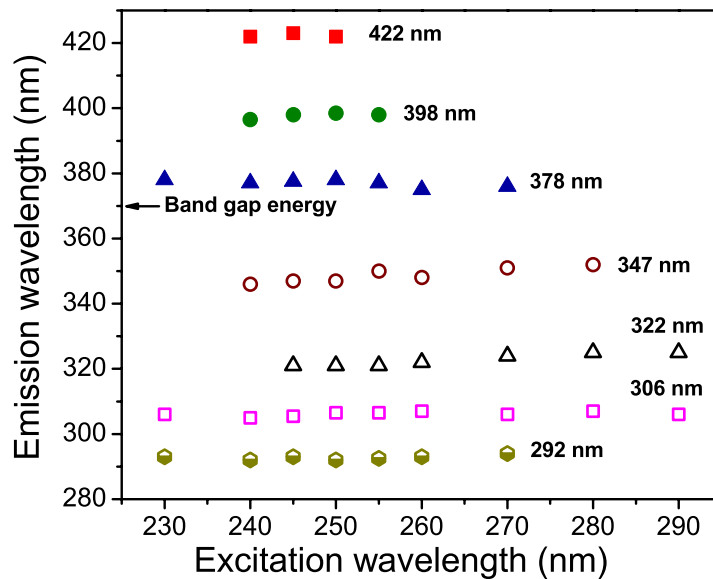
Figure 1.3: Photoluminescence peak positions appearing in undoped ZnO have been located by varying the excitation wavelength.
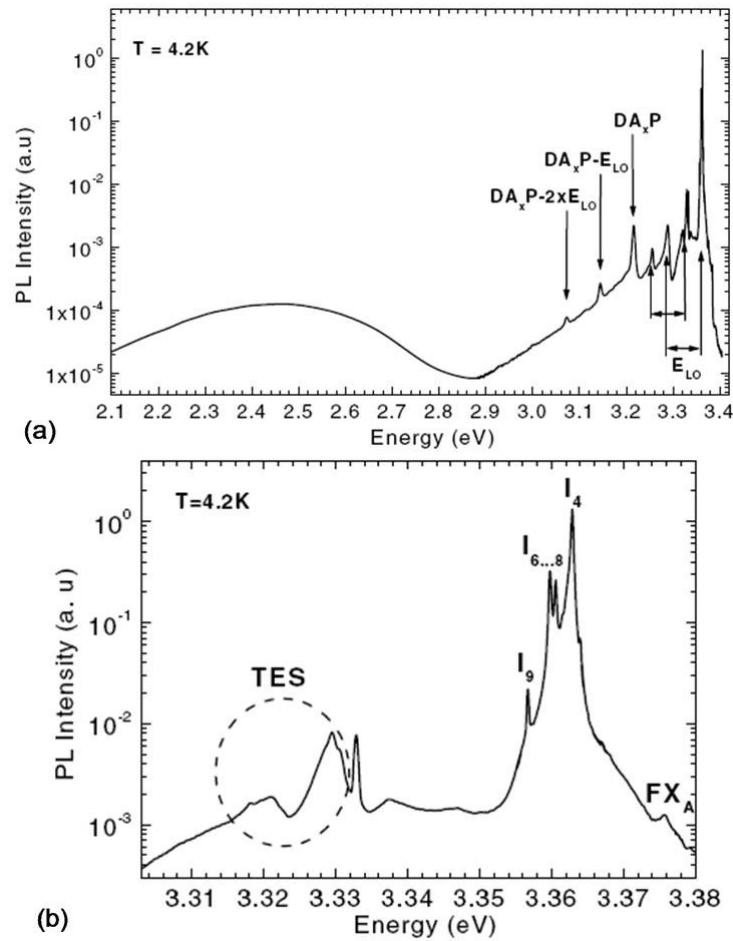
Figure 1.4: (a)Photoluminescence spectrum of bulk ZnO showing excitonic, donor acceptor pair (DAP) and deep level emission. The corresponding phonon replica with longitudinal optical phonons (LO) are indicated (HeCd excitation). (b) Photoluminescence spectrum in the excitonic range. FX_A is the transversal free exciton, I_4 to I_9 are bound exciton lines. The region where the two-electron-satellite (TES) transitions occur is indicated (HeCd excitation). Figures are reproduced with permission from ref. [13].

the room temperature PL spectra is dominated by free excitonic recombination which does not contain the finer spectroscopic details as seen in the low temperature data (see figure 1.4 and figure 1.5), although a clear picture still has not emerged. In high quality bulk crystals the luminescence line width of excitonic recombination is as narrow as 40 μeV. At low cryogenic temperatures bound exciton emission is the dominant radiative channel. Up to eleven excitonic recombinations where excitons bind to neutral donors and/or acceptors have been observed ([6], [7], [8], [9], [10]). In a more recent report by Reynolds et al (ref. [11]), it is suggested that the neutral donors are pair type complexes and the optical transitions result from the collapse of excitons bound to the neutral donors. It is also predicted that the higher-energy emission lines are due to neutral-donor-bound-exciton transitions in which the pairs making up the neutral
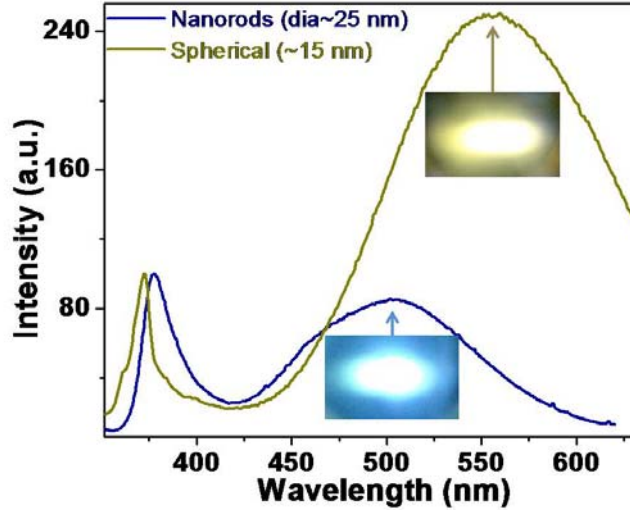
Figure 1.5: Photoluminescence of ZnO nanorod showing emission in the green region (500 nm) whereas nanospheres show intense emission in the dark yellow region(550 nm).

donors are more distantly spaced. In bulk ZnO crystals the free exciton is observed at about 3.377 eV. The emission at 3.367 eV is commonly assigned to ionized donor bound excitons [9] and the neutral donor bound excitons are positioned between 3.3628 and 3.359 eV. Finally, bound excitons previously attributed to the Na and Li acceptors [7] occur at 3.356 and 3.353 eV, respectively. In ref [13] by Meyer et al. a detailed low temperature magneto-optical studies of the ionised donor bound exciton complex of a nominally undoped bulk ZnO is documented. By determining the position of the two electron satellite (TES) the related donor binding energy is obtained with high precision. The major findings of this investigation are described below.

The luminescence from bulk ZnO extends from the band edge to the green/orange spectral range (figure 1.4). Very common is a broad band centred around 2.45 eV extending from the blue into the green range. The lines dominating the spectra originate from bound exciton (BE) recombinations (excitons bound to neutral donors (D_0X) and/or acceptors (A_0X)) followed by longitudinal optical (LO) phonon replicas with an energy separation of 72 meV. In some samples a donor-acceptor-pair (DAP) transition is found, the chemical identity of the acceptor A_x is unknown. The transition energy is around 3.22 eV again followed by phonon replicas (figure 1.4(a)). There is no definite assignment of the bound exciton recombinations to a specific donor or acceptor, they are numbered I_0 to I_{11} in the early work of Reynolds et al. (ref [9]). The prominent lines in the bulk ZnO are the bound excitons positioned at 3.3628, 3.3608 and 3.3598 eV (labeled in figure 1.4(b) as I_4, $I_{6...8}$). At 3.357 eV another bound exciton (I_9) can also be observed. The free exciton emission with the A-valence band (FX_A) positioned at 3.375 eV can already be seen. At lower energies from 3.34 to 3.31 eV further recombination lines appear. It is the region where one can expect the two-electron satellite (TES) recombination lines of the neutral donor bound excitons. During the recombination of an exciton bound to a neutral donor the donor final state can be the 1s state (normal D^0X line) or the 2s, 2p state (TES-line).

The energetic distance between the D^0X and its TES is consequently the difference between the donor energies in the 1s and 2p states, which is 3/4 of the donor binding energy (E_D) in the hydrogenic effective-mass-approach (EMA).

Although room temperature PL spectra do not show the various bound exciton lines, very often the contribution from Raman scattering from sample and solution or substrate holding the sample arises. So, identification of the photoluminescence peak becomes difficult due to overlapping of peaks from different origins. The most convenient way of separating the photoluminescence peak from the Raman peak is to vary the excitation wavelength. Raman peak will shift in accordance to the excitation wavelength but the PL peak positions remain more or less unchanged. In figure 1.3, commonly occuring PL peaks of undoped ZnO nanostructures have been identified by varying the excitation wavelength. Prominent PL peaks near the band edge are located at 378 nm, 398 nm and 422 nm. Few more peaks appear when excited well above the band gap energy as demonstrated in the figure.

Apart from the the well known emission in the UV region, the nanostructures of ZnO show surface related visible emission which depends on the size and morphology of the nanostructures (figure 1.5). The excitonic UV emission energy shows $1/diameter$ dependence and decreases as the size of the nanostructures increase due to quantum confinement effect (figure 3.6 in chapter 3). As the size decreases, surface to volume ratio increases and the optical properties are gradually dominated by the surface defect states [58]. An intense and broad emission in the blue-yellow wavelength range emerges. This visible emission has defect related origin and show dependence on the factors like size, shape and surrounding environments of the nanostructures. For example, spherical ZnO nanoparticles of size less than 20 nm show broad visible photoluminescence around 550 nm (yellow) but the nanorods (of diameter >20 nm and length $\sim$ 100-150 nm) show a peak around 500 nm (figure 1.5). In the same figure, corresponding images of the illuminated sample have been given for visualization of the luminescence colour. The effect of size and morphology on the defect related visible luminescence is important in finding out the origin of the visible luminescence and will be discussed at length in this thesis. Sometimes this green band near 500 nm includes fine structure, which consists mainly of doublets, repeated with a longitudinal-optical-phonon-energy spacing (72 meV) [12]. Reynolds et al. (ref. [12]) explained the green band from vapour phase grown ZnO platelets, as phonon assisted transitions between two different shallow donors, of energies 30 and 60 meV, respectively, and a deep acceptor. The energies of the two donors found to agree well with those determined from Hall-effect measurements although the donors and the acceptor were not identified.

From the temperature dependent photolmuminescence study, Cao et al. (ref. [14]) provided a clearer picture about the occurrence of UV (3.3 eV) and yellow-green (2.2 eV) emission. The ZnO nanoneedle arrays in their study also shows a violet (3.03 eV) band in between the UV and green emission. With increasing temperature, the UV peak shows an obvious redshift, but the green peak blue shifts and its relative intensity to UV peak decreases. The UV emission of a ZnO crystal is usually attributed to the interband recombination of electrons and holes in form of excitons. Two defect levels have been predicted by EPR and XPS investigation. There exist Zn_i shallow donors, which has a 0.22 eV energy gap below the conduction band (ref. [15]) and oxygen-deficient states in the nanoneedle surface layer, which is a deep level situated at 0.9 eV above the valence band (ref. [16]). Based on these two existing defect levels, it is predicted that the violet emission (3.03 eV at 10 K) is from exciton recombination between the electrons localized at the Zn_i shallow donor levels and holes in the valence band, as shown in figure 1.6(a). Its emission energy is consistent with the theoretical value between these two levels. As
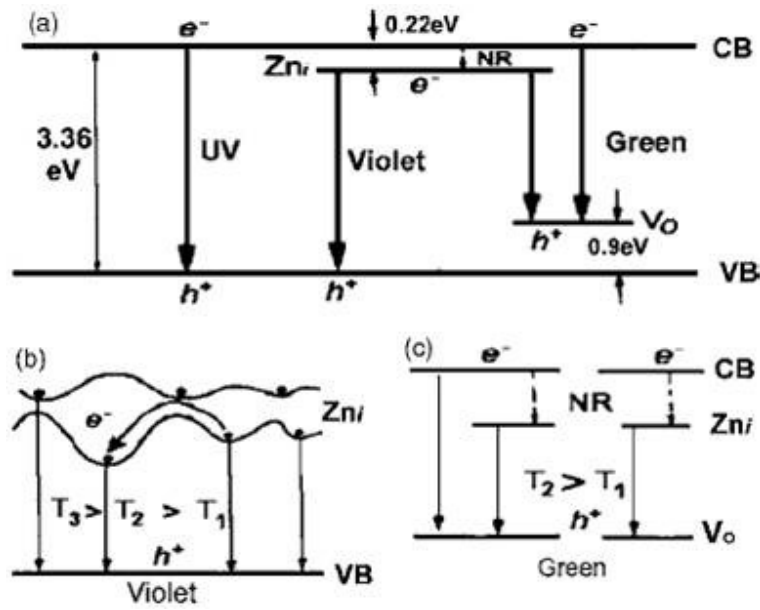
Figure 1.6: (a) Schematic illustration of the ZnO band structure and the proposed UV, violet, and green emission processes, NR: Nonradiative transition. (b) Model of the localized electrons at Zn_i defect levels and their transition process with increasing temperature. (c) Model of the green emission with increasing temperature. Figure is reproduced with permission from ref. [14].

the temperature increases from 10 K to 70 K, a red shift appears because the excitons gain in thermal energy sufficiently to overcome small energy barriers and are trapped in adjacent lower levels of the localized states from where the recombination takes place [T_2 process in figure 1.6(b)]. This redshift also includes the contribution from the temperature-induced band-gap shrinkage. The following blue shift of 160 meV at the temperature from 70 K to 150 K is caused by the thermal population of electrons localized at higher energy states, and transitions from these higher levels to the valence band [T_3 process in figure 1.6(b)]. Considering the monotonous blue shift and decreasing relative intensity with increasing temperature, it was suggested that the green emission is composed of two transitions: From the conduction band to V_o levels and from Zn_i levels to V_o levels, as shown in figure 1.6(a) and 1.6(c). In fact, the existence of these two types of transitions have been confirmed by optically detected EPR experiments ([17], [18]). With decreasing temperature, more electrons in conduction band first relax to lower Zn_i levels non-radiatively, and then recombine with holes at V_o levels, which results in the green emission shift to lower energy with narrower full width at half maximum, changing from 600 meV at 300 K to 400 meV at 50 K. Correspondingly, the green and violet emission intensities, compared with that of UV emission, are increased since more electrons at the Zn_i levels recombine with holes at oxygen vacancy and in valence band.

Electrical properties: As a direct and large-band-gap material, ZnO finds specific applications in electronic and optoelectronic devices. Characteristics associated with a large band gap include higher breakdown voltages, ability to sustain large electric fields, lower noise generation, high temperature and high-power operation. Inherently ZnO is an n-type semiconductor with

Table 1.2: Effect of common impurities in ZnO

Elements	Conductivity	Effect
H	n-type	Source of native donors
Mg, Cd	n-type	Band gap tuning
Al, Ga, In	n-type electron conc. 10^{20} cm^{-3}	highest conductivity transparent material
N	p-type hole conc.$10^{13} - 10^{17}$ cm^{-3}	–
P	p-type hole conc. $10^{16} - 10^{19}$ cm^{-3}	–

carrier concentration in the range of $10^{16} - 10^{18}$ cm^{-3}. In the past, Zn interstitial or O vacancy defects have been attributed as the native donors [67]. Recently, it is established that H, along with the Gr-III elements such as Al and Ga are the background donors which contributes significantly to the conductivity of as grown ZnO [68]. Realization of p-type ZnO was initially thought challenging. Recently it has been shown that elements like P [69] and N ([70], [71]) can produce weakly p-type ZnO with a hole concentration of about $10^{13} - 10^{18}$ cm^{-3} as shown in table 1.2. The background carrier concentration varies a lot according to the quality of the samples, however the average value is of the order of $\sim 10^{16}$ cm^{-3}. The highest reported donor concentration is $\sim 10^{20}$ electrons/cm^3 and the highest reported acceptor concentration is $\sim 10^{19}$ holes/cm^3, however such high level of p type conductivity are questionable and have not been experimentally verified. The electron effective mass is $0.24m_0$ and that for holes is $0.59m_0$ [72]. The corresponding electron hall mobility for low n-type conductivity is $\mu = 200$ $cm^2V^{-1}s^{-1}$ and for low p-type conductivity is $\mu = 5 - 50$ $cm^2V^{-1}s^{-1}$.

1.3 Previous studies on ZnO based optical materials

The study on optical properties of ZnO has started as early as 1960 [2], however they were restricted to those of the bulk materials. With the development of new growth techniques for synthesizing naostructures, renewed interest has arisen because of its promising application in electronic and opto-electronic devices [3]. Major part of the efforts has been devoted to fabricate various kinds of nanostructures/microstructures for specific application. So far all the three kinds of materials viz. single crystal, oriented film and polycrystalline nanomaterials have been investigated. Oriented thin film of ZnO have been mostly synthesized by vapour phase methods. Widely used vapour phase methods employed for growing thin film of ZnO based material are Pulsed Laser Deposition (PLD) [146], Metal Oxide Vapour Phase Deposition (MOCVD) [163] and Moleculer Beam Epitaxy (MBE) [162]. In many cases films produced by these vapour phase methods are oriented along [002] direction ([145], [4]). Samples prepared by these methods are obtained in smaller quantities and grown over a small area.

ZnO nanostructures having sizes smaller than 5 nm synthesized by solution growth method, has been reported by Dijken et al [75]. A detailed study on their optical properties has been done and the origin of the photoluminescence properties of ZnO is discussed. But the synthesized nanostructures of size below 5 nm were not separated from the dispersion. So colloidal ZnO

based nanostructures which can be easily separated out from the solution were in high demand. However, fabrication of nanomaterials with sizes that can be controlled over a wide range using a single method has not been reported earlier. Also the control over the morphology is very important for tuning the all important optical properties of the semiconducting ZnO nanostructures as will be shown in this thesis. Several kinds of nanostructures have been prepared by using different techniques ([38], [39]). The effect of morphology of the nanostructures prepared using the method on their optical properties has not been clearly addressed earlier.

Another important physical form of ZnO nanostructures that have attracted considerable attention is the one dimensional (1D) nanorods. Formidable amount of research work has been done on synthesizing 1D nanostructures of ZnO using different routes ([32], [22], [23]). Recently 2D periodic array of ZnO micro-rods and micro-tunnels have been demonstrated [24]. This kind of carefully regulated nanostructures can find applications as mentioned earlier. Hydrothermally grown disk shaped 2D nanostructures exposing the (0001) face of hexagonal ZnO lattice was found ideal for generation of green oxidizer H_2O_2 by photocatalytic reaction [27]. Density of the 2D arrays of ZnO nanorods is a crucial parameter for optimization of their field emission properties as seen in the ref. [31]. It is found that the density of grown nanorod arrays is closely related to their average diameter and preferred orientation which was not addressed in great detail. We note that the synthesis of microstructures/nanostructures of ZnO by hydrothermal /chemical method has already proven to be advantageous because of its low cost, freedom from strain and morphology controllable extended area synthesis compared to the other vapour phase methods like evaporation and condensation ([44], [45]), physical vapour deposition ([46], [47]) and chemical vapour deposition ([49], [48]). In the hydrothermal method, the morphology of the ZnO crystals can be easily controlled by varying the growth conditions such as growth time ([50], growth temperature ([51]), pH ([52]), and absorbing molecules ([56]). The resulting nanocrystals show different optical properties depending on their growth conditions ([57] and [58]). Optimization of growth parameters for the aligned arrays of nanorods by this method is thus important for tailoring its properties.

The room temperature photoluminescence of ZnO nanostructures typically exhibits a sharp emission in the near UV range (originating from excitonic mechanism) and a broad emission band in the visible region of the spectrum which is linked to defects in ZnO [88]. Different types of defects have been proposed to explain the two commonly observed defect emission bands in the visible range - a blue-green band ($\lambda_{bg} \sim 450 - 500\ nm$) and an orange-yellow band at ($\lambda_{oy} \sim 550 - 650\ nm$) [73]. The specific identification of the nature of defects for the emission in the visible region is difficult because of simultaneous existence of various types of defects in ZnO nanostructures which often depend on the method of preparation [77]. Fundamental questions like, evolution of the visible emission with the nanostructure size and morphology remain unresolved ([73], [74]). As a specific example, the defect related green emission is observed to shift towards higher energy when the size of the nanostructures increases from 25 nm to 75 nm [79]. In contrast, a clear blue shift (towards higher energy) in the visible luminescence is observed when the size of the nanospheres decreases from 18 nm to 4 nm [93]. In a recent report, the blue green emission of ZnO nanostructures grown by Pulsed Laser Deposition was found to exhibit blue shift and reduced intensity when the size increases and the morphology was found to change from spherical to rods and hexagonal plate [78]. However, the origin of this anomalous shift in emission energies has not been explained and the role of morphology of the nanostructures on the visible emission has not been investigated.

There have been numerous number of efforts in the literature to find out the origin of this

defect related visible emission from ZnO nanostructures. The energy levels of different defects and their formation energies have been calculated ([107], [108], [109], [110], [111]). However, a number of controversial hypotheses have been proposed to explain the different defect emissions (blue, green, yellow and orange-red) and the the origins of different defect emissions are still a mater of debate. It is known that different types of defects are responsible for green, yellow and orange-red emissions [76]. Among them green defect emission is most commonly observed and is also a topic of much discussion, for which various hypotheses have been proposed([74], [79], [90], [123]). The defects for this visible emission are located at the surface ([112], [58]) and will be discussed at length in this thesis. There have been reports of less commonly observed defect related emissions in the yellow and orange-red region of the spectrum [73]. It is proposed that these two emissions may involve similar deep levels but different initial states (conduction band and shallow donors) [113], and they were also found to exhibit different dependences on the excitation wavelength [114]. The yellow emission is commonly attributed to oxygen interstitial defects ([115], [116]), although some impurities such as Li may also play a role [116]. Also the presence of $Zn(OH)_2$ at the surface was identified as a possible reason for the weak UV and the strong visible (broad yellow and green) emission for chemically synthesized ZnO nanoparticles [117]. The orange-red emission centred at $\sim$640-650 nm is also commonly attributed to the presence of excess oxygen in the samples ([118], [119], [120]). Zinc interstitials [121] and surface dislocations [122] were also claimed to be responsible for this orange-red emission. Therefore, different types of defects have been proposed to explain the emissions appearing at different region of the visible spectrum. The explanations proposed for a single particular observation generally failed to explain other contradictory results.

In spite of the debatable origin or in few cases its peculiar behaviour on growth parameters, almost all kinds of ZnO nanostructures below 20 nm regularly shows this visible emission. Therefore application of ZnO based nanostructures in optoelectronic devices demands fine control of this visible emission. Due to the surface related origin of this emission, it is highly sensitive to the environment. In particular, non-toxic ZnO nanostructure/microstructure is a promising candidate as a sensor for the biomedical applications such as detection of specific protein interactions ([25], [26]). Therefore, fine control of the visible luminescence for specific purposes is an important development. As we have discussed, the defect related visible emission can be controlled by factors like nanostructure size and shape. It has been demonstrated that the positive surface charge associated with the surrounding space charge creates depletion layer at the nanostructure surface which is responsible for band bending and the resulting change in the visible emission [93]. Therefore, any change in the ioninc environment of the colloidal ZnO will be reflected by the change in surface charge which eventually controls the visible emission from the nanostructures [94]. Now the question is that can one control this visible luminescence by simple application of voltage which is completely reversible. Quenching of fluorescence from the phosphors like ZnS by application of few volts has been reported [128]. In a recent report quenching of the visible emission and enhancement of the UV emission by application electric field has been observed [127]. But a reversible control (quenching as well as enhancement) of the visible luminescence of ZnO nanostructures by application of very small voltage (< 5 V) has not been achieved earlier.

ZnO is an excellent absorber and emitter of UV light and displays change in electrical conductivity by Electron Hole Pair (EHP) generation by UV illumination. Remarkable photoresponse properties make ZnO a relevant material for UV detection, photovolatics and solar cell applications. Fabrication of ZnO based devices for UV detection requires good Schottky as well as

Ohmic contact with those dissimilar materials. In a recent report, an excellent Schottky contact of ZnO with a conductive polymer has been demonstrated [133]. Furthermore, the area of nanostructured film should be larger and the consisting nanoparticles should be smaller for efficient performance by maximizing the light absorbance. Wide area electrode transparent in the range of excitation wavelength is essential for polycrystalline nanostructured materials. ZnO is inherently an n-type material. Since the p-type ZnO is not very common, p-n junction in ZnO crystal is difficult to fabricate. In addition to that only few metals such as gold and platinum are reported to have Schottky contact with ZnO ([130], [129]). So use of conductive polymer for better device performance is preferable. ZnO based Metal Semiconductor Metal UV detector having high gain and high speed is reported where I-V characteristics is Ohmic in nature [132]. In another report photoresponse of ZnO tetrapod nanocrystal Schottky diode is demonstrated although gain is comparatively less [129]. For practical applications, improved devices with high gain, large light exposure area and cost effective fabrication is essential.

ZnO is a wide band gap semiconductor with a direct band gap of ∼3.3eV. One of the interesting features of ZnO is the possibility to tune its band gap by substituting (alloying) bivalent metals like Be, Mg, and Cd in place of Zn. This raises the possibility of band gap engineered heterostructure for optoelectronic application in the UV range ([142], [143]). Oxides such as BeO and MgO have higher band gap than ZnO whereas CdO has a smaller value. From figure 1.7 (ref. [41]), it can be seen that BeZnO alloys are good candidates for achieving band gap modulation to values larger than that of ZnO, and that (Zn, Cd)(Se and/or S, O) quaternary alloys are good candidates for achieving smaller band gap values. However, crystal phase segregation between ZnO and MgO/CdO occurs for higher Mg, Cd concentration due to the different crystal structures and large lattice mismatch between ZnO and MgO. The a-axis lattice constant values for hexagonal ZnO, BeO and cubic MgO are 3.249Å, 2.698Å and 4.22Å
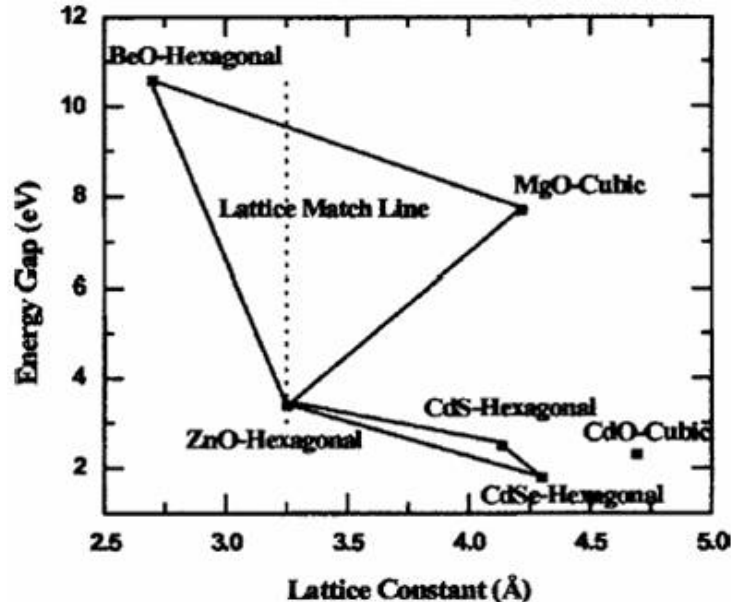
Figure 1.7: Energy band gaps, lattice constants and crystal structures of selected II-VI compounds. Taken with permission from ref. [41]

respectively. It has been proposed that improved lattice matching between ZnO and BeZnO can be achieved by adding an appropriate amount of Mg into a BeZnO alloy [41]. Likewise it is important to reduce the high band gap value of ZnO by alloying with a suitable candidate like CdO to widen the applicability of ZnO based devices in the visible region [161]. Due to the large lattice mismatch and the difference in crystal structure between cubic CdO and hexagonal ZnO with lattice constants 4.69 Å and 3.25 Å respectively, the phase segregation occurs at lower concentration of CdO than that of MgO in ZnMgO alloy [60].

Synthesis of $Zn_{1-x}Mg_xO$ for optoelectronics applications are generally done through vapor phase deposition with or without catalyst. Routes that have been used are Molecular Beam Epitaxy (MBE) [145], Vapor liquid solid phase growth [159], Pulsed Laser Deposition (PLD) [146] and Metallo-organic Vapor Phase Epitaxial growth (MOVPE) [147]. Materials obtained are mostly films or rods. In addition, a very low temperature ($< 100^0 C$) solution route has been used to fabricate aligned nanorods of pure ZnO [23]. In a recent paper Mg substituted ZnO ($Zn_{1-x}Mg_xO$) nanorods synthesized by hydrothermal method ($< 100^0 C$) has been reported [148]. The advantage of the solution route is that it can give high quality crystalline materials through an energy efficient route that allows wide area growth (e.g., 4 inches Si wafer). In the solution route for material synthesis the mixing occurs at the atomic level and the material made by this method is close to the thermodynamic equilibrium phase. In this thesis a low temperature route has been demonstrated to synthesize colloidal $Zn_{1-x}Mg_xO$ alloy nanocrystals.

As already mentioned, it is also possible to reduce the band gap of ZnO by alloying with suitable candidates like CdO. In this thesis, lowering of band gap from 3.3 eV to 2.9 eV by isovalent substitution of Cd into ZnO lattice will be demonstrated. The Cd substituted ZnO has been prepared so far by vapour phase methods. Epitaxial films of alloyed $Zn_{1-y}Cd_yO$ grown on a substrate have been mostly fabricated by pulsed laser deposition (PLD) [161], molecular beam epitaxy (MBE) [162] and remote plasma enhanced metallorganic chemical vapor deposition (RPE-MOCVD) [163]. Recently $Zn_{1-y}Cd_yO$ nanorods have been fabricated by the thermal evaporation of precursors containing Zn and Cd [164]. Production of nanocrystals of Cd substituted ZnO by vapour phase methods has its limitations because it is expensive and materials obtained are in small quantities. Thus the synthesis of Cd substituted ZnO nanostructures by a low temperature solution method is a very desirable step. There are a large number of reports of synthesis of undoped ZnO by solution or hydrothermal method ([165]-[167]). Undoped ZnO nanorods have been synthesized by hydrothermal method very recently [169]. However there has been no published report so far on solution route synthesis of $Zn_{1-y}Cd_yO$ nanostructures. Demonstration that one can produce band gap tuned good quality nanocrystals of Cd substituted ZnO by a low temperature solution route opens up the possibility of large scale synthesis of this material.

1.4 Specific issues to be addressed

The major aspects of this thesis can be broadly classified into five topics viz.

- Synthesis of various kinds of pure ZnO and ZnO based alloy nanostructures.

- The effect of size reduction on the optical properties of ZnO nanostructures having different morphologies.

- Electric Field and charge induced intensity modulation of ZnO nanostructures.

- High gain photoresponse in thin ZnO film for application in the area of UV detection.

- Band gap engineering of $Zn_{1-x}Mg_xO$ and $Zn_{1-y}Cd_yO$ ternary alloy nanostructures.

Below we give a brief summary of the work done on these topics.

Synthesis of various kinds of pure ZnO and ZnO based alloy nanostructues: Colloidal ZnO nanostructures of uniform size ranging from 4 nm to 80 nm with different morphologies have been synthesized by varying the precursor concentration and growth time in a cost effective, low temperature wet chemical method which is scalable for mass production. Following similar procedure, alloy ZnO nanostructures such as colloidal $Zn_{1-x}Mg_xO$ and $Zn_{1-y}Cd_yO$ of sizes ranging from 10-15 nm have been synthesized by the addition of source material for the impurity atoms.

A two step solvothermal method has been employed to grow long aligned arrays of ZnO nanorods on substrates like glass, quartz and silicon at a low temperature. This method uses a seed layer of ZnO nanoparticles to nucleate the growth process and falls in the general class of nanostructure growth through site specific nucleation. An easy way to control the density and overall orientation of the nanorod arrays by controlling the aerial density of the random array of nucleation sites has been described.

The effect of size reduction on the optical properties of ZnO nanostructures having different morphologies: The room temperature photoluminescence (PL) of ZnO nanostructures typically exhibits a sharp emission in the near UV range (originating from excitonic mechanism) and a broad emission band in the visible region which is linked to surface defects. Size and morphology controlled ZnO nanostructures show clear shape transition from spherical to hexagonal or rod shape as the size increases beyond ∼20 nm. This leads to a sharp change in the spectral content of visible emission. Nanostructures with spherical shape (10-20 nm) show emission near 550 nm whereas rods and hexagonal platelet with flat faces emits near 500 nm. Both these emissions show very systematic dependence on the surface to volume ratio which confirms the surface related origin of this emission. Variation in the relative contribution of the two spectral components present in the broad visible emission has been explained by the band bending effect arising due to the presence of positive surface charge on the ZnO nanostructure surface.

Electric Field and charge induced intensity modulation of ZnO nanostructures: The visible photoluminescence from ZnO nanoparticles can be controlled by changing the ionic or polar nature of the medium in which the nanoparticles are dispersed. The electric field produced at the interface controls the visible luminescence and eventually helps to explain its origin. Presence of sufficient amount of electrolyte can quench the visible photoluminescence from ZnO nanostructures. This phenomenon is reversible and can be successfully explained by surface charge of the nanoparticles obtained from the Zeta potential. In particular, it can be used as a visible bio-sensor for biochemical/biophysical processes that leads to a change in the surface charge and the zeta-potential.

Yet another discovery of the thesis is that a reversible control over the visible luminescence can be achieved by the application of a few volts (<5V) to ZnO nanostructure film sandwiched between ITO and $LiClO_4/PEO$ solid electrolyte. We find that when the solid polymer electrolyte is negatively biased, up to 107 percent enhancement in the visible luminescence has been observed, whereas a near complete quenching (87 percent reduction) of the visible emission has been seen when it is positively biased. The sharp NBE (near band edge) emission in the ultraviolet region however has no dependence within the voltage range we are working.

High gain photoresponse in thin ZnO film for application in the area of UV detection: The same device (in which we could achieve voltage control photoluminescence) exhibits high gain photoresponse when illuminated by a 345 nm light passing through the transparent (above 325 nm) ITO glass substrate. The highest photo-response is detected when the device is excited in the UV region. Maximum responsivity of 10 A/W in the photocurrent is observed. A likely explanation of this effect can be photo-induced reduction of the barrier potential created at the ZnO-polymer interface by UV illumination which in turn enhances the current passing through the junction. However, the response time to the illumination is limited by reaction time of the ions in the solid polymer electrolyte and found to be 10 sec. The total current flowing through the device is determined by the excess carriers generated by UV illumination as well as carrier injected by the application of voltage.

Band gap engineering of colloidal $Zn_{1-x}Mg_xO$ and $Zn_{1-y}Cd_yO$ ternary alloy nanostructures: One of the important issues that have not been addressed earlier is the effect of alloying on electronic and optical properties of ZnO nanostructures in the size range of 10-20 nm. An important issue that limits synthesis of MgO alloyed ZnO is the fact that the thermodynamic solubility limit of MgO in ZnO is ∼4 at. % [149]. The issue of Mg incorporation in ZnO in excess of 4 at% without phase segregation is an important and topical research problem. It has been claimed that using the vapor phase route such as pulsed laser deposition it is possible to incorporate Mg up to ∼40 at.% [146]. For MOVPE grown films the Mg incorporation has been reported to be ∼49 at% [147]. For $Zn_{1-x}Mg_xO$ nanorod, grown by solution route, x∼0.25 has been reported to be achieved [148]. In this thesis we would like to explore a very specific question - to what extent one can incorporate Mg into ZnO nanocrystals using low temperature solution route (growth temperature $< 750^0C$) and the resulting quality of the material as characterized by structural and optical means. We show that such a low temperature route can be used to make the alloy $Zn_{1-x}Mg_xO$ with x as large as 0.17. Above this composition the MgO segregates. Up to this composition the alloy retains a Wurzite structure and the lattice constants change smoothly as x is varied albeit by a small amount. The phase segregation for x>0.20 has been established by XRD as well as TEM studies.

Another step of technological relevance is to reduce the band gap of ZnO by incorporating Cd into it. We describe the synthesis of $Zn_{1-y}Cd_yO$ nanostructures by an energy efficient high pressure solution route which can produce large amount of the $Zn_{1-y}Cd_yO$ nanocrystals of good structural and optical qualities. The major challenge faced in the solution route synthesis process is that the CdO is formed at relatively high temperature (230^0C) which is much higher than the boiling point of most of the solvents generally used for solution synthesis. Also because of different crystal structures of ZnO (wurtzite) and CdO (rock salt), they tend to get phase separated very easily. To overcome these problems, the $Zn_{1-y}Cd_yO$ has been synthesized in an autoclave at high pressure (∼55 atm.) which can increase the boiling point of solvents like ethanol which allow relatively higher temperature synthesis. At this high temperature and pressure, $Zn_{1-y}Cd_yO$ nanostructures form along with CdO. The nanostructures formed consist of both particles and as well as rods of good crystalinity and optical quality. The nanocrystals tend to have the shape of nanorods .We show that such nanocrystals have near band edge PL that is red shifted significantly and have relatively large PL decay time (∼10 ns) as revealed through time resolved PL measurements. The nanocrystals do not show the defect related green emission often seen in ZnO nanostructures.

1.5   Layout of the thesis

In chapter 2 we describe different methods adopted for synthesizing samples having different forms and purpose. Preparation of ZnO nanostructures of different sizes and morphologies by cost effective chemical methods will be discussed in detail. The adopted methods are compared with other standard methods in respect to the ease of fabrication, cost and quality of the grown sample. A brief overview of the techniques and analysis method employed in this work have been supplied. Spherical nanoparticles, nanorods suspended in a liquid as well as arrays on a substrate and hexagonal particles of sizes varying from 4 nm to 100 nm have been prepared by changing the growth parameters like precursor concentrations and growth time. After successful synthesis of the nanostructures and their characterization by complimentary technique we move on to the study of structural and optical properties.

In chapter 3, it will be demonstrated that the nanostructures change their shape from spherical to rod shaped and hexagonal morphology as the size increases. This shape transition affects the optical and structural properties of the nanostructures. Specially, the emission energy of the visible emission shows sudden change when the shape changes from spherical to rod like or hexagonal morphology. In chapter 4, we establish that the visible emission from ZnO nanostructures can be controlled by changing the ionic concentration of the surrounding liquid medium which is relevant for application of the non-toxic ZnO quantum dot as biosensor. In chapter 5 we describe fabrication of the ZnO based device which shows high gain photoresponse and capable of modulating the visible luminescence by 100 percent (enhancement as well as quenching) through application of voltages below 5 V. In chapter 6 we will focus on the the ZnO based alloy nanostructures of size 10-20 nm . Synthesis of $Zn_{1-x}Mg_xO$ ($0 < x < 0.2$) and $Zn_{1-y}Cd_yO$ ($0 < x < 0.1$) ternary alloy nanostructures of sizes $\sim$10-15 nm, suspended in a liquid medium will be described. We will also discuss the effect of alloying on the structural and optical properties of these nanostructures.

Chapter 2

Sample Preparation and Experimental Techniques

ZnO is a cheap, human friendly and easily synthesizable material. Acetates and nitrates of zinc can be easily decomposed to its oxide below a temperature of 100^oC. Therefore the chemical methods are the most convenient for growing good quality ZnO nanostructures with a uniform size distribution. There are several advantages of the chemical methods over the vapour phase methods such as cost effectivity, better quality, larger quantity, wide coverage area, repeatability and finally better control. After the reaction, the nanostructures are precipitated and then dispersed in ethanol. The separation of the nanostructures from the solution is indeed an easy task if their sizes are more than 20 nm as most of them will be deposited at the bottom after one or two hours. If the nanostructure sizes are less than 20 nm then one needs to use the method of centrifugation for the separation purpose. In our work we have mainly used zinc acetate dihydrate $[Zn(CH_3COO)_2.2H_2O]$ and zinc Nitrate hexahydrate $[Zn(NO_3)_2.6H_2O]$ as the commercially available source material for ZnO. zinc acetate dihydrate has been used to synthesize nanostructures of smaller sizes (below 50 nm) having different morphologies. On the other hand zinc nitrate hexahydrate has been used to produce nanorods of larger sizes (greater than 100 nm).

2.1 General methodology and basic chemical reactions

Nanocrystalline ZnO particles can be prepared from alcoholic solutions of zinc acetate dihydrate with or without using a base solution such as NaOH or KOH through a colloid process carried out at a temperature above 60^oC. Reaction performed above 60^oC avoids precipitation of $Zn(OH)_2$ and results in the formation of colloidal ZnO nanostructures of such a size range which appear sky blue because of Rayleigh scattering. It is revealed that a layered hydroxide zinc acetate is formed as an intermediate and its transformation into ZnO is a key reaction step in any of the alcoholic solutions [33]. The overall chemical reaction leading to the formation of ZnO from zinc acetate precursor is [34]:

$5Zn(CH_3COO)_2.2H_2O \Rightarrow Zn_5(OH)_8(CH_3COO)_2.2H_2O + 8CH_3COOH$

$Zn_5(OH)_8(CH_3COO)_2.2H_2O \Rightarrow 5ZnO + 2CH_3COOH + 5H_2O$
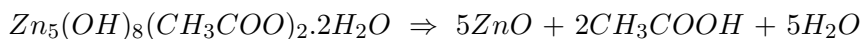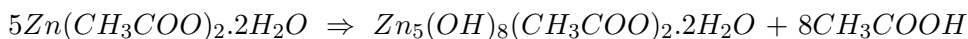
The reaction time necessary for the precipitation of ZnO is greatly influenced by the solvents used. Methanol (boiling point 60^oC), is useful for the preparation of the ZnO nanoparticles which are chemically pure in terms of cation impurities [33]. Ethanol with boiling point 78^oC is generally used to perform synthesis at slightly higher temperatures to ascertain formation and precipitation of ZnO nanoparticles.

Addition of NaOH to the solution makes it basic (pH = 8) preventing agglomeration of the nanoparticles (cluster formation) and thus helps in synthesizing particles of smaller sizes. Detailed investigation on the role of NaOH in the medium reveals that there is a strong non-monotonic variation in the growth as a function of NaOH concentration [36]. There is an initial increase in the size with increasing base concentration up to a maximum 0.4 mM of NaOH, followed by a rapid decrease and finally a slow increase in the most concentrated regime (above 0.5 mM of NaOH). It is proposed that NaOH is not only a source of hydroxyl ions acting as a reactant forming $Zn(OH)_2$ that dissociates to form ZnO and water, but also provides the counterion, Na^+. This Na+ ion being attracted by the hydroxyl ions around the nanocrystal acts as a capping agent, thus impeding the growth of the nanocrystal [36].

2.2   Synthesis of ZnO nanostructures of various shapes and sizes

The general methodology used in synthesizing ZnO nanostructures using zinc acetate dihydrate as precursor is as follows: The NaOH solution in ethanol is slowly added into the solution of zinc acetate dihydrate in ethanol kept at $60-75^oC$ (the volume ratio of the two solutions is maintained

Figure 2.1: The specially designed temperature bath used for uniform heating during solution growth of ZnO nanostructures. The outer cylindrical shell contains a liquid like water or oil to maintain a uniform temperature all through the sample column.

at $Zn(CH_3COO)_2.2H_2O$:NaOH = 2:1). The final solution is stirred for 2 hrs maintaining the temperature within the range $60 - 75^oC$. This method allows precipitation of ZnO nanoparticles but avoids precipitation of hydroxides if the temperature is above 60^oC. A simple temperature bath is fabricated by joining two concentric beakers (a cylindrical shell)(figure 2.1) is used to maintain the temperature. In between the two walls one can use either water or oil (to achieve temperatures higher than 100^oC) as the situation demands.

2.2.1 To achieve the control on size

The method described above produces spherical nanoparticles in the size range of 5-15 nm, depending on the concentration of precursors and synthesis temperature. In table 2.1 we have listed the reaction conditions for the synthesis of nanostructures of different sizes. Gr-I samples are prepared under ambient pressure and temperature less than 75^oC. If a very dilute precursor solution (5 mM of zinc acetate dihydrate and 15 mM of NaOH solution) is reacted under 60^oC then one can obtain nanospheres of size ~ 5 nm. Subsequently, as the precursor concentration and reaction temperature increases, the particle sizes are also observed to increase. When 15 mM of zinc acetate dihydrate and 45 mM NaOH are reacted for six hour at a temperature of 75^oC, particle having sizes as large as 15 nm can be synthesized. The synthesized nanoparticles remain suspended in the solution and need to be separated for different measurement purposes. Before collection of the nanoparticles from the solution it is necessary to wash them with deionized water to remove the NaOH completely. Applying the method of centrifugation, nanoparticles having a selected size range can be collected. For washing purpose, the nanoparticles suspended in ethanolic solution of NaOH is first centrifuged at the speed of 7000 r.p.m.(rotations per minute), which is sufficient for the sedimentation of all the nanoparticles. Then the deposited naoparticles are again dispersed in water and centrifuged for 4-6 minutes at the speed of 7000 r.p.m. Then, the naoparticles are centrifuged for 2 minutes at the speed of 2000 r.p.m in order to sediment particles of sizes >15 nm. The rest of the solution centrifuged at the speed of 4000 r.p.m. for 3 minutes deposits nanoparticles of size >7-8 nm. For sedimentation of the nanoparticles in the size range 4-8 nm, 3 minute centrifugation at the speed of 6000 r.p.m is necessary. The prescription described above is applicable only when the sample contains nanoparticles having a wide range of size such as 4-20 nm. But in most of the cases, samples synthesized using acetate route within an uniform temperature bath produces nanoparticles with a narrow size distribution ($\pm 1 nm$). Therefore one step centrifugation at the required speed suffices in most of the cases.

2.2.2 Control on morphology by reaction within autoclave

One major advantage of the method described above is the production of ZnO nanoparticles having a uniform size distribution (± 1 nm). But this method is capable of producing nanostructures in the size range of 4-15 nm only. Nanostructures of larger size can not be synthesized within the working temperature range of this method. Also the morphology of the nanostructures synthesized by the above method (performed in ambient pressure) is mainly spherical. To achieve greater control over their size and morphology, the above mentioned reaction has been performed under high pressure and temperature. For that purpose we have used an autoclave made of steel which can sustain up to 270^oC (shown in figure 2.2).

First of all two precursor solutions viz. zinc acetate dihydrate and NaOH in ethanol of desired concentration have been prepared. Then these two solutions were mixed in the volume

Figure 2.2: Autoclave used for high pressure synthesis. The teflon beaker and the steel plates are parts of this autoclave

ratio of $Zn(CH_3COO)_2.2H_2O$:NaOH = 2:1. Less than 70 percent of the autoclave volume has been filled up with this mixture. After that the tightly closed autoclave was kept in an oven preset at 230^oC. The vapour pressure of ethanol at 230^oC has been calculated to be 54.2 atm. as described below.

Calculation of vapour pressure within the autoclave:

Standard enthalpy change of vaporization for ethanol $(\triangle H_{vap})$ = 38.56 KJ/mole

The Clausius Clapeyron equation can be written as,

$$P = Aexp(-\frac{\triangle H_{vap}}{RT}) \tag{2.1}$$

$$\Rightarrow -\frac{\triangle H_{vap}}{RT} = ln(\frac{P}{A}) \tag{2.2}$$

where R = 8.3145J/mole/K.

If P_1 and P_2 are the pressures at two temperatures T_1 and T_2 then,

$$ln(\frac{P_1}{P_2}) = \frac{\triangle H_{vap}}{R}(\frac{1}{T_2} - \frac{1}{T_1}) \tag{2.3}$$

The vapour pressure of ethanol is 1.0 atm. at $(273 + 78)^0K = 351^0K$

The vapour pressure of ethanol at $(273 + 230)^0K = 503^0K$ has to be determined.

From the above equation,

$$P_{503} = 1.0exp[-(\frac{38560}{8.3145})(\frac{1}{503} - \frac{1}{351})] \tag{2.4}$$

$$= e^{3.993}$$

$$= 54.2 \; atm. \text{ pressure.}$$

This method is very sensitive to the reaction time and precursor concentration because the reaction takes place at relatively high temperatures (230^0C) and pressures (54.2 atm). Nanostructures of different sizes and morphologies have been prepared by this method with a little change in the reaction condition as listed in table 2.1 (Gr-II and Gr-III samples). We note that this method produces spherical nanoparticles when grown for short duration (less than 1.5 h) with precursor concentration such as 10 mM of zinc acetate and 30 mM of NaOH in ethanol (Gr-III samples in table 2.1). When 20 mM of zinc acetate and 60 mM of NaOH solution is reacted for more than two hours, nanorods of dia ∼20-25 nm can be produced (Gr-II). If we further increase the reaction time and precursor concentrations then hexagonal platelets of relatively larger sizes (∼50-60 nm) are produced. At this point it has to be clearly mentioned that the concentrations of precursors mainly control the morphology of the nanostructures whereas size of the nanostructures is mainly determined by the reaction time. It is possible to grow rods and hexagonal platelets of almost same size by simply changing the precursors concentrations. But the minimum size of the rods and hexagonal platelets is about 20 nm. Below that size limit the dominant morphology of the nanosructures is spherical. So the nanostructures undergo a shape transition near 20 nm (discussed in detail in chapter 3). Using this method nanostructures of wide size range (from 8-80 nm) can be synthesized. The general trend is that the size distribution is narrower for nanostructures of smaller sizes.

Table 2.1: Synthesis scheme of ZnO nanostructures

Identification		Morphology	Size by TEM (nm)	Size by XRD (nm)	E_{NBE} (eV)	Zinc acetate (mM)	Sodium acetate (mM)	Reaction condition
I	(i)	Spherical	4	5	3.45	5	15	75^oC, 1 min, μ wave
	(ii)	Spherical	9.5	10	3.35	10	30	65^oC, 1 hr, stirring
	(iii)	Spherical	15	15	3.33	20	60	75^oC, 6 hrs, stirring
II	(iv)	Rod diameter	24	23	3.33	20	60	230^oC, 2.5 hrs, 54 atm.
	(v)	Hexagonal platelet	55	44	3.29	50	150	230^oC, 6 hrs, 54 atm.
III	(vi)	Spherical	12	12	3.35	5	15	230^oC, 0.5 hr, 54 atm.
	(vii)	Spherical	20	19	3.33	10	30	230^oC, 1.5 hr, 54 atm.

2.3   Preparation of alloy nanostructures

2.3.1 $Zn_{1-x}Mg_xO$ alloy nanostructures

Alloying of ZnO has been done by adding requisite amount of $Mg(CH_3COO)_2.4H_2O$ to the $Zn(CH_3COO)_2.2H_2O$ solution in ethanol and the same procedure as described above has been followed (see figure 2.3). To vary the alloy concentration, the relative concentrations of $Mg(CH_3COO)_2.4H_2O$ and $Zn(CH_3COO)_2.2H_2O$ in the solution were varied. The temperature at which reaction occurs can be varied from $60-75^oC$. To eliminate the large particles, the samples in solution phase were centrifuged for 2 mins at 2000 r.p.m. The dispersion containing the smaller particles was again centrifuged for 6 min at 7000 r.p.m. The precipitates were collected, washed by water, and centrifuged again at 7000 r.p.m. The final precipitates were collected by dispersing them in ethanol. All the optical measurements have been performed in solution phase taking the dispersed sample within a cuvette. For XRD investigation, washed residues were collected and dried within a hot air oven at a temperature of 120^oC.
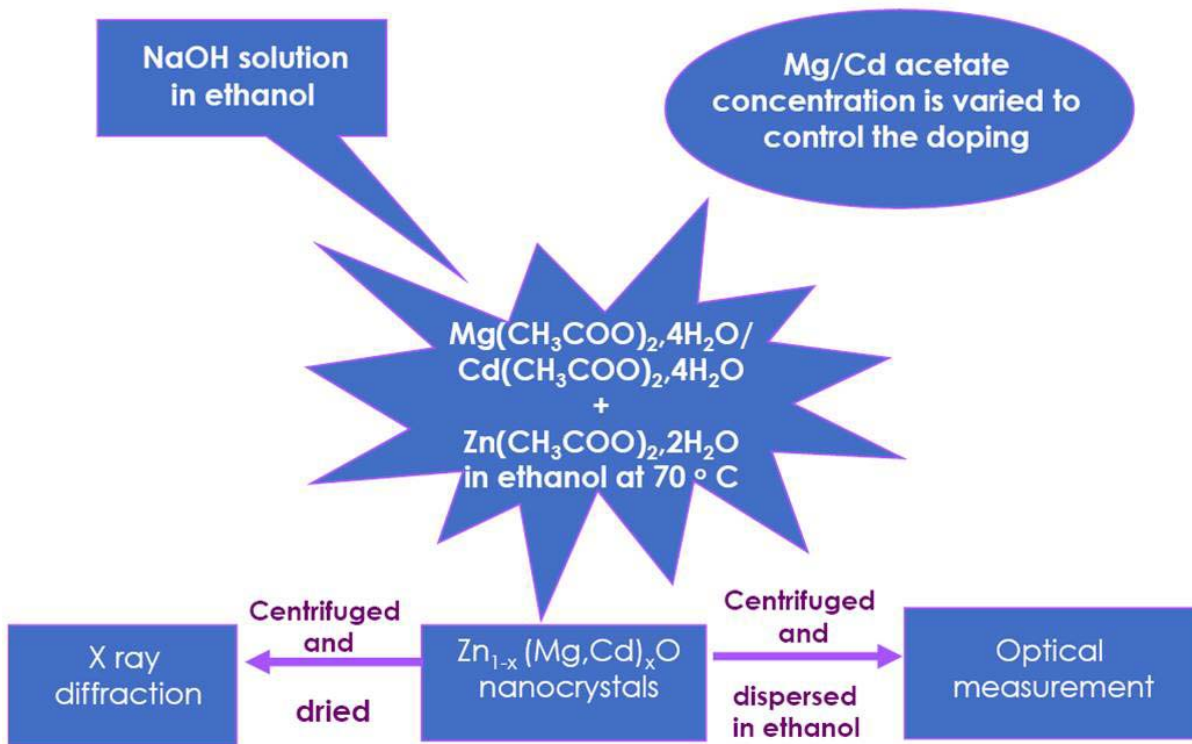
Figure 2.3: Flow diagram describing the synthesis of Mg and Cd substituted ZnO nanostructures.

2.3.2   Stoichiometric mixing

For the stoichiometric mixing of $Mg(CH_3COO)_2.4H_2O$ and $Zn(CH_3COO)_2.2H_2O$ the following procedure has been performed: Below we describe a typical scheme for obtaining $Zn_{1-x}Mg_xO$

with Mg content x = 0.2.

Suppose the volume of the total solution is 300 ml. Therefore, volume of the NaOH solution is 103 ml and volume of the zinc and magnesium acetate solution is 197 ml (maintaining the ratio 65:125).

For 45 mM and 103 ml NaOH solution in ethanol, NaOH required is 185.5 mg.

For stoichiometric doping the molecular weight has to be considered in the following way:

The mole fraction x of Mg in ZnO (Mg content) considered in this case is 0.2. Hence, the molecular weight fraction of $Zn(CH_3COO)_2.2H_2O$ is 219.49×(1-0.2) = 175.592.

The molecular weight fraction for $Mg(CH_3COO)_2.4H_2O$ is 214.46×0.2 = 42.892.

Hence, the total molecular weight that has to be considered in case of stoichiometric mixing of $Mg(CH_3COO)_2.4H_2O$ in to $Zn(CH_3COO)_2.2H_2O$ with x=0.2 is (175.592 + 42.892) = 218.484.

Therefore the total amount of $Mg(CH_3COO)_2.4H_2O$ and $Zn(CH_3COO)_2.2H_2O$ required for 197 ml solution is (218.48)×15×197/1000 = 645.60 mg.

Finally the amount of $Zn(CH_3COO)_2.2H_2O$ required is (175.592×645.6)/218.484 = 518.85 mg, and $Mg(CH_3COO)_2.4H_2O$ required is (42.893×645.6)/218.484 = 126.75 mg.

The chemical compositions x were confirmed by inductively coupled plasma atomic emission spectroscopy (ICPAES) and energy dispersive x-ray analysis. The synthesized nanostructures are in the size range of 10-20 nm. It has been observed that the synthesized alloy nanostructures show phase segregation for higher concentrations of $Mg(CH_3COO)_2.4H_2O$ and forms a core shell type structure (with ZnMgO as core and $Mg(OH)_2$ as shell) for x= 0.55 in the solution.

2.3.3 Synthesis of $Zn_{1-y}Cd_yO$ alloy nanostructures

The major challenge faced in the solution route synthesis of $Zn_{1-y}Cd_yO$ alloy nanostructures is that the CdO is formed at relatively high temperature (more than 200^0C) which is much higher than the boiling point of most of the solvents generally used for solution synthesis. Also because of different crystal structures of ZnO (wurtzite) and CdO (rock salt), they tend to get phase separated very easily. To overcome these problems, the $Zn_{1-y}Cd_yO$ has been synthesized in an autoclave at high pressure (∼55 atm.). High vapour pressure increases the boiling point of solvents like ethanol which allow relatively higher temperature synthesis. At this high temperature and pressure, $Zn_{1-y}Cd_yO$ nanostructures form along with CdO. The nanostructures formed consist of both particles and as well as rods of good crystallinity and optical quality. As described earlier in figure 2.3, $Zn_{1-y}Cd_yO$ nanostructures are synthesized by the same acetate route using a mixture of cadmium acetate and zinc acetate in ethanol. The synthesis of undoped ZnO nanostructures have been also done under high pressure where 15 mM zinc acetate dihydrate and 45 mM sodium hydroxide solution in ethanol have been used as precursors. The ZnO nanostructures of average sizes varying from 15-20 nm are formed after two hours reaction within the autoclave. The nanostructures thus fabricated are sonicated for half an hour to reduce the agglomeration. To obtain the $Zn_{1-y}Cd_yO$ nanostructures, an ethanol based solution with desired amount (to achieve stoichiometric mixing) of zinc acetate dihydrate, cadmium acetate dihydrate and sodium hydroxide was prepared and similar steps as described above have been followed. The dispersed solution contains two phases: the hexagonal $Zn_{1-y}Cd_yO$ of average size 15-20 nm and CdO of average size 70 -80 nm having rock salt structure. Precipitation of only CdO particles is possible by centrifuging the solution at 2000 r.p.m. for one minute. The filtrate containing $Zn_{1-y}Cd_yO$ is again centrifuged at 5000 r.p.m. for four minutes to get the precipitation. The $Zn_{1-y}Cd_yO$ precipitate is again dispersed in
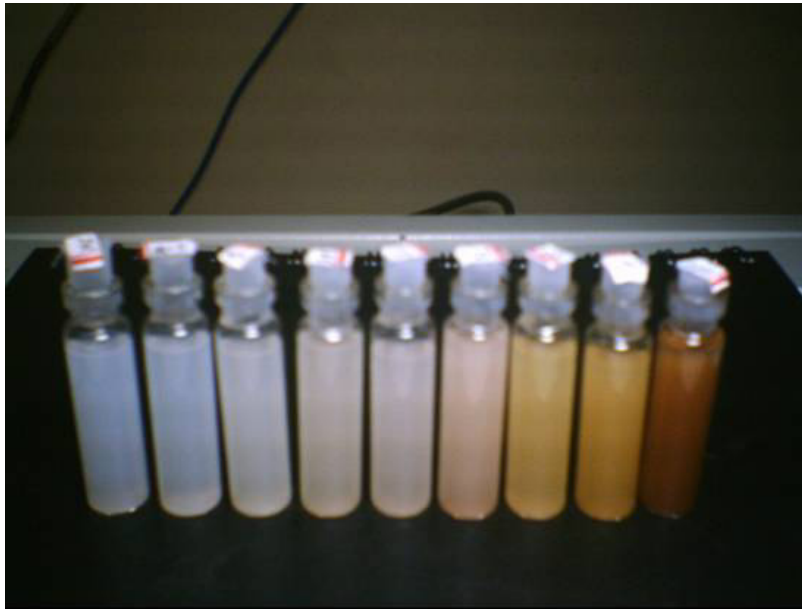
Figure 2.4: ZnO and ZnCdO nanostructues dispersed in ethanol. Colour changes gradually from bluish to redish for increase in Cd concentration is clearly visible.

ethanol and centrifuged for several times to wash the material. Figure 2.4 shows the colour contrast seen for various concentration of Cd in the synthesized $Zn_{1-y}Cd_yO$ nanostructures. The colour become reddish as the concentration of Cd increases due to the presence of increased amount of CdO in the sample.

2.4   Growth of compact and aligned ZnO nanorod arrays

One of the important physical forms of ZnO nanostructures that have attracted considerable attention is the one dimensional (1D) nanorods. A cost effective method to grow large aligned arrays of ZnO nanorods is a low temperature chemical method [32]. This method which uses a seed layer of ZnO nanoparticles to nucleate the growth process falls in the general class of nanostructure growth through site specific nucleation. In this method, aerial density of the random array of nucleation sites provides an easy way to control the density and overall orientation of the nanorod arrays [43]. An important challenge in this method of growth is the optimization of preferred orientation as well as the size of the nanorod arrays by controlling the density of the seed nanoparticles. In this section we address this specific issue which has not been addressed to in details in earlier work in this field. The purpose of this work is to establish the different growth parameters and how they control the growth of the array and the alignment of the nanorods. We study the effect of seeding density, the microstructure of the seeding layer as well as the growth time on the growth and alignment of the nanorods.

We note that the synthesis of microstructures/nanostructures of ZnO by hydrothermal /chemical method has already proven to be advantageous because of its low cost, freedom from strain and morphology controllable extended area synthesis compared to the other vapour

phase methods like evaporation and condensation ([44], [45]), physical vapour deposition ([46], [47]) and chemical vapour deposition ([48], [49]). In the hydrothermal method, the morphology of the ZnO crystals can be easily controlled by varying the growth conditions such as growth time ([50]), growth temperature ([51]), pH ([52]), and absorbing molecules ([56]). The resulting nanocrystals show different optical properties depending on their growth conditions ([57], [58]). Optimization of growth parameters for the aligned arrays of nanorods by this method is the principal motivation of this work.

Now let us focus on the synthesis and optical properties of compact and aligned ZnO nanorod arrays (dia∼50-200 nm) grown on a glass substrate with varying seed particle density. The suspension of ZnO nanoparticles (size ∼15 nm) of various concentrations are used as seed layer for the growth of nanorod arrays via self- assembly of ZnO from the solution. We have studied the effect of various growth parameters such as seeding density, microstructure of the seed layer as well as the growth time on the growth and alignment of the nanorods. We found that the growth, aerial density and alignment of the nanorods depend on the density of seed particles which can be controlled. It is observed that there is a critical density of the seed particles at which nanorod arrays show maximum preferred orientation along [002] direction. The minimum and maximum radius of the aligned nanorods synthesized by this method lie in the range 50-220 nm which depend on the seeding density and the time of growth. These nanorods have a band gap of 3.3 eV as in the case of bulk crystals and show emission in the UV region of the spectrum (∼400 nm) due to excitonic recombination and also defect related emission in the visible region.

2.4.1   Growth protocol

A two step process has been followed to grow the ZnO nanorods from ZnO seed particles in this low temperature method ([23], [50]). In the first step, we have synthesized ZnO nanoparticles of diameter ∼15 nm to use them as a seed layer on a glass substrate. In the second step ZnO nanorods have been grown on the seeded layer as described by the flow diagram in figure 2.5.

Step-I: ZnO nanocrystals to be used as seed layer have been synthesized by acetate route as described elsewhere ([59], [60]). Briefly, 50 mM zinc acetate dihydrate and 100 mM NaOH solution in ethanol were reacted for six hours at temperature $70 - 75^0C$ to produce ZnO nano crystals of size 15 nm. Our objective is to control the density of the nanorods that were grown on these seeds. The density of the rods grown, depend on the density of the seed particles. To grow the nanorod arrays with controlled density we have prepared ZnO nanoparticles suspended in ethanol with different concentrations over a wide range (3 orders). This was done by the method of evaporation and dilution of the mother solution obtained as described above. For the labeling purpose nanoparticle suspensions are assigned by the strength of relative concentrations. The mother ZnO suspension corresponding to the $Zn(CH_3COO)_2.2H_2O$ concentration of 50 mM has been assigned as 1. Relative concentration of 0.01 and 0.1 is achieved by 100 and 10 times dilution respectively. Relative concentration higher than 1, such as 5 and 10 have been achieved by maintaining the final volume at 1/5th and 1/10th of the initial volume of the mother solution by the method of evaporation. These nanocrystal suspensions are then used to produce a seed layer of different seed particle density by dip coating on a glass substrate. The seeded substrates were heat treated for 1 hour at temperature 120^0C for better adhesion of the seed particles to the substrate. The seed layers thus prepared, act as nucleating sites leading to aligned growth of nanorods. It is important to realize, as we will show below that the seed layer thus formed has varying microstructure and that changes the growth pattern of the rods. We study and

characterize the microstructure and show that the size and density of the rods grown depend on the nature of the microstructure of starting seed layer.

Prior to seeding, the substrate has been cleaned by the following method to make the surface hydrophilic. First, the substrates have been boiled in tricloroethylene, acetone and methanol in sequence for 5 minutes each. In between each step the substrates were cleaned with enough de-ionized water. Then the substrates were dipped into the concentrated NaOH solution (1M) and sonicated for 15 minutes. After that the substrates were again rinsed using enough deionized water and finally one drop of dilute HCl was added into the water containing the substrate. To avoid dust particle coating on the surface the substrates were generally kept ready inside a water column for future use.

Step-II: The seeded quartz substrate was placed upside down inside a beaker containing an aqueous solution of 30 mM zinc nitrate hexahydrate and 30 mM HMT solution in water kept at 95^oC. Synthesis of nanorods on the substrate, kept inside the solution have been performed by allowing a growth time of 3-30 hours along with constant stirring. To control the rod diameter and length, the growth time and seed particle diameters were varied. To grow the density controlled nanorod arrays we have prepared ZnO nanoparticles with five different concentration of $Zn(CH_3COO)_2.2H_2O$, viz. 0.5 mM, 5 mM, 50 mM, 200 mM and 500 mM by the method described in step-I. For the analysis purpose ZnO dispersions are assigned by a relative concentration. ZnO dispersion corresponding to the $Zn(CH_3COO)_2.2H_2O$ concentration of 50 mM has been assigned as 1 and so the others by maintaining the ratio. The density controlled ZnO nanorod arrays have been grown on the substrate coated with seed particles of different concentrations for five hours. The seeded substrates were heat treated for 1 hour at a
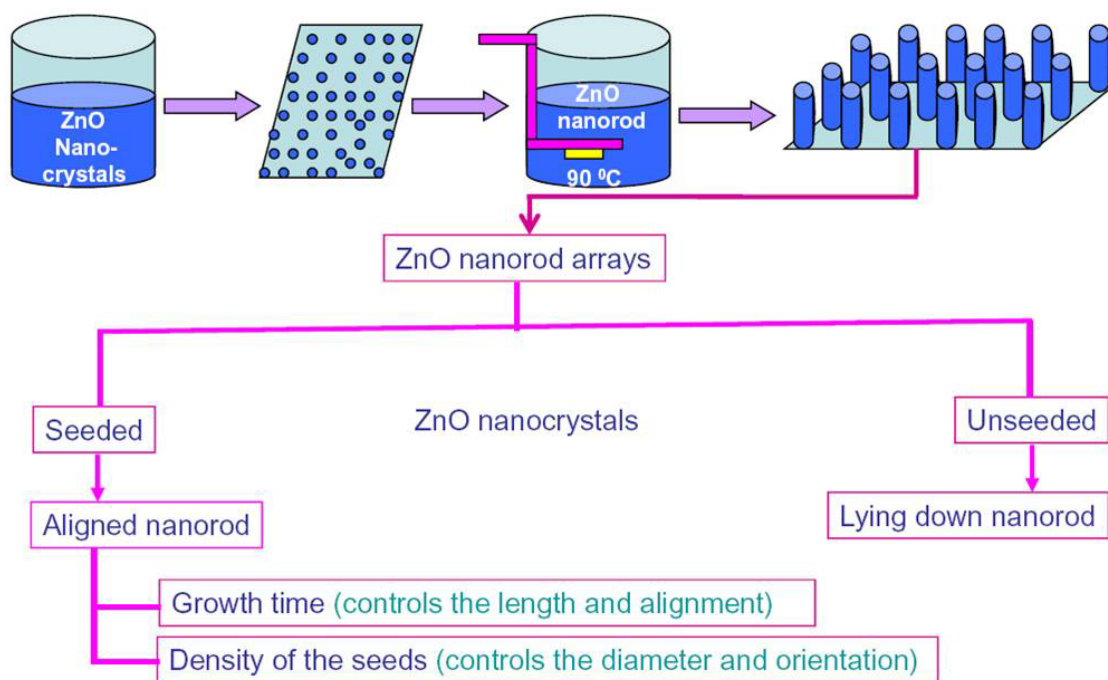
Figure 2.5: Outline of the synthesis scheme of ZnO nanorods.

Figure 2.6: Arrangement showing the nanorod growth in a solution. The seeded substrates were kept upside down at the bottom of the tefflon stand dipped into the solution.

temperature of $60^o C$. The substrate seeded with ZnO nanoparticles has been carefully placed on a specially designed substrate stand using which upto 10 substrates can be used in parallel to grow nanoparticles [figure 2.6]. The substrates were fixed upside down on the stand and dipped into the solution bath with constant stirring. After desired time of growth, the samples were taken out of the solution, rinsed with de-ionized water and dried in an oven preset at $120^o C$.

In the synthesis process, zinc nitrate hexahydrate $(Zn(NO_3)_2.6H_2O)$ and hexamethylenete-tramine $(C_6H_{12}N_4)$ were used to prepare the solution, in which the hexamethylenetetramine acts as a pH buffer to regulate the pH value (pH = 6.5) of the solution by slow supply of OH^- ions and produces a buffer effect to maintain the final pH at constant level [35]. This has been explained by the following chemical reactions:

$$(CH_2)_6N_4 \ + \ 6H_2O \ \Rightarrow \ 6HCHO \ + \ 4NH_3$$

$$NH_3 \ + \ H_2O \ \Rightarrow \ NH_4^+ \ + \ OH^-.$$
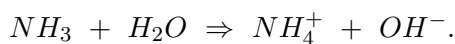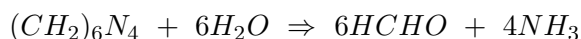
As the concentration of these Zn^{2+} and OH^- ions exceeds a critical value, the precipitation of ZnO nuclei starts. The $Zn(OH)_2$ can be transformed into ZnO crystals via these simple chemical reactions:

$$Zn^{2+} \ + \ 2OH^- \ \Rightarrow \ Zn(OH)_2$$

$$Zn(OH)_2 \ \Rightarrow \ ZnO \ + \ H_2O.$$
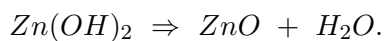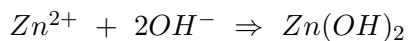
The precipitates of $Zn(OH)_2$ are more soluble as compared to the ZnO precipitates. There-

fore it is proposed that the $Zn(OH)_2$ precipitates formed tend to continuously produce Zn^{2+} and OH^- ions, which form the ZnO nuclei. The ZnO nuclei thus formed are the building blocks for the formation of the final products.

2.4.2   Important growth parameters and quality of the rods grown

Now we focus on the growth process of the nanorods and the important parameters that need be varied to get control on the diameter and alignment of the rods. In this subsection we establish these parameters and also show the structural as well as the optical quality of the rods grown by this method.

From an analysis of the growth process as described below we make the hypothesis that there are two important factors in the growth process that make crystallographically aligned nanorods. The first factor is the anisotropy in the growth rate of ZnO for different crystal faces which determines the morphology as well as the aspect ratio of the crystal ([61]). In this crystal the c-axis has the fastest direction of growth and in any growth process growth along this direction wins over. Thus one obtains nanorods which have their growth axis along the c-axis. It is demonstrated that the grown rods have a limiting average aspect ratio (length/diameter
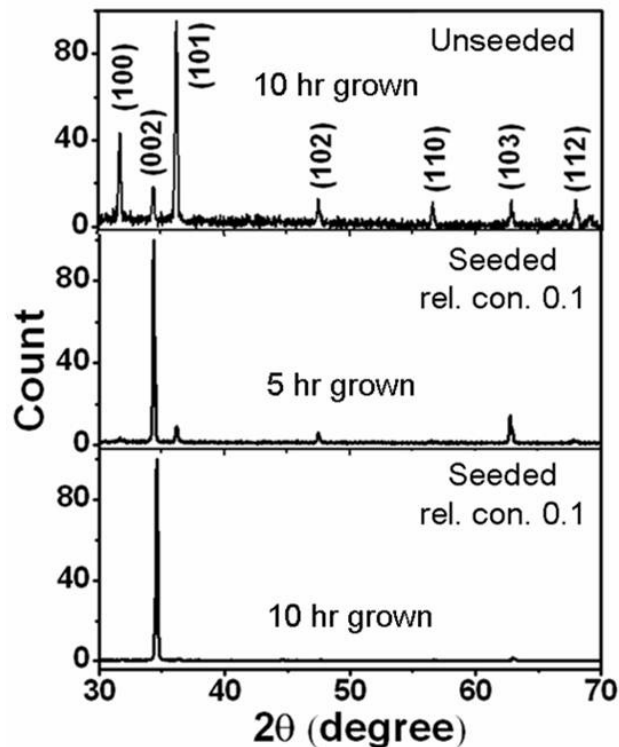
Figure 2.7: XRD data of the ZnO nanorods for the growth condition as indicated on the graph. The lower and middle panel shows the XRD data for 10 hour and 5 hour grown samples respectively. The rel. conc. of seed particle is 0.1 for both the cases. Preferred growth along [002] direction is higher in case of longer growth time. The top panel shows the XRD data of ZnO nanorods grown on an unseeded surface.

= 7) [ref. [50]]. The second issue is that of alignment of the grown rods. We propose that the alignment of the grown rods is mainly from crowding effect which limits axial growth of the rods parallel to the substrate. We explain this in the subsection below.

In the present study, unmodified surface of the glass substrate has been pre-coated by a seed layer of ZnO nanoparticles. The seed layer as well as the grown rods have been characterized by the techniques like Transmission Electron Microscope (TEM), Scanning Electron Microscope (SEM) and X-ray Diffraction (XRD) as briefly described in the last section of this chapter. The TEM image of nanoparticles used for seeding is shown in figure 2.8(a). It is the same material as the nanorods to be grown, and hence provides a homogeneous nucleation site for the growth of ZnO nanorods. Seeding the substrate by the nanocrystals is an effective way to control the orientation of the deposited crystals. Site-specific nucleation at the seed particles is essential to obtain aligned nanorod arrays perpendicular to the substrate. In this investigation we want to establish the extent to which the aerial density of the seed particles is a key factor in determining the overall orientation of the nanorod arrays. This will be discussed in the next section.

Longer growth time results in better alignment along the direction perpendicular to the substrate. The XRD patterns of the nanorod arrays grown on a seed layer of relative concentration 0.1 for 10 hrs (figure 2.7) shows a single peak due to the reflection from (002) planes. Nanorod arrays grown for 5 hrs on seed layer of similar concentration show almost all the peaks of wurtzite ZnO. However the intensity profile is radically different from a powder diffraction pattern.

Growth of ZnO nanorods is also possible on an unseeded surface. But these nanorods are not at all aligned in a certain direction and they follow a random growth pattern. This fact is also reflected in the XRD results indicated in figure 2.7. The intensity ratios of (100) and (002) peaks to the highest intensity peak (101) of wurtzite ZnO (indexed in the figure 2.8) agree well with the bulk ZnO (Zinc white) values 0.71 and 0.56 respectively, which confirms the random orientation of the nanorods grown on the substrate. Since the seed crystal provides a homogeneous nucleation site, which has (002) planes parallel to the substrate, further deposition occurs along [002] direction perpendicular to the substrate. On the other hand unseeded surface
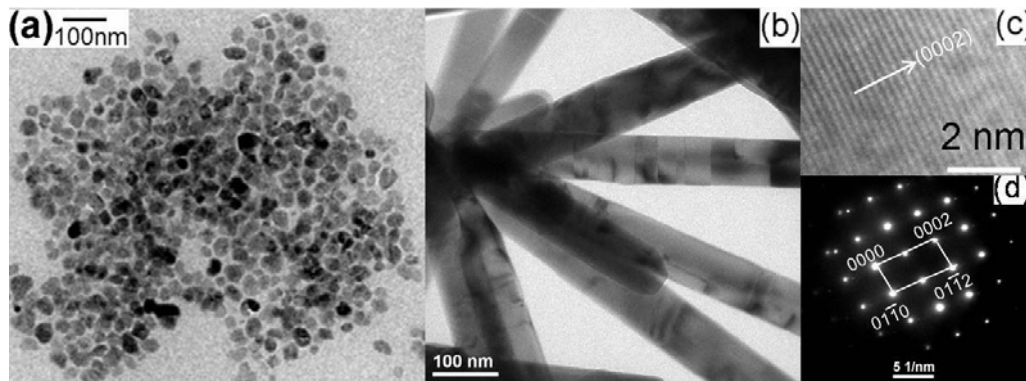
Figure 2.8: (a) TEM image of the seed nanoparticles taken on a grid from a suspension in ethanol. (b) TEM image of ZnO nanorods grown for 5 hours. (c) The lattice image of the nanorods. The distance between lattice fringes is 2.66 Å which confirms the nanorods growth along [002] direction. The indexed SAED pattern of the nanorods confirms the hexagonal symmetry of the single crystalline ZnO nanorods (d).

provides heterogeneous nucleation sites ([62]) which has complex nature and prompts growth of nanorods along random directions as discussed in the next section.

These nanorods grown using the low temperature growth method are crystalline and show good optical properties. The lattice image of the nanorods shown in figure 2.8 (b) is depicted in figure (c). The distance between lattice fringes is 2.66 Å which confirms that the nanorods grow along [002] direction. The indexed SAED pattern confirms single crystalline nature of the hexagonal ZnO nanorods as shown in figure 2.8 (d).

2.4.3   Effect of aerial density and size of seed particles on the grown ZnO nanorods

In the growth of nanorod arrays by site specific homogeneous nucleation via seeding of the substrate, it is expected that the density of the seed particles should have a close correlation with the density of the nanorods grown on them. This particular aspect, however, has not been investigated in quantitative details before. In our experiment we study this specific issue. Also the minimum and the maximum size of the grown nanorods have been determined.

The important point that emerges from our investigation is that there is no one to one relation between the number of nanoparticles and the number of nanorods grown. The number of seed particles is always much larger than the number of the aligned rods. The ideal situation where one nanorod growth takes place from a single seed particle is not valid. This would have happened if each of the seed particles were oriented in one direction and all of them acted as a nucleus. To examine the actual scenario we have performed analysis of seeding layers with four different densities and then the nanorod arrays are grown on them. (The seed layer has random crystallographic orientation as confirmed by XRD). From this analysis we observe that processes
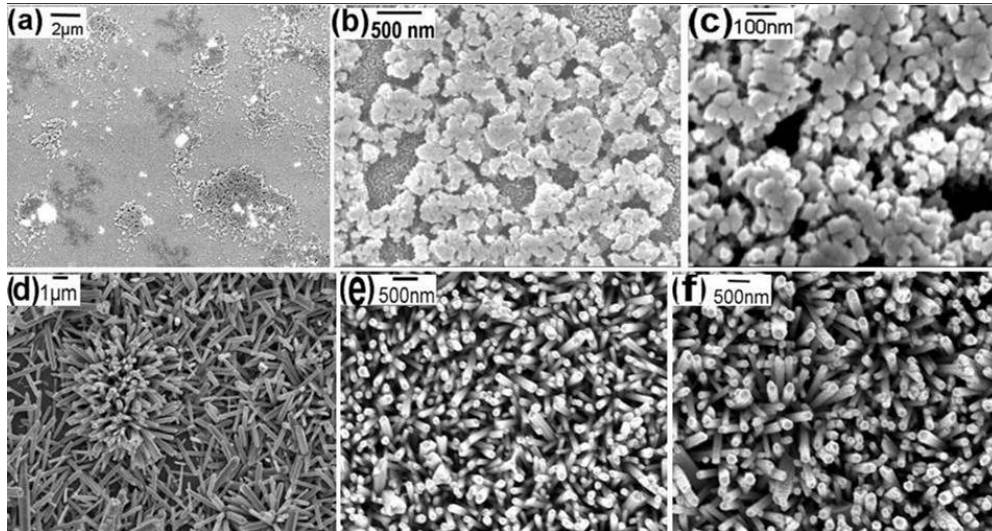
Figure 2.9: SEM images of ZnO seed particles dip coated on the glass substrates and the nanorods arrays grown on them for 5 hour. (a), (b) and (c) are the SEM images of seeded layers having relative concentrations of seed particles 0.01, 1 and 10, respectively. (d), (e) and (f) are the top view of the nanorods arrays grown on (a), (b) and (c) respectively.

like dip coating or spin coating of the substrate by the nanoparticle solution do not produce a uniform seed layer of same seed particle diameter as in the suspension. There is formation of aggregate that accompanies these coating processes as the particles are not capped. TEM image of a collection of seed particles (figure 2.8 (a)) taken from the suspension, reveals a narrow diameter distribution with mean value around 15 nm. But the seed layer on the substrate produced after dip coating of the same particles, followed by a heat treatment for 1 hr at $120^0 C$, shows that the seed particles get agglomerated and formation of multiple layers of seed particles is observed for higher concentration.

Table 2.2: Density and diameters of the nanorods grown for 5 hrs on seed layer of different concentrations

Rel. conc. of seed particles	Rod-density (m^{-2})	Rod diameter (nm)	$I_{(002)}/I_{(101)}$
0.01	No aligned rods	150 - 220 length $\sim$ 2 m	1.9
0.1	41	50 - 150	22.9
1	60	50 - 100	226.7
10	45	75 - 175	108.6

Figure 2.9 (a), (b) and (c) show the SEM images of seeded layers for seed particle relative concentrations (see experimental section) of 0.01, 1 and 10 respectively and (d), (e) and (f) are the respective nanorod arrays grown on them for 5 hrs. In table 2.2 we collect the relevant data. In the last column we show the ratio $I_{(002)}/I_{(101)}$ which is the ratio of the intensities of the (002) and (101) lines in the XRD data and is a measure of the alignment. Higher the ratio, better is the alignment of the grown rods in the (002) direction. Dip coating of lowest concentration (rel. conc. 0.01) seed particles on a large area produce highly discontinuous seed layer (figure 2.9 (a)). Major part of the surface does not have any seed nanocrystals. This prompts growth of nanorods in random direction on most part of the substrate as shown in figure 2.9 (d). For higher relative concentration such as 1 and 10 shown in figure (b) and (c), improved continuity of the seed layer is observed. Formation of multiple layers of the seed particles is seen for rel. conc. 10 as shown in figure (c). Figures 2.9 (d), (e) and (f) show compact growth of nanorods on these seed layers. As discussed in the next section, formation of multiple layers has implication on the preferred orientation of nanorod arrays grown on them. However, the number density of rods is maximum for the nanorod arrays [figures 2.9 (e)] grown on almost uniform single layer of seed particles, corresponding to rel. conc. 1 (see Table 2.2). Smaller number density as well as poorer alignment (see table 2.2) is observed for nanorods grown on seed layers of rel. conc. higher or lower than 1.

Analysis of the growth data shows that the average diameter of the nanorods grown increases when the density of the nanorods decreases. It is due to the fact that lateral growth of the nanorods gets limited by the surrounding nanorods due to crowding effect when the density is higher. It is interesting to note that the approximate grain sizes of the agglomerated seed particles after dip-coating on the substrate is $\sim$40-50 nm although the exact size of the nanocrystal in the suspension was found to be $\sim$15 nm [see the TEM image in figure 2.8 (a)]. Thus there is clear evidence of agglomeration on coating the seed particles. Because of this reason, ZnO

nanorod arrays grown on such type of seeded layer is almost always greater than 40 nm [32] and rod diameter less than 40-50 nm obtained by seeded growth is rarely reported even when one starts with crystals of smaller size.

Nanorods have relatively higher average diameter (although with poorer alignment) on a seed layer of very low particle density [figure 2.9 (e)] which contains large surface area depleted of seed particles as in the case of relative concentration 0.01 (Table 2.2). This confirms that the upper limit of the diameter of the nanorods grown has a dependence on the average separation of distinct nucleation sites. A lower average density gives more space for lateral growth and hence larger diameter of the nanorods although absence of crowding leads to poor alignment.

2.5 Control of the preferred orientation of the ZnO nanorod arrays

The introduction of ZnO seed layers of different concentration on the substrate not only controls the rod density but also has a strong impact on the orientation of the nanorod arrays. However, the preferential growth of ZnO nanorods along [002] direction is reported to increase as the seed particle density increases ([43]). But in this thesis we show that there is a critical density of the seed particles for which the preferred orientation in [002] direction is maximum for a given growth time. A clear analysis of the preferential growth along [002] direction is possible if we follow the intensity ratio of the (002) peak to intensity of the peak (101). [Note: In ZnO powder diffraction pattern, the highest intensity peak is the (101) peak]. The XRD data of
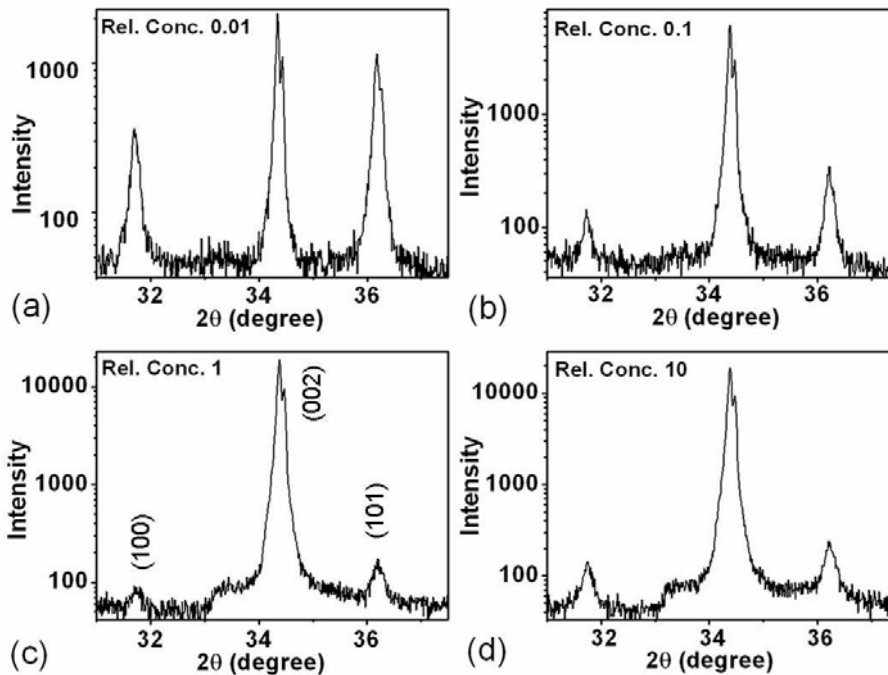
Figure 2.10: XRD data of the five hour grown nanorods on seed layer of rel. conc. (a) 0.01 (b) 0.1 (c) 1 and (d) 10. For clarity only three peaks have been shown.
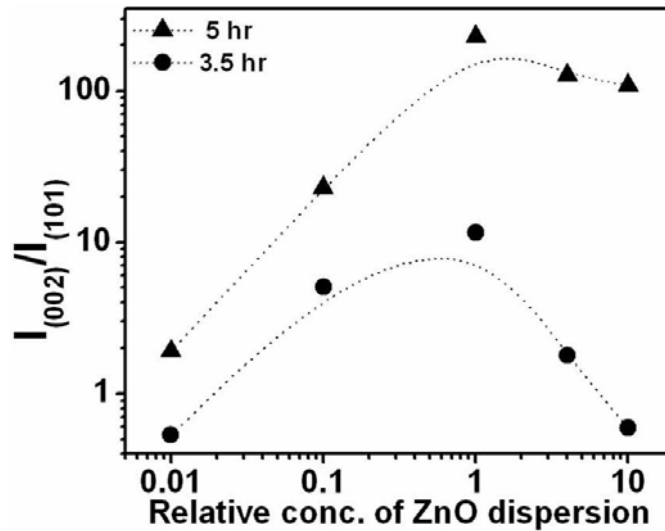
Figure 2.11: The intensity ratio between the peaks due to (002) and (101) reflections in the XRD data is plotted against the rel. conc. of seed particles for the nanorod arrays grown for 3.5 and 5 hrs as indicated in the figure. There is a critical concentration of the seed particles (rel. conc. 1) when the preferred growth along [002] direction is maximum.

five hour grown nanorod arrays for different seed particle density (indicated in the graph) is shown in figure 2.10. The ratio $I_{(002)}/I_{(101)}$ is a good measure of the orientation alignment of the nanorods. In figure 2.11 we plot the intensity ratio $I_{(002)}/I_{(101)}$ for 3.5 and 5 hours grown ZnO nanorod arrays. It can be clearly seen that there is a critical concentration of ZnO seed particles (relative concentration 1) for which preferred orientation of ZnO nanorods along [002] direction is maximum. The ratio, first increases as we increase the seed particle density (up to rel. conc. 1) and again decreases for higher values of seed particle densities (upto rel. conc. 10 has been shown). Much higher value of $I_{(002)}/I_{(101)}$ for 5 hours grown nanorod arrays compared to 3.5 hours grown rods is expected for obvious reason since longer growth time results in better alignment.

A plausible explanation for the existence of a critical density in the oriented growth is given below. At very low concentration of the starting solution, the coverage is low and there are islands of seed particles but a good fraction of the surface being exposed, it provides sites for heterogeneous nucleation that leads to random growth. As the coverage increases, the smooth layer forms a smooth film, and one obtains better orientation as the nucleation takes place from the large number of homogenous nucleation sites. At higher coverage the films becomes less smooth due to formation of a second layer that is not complete and there are sites where there are larger aggregates of the seed particles. This leads to large undulation (crest and trough) on the surface. The part of the exposed surface of seed layers parallel to the surface (top of the crest and bottom of the trough), contains seed nanoparticles with exposed top surface which has (002) plane parallel to the substrate which leads to aligned nanorods perpendicular to the substrate. But at the walls of the crest, the exposed part of the seed particles is not parallel to the substrate and the growth from these sites can be random leading to gradual reduction of the alignment.

For the unseeded surface the density of the growing nanorods is low. In this case though the growth preferentially occurs in the [002] direction, the wires are mostly lying down on the substrate with random orientation. However, for the seeded surface the aerial density is larger. The alignment in the direction perpendicular to the substrate happens due to crowding effect that prevents axial growth parallel to the substrate and the alignment generally becomes better as the growth time progresses. Thus the alignment of the nanorods as well as the aspect ratio depends on the growth time and the initial seeding density, which are the two important controllable parameters involved in the growth of nanorods. Both these factors in tandem decide the intimate extent of orientation achieved.

In conclusion, the density controlled ZnO nanorod arrays on seeded layers by a two step low temperature method have been successfully grown. The overall orientation of the nanorod arrays has been observed to be dependent on the density of the seed particles. The nature of the growth processes of the controlled nanorods arrays have been studied through SEM and XRD analysis. It is observed that there is a critical density of the seed particles (rel. conc. 1, corresponding to 50 mM zinc acetate dihydrate solution) at which nanorod arrays show maximum preferred orientation along [002] direction. These nanorod arrays are single crystals and show good optical quality.

2.6   Characterization techniques and methods of analysis

The principal characterization tools used are TEM (Transmission Electron Microscope), SEM (Scanning Electron Microscope) and X-ray diffraction (XRD). The nanoparticles were imaged and their lattice images were taken with a JEOL high-resolution transmission electron microscopy (HR-TEM) at 200 KeV. The seed layer and the nanorod arrays grown on them have been analyzed through scanning electron microscope (SEM). The X-ray diffraction data were collected by a Philips Xpert Pro X-ray diffractometer. Room temperature optical properties were studied by photoluminescence spectrometer (Jobin Yvon, FluoroMax-3) where a xenon arc lamp has been used as illumination source.

2.6.1   Microstructural analysis by TEM

Electron Microscopes are scientific instruments that use a beam of highly energetic electrons to examine objects on a very fine scale which yield information about (i) the surface features of an object (Topography), (ii) shape and size of the particles (morphology), (iii) elements and compounds that the object is composed of and the relative amounts of them (composition), and (iv) crystallographic information (how the atoms are arranged in the object).

In a conventional transmission electron microscope, a thin specimen is irradiated with an electron beam of uniform current density. Electrons are emitted from the electron gun and illuminate the specimen through a two or three stage condenser lens system (figure 2.12). Objective lens provides the formation of either image or diffraction pattern of the specimen. The electron intensity distribution behind the specimen is magnified with a three or four stage lens system and viewed on a fluorescent screen. The image can be recorded by direct exposure of a photographic emulsion or an image plate or digitally by a CCD camera. The acceleration voltage of up to date routine instruments is 120 to 200 kV. Medium-voltage instruments work at 300-500 kV to provide a better transmission and resolution, and in high voltage electron microscopy (HVEM) the acceleration voltage is in the range 500 kV to 3 MV. Acceleration
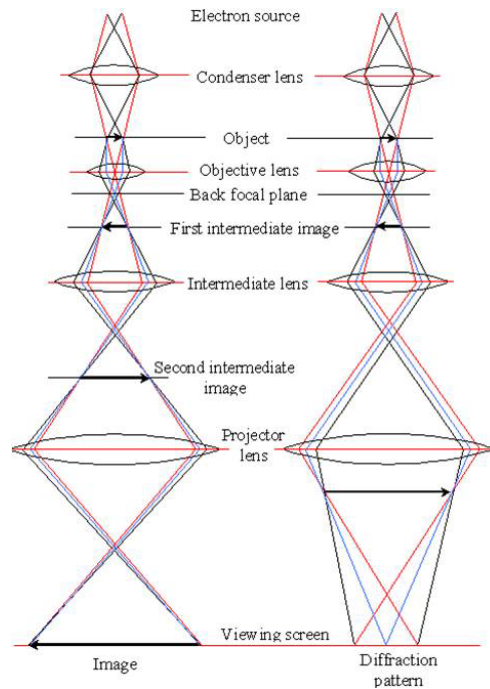
Figure 2.12: The electron optics and major components of a Transmission Electron Microscope.

voltage determines the velocity, wavelength and hence the resolution (ability to distinguish the neighbouring microstructural features) of the microscope. Depending on the aim of the investigation and configuration of the microscope, transmission electron microscopy categorized as i) Conventional Transmission Electron Microscopy ii) High Resolution Electron Microscopy iii) Analytical Electron Microscopy iv) Energy-Filtering Electron Microscopy v) High Voltage Electron Microscopy vi) Dedicated Scanning Transmission Electron Microscopy. The image of the specimen in conventional microscopy is formed by selectively allowing only the transmitted beam (Bright Field Imaging) or one of the diffracted beams (Dark Field Imaging) down to the microscope column by means of an aperture (figure 2.12). The origin of the image contrast is the variation of intensities of transmitted and diffracted beams due to the differences in diffraction conditions depending on the microstructural features on the electron path. Electrons of 200 kV excitation transmitted through about 0.1 micrometer thin foil specimen are diffracted according to Bragg's Law, forming a diffraction pattern (consisting of a transmitted and diffracted beam spots). Although diffraction phenomenon is a complex interaction of charged electrons with the periodic potential field of the lattice, Bragg's Law or Laue Conditions are sufficient approximations for usual practical applications. A diffraction pattern is, in the simplest sense, a Fourier transform of the periodic crystal lattice, giving us information on the periodicities in the lattice, and hence the atomic positions (table 2.3).

Indexing of the diffraction patterns: Using the reduced Bragg condition $\lambda = 2d_{(hkl)}\theta$ we have $\lambda L = Rd_{(hkl)}$, where L is the distance between screen and the sample (without imaging lens) and R is the distance of the diffracted spot of interest from the central spot (see figure 2.13). With imaging lenses effective L is considered as shown in the figure. For ring patterns, radius of each ring can be converted into interplanar spacing by the above equation. If the
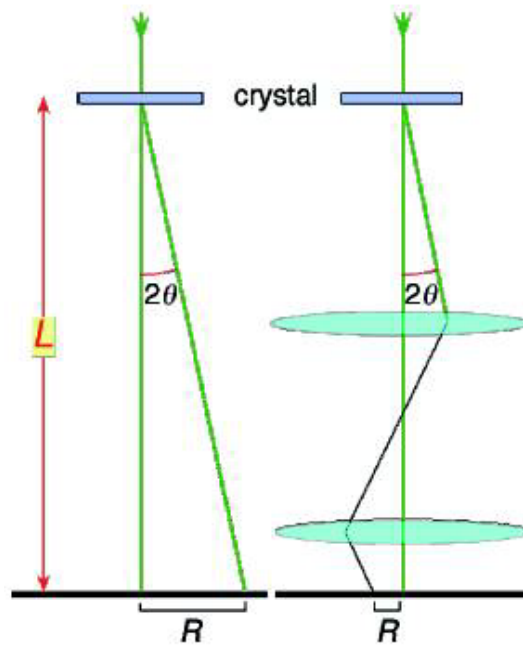
Figure 2.13: Camera length L in the presence and absence of imaging lenses.

Table 2.3: Types of diffraction pattern and their use

Type	Occurence	Use
Ring Pattern	Polycrystalline and amorphous specimen	Identification of phases
Spot Pattern	Single Crystal	i) Crystal Structure and the diffraction vectors ii) Specimen orientation in the microscope ii) Tilt axis by tilting about the bright spot
Kikuchi Lines	Inelastic scattering by a thick specimen. SADP from single crystal.	i) Accurate crystal orientation ii) Incident beam direction ii) Define the sense of tilt ii) Crystal symmetry

material is known, one can measure the ratios of the square of the diameters of the outer ring to that of the 1st or 2nd (lower index) ring. The ratios has to be checked against a table of ratios for the crystal structure of interest. For spot patterns, the distances R1, R2, of the diffracted spots from the central spot is measured. These distances correspond to the interplanar spacing of the reflecting planes and hence related to the camera length L. The angles between the lines drawn from the central spot to the diffracted spots $(h_1 k_1 l_1), (h_2 k_2 l_2)$ are the angle between the planes. In general three steps are there

- Measure R of the fundamental reflection

- Calculate the corresponding plane spacing $d_{(hkl)}$

- Index the reflections with (hkl).

In a good approximation primary beam is parallel to the reflecting planes. That is primary beam corresponds to the zone axis of the reflecting plane. If a zone includes the plane h_i and k_i, then it also includes the plane $(h_i + k_i)$. For the diffraction pattern of a single crystal this implies that after indexing two non-collinear fundamental reflections, the indices of the entire pattern follow from vector addition. The zone axis $[uvw] = Z = B$ can be determined by using the relations,

$$B = g_1 \times g_2 \tag{2.5}$$

where the spots are expressed in terms of reciprocal lattice vectors g_1 and g_2.

2.6.2 Analysis of X-ray diffraction data:

In this subsection we discuss the three analysis methods of the X-ray diffraction data adopted in this thesis.

Indexing and phase determination: The primary characterization of the nanoparticles and identification of its phase purity has been done by using powder X-ray diffraction technique. Ray optics and arrangement of the components for phase analysis in a Philips X'per Pro X-ray diffractometer which uses Cu-Kα line as a source is shown in figure 2.14. Phase identification
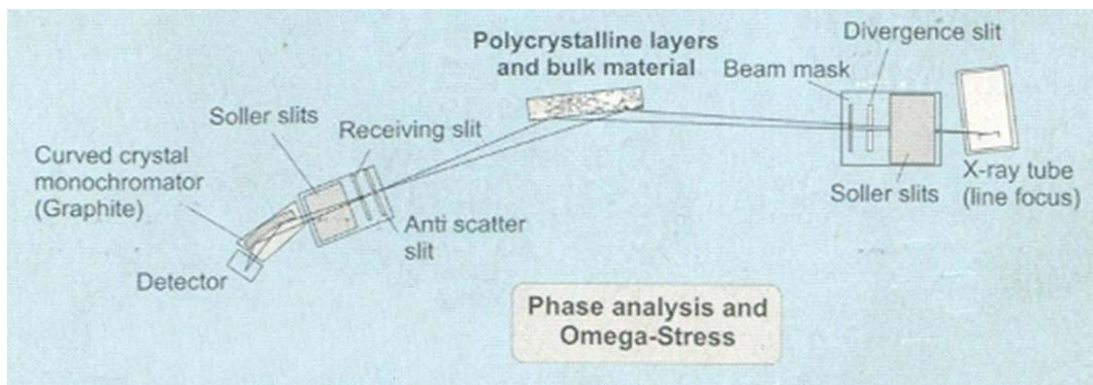
Figure 2.14: Ray optics and arrangement of the components in the X-ray diffractometer used for phase analysis.

has been done by comparing the collected data with the standard data base (powder diffraction file). An example of cubic indexing for ZnO powder profile is shown in figure 2.7.

Size and strain analysis: Two important parameters for the nanoparticles, namely crystallite size and microstrain can be obtained from the line width analysis of XRD data. There are three parameters which contribute to the broadening of the FWHM of a X-ray diffraction peak. These are i) Crystallite size ii) Strain and iii) Instrumental. The width of the diffraction curve increases as the thickness of the crystal decreases.The full width at half maximum (β) is measured in radians, at an intensity equal to half the maximum intensity. As a rough measure of β, take half the difference between the two extreme angles at which the intensity is zero, or $\beta = (2\theta_1 - 2\theta_2)/2 = \theta_1 - \theta_2$ and crystallite size (t) can be obtained by the Scherrer Equation

$$t = \frac{k\lambda}{\beta cos\theta} \tag{2.6}$$

where K is shape factor which depends on crystallite size. The value of β must be corrected for instrumental broadening i.e.,

$$\beta_{true}^2 = \beta_{measured}^2 - \beta_{instrument}^2 \quad \text{(Gaussian peaks)} \tag{2.7}$$

The Scherrers Formula is generally used when crystallite size $< 100 \ nm$ and peak broadening by other factors is negligible. If breadth is consistent for each peak then the broadening is due to crystallite size and strain. If it is inconsistent then it reflects shape anisotropy. The Scherrer
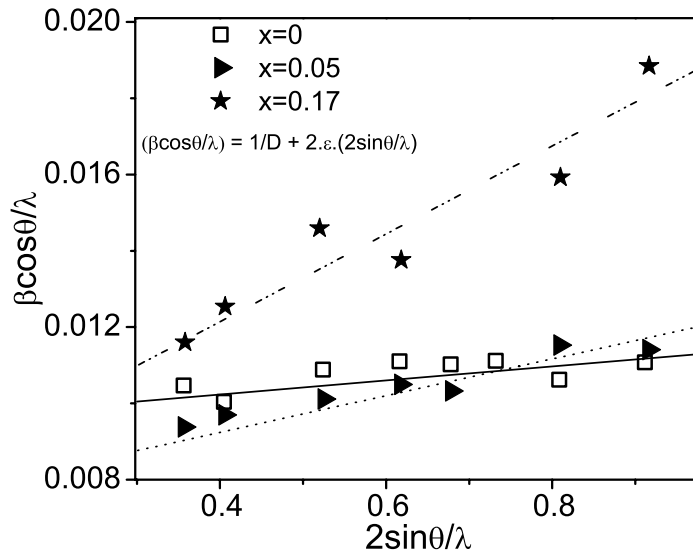
Figure 2.15: Williamson-Hall plot of three representative XRD data shown in figure 6.6. The solid line, dotted line and dashed dotted line are the linear fit of the data points corresponding to the samples undoped ZnO of size ~10 nm, x = 0.05 and x = 0.17 respectively. The average grain sizes and strain has been calculated from the y-intercept and slope of the linear fits respectively.

equation assumes that particle size is the only source of peak broadening. Average particle size and strain can be determined by a modified approach known as Williamson-Hall (W-H) analysis using simplified integral breadth method [81]. The Integral Breadth (β), defined as the ratio between peak area and the intensity maxima for both size and strain broadened profile is given by [81]

$$\beta^{\star} = \frac{1}{D} + 2\varepsilon s \quad (\text{in } sin\theta \text{ scale}) \tag{2.8}$$

where D is the average particle diameter, ε is the strain, $\beta^{\star} = \beta cos\theta/\lambda$, and $s = 2sin\theta/\lambda$. W-H analysis also allows us to find the average strain from the slope of the linear fit of the data points. This method has been applied to find out the microstrain for $Zn_{1-x}Mg_xO$ and $Zn_{1-y}Cd_yO$ nanostructures and discussed in chapter 6. An example of W-H plot extracted from the XRD data (given in figure 6.6, chapter 6) for three different concentrations (mole fraction x) of $Zn_{1-x}Mg_xO$ nanostructures is shown in figure 2.15.

Rietveld Refinement method

Theoretical background: Rietveld structure refinement [150] is a method for estimating the intensities of Bragg peaks in a powder diffraction pattern within the constraints imposed by a crystallographic space group. The entire diffraction profile is calculated (model) and compared with the observed (experimental) step profile point by point. The parameters of the model are then adjusted using the least square method. This method is introduced by Hugo Rietveld originally for neutron data. Applicability of the method has increased with increase in computing power and development of softwares like GSAS, FullProf, RIETAN, High-Score Plus etc. In this thesis XRD data analyzed by FullProf and High-Score Plus will be presented. For good results, accurate powder diffraction intensity data measured in intervals of $< 0.01^0$ (step-scan) is needed. The starting model should be reasonably close to the actual crystal structure. A mathematical model that accurately describes shapes, widths and any systematic errors in the position of the Braggs peak is used. Suppose S_y is the function to be minimized

$$S_y = \Sigma W_i(Y_i - Y_{ci})^2 \tag{2.9}$$

W_i = Weighing factor = $1/y_i$
Y_i = Observed intensity at the ith step
Y_{ci} = Calculated intensity at the ith step
Ideally $S_y = 0$

$$Y_{ci} = s\Sigma L_k|F_k|^2\Phi(2\theta_I - 2\theta_K)P_kA + Y_{bi} \tag{2.10}$$

S - Scale factor
K - Miller for a given indices reflections (hkl)
L_k - Lorentz, polarisation and multiplicity factor
Φ - Reflection profile function
P_k - Preffered orientation function
A - Absorption factor
F_k - Structure factor for the kth reflection
Y_{bi} - Background intensity at point i
$|F_k|$ depends on position of each atom

$$F_{hkl} = \Sigma N_j f_j exp[2\pi i(hx_j + ky_j + lz_j)]exp[-\frac{Bsin2\theta}{\lambda}] \tag{2.11}$$
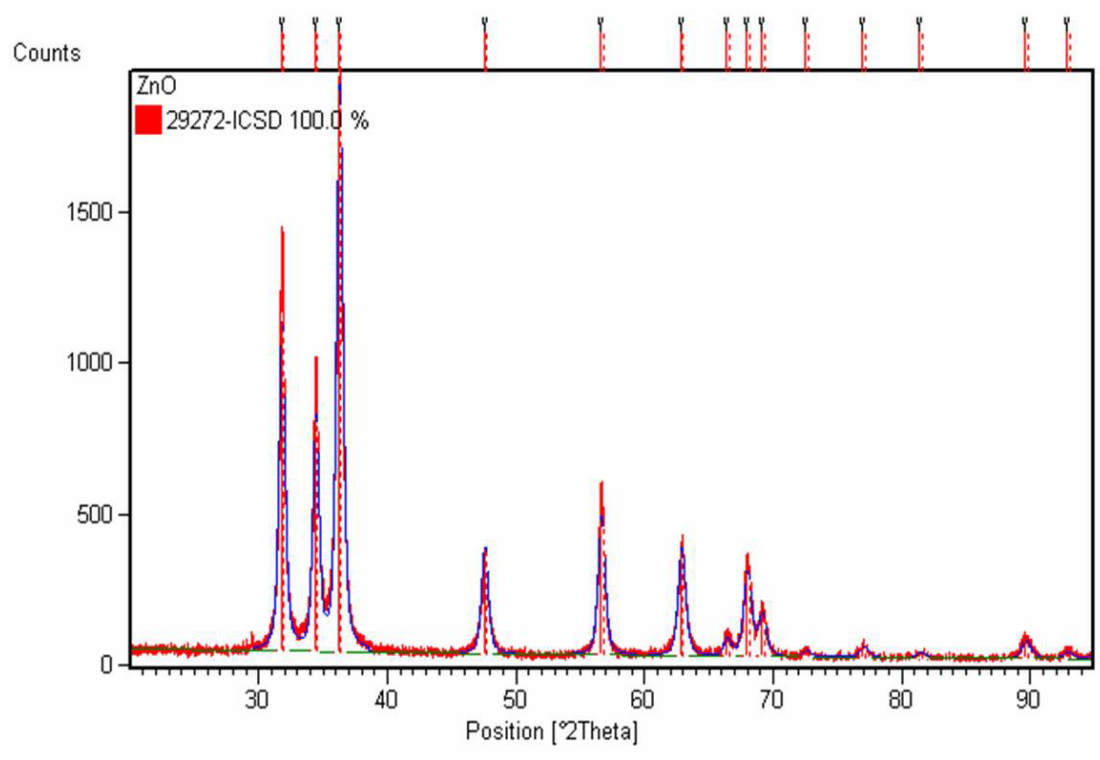
Figure 2.16: The XRD data of pure ZnO powder of size $\sim$15 nm is fitted by the HighScore Plus software following the Rietveld least square fitting procedure.

N_j - occupancy of site j (presence of vacancies)

f_j - Atomic scattering factor for atom j

$x_j y_j z_j$ -Coordinates for atom j

B -Temperature factor (thermal vibration of atoms)

Peak shape (Φ) is Convolution of sample and instrumental effects. In many applications it is described by Gaussian + Lorentzian functions (pseudo-Voigt) with refinable degree of mixing

$$pV = \eta L + (1 - \eta)G \tag{2.12}$$

pV = pseudo-Voigt function

L = Lorentzian function

G = Gaussian function

η = Mixing parameter

The Lorenzian and Gaussian functions are of fundamental importance since they reflect intrinsic contribution to the diffraction line shape from the radiation wavelength distribution, instrumental geometry and the specimen used. Pseudo-Voigt is used to model size and strain line broadening contribution simultaneously. It also allows the separation of instrumental and specimen contributions. The starting model consists of structure parameters like

1. Space group

Name	Refine	Value	Constr...
− Global Parameters			
Zero Shift [°2Theta]	✔	-0.004568	None
Specimen Displacement...	☐	0.000000	None
Wavelength [Å]	☐	1.540598	None
− Background Polyno...			
Flat background	✔	70.453110	None
Coefficient 1	✔	-0.781771	None
Coefficient 2	✔	0.002869	None
Coefficient 3	☐	0.000000	None
Coefficient 4	☐	0.000000	None
Coefficient 5	☐	0.000000	None
− 29272-ICSD	✔		
Scale factor	✔	0.010409	None
Preferred Orientation	✔	1.009807	None
B overall	✔	2.257280	None
Extinction	☐	0.000000	None
Flat Plate Absorption Co...	☐	0.000000	None
Porosity	☐	0.000000	None
Roughness	☐	0.000000	None
+ Unit Cell			
+ Atomic coordinates			
− Profile Parameters			
U	☐	0.344468	None
V	☐	0.000000	None
W	✔	0.298777	None
Anisotropic Broadeni...	☐	0.000000	None
Asymmetry (Rietveld)	☐	0.000000	None
Peak Shape 1	☐	0.600000	None
Peak Shape 2	☐	0.000000	None
Peak Shape 3	☐	0.000000	None

Name	Refine	Value	Constr...
+ Global Parameters			
− 29272-ICSD	✔		
Scale factor	✔	0.010409	None
Preferred Orientation	✔	1.009807	None
B overall	✔	2.257280	None
Extinction	☐	0.000000	None
Flat Plate Absorption Co...	☐	0.000000	None
Porosity	☐	0.000000	None
Roughness	☐	0.000000	None
− Unit Cell			
a [Å]	✔	3.248835	Multiple...
b [Å]	☐	3.248835	Multiple...
c [Å]	✔	5.207958	None
alpha [°]	☐	90.000000	None
beta [°]	☐	90.000000	None
gamma [°]	☐	120.0000...	Multiple...
− Atomic coordinates			
− Zn1			
X	☐	0.333333	None
Y	☐	0.666667	None
Z	☐	0.000000	None
B isotropic	☐	0.310000	None
Occupancy	☐	1.000000	None
+ B anisotropic			
− O1			
X	☐	0.333333	None
Y	☐	0.666667	None
Z	☐	0.382600	None
B isotropic	☐	0.550000	None
Occupancy	☐	1.000000	None
− B anisotropic			

Figure 2.17: Values of the fitting parameters for pure ZnO powder.

2. Lattice parameters

3. Atom co-ordinates

4. Site occupation factors

5. Displacement factors (temperature factors)

and global parameters (which affect the entire pattern, regardless of phase) like

1. Pattern background

2. Zero point

3. Wavelength.

Example: The least square fitting algorithm described above has been incorporated in numerous number of softwares. Two popular softwares such as HighScore Plus and FullProf have been used in our analysis. In this section, the result of two representative systems (pure ZnO and
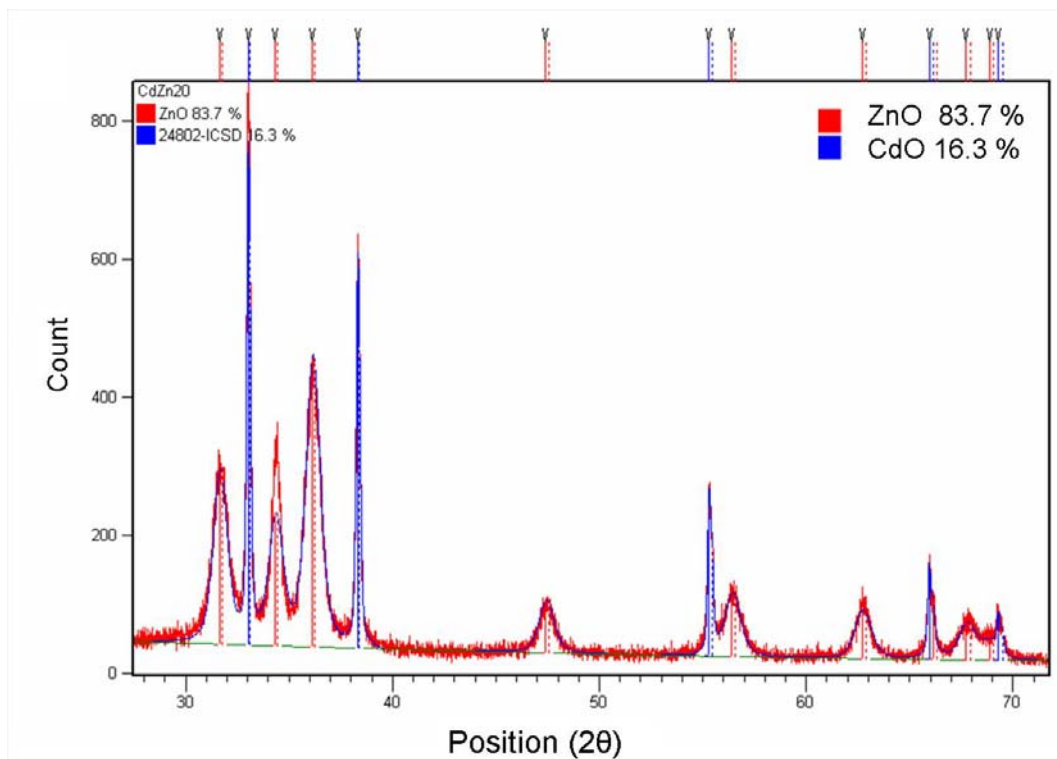
Figure 2.18: The XRD data of a mixture of CdO and $Zn_{1-y}Cd_yO$ powder fitted by the HighScore Plus software following the Rietveld least square fitting procedure.

a mixture of $Zn_{1-y}Cd_yO$ and CdO powder), extracted by fitting through the software HighScore Plus will be summarized. In the subsequent chapters few more cases will be investigated where the FullProf software is applied. In HighScore Plus the starting model can be incorporated directly from the ICSD (Inorganic Crystal structure Database). In FullProf the parameters of the starting model have been entered manually from ICSD.

In figure 2.16, pure ZnO powder data (S.G. P63mc) has been fitted by using Rietveld technique. The fitting parameters for the wurtzite ZnO phase is shown in figure 2.17. The parameters extracted is compared with that of Cd incorporated ZnO as discussed below.

The Cd substituted ZnO samples have been prepared by following the high pressure synthesis method described in this chapter. Due to high lattice mismatch and difference in crystal structure between the ZnO and CdO (described in chapter 1), the phase separation occurs at very low concentration of the source material for Cd. In this example during the method of synthesis, the starting concentrations of the $Cd(CH_3COO)_2.4H_2O$ (source material for Cd) and $Zn(CH_3COO)_2.2H_2O$ in the solution were fixed at wt.% ratio 20:80. After the reaction, two phases are formed viz. rock salt CdO and wurtzite $Zn_{1-y}Cd_yO$. This has been easily verified by the compositional analysis of the XRD data shown in figure 2.18. The final weight ratio of the CdO (16.3 wt.%) is less by 3.7 wt.% , compared to the initial weight ratio. Therefore, it can be predicted that some fraction of the CdO has been incorporated into the ZnO lattice. The ICPAES analysis of only $Zn_{1-y}Cd_yO$ powders confirms Cd content y = 0.034. The $Zn_{1-y}Cd_yO$ particle in the solution have been easily separated from the CdO particles by the following

Name	Refine	Value	Constr...
– Global Parameters			
Zero Shift [°2Theta]	✓	-0.015310	None
Specimen Displacement...	☐	0.000000	None
Wavelength [Å]	☐	1.540598	None
– Background Polyno...			
Flat background	✓	80.547090	None
Coefficient 1	✓	-1.451741	None
Coefficient 2	✓	0.008283	None
Coefficient 3	☐	0.000000	None
Coefficient 4	☐	0.000000	None
Coefficient 5	☐	0.000000	None
– ZnO	✓		
Scale factor	✓	0.003606	None
Preferred Orientation	✓	0.999567	None
B overall	✓	3.120099	None
Extinction	☐	0.000000	None
Flat Plate Absorption Co...	☐	0.000000	None
Porosity	☐	0.000000	None
Roughness	☐	0.000000	None
+ Unit Cell			
– Atomic coordinates			
+ Zn1			
+ O1			
– Profile Parameters			
U	☐	0.684837	None
V	☐	0.000000	None
W	✓	0.604167	None
Anisotropic Broadeni...	☐	0.000000	None
Asymmetry (Rietveld)	☐	0.000000	None
Peak Shape 1	☐	0.600000	None
Peak Shape 2	☐	0.000000	None
Peak Shape 3	☐	0.000000	None
+ 24802-ICSD	✓		

Name	Refine	Value	Constr...
+ Global Parameters			
– ZnO	✓		
Scale factor	✓	0.003606	None
Preferred Orientation	✓	0.999567	None
B overall	✓	3.120099	None
Extinction	☐	0.000000	None
Flat Plate Absorption Co...	☐	0.000000	None
Porosity	☐	0.000000	None
Roughness	☐	0.000000	None
– Unit Cell			
a [Å]	✓	3.259256	Multiple...
b [Å]	☐	3.259256	Multiple...
c [Å]	✓	5.215812	None
alpha [°]	☐	90.000000	None
beta [°]	☐	90.000000	None
gamma [°]	☐	120.0000...	Multiple...
– Atomic coordinates			
– Zn1			
X	☐	0.333333	None
Y	☐	0.666667	None
Z	☐	0.000000	None
B isotropic	☐	0.630000	None
Occupancy	☐	0.998620	24802-I...
+ B anisotropic			
– O1			
X	☐	0.333333	None
Y	☐	0.666667	None
Z	☐	0.382500	None
B isotropic	☐	0.680000	None
Occupancy	☐	1.000000	None
+ B anisotropic			
+ Profile Parameters			
+ 24802-ICSD	✓		

Figure 2.19: Values of the fitting parameters for the mixture of $Zn_{1-y}Cd_yO$ and CdO powder. In this table parameters for wurtzite ZnO phase have been shown.

method:

Particle sizes for the two segregated phases are determined by least square fitting of the experimental data after incorporation of input files for two separate phases viz. rocksalt CdO and wurtzite ZnO. The extracted particle size of CdO (~ 80 nm) widely differs from the particle size determined for $Zn_{1-y}Cd_yO$ ($\sim$12 nm). So, they have been easily separated out by filtration with a filter paper (Whatman 42) or by the method of decantation after allowing quick sedimentation of the CdO particles (whereas the $Zn_{1-y}Cd_yO$ particles remain suspended for about a week).

The important parameters like, lattice constants, preferred orientation and the occupancy of Cd and Zn atoms have been extracted separately for the two phases namely wurtzite $Zn_{1-y}Cd_yO$ (figure 2.19) and rocksalt CdO (figure 2.20). The c-axis and a-axis lattice parameters are observed to increase decreased for Cd and Mg incorporation respectively. This issue has been discussed at length in chapter 6. Another important outcome of alloying is that the occupancy of the parent ZnO (initially taken as 1) atom has been decreased. Simultaneously, the occupancy of impurity atoms such as Mg and Cd is observed to increase. In our analysis the occupancy of Zn atom has been reduced to 0.95 and 0.97 for Mg and Cd substitution respectively. One can also

Name	Refine	Value	Constr...	Name	Refine	Value	Constr...
+ Global Parameters				+ Global Parameters			
+ ZnO	✓			+ ZnO	✓		
− 24802-ICSD	✓			− 24802-ICSD	✓		
Scale factor	✓	0.000104	None	Scale factor	✓	0.000104	None
Preferred Orientation	☐	1.000000	None	Preferred Orientation	☐	1.000000	None
B overall	✓	2.904346	None	B overall	✓	2.904346	None
Extinction	☐	0.000000	None	Extinction	☐	0.000000	None
Flat Plate Absorption Co...	☐	0.000000	None	Flat Plate Absorption Co...	☐	0.000000	None
Porosity	☐	0.000000	None	Porosity	☐	0.000000	None
Roughness	☐	0.000000	None	Roughness	☐	0.000000	None
− Unit Cell				+ Unit Cell			
a [Å]	✓	4.692712	Multiple...	− Atomic coordinates			
b [Å]	☐	4.692712	Multiple...	− Cd1			
c [Å]	☐	4.692712	Multiple...	X	☐	0.000000	None
alpha [°]	☐	90.000000	None	Y	☐	0.000000	None
beta [°]	☐	90.000000	None	Z	☐	0.000000	None
gamma [°]	☐	90.000000	None	B isotropic	☐	0.500000	None
− Atomic coordinates				Occupancy	☐	0.988962	ZnO At...
+ Cd1				+ B anisotropic			
+ O1				− O1			
− Profile Parameters				X	☐	0.500000	None
U	☐	0.000000	None	Y	☐	0.500000	None
V	☐	0.000000	None	Z	☐	0.500000	None
W	✓	0.034063	None	B isotropic	☐	0.500000	None
Anisotropic Broadeni...	☐	0.000000	None	Occupancy	☐	1.000000	None
Asymmetry (Rietveld)	☐	0.000000	None	+ B anisotropic			
Peak Shape 1	☐	0.600000	None	+ Profile Parameters			
Peak Shape 2	☐	0.000000	None				
Peak Shape 3	☐	0.000000	None				

Figure 2.20: Values of the fitting parameters for the mixture of $Zn_{1-y}Cd_yO$ and CdO powder. In this table parameters for rocksalt CdO phase have been shown.

analyze the preferred growth direction in a polycrystalline material by observing the parameter called preferred orientation. Since, in many situation ZnO grows preferentially in the [002] direction, the preferred orientation parameter for the (002) reflection will show enhancement.

2.6.3   UV-visible absorption measurement

Absorption of light by solution is one of the oldest and still one of the more useful instrumental methods. The wavelength of light that a compound will absorb is characteristic of its chemical structure. Specific regions of the electromagnetic spectrum are absorbed by exciting specific types of molecular and atomic motion to higher energy levels. Absorption of microwave radiation is generally due to excitation of molecular rotational motion. Infrared absorption is associated with vibrational motions of molecules. Absorption of visible and ultraviolet (UV) radiation is associated with excitation of electrons, in both atoms and molecules, to higher energy states. All molecules will undergo electronic excitation following absorption of light, but for most molecules very high energy radiation (in the vacuum ultraviolet, <200 nm) is required. The amount of light, I, transmitted through a solution of an absorbing chemical in a transparent solvent can

D₂	: Deuterium Lamp		G	: Diffraction grating
WI	: Halogen lamp		S2	: Exit slit
S1	: Entrance slit		F	: Filters
W	: Quartz windows		CH	: Beam chopper
M1~ M10	: Mirrors		PM	: Photomultiplier
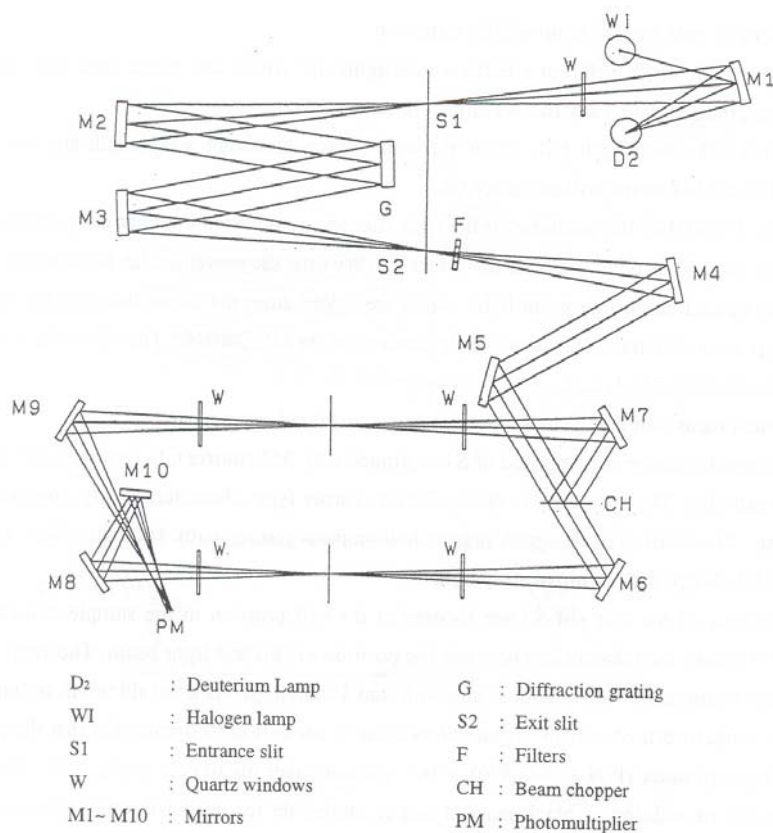
Figure 2.21: Ray diagram for absorption measurement.

be related to its concentration by Beers Law:

$$-log(\frac{I}{I_0}) \;=\; A \;=\; \epsilon.b.c \tag{2.13}$$

where I_0 is the incident light intensity, A is the absorbance (a defined quantity, also referred to as the optical density, or OD), b is the cell path length in centimete, c is the solution concentration in moles/litre, and ϵ is the molar absorptivity, (also referred to as the molar extinction coefficient) which has units of litre/mole/cm (i.e., A is a unit less quantity). Notice that ϵ is a function of wavelength. Thus absorption spectroscopy can be used mainly to quantify the amount of chemical present in an unknown solution.

The scanning spectrophotometer measures the intensity of transmitted light of a narrow bandpass, and scans the wavelength in order to collect a spectrum. Because absorption is a ratiometric measurement, these instruments generally require the user to measure two spectra, one sample and one blank (figure 2.21). The dual beam method is faster, and has the added advantage that lamp drift and other slow intensity fluctuations are properly accounted for in the ratio calculation. Collecting spectra with scanning spectrophotometers is slow, but the instruments often have very high resolving power owing to the use of photomultiplier tube detectors, which can be used with very narrow slit widths. A photodiode array is a 1 or 2 dimensional

stack of individual photodiode detectors, each of which makes an independent measurement of the incident light intensity at its particular location.

2.6.4   Photoluminescence measurement by a Spectrofluorometer

Photoluminescence spectroscopy is a contactless, nondestructive method of probing the electronic structure of materials. Light is directed onto a sample, where it is absorbed and imparts excess energy into the material in a process called photo-excitation. One way this excess energy can be dissipated by the sample is through the emission of light, or luminescence. In the case of photo-excitation, this luminescence is called photoluminescence. The intensity and spectral content of this photoluminescence is a direct measure of various important material properties. Photo-excitation causes electrons within the material to move into permissible excited states. When these electrons return to their equilibrium states, the excess energy is released and may include the emission of light (a radiative process) or may not (a nonradiative process). The energy of the emitted light (photoluminescence) relates to the difference in energy levels between the two electron states involved in the transition between the excited state and the equilibrium state. The quantity of the emitted light is related to the relative contribution of the radiative process.
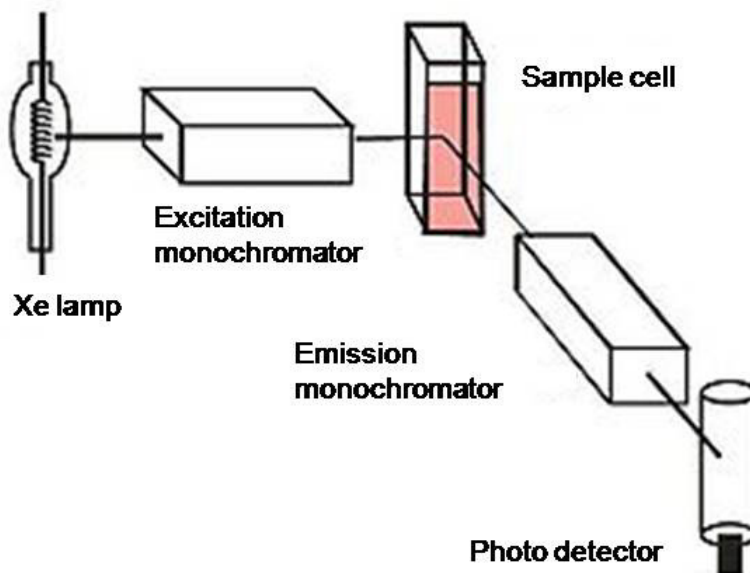
Figure 2.22: The components of the spectrofluorometer.

A spectrofluorometer is an analytical instrument used to measure and record the fluorescence of a sample (figure 2.22). While recording the fluorescence, either the excitation, the emission, or both the wavelengths may be scanned. A continuous source of light shines onto an excitation monochromator, which selects a band of wavelengths. This monochromatic excitation light is directed onto a sample, which shows luminescence. The luminescent light is directed into a second emission monochromator, which selects a band of wavelengths, and shines them onto a detector. The signal from the detector is reported to a system controller and host computer,

where the data can be manipulated and presented using a special software.

Various light sources may be used as excitation sources, including lasers, photodiodes, and lamps; xenon arcs and mercury vapor lamps in particular. A laser only emits light of high irradiance at a very narrow wavelength interval, typically under 0.01 nm, which makes an excitation monochromator or filter unnecessary. The disadvantage of this method is that the wavelength of a laser cannot be changed by much. By contrast, a xenon arc has a continuous emission spectrum with nearly constant intensity in the range from 300-800 nm and a sufficient irradiance for measurements down to just above 200 nm. Filters and/or monochromators may be used in fluorimeters. A monochromator transmits light of an adjustable wavelength with an adjustable tolerance. The most common type of monochromator utilizes diffraction grating, that is, collimated light enters a grating and exits with a different angle depending on the wavelength. The detector can either be single-channeled or multichanneled. The single-channeled detector can only detect the intensity of one wavelength at a time, while the multichanneled one detects the intensity at all wavelengths simultaneously, making the emission monochromator or filter unnecessary.

2.6.5   Determination of chemical compositions by ICP-AES analysis

Inductively coupled plasma atomic emission spectroscopy (ICP-AES), also referred to as inductively coupled plasma optical emission spectrometry (ICP-OES), is an analytical technique used for determination of chemical composition and detection of the trace metals. It is a type of emission spectroscopy that uses the inductively coupled plasma to produce excited atoms and ions that emit electromagnetic radiation at wavelengths characteristic of a particular element. The intensity of this emission is indicative of the concentration of the element within the sample.

The ICP-AES is composed of two parts. The ICP and the optical spectrometer. The ICP torch consists of 3 concentric quartz glass tubes that is water cooled and a coil of the radio frequency (RF) generator which surrounds part of this torch. Argon gas is typically used to create the plasma. When the torch is turned on, an intense magnetic field from the RF generator is turned on. The argon gas flowing through is ignited with few Tesla (typically a copper strip on the outside of the tube). The argon gas is ionized in this field and flows in a particular rotationally symmetrically pattern towards the magnetic field of the RF coil. A stable, high temperature plasma of about 7000K is then generated as the result of the inelastic collisions created between the neutral argon atoms and the charged particles.

A peristaltic pump (used for pumping fluids) delivers a liquid sample into a nebulizer where it is atomized and introduced directly inside the plasma flame. The sample immediately collides with the electrons and other charged ions in the plasma and is broken down into charged ions. The various molecules break up into their respective atoms which then lose electrons and recombine repeatedly in the plasma, giving off the characteristic wavelengths of the elements involved. A shear gas, typically nitrogen or dry compressed air is used to 'cut' the plasma flame at a specific spot. 1 or 2 transfer lenses are then used to focus the emitted light on a diffraction grating where it is separated into its component radiation in the optical spectrometer. The light intensity is then measured with a photomultiplier tube at the specific wavelength for each element line involved. The intensity of each line is then compared to previous measured intensities of known concentrations of the element and its concentration is then computed by extrapolation along the calibration line.

Chapter 3

Shape transition in ZnO nanostructures and its effect on blue green emission

3.1 Introduction

We have discovered that ZnO nanostructures prepared by chemical method undergo a shape transition as the size increases beyond 20 nm. Nanostructures in the size range $5 - 15$ nm are mostly spherical whereas beyond 20 nm flat faces arise leading to hexagonal platelet and rod like morphologies. It has been shown in chapter 2 that nanostructures with different morphologies can be obtained mainly by changing the concentration of the precursors and the growth time. Growth of the nanostructures occurs when the radius of the nucleation sites is greater than the critical radius. At the initial stage of growth after nucleation, the nanostructures shape remains spherical. Non-spherical structures such as rods (in [002] direction) are formed when the nanostructures are allowed to grow for longer time due to the anisotropy in the growth rate of ZnO for different crystal faces. This axial growth toward the easy axis [002] stops and nanostructures with different morphologies such as hexagonal platelets are formed if the precursor concentration is high enough to produce large number of nucleation sites which will eventually reduce the available free space for further growth in [002] direction. There are other factors like temperature and pressure which controls the morphology of the fabricated nanostructures. For example, spherical ZnO nanoparticles are obtained for relatively lower precursor concentration and short growth time. Slight increase in precursor concentration, growth time and temperature results in the formation of rods having higher aspect ratio. Further increase in the precursor concentration and growth time produces hexagonal platelets of bigger sizes (low aspect ratio). During the growth, the change from spherical to a shape with flat surfaces occurs due to widely different surface energies of the ZnO crystal faces [82]. The spherical shape will contain some high energy surfaces and in fact can expose in some places the high energy basal planes [84]. This excess energy will be lowered by a transition to a hexagonal (or rod like) shape that will expose the lowest energy (0001) surfaces. Such a surface energy driven shape transition by which the excess energy in the nanostructure is relaxed, is well documented in nanoparticles of many systems [85]. This shape transition in the nanostructures is reflected in their optical properties.

In a recent report, the blue green emission of ZnO nanostructures grown by Pulsed Laser

Deposition was found to exhibit blue shift and reduced intensity when the size increases and the morphology was found to change from spherical to rods and hexagonal plate [78]. In an effort to correlate size, defects and visible PL of ZnO nanoparticles [79], it has been observed that blue shift of the green emission for increasing size (from 25-75 nm) is opposite to that observed on nanowires of diameters ranging from $50-300$ nm [58]. However, the origin of this anomalous shift in emission energies has not been explained and the role of morphology of the nanostructures on the visible emission has not been investigated. Fundamental questions like, evolution of the visible emission with the nanostructure size and morphology remain unresolved [73]. In this chapter, we will focus on the sudden change in the properties of ZnO nanostructures when the shape transition occurs at size 20 nm. A sharp change in the spectral content of the blue-green visible emission is also observed when the shape transition takes place. Nanostructures with spherical shape ($10-20$ nm) show emission near 550 nm whereas rods and hexagonal platelet with flat faces emits near 500 nm. Both these emission show very systematic dependence on the surface to volume ratio which confirms the surface related origin of this emission. We find from X-ray studies that the shape transition leads to collapse of the microstrain in the system. In this chapter we specifically studied the shape transition and its effect on the blue green emission. We have also suggested a mechanism by which the optical property (emission) gets linked to morphology of the nanostructures.

3.2   TEM and XRD study - shape transition at the nanoscale

Shape transition in ZnO nanostructures have been investigated by using transmission electron microscope (TEM) and X-ray diffraction (XRD) technique. The methods of synthesizing the nanoparticles have been discussed in chapter 2. The observation below establish that in the size range $\sim$20 nm the ZnO nanoparticles show a shape transition from spherical to faceted sttructure. Representative TEM images of the samples are shown in figure 3.1. We find that the samples with size below 20 nm have a spherical shape. However, for sizes > 20 nm there is a shape transition and these samples show mostly hexagonal facets and some of them show rod-like morphologies. Representative TEM images of spherical ZnO nanostructures of average sizes 10 and 16 nm are shown in figure 3.1(a) and (b), grown for 0.5 and 1.5 h durations, respectively, within the autoclave. A magnified view of the samples in (a) is given in its inset while that of the samples in (b) are shown in figure (c). Samples with rod-like and hexagonal morphologies were obtained by growing for a longer time with little change in precursor concentration and have been shown in figures 3.1(d) and (e), respectively. The lattice image (figure 3.1(f)), indexed SAED pattern (figure 3.1(g)) and FFT of the lattice image (figure 3.1(h)) of the nanostructures shown in (e), confirm their single crystalline nature as well as their atomically flat face. The magnified view of a single rod is shown in the inset of figure 3.1(d). The TEM data (figure 3.1 and table 3.1) clearly establishes that spherical ZnO nanoparticles prepared by chemical routes undergo a shape change leading to hexagonal morphology with sharp edges (often rod-like) when the size exceeds the value of 20 nm. It is noted that the synthesized ZnO nanostructures are nominally oxygen deficient as established by energy dispersive X-ray analysis in a transmission electron microscope.

The change in shape as observed from the TEM images is accompanied by strain relaxation in the spherical particles. We confirm this by measuring the microstrain from the XRD data. The crystal structures and sizes of all the samples have been analyzed by X-ray diffraction
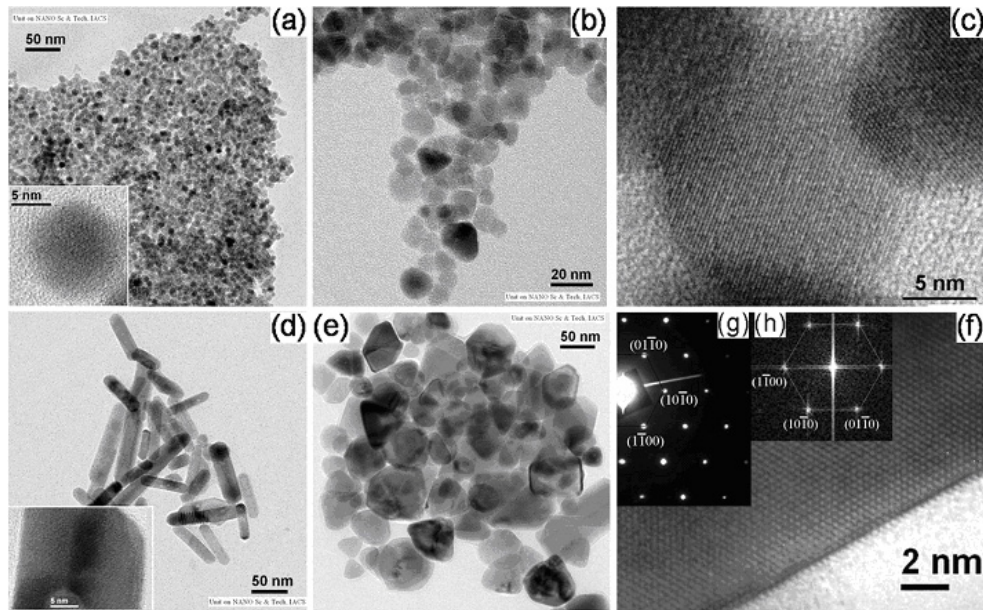
Figure 3.1: Upper panel: TEM images of spherical ZnO nanostructures of average sizes (a) 10 nm and (b) 16 nm. Inset of figure (a) shows the close view of a single particle shown in (a). The high resolution image of nanoparticles in (b) is shown in figure (c). Lower panel: TEM micrograph of (d) rod like and (e) hexagonal shaped ZnO nanostructures. Inset of figure (d) shows a close view of a single rod. The high resolution lattice image (f), SAED pattern (g) and FFT of the lattice image (h) are presented for the hexagonal particles shown in (e). The sharp boundary of the hexagonal particle can be seen.

Table 3.1: Size and morphology of ZnO nanostructures

Identification		Morphology	Size by TEM (nm)	Size by XRD (nm)	E_{NBE} (eV)
I	(i)	Spherical	10	11	3.34
	(ii)	Spherical	12	14	3.35
	(iii)	Spherical	16	18	3.33
II	(iv)	Rod diameter	24	23	3.33
	(v)	Hexagonal platelet	55	44	3.29
	(vi)	Rods and* square pillars	100	85	3.27

*commercial powder purchased from s.d.fine chem.

technique. Representative X-ray diffraction data for the samples investigated are indexed in figure 3.2 which confirms wurtzite symmetry of the synthesized nanostructures. Both microstrain as well as size contribute to the line width in the XRD peak. One can separate the contributions of both by Williamson-Hall analysis using the simplified integral breadth method [81]. The size determined by TEM and XRD analysis (listed in table 3.1) agrees well within the range of ± 2 nm for the nanostructures of size below 25 nm. At bigger sizes, the difference obtained by two methods arise mainly because the non-spherical shape of the particle leads to error in the XRD analysis. The root mean square (rms) distribution in size (d) of the samples can be quantified as $\triangle d_{rms}/d \approx 10\%$ for samples (i) and (iv) in table 3.1 and $\triangle d_{rms}/d \approx 20\%$ for rest of the samples investigated in this work. The integral breadth (β), defined as the ratio between the peak area and the intensity maxima for both size and strain broadened profiles is given by equation 2.8 ([81]). The average particle diameter was obtained from the y-intercept of the $\beta^{\star}$ versus s plot and this matches with that found from the TEM (table 3.1)(average diameters determined by XRD and TEM (table 3.1) agree within the range of $\pm 10 - 20\%$ for all the samples studied). W-H analysis also allows us to find the average strain from the slope of the linear fit of the data points. The strain values calculated by this method were plotted with the size of the nanostructures in figure 3.3. We note that the microstrain is higher for spherical particles ($Gr - I$) and then collapses when the shape changes for $Gr - II$ samples. Therefore it appears that the shape transition is driven by the relaxation of built in strain in the spherical particles.

The equilibrium shape of a crystal depends primarily on the surface energies of the different crystallographic planes [82]. In the case of growth from solution, additional issues like the presence of specific ions, as well as surfactants, that alter surface energy can change the shape of the grown crystal. The growth of a nanorod is a manifestation of a strongly anisotropic growth process due to different surface energies of the crystallographic faces [83].

In most of the situations, the growth of ZnO occurs in the form of nanorods (preferential growth along the c-axis) because this minimizes the contribution of the high energy polar basal planes [84]. The spherical shape, which occurs at smaller size, will contain some high energy surfaces and, in fact, in some places can expose the high energy basal planes. The curvature of the spherical particles will cause strain. This strain that develops can be inhomogeneous being maximum near the surface. The strain inhomogeneity will give rise to observable microstrain as seen by XRD. This excess elastic energy of the spherical particles will be lowered by a transition to a shape that exposes the lower energy surfaces as in a rod-like growth. Such a surface energy driven shape transition, by which the excess energy and the microstrain of the nanostructure is relaxed, has been studied in nanoparticles [85] as well as in self-assembled nanostructures [86]. The exact size (*"critical size"*) of shape transition will depend on the exact growth condition, the concentration of precursors and presence or absence of surfactant. In this work we obtain spherical ZnO nanoparticles for a relatively lower precursor concentration and short duration of growth. A small increase in precursor concentration and the growth time results in the formation of rods. At this stage the aspect ratio of the rods increases as we increase the rod growth time. Further increase in the precursor concentration produces hexagonal platelets of larger sizes (low aspect ratio). The exact size at which the change in shape (spherical to facetted) occurs thus depends on a number of factors, but it is typically in the range of $10 - 20$ nm. For the specific growth conditions used here, the transition occurs when the size is 20 nm.
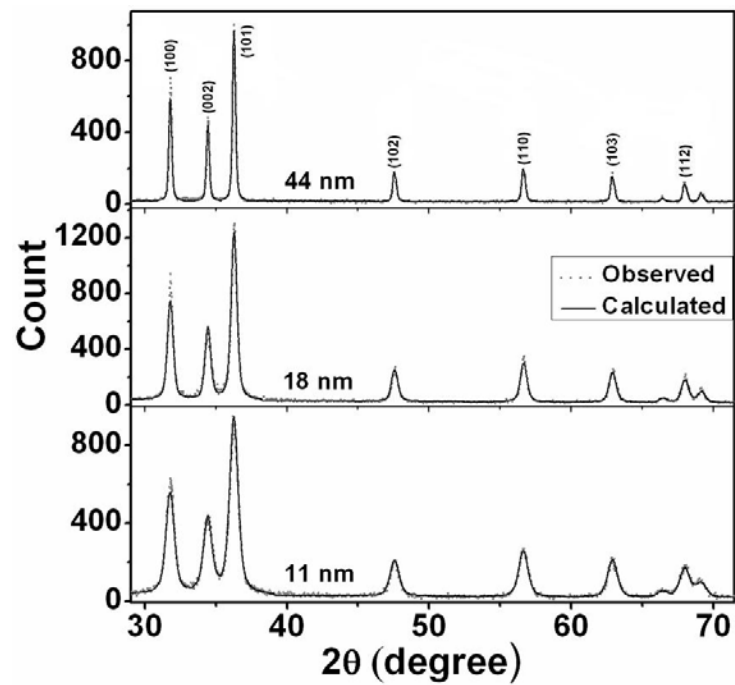
Figure 3.2: XRD data for select samples as indicated on the graph show the wurtzite type structure adopting symmetry P63mc (peaks are indexed).
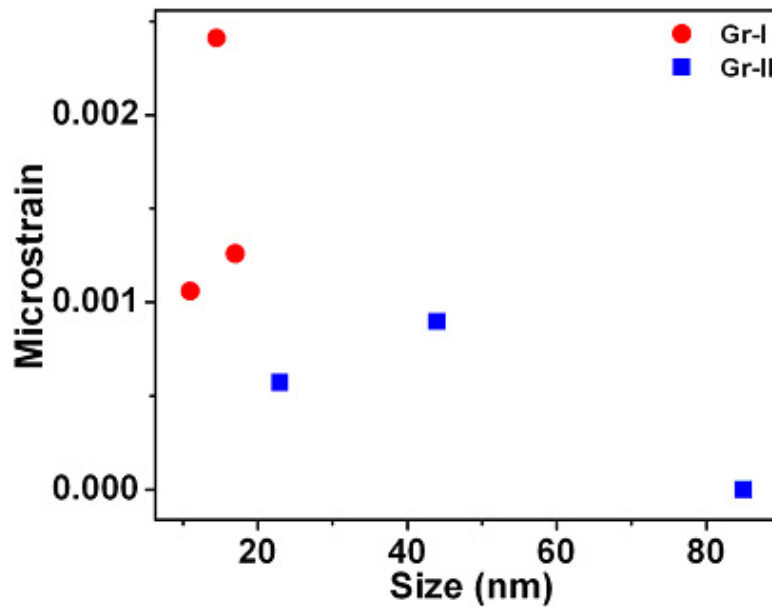
Figure 3.3: Microstrain calculated from XRD data by Williamson-Hall analysis is plotted as function of the size. The relaxation of the strain at the shape transition is apparent.

3.3   Photoluminescence study and its dependence on shape

The change in shape from spherical to hexagonal (or rod shaped) morphology, as evident from the TEM micrographs, leads to a non-monotonous change in the visible emission energy of their PL spectra (excitation at 325 nm). In figure 3.4 we show the emission spectra over the entire range. The emission in the range $370 - 380$ nm is the near band edge emission. It can be seen that the bluegreen emissions in the range $470 - 565$ nm show a distinct shift in the emission energies as the particle size as well as the shape changes. The visible emission from $Gr - I$ nanoparticles with spherical shape peaks around 550 nm while for $Gr - II$ nanostructures with hexagonal and rod shapes, the emission is centred at 500 nm. In this chapter we propose that the observed change in the emission energy for ZnO nanostructures as their size increases beyond 20 nm is actually related to their change in shape. It is noted that the shape transition (which occurs with size) as well as its impact on their photoluminescence has not been observed earlier in ZnO nanostructures.
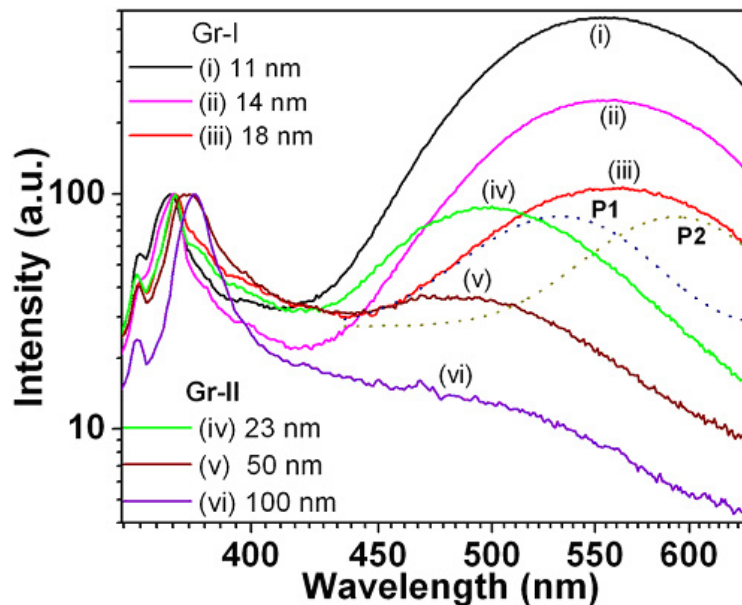
Figure 3.4: The emission bands of the ZnO nanostructures of different size and shape. The excitation was at 325 nm. The sharp dependence of the emission band at $490 - 565$ nm on the size can be seen. A typical emission band is composed of two components $P1$ and $P2$ (see text) as shown for the emission curve (iii). The shift in the spectral components when the size increases beyond 20 nm is prominent.

Analysis of the broad emission in the blue-green region shows that it is composed of two emission bands (shown as dotted lines in figure 3.4 for sample (iii)) which are marked as $P1$ and $P2$ [87]. The spectral content of the blue-green band is determined by the relative weight of the two lines. We find that the change in shape brings about a sharp change in the relative contribution of the two lines. $P2$ line is dominant in $Gr - I$ samples (size ranging from $10 - 20$ nm) having spherical morphology. As faceting starts appearing for nanostructures greater than 20 nm ($Gr - II$ samples), intensity of $P2$ line gradually reduces and $P1$ emerges as the dominant
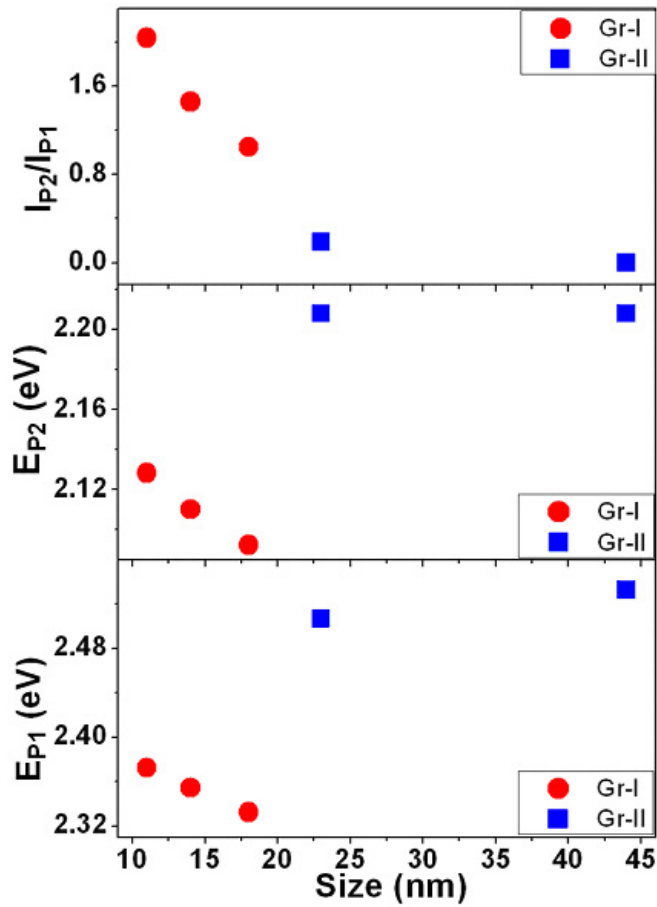
Figure 3.5: Important physical parameters as a function of size. Lower panel: energy of $P1$ band. Middle panel: energy of $P2$ band. Upper panel: intensity ratio of $P2$ to $P1$ emission bands.

emission band. This can be seen in figure 5 (upper panel) where we show the variation of the intensity ratio of the two lines (I_{P2}/I_{P1}). The shape change suppresses the intensity of $P2$ emission and changes sharply the energies of emission of both the bands. Emission energies of $P1$ (E_{P1}) and $P2$ (E_{P2}) also show a sudden rise when the shape transition occurs (middle and lower panel of figure 3.5). Both E_{P1} and E_{P2} shift to lower energies as particle size increases for $Gr - I$ samples (spherical morphology). In case of $Gr - II$ (rods and hexagonal platelets) samples, the energies of emission of both the lines remain more or less size independent after the sharp change that occurs at the shape transition. The above discussion leads us to the conclusion that the anomalous size dependence in the visible emission of the ZnO nanostructures appears to be related to their morphology.

It is important to note that the emission in the UV range (from $370 - 380$ nm) is an intrinsic property of the wurtzite ZnO and originates due to excitonic recombination. Due to quantum confinement it shifts to higher energy as we reduce the size of the nanostructures (see figure 3.6). Emission energy of this band edge emission (NBE) obeys an inverse dependence on the diameter ($1/diameter$), irrespective of the morphology and the method of preparation [Table
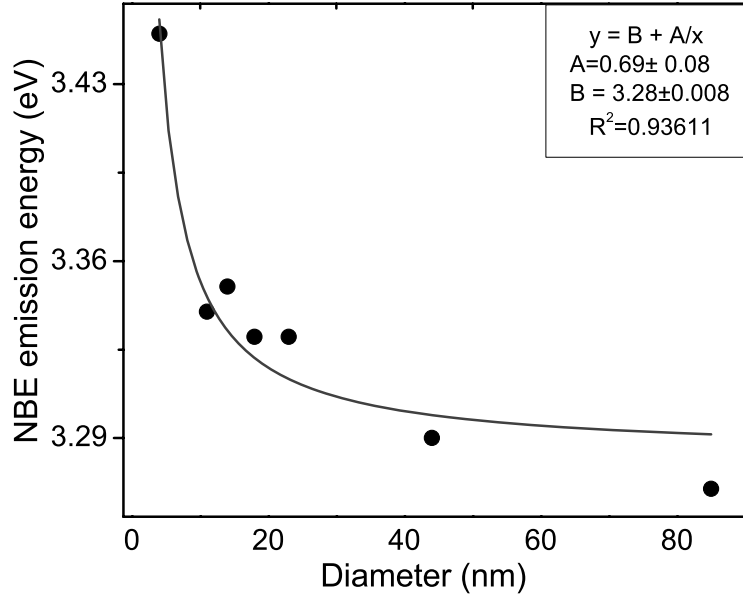
Figure 3.6: The NBE emission energies of the ZnO nanostructures with different sizes has been fitted by a function indicated on the graph.

3.1]. Thus the visible emission is specific to the mechanism and the change in visible emission energy indicates the presence of two different mechanisms for $Gr - I$ and $Gr - II$ samples. It is known that the strong confinement effect is observed when the particle size is comparable to the excitonic Bohr radius ($\sim$2nm for ZnO). In figure 3.6, it can be clearly seen that the NBE emission of a sample with average diameter $\sim$5 nm (prepared under ambient pressure and described in table 2.1) shows much higher energy of emission than the rest. There is a sharp increase in the emission energy when the particle sizes are below 10 nm. Therefore, the samples considered in this investigation (size ranging from 10 nm to 85 nm) are not in the size regime of strong confinement (sample size$\gg$excitonic Bohr radius$\sim$1 nm).

   To establish that the defect centres responsible for the visible PL are located near the surface, we have analyzed the ratio of the intensities of NBE to visible emission (I_{NBE}/I_{VIS}) as function of size (figure 3.7). Increase in this ratio as the size increases shows the decreasing contribution of the visible emission which is expected if the centres responsible for the visible emission are primarily located at the surface. A simple model [58] can be used to explain the intensity dependence on the size and thus obtain the thickness of the surface layer emitting visible light. The model essentially measures relative strength of surface to volume. The intensity ratio of the NBE to visible emission for cylindrical wires ($Gr - II$) of radius r and with a surface recombination layer of thickness t, is given by [58]

$$\frac{I_{NBE}}{I_{VISIBLE}} = C\left(\frac{r^2}{2rt - t^2} - 1\right)$$
(3.1)
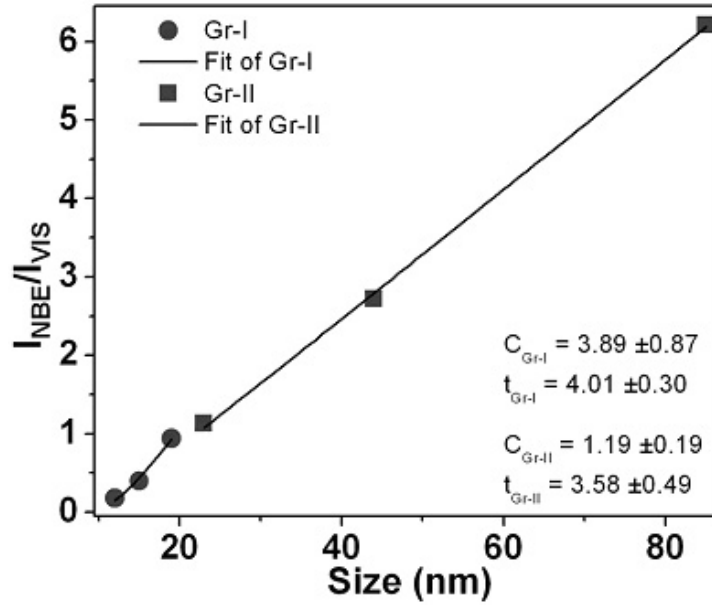
Figure 3.7: Intensity ratio of NBE to visible emission for $Gr-I$ and $Gr-II$ samples. The data are fitted by a surface recombination model with surface layer thicknesses of 4 and 3.6 nm for $Gr-I$ and $Gr-II$ samples respectively.

By similar approach we can find out the same ratio for spherical particles ($Gr-I$) of radius r and a surface recombination layer of thickness t

$$\frac{I_{NBE}}{I_{VISIBLE}} = C\left(\frac{r^3}{3rt(r-t)+t^3} - 1\right) \tag{3.2}$$

The constant C, along with the other quantities contains the oscillator strengths which in turn depend on the particle morphology, is expected to be different for the two groups of particles. Equations 3.1 and 3.2 have been employed to fit the experimental data for $Gr-II$ and $Gr-I$ samples respectively as shown in figure 3.7. The thickness of the surface recombination layers as obtained from the model is $t \sim 4.0$ nm and $t \sim 3.6$ nm for $Gr-I$ (spherical) and $Gr-II$ (rods and hexagonal platelets) particles respectively. It is important to note that the thickness of the surface layer (t) is comparable but somewhat higher in case of smaller spherical particles than that in the rods and hexagonal platelets of relatively bigger size. Thus the relative volume associated with surface layer is much higher for small spherical particles compared to the rods and hexagonal nanostructures. The simple model above establishes that the visible emission centres are indeed located in a small region around the surface. This is an important issue because as we will see below the physical location near the surface makes the emission sensitive to surface charges and the band bending that occurs near the surface.

3.4   Discussions of the results

The main result of this chapter is the shape transition in the ZnO nanostructure when the size becomes more than ~ 20 nm which severely affects the visible emission arising from the

defects located near the surface. This effect on optical properties occur when the size is taken to nanometer regime. In the following we discuss the likely origin of this phenomenon with a model and validate this model with additional experiments which we will describe in the next chapter. The model is qualitative and is based on earlier suggestions used to explain the PL from ZnO nanoparticles.

First we discuss the spectral shift of the blue-green band on shape change. As shown earlier, the emission band in this region is composed of two lines ($P1$ and $P2$). It has been shown through figures 3.4 and 3.5 that the change in the spectral content occurs because of suppression of the $P2$ line relative to the $P1$ line when nanostructures with flat faces emerge. It has also been shown before that there is a surface region from where the defect related emission occurs.

Based on the suggestion of references ([87]-[90]), in figure 3.8 we show the proposed origin of the two emission lines $P1$ and $P2$. In ZnO the defect responsible for visible emission in this wavelength range is the oxygen vacancy denoted as V_O [90]. The two lines originate depending on whether the emission is from doubly charged vacancy centre V_O^{++} ($P2$) or singly charged vacancy centre V_O^+ ($P1$). The suggested emission process is shown schematically in figure 3.8. The V_O^{++} centre, created by capture of a hole by the V_O^+ centre in a depletion region, leads to emission in the vicinity of 2.2 eV (E_{P2}), which is the $P2$ line. The singly charged centre (V_O^+) in the absence of a depletion region becomes a neutral centre (V_O^X) by capture of an electron (n-type ZnO) from the conduction band which then recombines with a hole in the valence band giving rise to an emission ($P1$) at 2.5 eV (E_{P1}). The shift in the visible emission is thus related to the change in the relative strengths of the two emission bands. Now we show that the relative occupation of the two charged centres (V_O^{++} and V_O^+) is related to the band bending at the depletion layer near the surface which in turn is related to the surface charge of
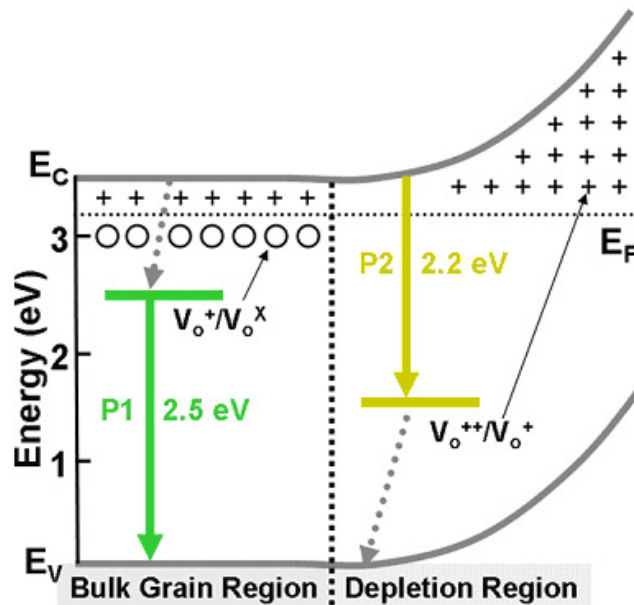
Figure 3.8: Schematic diagram depicting the origin of P1 and P2 emission bands. The defect distributions in the bulk and depletion regions are shown. E_c, E_v and E_F are the conduction band, valance band and Fermi energy levels, respectively.

the nanostructures.

In spherical nanoparticles of small size, there will be an appreciable depletion layer near the surface [87]. The thickness of the depletion layer depends on the density of native carrier concentration in the nanoparticles. For an n-type semiconductor in an open circuit condition as is the case here, the Fermi energy level is typically higher than the redox potential of the medium in which it is suspended [91]. As a result, electrons will be transferred from the n-type nanoparticles into the solution. This creates a depletion region where there is a positive charge associated with the space charge region, and this is reflected in an upward bending of the band edges. In ZnO with native defects (n-type), the depletion region has a typical thickness in the range $5 - 10$ nm. Such a depletion layer, as stated before, will give rise to band bending in spherical nanoparticles whose physical size is comparable to depletion width [92]. The band bending changes the relative occupancy of the defect levels in such a way that it populates doubly charged V_O^{++} preferentially by which the $P2$ emission predominates. The fact that the shape transition indeed changes the charged condition at the surface can be measured by monitoring the zeta potential. The existence of the positively charged depletion layer can be directly seen from the positive value of the zeta potential ($18\ mV$) in these nanoparticles of small size dispersed in ethanol. The shape change leads to hexagonal particles or rods with flat surfaces. These particles/rods have severely reduced zeta potential ($\sim 8\ mV$). This reduces the depletion layer and the associated band bending. As a consequence this will change the occupancy of the electron energy levels in these larger faceted particles which decreases the occupancy of the V_O^{++} centres leading to reduction in emission of the $P2$ band. The occupancy will be like the bulk energy level and the predominant emission will be from the singly charged vacancy (V_O^+), namely the $P1$ line. Thus the shape change suppresses the band bending leading to stronger emission at $P1$. Therefore the role of shape change is to modify the band bending and the relative occupancy of the V_O^{++} and V_O^+ levels which in turn changes the dominant emission channel. The substantial reduction in zeta potential value on shape change is a proof that the surface charge (and the depletion layer) is responsible for this process.

Briefly, the above model is based on the fact that the visible luminescence is linked to the oxygen vacancy and the depletion layer near the surface plays an important role in determining the band bending and the associated consequences in the emission. The shape transition, leads to a change in the surface charge which in turn changes the extent of band bending. So, there is a link between the visible emission and the charge at the nanostructure surface. To establish this relation, we actually modify the surface charge of the nanoparticles by embedding them in electrolytes which leads to a change in their visible emission. This effect is investigated in the next chapter.

3.5 Conclusions

To summarize, ZnO nanoparticles undergo a shape change at a size $\sim$20 nm from spherical to hexagonal shape. The change in shape is associated with a collapse of the microstrain. It also leads to a sharp change in the blue-green emission band from ZnO nanostructures. The change in spectral nature of the emission band on shape change has been explained as due to change in band bending arising from depletion layer on the surface of nanoparticles.

Chapter 4

Ionic environment control of visible photo-luminescence from ZnO nanoparticles

4.1 Introduction

A very important outcome of this thesis is the observation that the surface charge on the ZnO nanoparticles can control their visible photoluminescence. In this chapter we elaborate on this. The surface charge driven shift in the relative contribution of the spectral components in the broad visible emission can be seen even in case of nanostructures having the same shape and size by dispersing them in electrolytic solution of varying strength. The basic observation that we made is that the visible photoluminescence from ZnO nanoparticles can be controlled by changing the ionic or polar nature of the medium in which the nanoparticles are dispersed. We find that presence of sufficient amount of electrolyte can even quench the emission which is a new result of this thesis. From our experiment we could establish a clear correlation between the intensity of the visible emission as well as of its spectral component to the measured strength of the double layer. This correlation enabled us to propose an explanation of the observed phenomenon based on the surface charge of the ZnO nanoparticles, which is interesting because of its application potential. Motivation of the present chapter arose from the result of the last chapter where charged vacancies were found responsible for band bending which in turn controls the spectral contents of the visible luminescence. In this chapter we extend this idea to show that the band bending in colloidal ZnO nanoparticles can be controlled by the ionic nature of the medium which in turn decides the predominant nature of the visible emission.

In this study, two kinds of nanostructures have been chosen: the spherical particles in which 550 nm (~ 2.2 eV) emission band dominates and the cylindrical nanorods whose visible emission is dominated by the 500 nm (~ 2.5 eV) band (figure 3.4 in chapter 3). The spherical particles [figure 4.1 (a)] with typical average diameter of 10 nm have been synthesized by acetate route under ambient pressure [59]. The nanorods of diameter ~ 20 nm and length $100-150$ nm [figure 4.1 (c)] were prepared in an autoclave by the same chemical route but under 54 atm. pressure at 230^0C [60](discussed in chapter 2). The nanostructures were imaged with a JEOL high-resolution transmission electron microscope (TEM) at 200 keV. X-ray diffraction data confirms the wurtzite symmetry of the synthesized nanostructures. The TEM images along with high
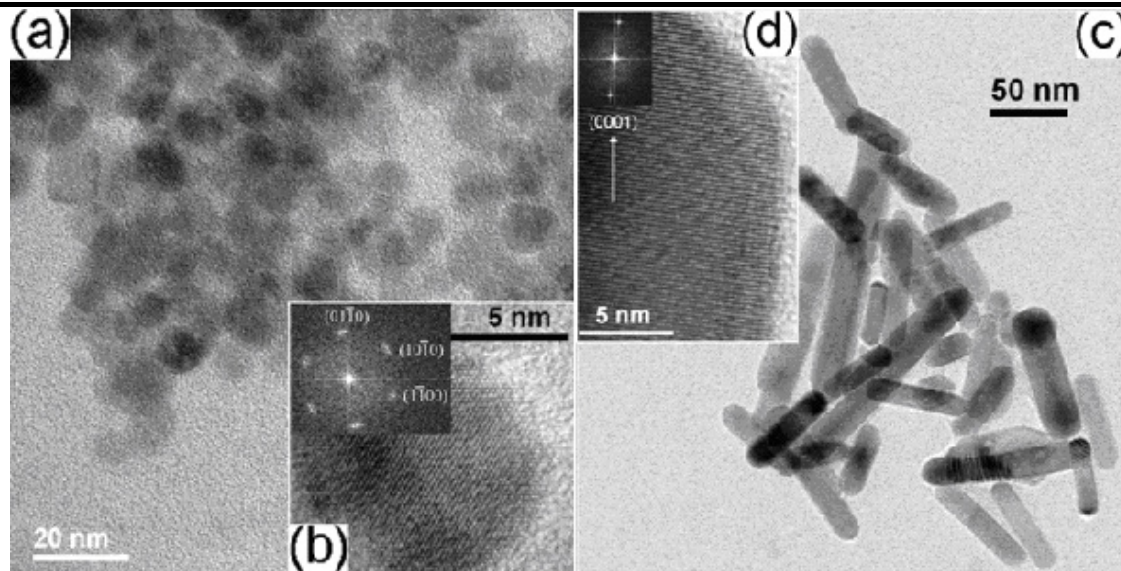
Figure 4.1: TEM micrographs for the (a) nanosphere and (c) nanorods of ZnO. The fast Fourier transform (FFT) of the HRTEM of a nanosphere shown in (b) confirms the hexagonal symmetry. Nanorod growth in the (0001) direction is shown (d) by the lattice image and its FFT of a single rod.

resolution microscopy data are shown in figure 4.1 for both the nanostructures. The materials synthesized have also been characterized by X-ray-diffraction. The average size calculated from the X-ray diffraction data matches well with that found from TEM micrograph. Below we first describe the basic phenomenon as observed. In this experiment we measure the PL spectra of the nanostructures dispersed in a solution with different strengths of the electrolytes such as $LiClO_4$ (in ethanol) and NaCl (in water). Prior to taking the PL data the absorbance data were taken and the fundamental absorption edge was found to be at 3.447 eV (360 nm) for the particles and 3.345 eV (371 nm) for the nanorods. The absorption edge of the nanospheres (size$\sim$ 10 nm) shifts to higher energy compared to the nanorods (dia$\sim$ 23 nm) due to quantum confinement effect [96]. It is important to note that the fundamental absorption edge of the nanostructures remains essentially unchanged in the presence of electrolytes as shown in figure 4.2, although due to the presence of $LiClO_4$ there is significant absorption at wavelength longer than that corresponding to the absorption edge.

4.2   Observation of change in photoluminescence by ionic environment

Room temperature optical properties were studied by photoluminescence spectrometer (Jobin Yvon, FluoroMax-3) using a xenon arc lamp as illumination source at an excitation wavelength of 325 nm. In figure 4.3(a), we plot the PL spectra of spherical ZnO nanoparticles dispersed in ethanol having different concentrations of $LiClO_4$ as indicated in the graph. It can be clearly seen that as the concentration of the electrolyte increases, there is a significant change in the emission
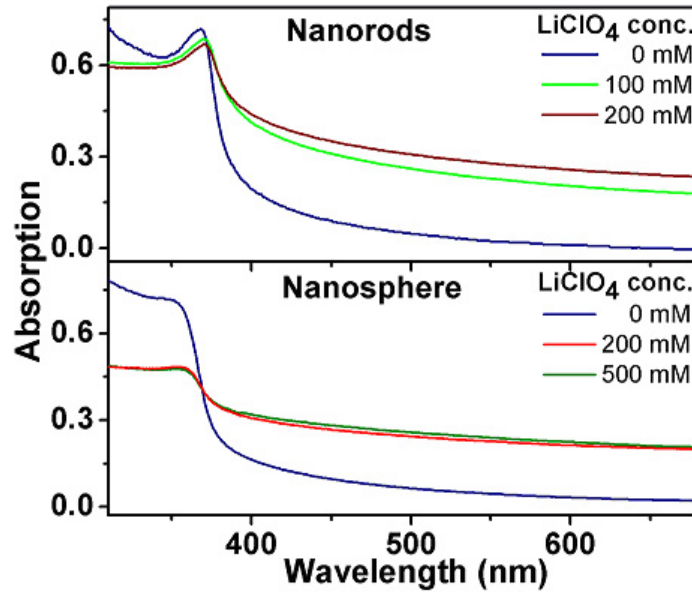
Figure 4.2: Absorption spectra of the nanorods (upper panel) and nanosphere (lower panel) with different concentration of $LiClO_4$ in ethanol.
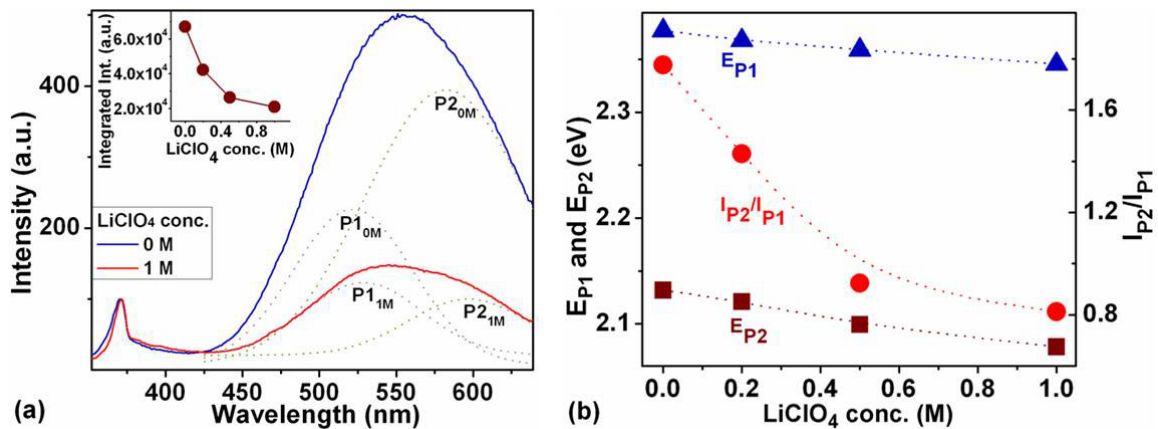
Figure 4.3: (a) PL spectra of ZnO nanospheres for different $LiClO_4$ concentrations in ethanol as indicated in the graph. Inset shows the integrated intensity with different concentrations of electrolyte. (b) Emission energies and the relative intensity ratios of the spectral components have been plotted

spectra. In fact for higher concentration of the electrolyte there is almost complete quenching of the visible emission. Maximum 70% decrease in total intensity can be seen on changing the electrolyte concentration. In the inset of figure 4.3 (a) we show the integrated intensity of the visible emission as a function of ionic concentration. Similar effect is also observed for the nanorods. The data are plotted in figure 4.4(a), (b) and (c) for different electrolyte concentration. The inset of figure 4.4(d) shows dependence of the integrated emission intensity as a function of the electrolyte concentration. The observed data, both for the nanoparticles and the nanorods, show unambiguously that the intensity of the visible emission from ZnO nanostructures can be very effectively controlled by the ionic nature of the environment in which they are suspended.

This is also evident from the increase in visible emission intensity when ZnO is suspended in water compared to that in less polar ethanol [figure 4.5]. Interestingly, a small reduction in visible emission ($\sim 25\%$) is observed when NaCl is added to the water-ZnO suspension which is elaborated later on. Therefore, salt of strong base and strong acid like $LiClO_4$ and $NaCl$ have similar effect on the visible emission from ZnO nanostructures. We note that the observed change in PL intensity on increasing the electrolyte concentration is exactly similar to that obtained when the concentration is decreased from its maximum value. Therefore the electrolyte solution does not induce any permanent change on the optical properties of the ZnO nanostructures. The effect of the electrolyte (or the ionic nature of the medium) on the visible emission of ZnO nanostructures is a rarely investigated area and has potential application as biosensors.

Below we carry out a quantitative evaluation of the observed changes. This will be followed by an explanation for the observed phenomena in the next section. It has been known before that the visible emission in the blue-green region, as we see here is a composite of two broad lines located approximately at 2.2 eV (550 nm) and at 2.5 eV (500 nm) [87]. The spectral nature of the visible emission band in this region depends crucially on the exact position as well as the relative emission intensities from these two lines. The nature of the visible emission in the spherical particles as well as the nanorods changes because of the relative strengths of the two emission lines [[93], [87]]. In figure 4.3(a) we show the two decomposed peaks of the broad visible emission for the particles dispersed in pure ethanol (marked $P1_{0M}$ and $P2_{0M}$) and 1 M $LiClO_4$ solution in ethanol (marked $P1_{1M}$ and $P2_{1M}$). Similar decomposition into the two lines is shown for the emission from the nanorods in figure 4.4. The important thing to note is that the relative strength of the two lines changes as the electrolyte concentration changes. In figure 4.3 (b) and 4.4 (d), we plot the emission energies and the intensity ratios (I_{P2}/I_{P1}) between the two spectral components $P2$ and $P1$ for nanospheres and nanorods respectively. The change in the emission spectra originates predominantly due to a reduction in the relative contribution of the $P2$ line on increasing the $LiClO_4$ concentration. (The ratio I_{P2}/I_{P1} decreases monotonously for both types of nanostructures, although it is most prominent in the smaller nanoparticles.) The spectral positions of the two components show a small but gradual shift on increasing the electrolyte concentration. In case of the nanoparticles, for maximum concentration of $LiClO_4$ the observed shift in the spectral position of $P2$ (E_{P2}) is more (0.054 eV) in comparison to that of $P1$ (0.032 eV). This shows that the $P2$ emission is more sensitive to the ionic environment. An important point needs to be noted. The near band edge emission energy (at ~ 380 nm, related to excitons) is not affected at all by the presence of the electrolyte. As stated, in the nanorods of relatively larger size ($dia \sim 20$ nm) dispersed in ethanol, there is a rapid fall in $P2$ emission on addition of $LiClO_4$ to the solution [figure 4.4] and $P1$ emerges as the dominant component. For the maximum concentration of $LiClO_4$ (1M), $P2$ does not have any contribution at all. Thus the nanorods show $P1$ as the dominant emission band which remains almost unchanged.
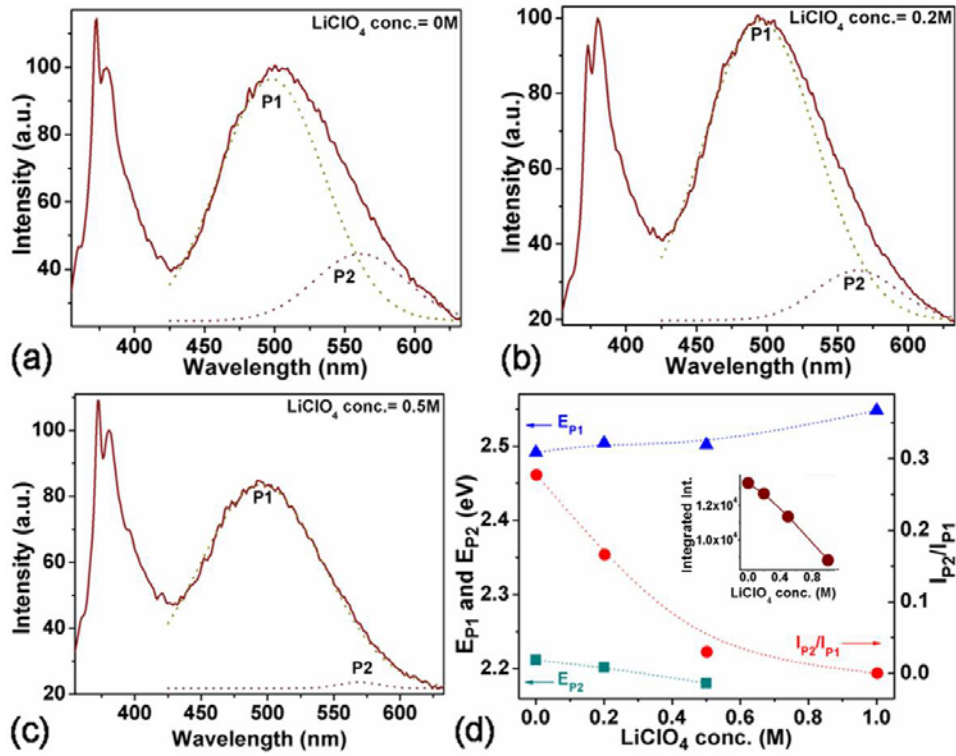
Figure 4.4: (a), (b) and (c) show PL spectra of ZnO nanorods showing the contributions of the two spectral components for 0, 0.2 and 0.5 M $LiClO_4$ in ethanol respectively. (d) The emission energies and the relative intensity ratios are plotted with different concentrations of electrolyte. The inset shows the integrated intensity for different electrolyte concentrations.

In the previous chapter we proposed that the band bending at the depletion layer is responsible for the observed change in the relative contribution of the $P1$ and $P2$ lines when the spherical particles grow in size and finally change their shape. The relative volume associated with the depletion layer for smaller nanospheres is higher than that of larger rods and hexagonal particles. Therefore the effect of band bending is more prominent in the nanospheres and the relative contribution of $P2$ band was observed to decrease on increasing the size. This observation totally agrees with the trend observed in this chapter viz. the relative contribution of the $P2$ band decreases when the $LiClO_4$ concentration increases. Therefore the depletion layer is linked to the net positive charge residing at the surface on the nanoparticles. Also the spectral position of the two components show a gradual decrease in energy on increasing the electrolyte concentration as observed in the case when nanostructures grow in size ($Gr - I$).

In the remaining part of the section we discuss the likely origin of the observation. We first propose the postulate that the change in the visible emission (or the change in the components $P1$ and $P2$) occur due to change in the surface charge or surface potential of the nanoparticles or nanorods. We prove correctness of this model by actually measuring the zeta potential (ζ) of the nanostructures and correlating with the intensity of the $P2$ line. The zeta potentials were measured at 20 ^oC using Malvern Instruments Zetasizer systems Nano ZS. The strong correlation of the zeta potentials (ζ) with the spectral content of the emission intensity can be
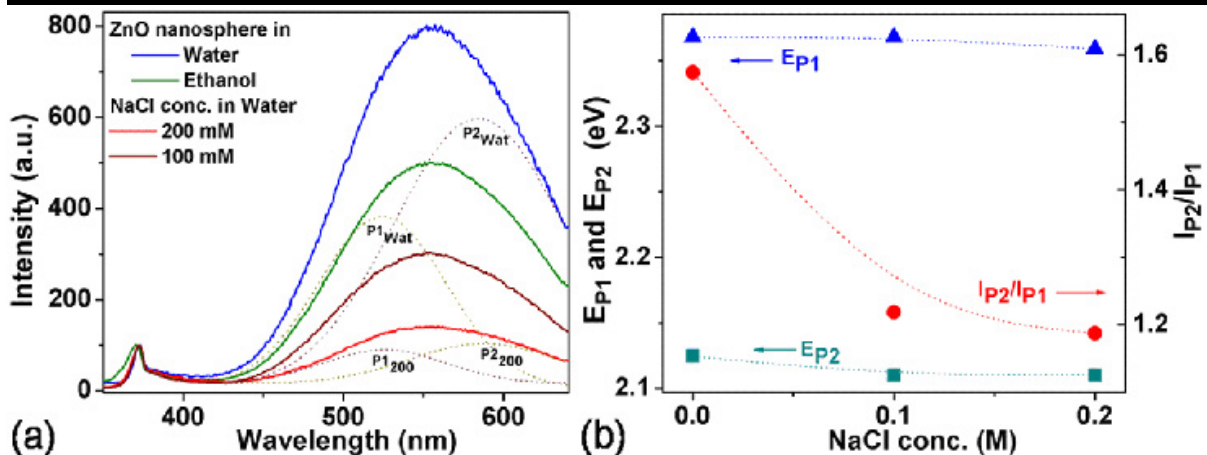
Figure 4.5: PL spectra of ZnO nanospheres for different NaCl concentrations in ethanol as indicated in the graph. Inset shows the integrated intensity with different concentrations of electrolyte. (b) Emission energies and the relative intensity ratios of the spectral components have been plotted.

seen in figure 4.6 where we have plotted the ratio (I_{P2}/I_{P1}) as a function of ζ. It is seen that presence of electrolyte like $LiClO_4$ and NaCl to the dispersion of ZnO nanoparticles in ethanol reduces the zeta potential which is strongly correlated with their visible luminescence. The value of ζ for the ZnO nanostructures in different media first decreases rapidly and then slowly
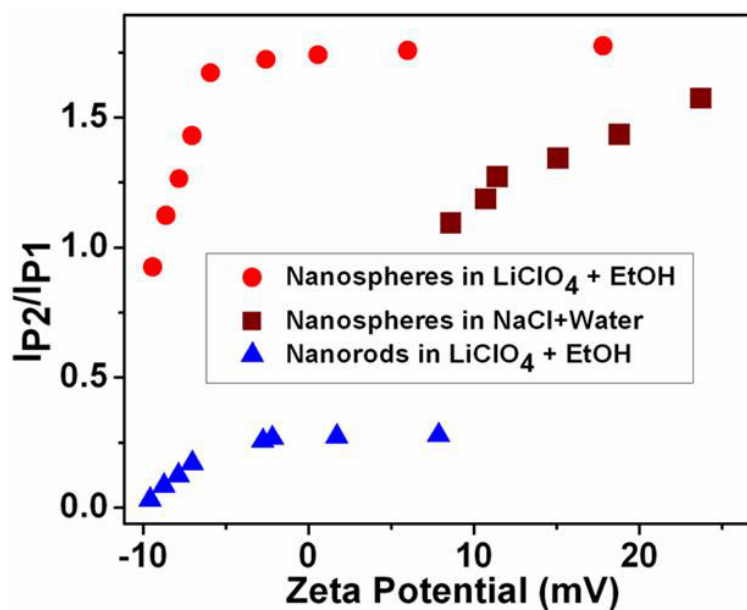
Figure 4.6: The intensity ratios of $P2$ and $P1$ bands (I_{P2}/I_{P1}) are plotted as a function of zeta potential for both the nanostructures suspended in different media as indicated in the graph.

Table 4.1: Zeta potential at the nanostructure-medium interface and pH of the medium

Medium	Conc. of Electrolyte (mM)	Nanosphere of dia $\sim$ 10 nm		Nanorods of dia $\sim$ 23 nm	
		Zeta mV	pH	Zeta mV	pH
Ethanol	0	17.8	7.35	7.85	6.93
$LiClO_4$	10	5.99	7.27	1.69	6.85
in	20	0.586	7.32	-2.21	6.97
ethanol	40	-5.77	7.45	-2.79	7.14
	200	-7.06	7.6	-7.04	7.36
water	0	23.7	7.91	14.0	7.42
NaCl in	100	11.4	7.94	9.33	7.50
water	200	10.7	7.97	...	...

reduces to a constant value as we increase the electrolyte concentration (see table 4.1). Even in pure ethanol, the small spherical particles of size $\sim$ 10 nm show higher ζ value ($\sim$ 18 mV) at pH 7.3 than the nanorods of relatively larger diameter ($\zeta \sim 8$ mV at pH 7). This reduction in positive ζ thus leads to a reduction in the visible emission intensity and in particular the reduction of the ratio (I_{P2}/I_{P1}). When $NaCl$ is added into $water - ZnO$ dispersion, there is a small reduction in ζ which saturates for concentration above 200 mM. The ratio (I_{P2}/I_{P1}) decreases by 25% for the spherical particles. In contrast for $LiClO_4$:EtOH system, the reduction in ζ has been substantial and the intensity change is also much larger ($\sim$ 53%). Evidently, the increase in electrolyte concentration reduces ζ in both nanoparticles and nanorods significantly. Decrease in ζ reduces the relative strength of the $P2$ line. From figure 4.6, it can be seen that in the $LiClO_4$:EtOH system, the (I_{P2}/I_{P1}) ratio is nearly constant for $\zeta \geq 5$ mV. In the spherical nanoparticle, since (I_{P2}/I_{P1}) is large to begin with, the drop is also substantial. This result clearly shows that drop in (I_{P2}/I_{P1}) is completely determined by the nature of the electrolyte. Therefore the spectral control of the relative strengths of the two lines can be done by controlling the electrostatic environment of the nanostructures. We find that the nanoparticles in ethanol have positive zeta potential. The positively charged ZnO nanoparticles dispersed in a solution are surrounded by oppositely charged ions. The net (+)ve charge developed at the particle surface affects the distribution of ions in the surrounding interfacial region, resulting in an increased concentration of counter ions (ions of opposite charge to that of the particle) close to the surface. Thus an electrical double layer exists around each particle. By measuring the zeta potential we could establish a direct correlation between the surface potential of the nanostructures (nanoparticles and nanorods) and the visible emission.

It had been established in the last chapter that the visible emission from ZnO in the blue-green region originates from defects (oxygen vacancy in particular) which are located predominantly near the surface of the nanoparticles. Free-carrier depletion at the particle surface and its effect on the ionization state of the oxygen vacancy has strong impact on the visible emission intensity [89]. As we already discussed, emission band appearing around 550 nm ($P2$) originates from doubly charged oxygen vacancy (V_o^{++}) whereas singly charged oxygen vacancy (V_o^{+}) is responsible for the emission band around 500 nm ($P1$). The relative intensities of the two

lines will depend on their relative occupancy (see figure 3.8). For positive charge on the surface, the band bending changes the chemical potential which populates the level (V_o^{++}) preferentially compared to the other level, leading to a relative enhancement of the intensity of the line $P2$. It establishes the essential roles of the surface charge and the band bending in determination of the spectral components of the blue green visible emission from ZnO nanoparticles. The band bending in the near surface depletion layer in the nanoparticles is linked to their surface charge. So any modification of the surface charge will be reflected by change in the level of band bending. This will be more predominant when the size of the nanoparticles decreases. The direct correlation between the visible emission and the zeta-potential thus leads to the explanation that the change in the visible emission in an electrolytic medium occurs due to change in the band bending which in turn is caused by a change in the effective surface charge of the ZnO nanoparticles. When ζ decreases due to reduced positive charge on the nanoparticles surface, the band bending is reduced and the component $P2$ arising from the (V_o^{++}) state, makes diminishing contribution.

The above explanation of the quenching of the visible emission by controlling ionic environment opens up a way to control the visible emission from the ZnO nanoparticles. In particular, it can be used as a visible bio-sensor for biochemical/biophysical processes that leads to a change in the surface charge and the zeta-potential. We note that this effect will depend on size of particles and will be enhanced in smaller particles whose size will be comparable to or smaller than the depletion width. In larger particles, where predominant contribution arises from the level (V_o^+) (line $P1$), the effect of band bending will be reduced and correspondingly the effect of the ionic environment is also reduced.

4.3   Conclusions

To summarize, we have shown that visible luminescence from small nanoparticles of ZnO can be effectively controlled and even quenched by simply varying the ionic content or polar nature of the suspending medium. To validate the assumption that the shift in the relative contribution of the spectral components in the broad visible emission is driven by the surface charge, the nanostructures having the same shapes and sizes are dispersed in different ionic environment (electrolytic solution of varying strength). An explanation has been proposed that depends on control of the predominant emission centres (V_o^{++} or V_o^+) by controlling the band bending in the depletion layer near the surface which in turn can be controlled by the surface charge.

Chapter 5

Photoresponse and Electrophotoluminescence in thin film of ZnO nanostructures

5.1 Introduction

ZnO is an excellent absorber and emitter of UV light and displays change in electrical conductivity through the process of Electron Hole Pair (EHP) generation by UV illumination. Remarkable photoresponse properties make ZnO a relevant material for UV detection [131] and photovoltaics [135]. Fabrication of ZnO based devices for UV detection requires contact that can separate the electron hole pair. It also needs Ohmic contacts with those dissimilar materials. ZnO is inherently an n-type material. Since the p-type ZnO is not very common, p-n junction in ZnO crystals is difficult to fabricate. In addition to that, only few metals such as platinum and gold are reported to have Schottky contact with ZnO ([129], [134]). In this thesis we explore the use of conductive polymer for realization of contact that has nonlinear IV characteristics. In a recent report, an excellent Schottky contact of ZnO with a conductive polymer has been demonstrated [133]. In a similar manner, we use nanocrystalline ZnO and conductive polymer for realization of a device for UV detection. The nanocrystalline ZnO film offers large collection area for the incident optical radiation. Simple techniques like spin coating or drop coating can be used to make large area nanocrystalline film. High gain and high speed ZnO based Metal Semiconductor Metal (Al) UV detector having Ohmic contact between Al and ZnO is reported [132]. In another report photoresponse of ZnO tetrapod nanocrystal (with two tungsten and one platinum lead) Schottky diode is demonstrated although the gain is comparatively less. For practical applications, improved devices with high gain, large collection area of light and cost effective fabrication by the use of polymeric solid electrolyte on nanocrystalline ZnO film is essential.

In the second part of this chapter we report on yet another important discovery made during this thesis. We show that the "device" that we made as UV-detector also shows visible photoluminescence that can be controlled by an electric field. The room temperature photoluminescence (PL) of ZnO nanostructures (size ∼10-15 nm) typically exhibits a sharp emission in the near UV range (originating from excitonic mechanism) and a broad emission band in the visible region of the spectrum which is linked to surface defects as has been discussed in the

previous chapter. Control of this visible emission is technologically as well as academically very relevant. In the previous chapter we have established a direct link between the visible photo-luminescence (originating from surface defects) and the surface charge on the nanoparticles. It is also addressed that the visible emission depends on many factors like size and shape of the material, surrounding media and type of defects involved in the emission processes. The influ-ence of these factors on this broad visible luminescence is reported and the positively charged oxygen vacancies were claimed to be responsible for this emission in many circumstances ([90] ,[89]). Fine control of this visible emission by the application of a voltage is a very important step for its application. Recently it is demonstrated that the charge environment surrounding the nanoparticles is capable of controlling this visible emission [94]. Quenching of fluorescence from the phosphors like ZnS by application of few volts has been reported [128]. In a recent report quenching of the visible emission and enhancement of the UV emission by application of an electric field has been observed [127]. To our knowledge, a reversible control (quenching as well as enhancement) of the visible luminescence of ZnO nanostructures by application of very small voltage (< 5 V) has not been achieved earlier. The phenomenon of Electric Field Controlled Photoluminescnce or Electrophotoluminescence on a device based on nanostructured ZnO will be demonstrated in the subsequent sections.

The presentation in this chapter is mostly descriptive. We made some suggestions for the explanation. However, a comprehensive explanation would need additional experiments which were not possible due to time frame of a thesis.
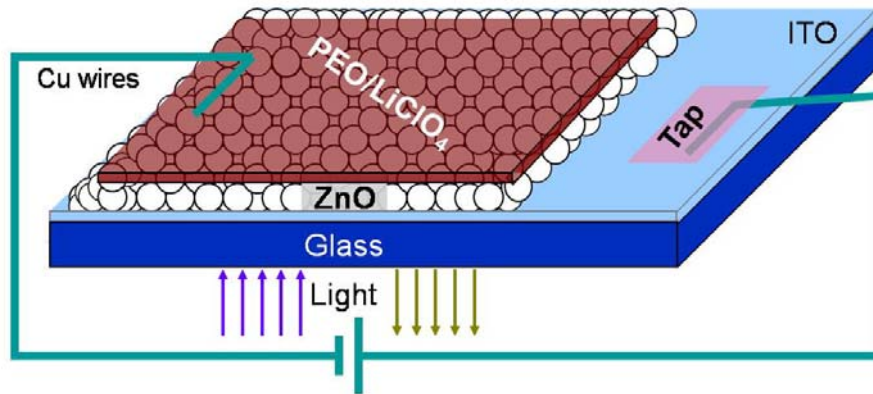
Figure 5.1: Illustration of the device fabricated. The biasing arrangement demonstrated here leads to enhancement of intensity and vice versa.

5.2   Device fabrication and the arrangement

The basic phenomenon of UV photodetection as well as field control of visible luminescence were investigated on a nanostructured ZnO film. In the following we give description of the device consisting of ITO/ZnO nanostructures/Polymeric electrolyte, in which we carried out our investigation. Figure 5.1 shows the experimental arrangement adopted for the fabricated device. ZnO nanoparticles of size $\sim$10-15 nm have been synthesized by acetate route described in

ref ([59], [60]). The nanostructured ZnO film (thickness varying from 200-300 nm) is obtained by adding these nanoparticle dispersion in ethanol drop wise on a pre-decided area of a commercially available conducting ITO layer supported by a glass substrate. The ZnO dispersion has been spread over the surface uniformly and dried at room temperature. Equal number of drops were added to obtain films of similar thickness repeatedly. For analysis purpose, ZnO film of thickness up to $\sim$2.5 μm is occasionally deposited to assure the presence of a ZnO layer all over the ITO surface. After the ZnO film dries off, a gel containing 10:1 weight ratio of PEO (polyethylene oxide, MW 1000) and $LiClO_4$ is deposited on the ZnO layer at room temperature. After 3-4 hours duration, the gel becomes solid and holds the electrical connections (through Cu wires) tightly as shown in figure 5.1. The ZnO-ITO interface has been illuminated by a 345 nm light passing through the ITO glass substrate and the emitted light (of wavelength 545 nm) has been collected in reflection mode. The biasing arrangement of the device is shown in figure 5.1. The device is said to be positively (negatively) biased when the positive (negative) terminal of the source is connected to the $PEO/LiClO_4$ layer through a copper wire.
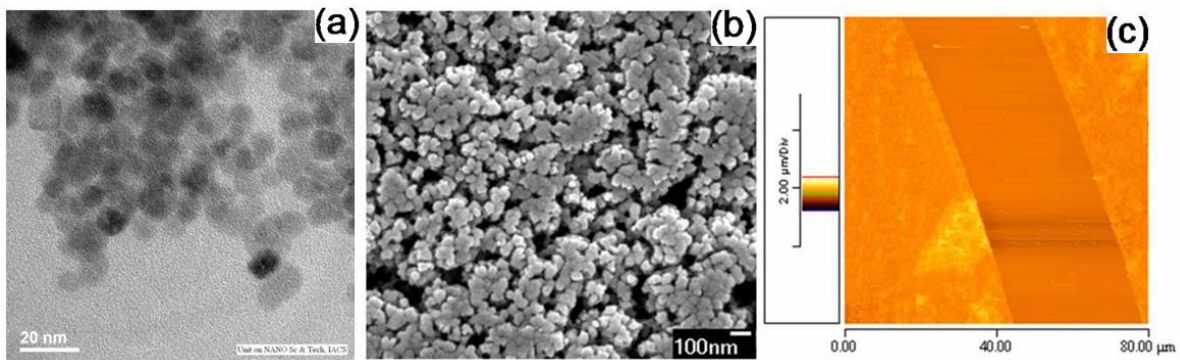
Figure 5.2: (a) TEM image of the ZnO nanoparticles on a grid. (b) SEM image of the nanostructured film obtained by depositing ZnO nanoparticles shown in (a) on a ITO substrate. (c) AFM image of the scratched film of ZnO nanostructures [shown in (b)] used for obtaining the film thickness. Thickness of the ZnO film investigated in this work varies from 200-300 nm as determined at the step of substrate-ZnO film.

UV light is allowed to pass through the ITO-Glass substrate from a Xenon arc lamp and the monochromator of a Spectrofluorimeter (Jobin Yvon Fluromax 3). The light intensities were varied by changing the slit width and measured by a power meter. The bias voltages were supplied by a Stanford Research System DS345 synthesized function generator and the device current is recorded by a Keithley, 6514 System Electrometer. The sizes of the nanoparticles were determined by JEOL High Resolution Transmission Electron Microscope (HR-TEM) operated at 200 KeV. TEM image of the collection of ZnO nanoparticles shown in figure 5.2 (a) shows that the average size of the nanoparticles is $\sim$10 nm. When the dispersion of such nanoparticles is deposited on a substrate, agglomeration takes place. The average size of these agglomerated nanoparticles is found to be 40-50 nm [figure 5.2(b)] when imaged by Field Emission Gun Scanning Electron Microscope (FEG SEM). The thickness of such a film of ZnO nanoparticles is determined from the AFM image operated in contact mode with a scratch on the film as shown in figure 5.2(c). The average thickness measured at the step of ZnO-ITO was found to vary from

200 to 300 nm.

5.3   Role of various components of the device

The electrical behaviour of the device depends on the properties of individual junction created at the interface of the different layers. Therefore investigation of various junction properties in dark mode is essential before we explore the photoresponse of the device.

   The device as shown in figure 5.1 comprises of three components viz. ITO layer at the bottom, ZnO layer on top of ITO and finally the $PEO/LiClO_4$ layer on top of ZnO film. The thin film of conducting ITO behaves like traditional conductors below their plasmon frequency and can be treated as metal for the low frequency electrical signal. But it is transparent in the optical frequency range we are interested in. On the other hand ZnO is inherently a n-type semiconductor and responsible for visible PL as well as photo-response in this work (will be discussed later on). Due to the conductive nature of ITO, it acts like a metal electrode to ZnO which is transparent in visible region. The $PEO/LiClO_4$ layer is used to make electrical contact on ZnO film. There are three junctions involved at the interface of ITO-ZnO, ZnO-$PEO/LiClO_4$ and ITO-$PEO/LiClO_4$ if accidental contact happens due to the porousness of the ZnO film. To explore the different contact behaviour, the I-V characteristics of devices fabricated in the absence of i) polymeric electrolyte and ii) ZnO layer are investigated. The dark I-V characteristic of the ITO-ZnO-Al junction show linear behaviour [figure 5.3 (a)]. To avoid direct contact between ITO and Al, a thick ZnO film ($\sim$2.5 μm) is used. So the dark current observed in the ITO-ZnO-Al arrangement is much lower than that of ITO-ZnO-$PEO/LiClO_4$ as shown in figure 5.6. Further ITO-$PEO/LiClO_4$ junction also exhibits almost linear characteristics [figure 5.3 (b)]. On the other hand the entire arrangement ITO-ZnO-$PEO/LiClO_4$ show nonlinear behaviour (figure 5.6). Note that the graphs are plotted in semi-log scale to blow up the low current regime. The above observation shows that nonlinearity in the I-V characteristic of the device mainly arises due to the ZnO-polymer junction. Only use of polymer (in the absence of electrolyte $LiClO_4$) also shows nonlinear I-V characteristics. The electrolyte in the polymer enhances its conductivity and acts as a source of electrical charge. If only the polymer (without the electrolyte) is used for coating the ZnO film, the current through the device reduces by 75 percent of the current when $LiClO_4$ is used in the weight ratio of ($PEO : LiClO_4 = 10 : 1$).

5.4   The excitation wavelength and spectral response of the device

Now we first work out the suitable range of optical wavelength over which the device can perform. We find that 345 nm is the most suitable window for excitation of this device. In the range of 320-375 nm ZnO is a good absorbing material but ITO-Glass substrate is transparent as shown in figure 5.4. Therefore, UV light of wavelength in the range 320-375 nm can easily pass through the ITO glass substrate but will be absorbed fully by the thick ZnO layer. Simultaneously, the visible light emitted from ZnO can pass through the ITO glass substrate without much absorption. Therefore, one can excite the device through ITO glass interface and the emitted signal can be collected in the reflection mode. This is an important observation for fabrication of optoelectronic devices which is a combination of conductive ITO and a semiconductor ZnO, specially, for the kind of device which uses non-transparent top layer. More importantly we have
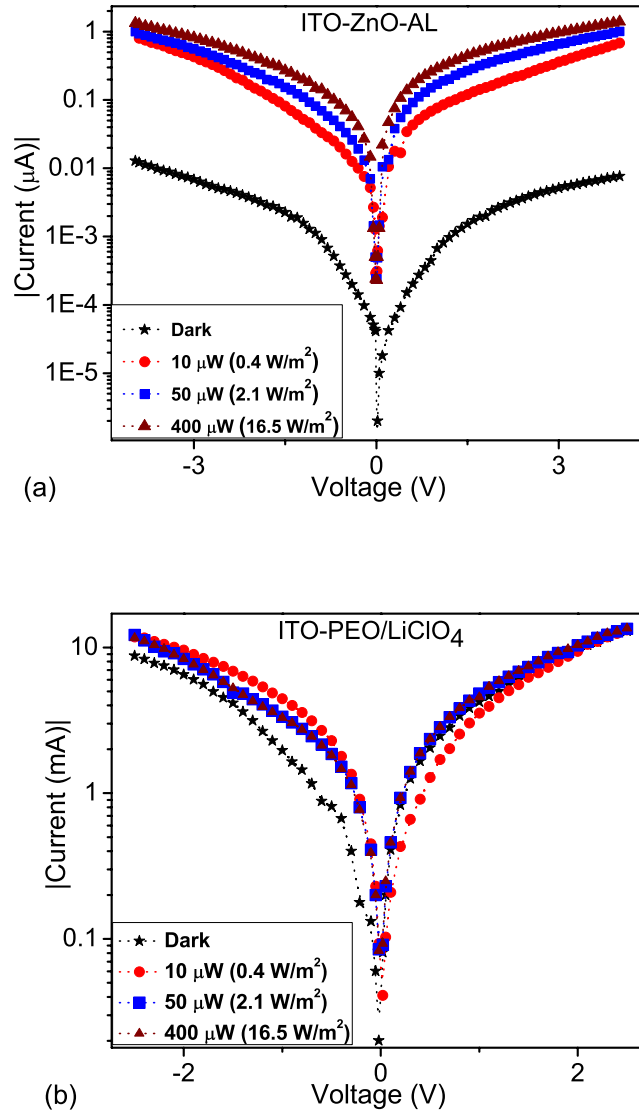
Figure 5.3: Response to the 345 nm light on (a) nanostructured ZnO film of thickness $\sim$2.5 μm sandwiched between ITO and conducting Al layer and (b) without ZnO film in between ITO and PEO/$LiClO_4$ layer. Reference of bias is on ITO layer. Device is positively biased when the positive terminal of the source is connected to the top electrodes (Al or PEO/$LiClO_4$) and the ITO is connected to the negative terminal.

achieved an undistorted visible PL signal by eliminating effect of the polymer electrolyte which gives a broad PL peak in the blue region. For that purpose we have used a thick ZnO film which completely absorbs the excitation light.

Figure 5.5 shows typical spectral response of the photodetector device we have fabricated.
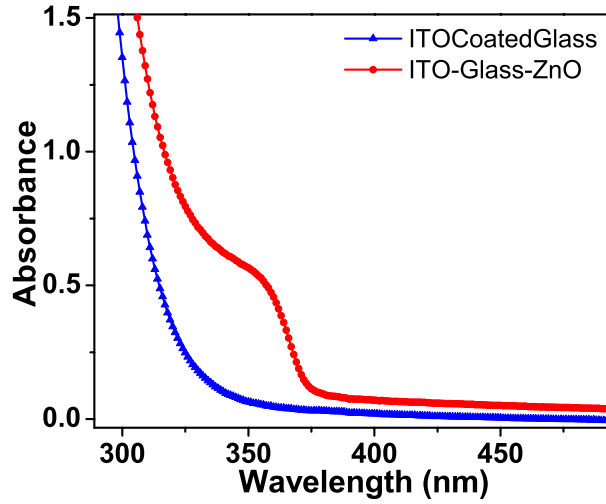
Figure 5.4: Absorption spectra of a bare ITO coated glass substrate and the other drop coated with a ZnO nanostructured film.
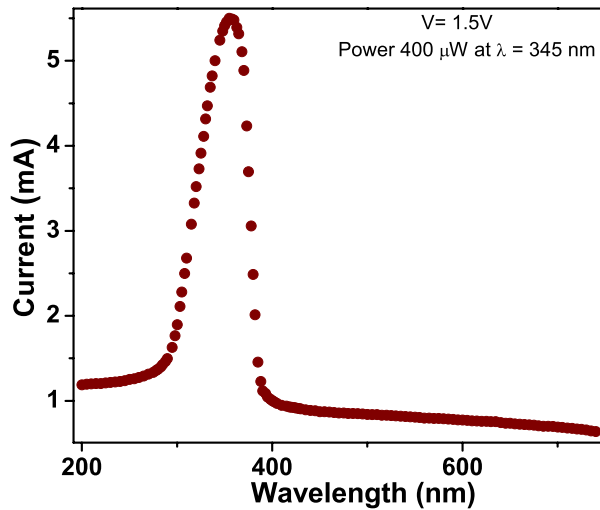
Figure 5.5: The spectral response of the device shows a maximum when illuminated with light of wavelength around 320-355 nm.

The device is biased at 1.5 V and irradiated by radiation of power 400 μW. The spectral response of the device as can be seen is what is expected from the absorption profile of ZnO and

ITO (figure 5.4). The current through the device is maximum when illuminated in the range of 355±15 nm. Therefore the device is illuminated by a light of wavelength 345 nm where it shows highest photoluminescence intensity as well as large photoresponse. It is interesting that the device so fabricated has a narrow band response. One can change the spectral band by engineering the absorption edge of ZnO as well as that of the transparent conducting oxide. The sharp rise in the spectral response at the absorption edge around 380 nm clearly shows that the effect arises due to absorption of light at the fundamental edge and the subsequent electron-hole pair creation.

5.5   Photo-response of the ZnO-Polymer device

As we have seen, the dark I-V characteristics of the device shows strong nonlinearity. Unlike a p-n junction within a single crystal of a semiconductor, in this work a Schottky barrier junction may forms which includes termination of the semiconductor crystals and deals with the effects of two dissimilar materials. The ZnO surface contains surface states due to incomplete covalent bonds which can lead to charges at the ZnO-polymer interface. Because of surface states, the
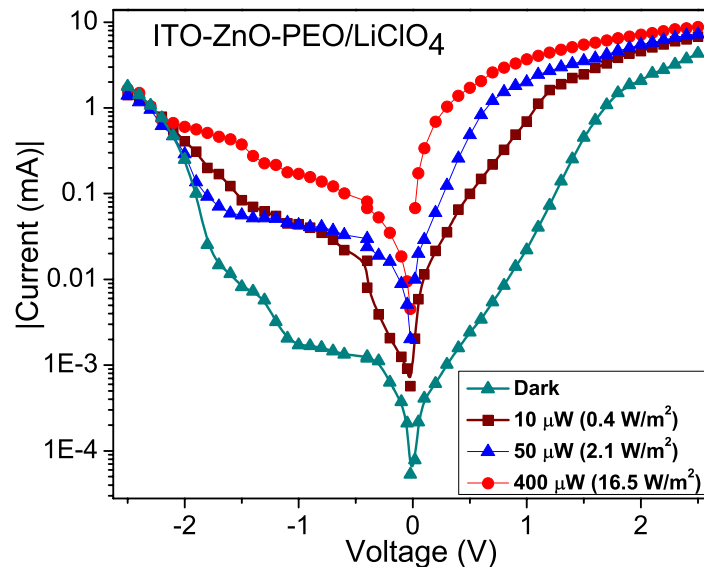
Figure 5.6: I-V curves of the ITO-ZnO-$PEO/LiClO_4$ device for different intensity of UV illumination (345 nm) as indicated on the graph. Reference of bias is on the ITO layer. Device is positively biased when the positive terminal of the source is connected to the $PEO/LiClO_4$ and the ITO is connected to the negative terminal.

interfacial layer and polycrystalline nature of the ZnO nanostructures, it is difficult to fabricate junctions with barriers near the ideal values predicted from the work function of the two isolated materials.

The I-V characteristic of the device recorded at different illumination level is shown in figure 5.6. The current through the device increases by maximum 400 times from its dark value on mere application of light with power 400 μW. Maximum responsivity of 10 A/W at 1.5 V is observed when illuminated by 345 nm light. It is important to note here that the device fabricated in the absence of polymeric electrolyte (ITO-ZnO-Al) also exhibits significant gain in the photoresponse [figure 5.3 (b)]. Maximum photoresponse of 2.5 A/W is observed after UV illumination. Therefore 4 times enhancement in the photocurrent gain is observed after the use of polymeric electrolyte.

These photo-responses were not seen in the absence of ZnO layer and is solely depends on the electron hole pair (EHP) generation and recombination by photo-excitation within a semiconductor. In the absence of ZnO, a linear I-V curve is observed which shows that the ITO-polymer contact behaves as Ohmic [figure 5.3 (b)]. There is no significant change in the dark current after the application of light. Therefore, the optical generation occurs only in the ZnO layer and not within the ITO layer. The ITO layer acts as a conducting layer where electrical contacts (Ohmic in nature) have been placed. The ZnO-polymer junction exhibits nonlinear I-V characteristics and is responsible for the photo-response.
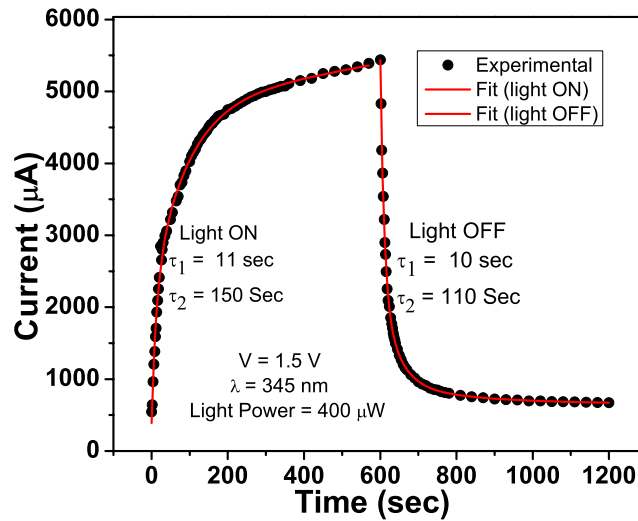
Figure 5.7: Photodetection speed or the rise and fall time of current after application and release of light of wavelength 345 nm respectively.

The photoresponse time of the device have also been measured. We have recorded the sharp rise in current after switching the light ON. The current falls quickly from its saturation level when the light is switched OFF (figure 5.7). The rise as well as fall time are found to be 11 sec and 10 sec respectively by exponential fitting of the experimental data. As compared to the earlier published data, the photoresponse times (both rise time and fall time) of this device consisting of ZnO nanoparticles are not as fast as the response time reported in MSM structure UV detector ([132]) or ZnO Schottky photo-detectors ([140]). The slow response is related to the response of charged ions in the polymer electrolyte to the applied voltage. This device easily

fabricated using a low cost convenient method exhibits high gain photoresponse with response time faster than that reported in sol-gel-synthesized ZnO film photodetectors ([141]). The likely explanation of the photo-response will be briefly discussed the discussion section.

5.6   Reversible control of visible luminescence

An important result of this work is the control of the photo-luminescence properties of the device fabricated in the way described in figure 5.1. In figure 5.8 we show the photoluminescence spectra of the device after the excitation by a light of wavelength 345 nm through the ITO layer for which the emitted photons were collected in reflection mode. Along with the UV peak at 400 nm, there is a broad peak at 545 nm. The photoluminescence spectra from the device (shown in figure 5.8), matches qualitatively with the data obtained for the colloidal ZnO nanoparticles. But we observe a reduction in relative intensity of the surface related visible emission from ZnO due to surface passivation when kept sandwiched between the ITO and $PEO/LiClO_4$ layer. Partial reduction also arises due to agglomeration of ZnO nanoparticles to size $\sim$50 nm. The intensity ratio of the visible to UV emission of the ZnO nanoparticles in the device is 5 times lower than that of the colloidal ZnO nanoparticles.
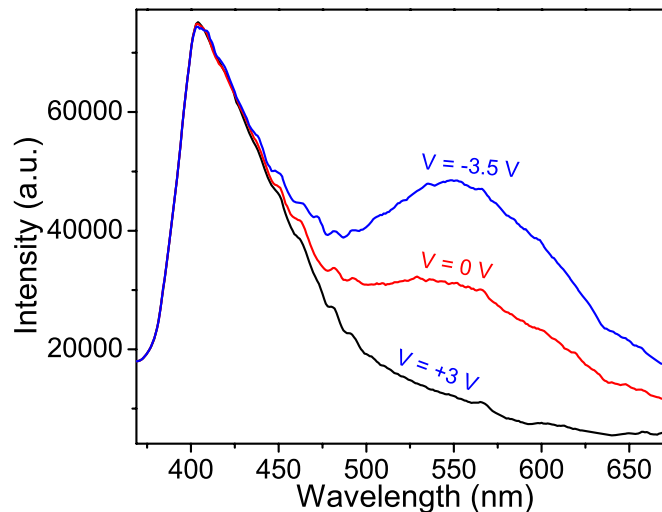
Figure 5.8: Photoluminescence spectra showing reversible control of the visible luminescence near 544 nm by the application of voltage as indicated on the graph. The NBE emission around 400 nm remains unchanged by the application of voltage. Reference of bias is on ITO layer. The enhancement in the visible luminescence is observed when the negative terminal of the source is connected to the $PEO/LiClO_4$ as shown in figure 5.1 and vice versa.

Now we apply a DC bias on the two terminals (ITO and $PEO/LiClO_4$) as shown in figure 5.1. When the illuminated surface (ITO-ZnO interface) is positive or the polymer interface is negative (biasing arrangement shown in figure 5.1), nearly 100 percent enhancement in the visible
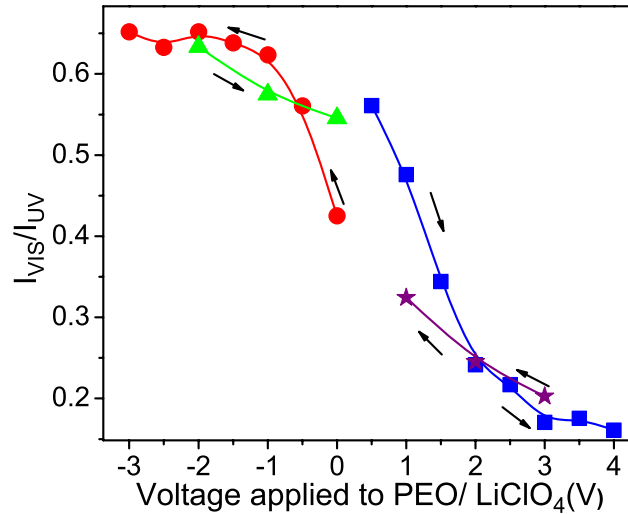
Figure 5.9: The intensity ratio of the visible ($\sim$400 nm) to the NBE emission ($\sim$544 nm) has been plotted with decreasing or increasing applied voltage as indicated on the graph. There exists a hysteresis loop due to the delay in the voltage controlled visible luminescence process. Reference of bias is on ITO layer.

luminescence has been observed(figure 5.8). A complete quenching of the visible luminescence is possible by the application of positive bias at the $PEO/LiClO_4$ top layer. The intensity ratio of the visible ($\sim$400 nm) to the NBE emission ($\sim$544 nm) has been plotted with decreasing or increasing applied voltage as indicated on the graph (figure 5.9). There exists a loop due to the delay in response of the voltage controlled visible luminescence process. In the current situation, time gap between two zero bias measurement was 20 minutes which is not sufficient for the complete relaxation of the excited state electrons. The quenching and enhancement of the visible luminescence can be very nicely demonstrated if we apply an AC voltage of frequency 0.1 Hz and amplitude 4.5 V.

For negative half cycles, up to 107 percent enhancement in the visible luminescence has been observed [figure 5.10] whereas a complete quenching (87 percent reduction) of the visible emission has been seen when the $PEO/LiClO_4$ layer is posively biased. The sharp NBE emission (near band edge) in the ultraviolet region however has no dependence on the applied voltage (figure 5.12). The response time of the luminescence output to the applied voltage lies within the range of 20 -30 sec. AC response of the luminescence output remains constant with a square wave of time period faster than 20 sec. The response of visible PL intensity with voltage follows the variation in current through the device. In figure 5.11 (a) and (b), response of the visible PL intensity and variation in current respectively after application of a step voltage of 4.5 V have been plotted. The time constants of the visible PL as well as the current are obtained by exponential fitting of the voltage response data shown in figure 5.11. The rise time after application of voltage, decay time at a constant voltage, decay time after release of the voltage, quenching by application of reverse voltage and rise by release of reverse voltage have been
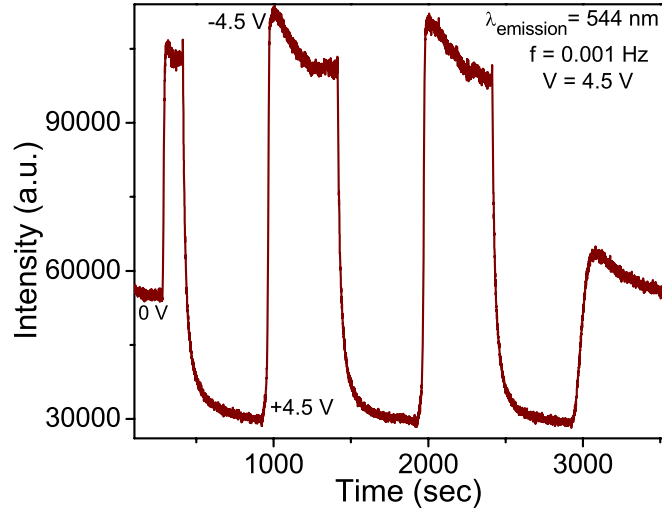
Figure 5.10: AC voltage response of the visible luminescence intensity as a function of time collected at 544 nm exactly follows the amplitude and the polarity of the applied voltage. Nearly 100% modulation of the visible luminescence is achieved. Reference of bias is on ITO layer. The enhancement in the visible luminescence is observed when the negative terminal of the source is connected to the $PEO/LiClO_4$ as shown in figure 5.1 and vice versa.

tabulated in Table 5.1. The interesting point is that the rise and decay time of this surface related visible emission is indeed very slow because of the two possible reasons, such as 1) the slow voltage response of the ions in polymeric electrolyte and 2) the well known phosphor nature of the ZnO nanoparticles.

There is a prominent kink when we apply a reverse voltage for quenching (see figure 5.11). The decay and rise time of the kink has also been listed in Table 5.1. This is because when the polarity of the applied voltage changes, a reverse current flows through the junction during

Table 5.1: Rise and fall time for PL intensity and current after application and release of voltage respectively

	Time components	Rise with voltage	Relaxation with voltage ON	Relaxation when voltage taken off	Kink Growth	Quenching by applied voltage	Rise by release of voltage
PL	$\tau_1(\text{sec})$	28	2700	21	27	76	780
	$\tau_2(\text{sec})$	–	–	88	–	334	–
Current	$\tau_1(\text{sec})$	1	3600	1	2	–	–
	$\tau_2(\text{sec})$	–	–	–	12	–	–
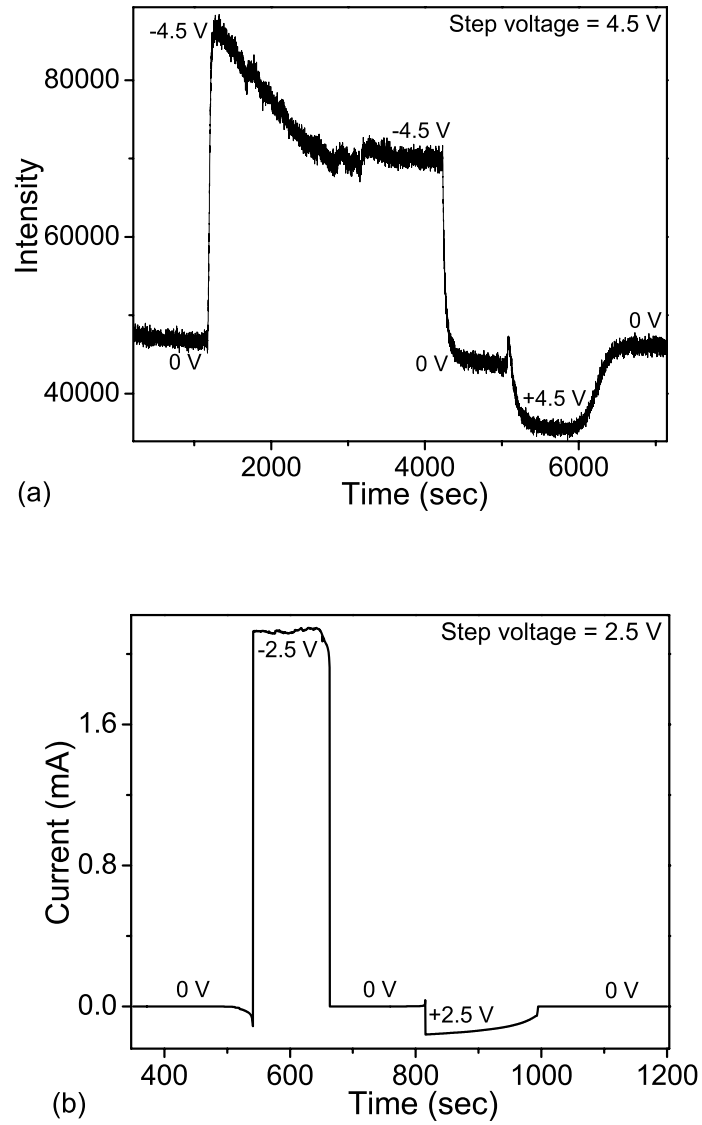
Figure 5.11: Time delay in voltage response of (a) photoluminescence intensity and (b) current of the device is determined by the application of step voltage of amplitude 4.5 V and 2.5 V respectively. The rise and fall with application and/or release of voltage is fitted with exponential function and the extracted decay times are listed in table 5.1. Reference of bias is on ITO layer.
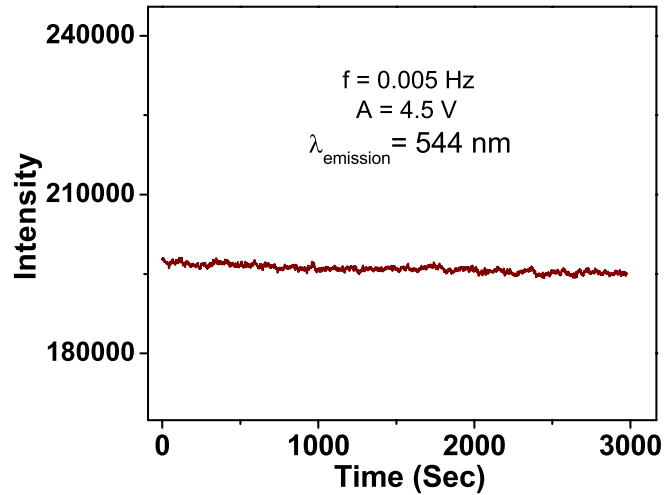
Figure 5.12: The NBE emission at 400 nm does not have any dependence on the polarity and amplitude of the AC voltage (shown in the same intensity range as in the case of visible emission).

the time required for re-adjustment of the stored charge. Let us assume that a junction is periodically switched from +E to E volts. While E is positive, a steady state current $I_f = $ E/R flows through, the source voltage appears almost entirely across the junction. After the generator voltage is reversed (t>0), the current must initially reverse to $I_r = $ -E/R. The reason for this unusually large reverse current through the junction is that the stored charge (and hence the junction voltage) can not change instantaneously. Therefore, just as the current is reversed, the junction voltage remains at the small forward bias value it had initially i.e., at t = 0. A voltage loop equation then tells us that the large reverse current E/R must flow temporarily. After the readjustment of the stored charge, the current starts decaying from a value determined by that particular reverse voltage. When the voltage changes from 0 to E, a small enhancement in the current as well as in PL intensity is observed. This is because there is a short circuit (E=0) current in the device and when the polarity has changed to E, an enhanced current (equal to the short circuit current) flows through the junction to satisfy the KVL.

5.7   Discussion

The phenomenon described above can be explained by the following way. There are two main effects that have been observed. First, there is enhancement of current through the device after illumination by light (Photoresponse). Secondly, reversible tuning of the visible luminescence from ZnO nanostructures by the application of voltage is observed (electrophotoluminescence). For the purpose of electro-photoluminescence measurement one need to illuminate the device which eventually enhances the current by EHP generation. Below we try to find out the origin of these two effects for clear understanding of the device performance.

5.7.1 The role of the electrolyte and the nature of the semiconductor (ZnO)-polymeric electrolyte interface

The observations in this chapter, as can be seen are many fold as well as novel. These effects essentially arise from the ZnO-electrolyte interface. To check that these effects are predominantly related to the semiconductor-electrolyte interface, we fabricated a device consisting of top Al layer in place of polymeric electrolyte. The dark and illuminated I-V of this device is shown in figure 5.3(a). The junction has predominantly linear I-V as noted before, however, there is an effect of illumination and the current increases by nearly 2 orders for both bias. We relate this to photoconductivity of ZnO. In fact this experiment is important because it shows the extent of photoresponse due to photoconductivity of ZnO. Definitely the presence of the electrolyte causes more pronounced photoresponse (for comparison see figure 5.6) as well as the strong non-linear and non-ohmic I-V curve is affected more strongly by the electrolyte. As for voltage control of visible PL we show the effect in figure 5.13. There is a small decrease of visible PL at a much higher voltage when a positive bias is applied to the Al (ZnO is negatively biased). No enhancement is seen as in the case of electrolyte based junction.
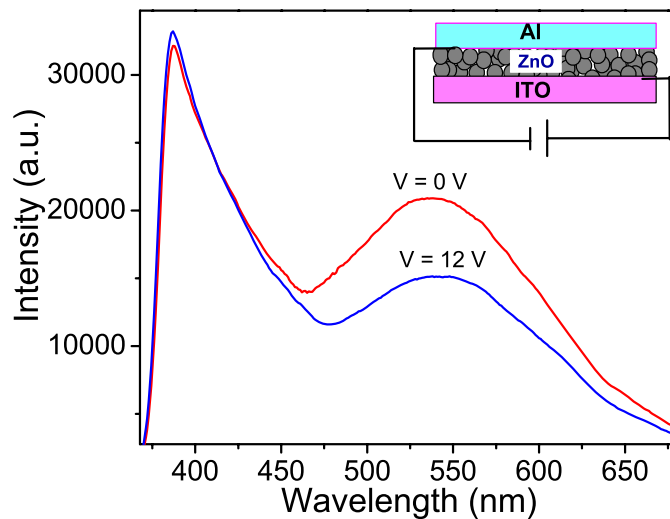
Figure 5.13: The PL spectra of a device with a conducting Al layer (replacing the $PEO/LiClO_4$ layer) on top of ZnO film as shown in the graph. Reference of bias is on ITO layer.

The choice of the electrolyte in this work needs elaboration. A number of PEO-electrolyte blends are used as an instrument to create large charge density; in particular in use as ion-gated FET [204]. Recently it has been shown that $PEO/LiClO_4$ is capable of inducing large charge into ZnO [125]. Large charge density of the order of 0.33 holes/molecules has been reported in use of $PEO/LiClO_4$. Inducing charges in ZnO by gate effect they could make ZnO (nominally n-type) undergo insulator-metal transition at a positive voltage $\sim$1.3 V applied to the electrolyte. The applied bias steadily reduces the resistance of the ZnO. The positive voltage applied to the electrolyte will move the negative ions to the electrodes which in turn will induce a negative

charge in ZnO.

$PEO/LiClO_4$ is a blend composed of the polymer and the electrolyte. The conductivity of the blend can be changed by changing the relative weight fraction of the $LiClO_4$. In this work we use the relative weight $\sim$ PEO:$LiClO_4$ = 10:1. The ion dynamics using dielectric spectroscopy has been investigated recently [205] and it has been found that the $PEO/LiClO_4$ electrolyte behaves as a glassy system with d.c conductivity (extrapolated form the a.c conductivity) in excess of $\sim 10^{-5}$ S/cm at room temperature.

The device as well as the photoresponse of the junction is determined by the ZnO-electrolyte interface. This is a complex issue inspite of extensive studies over the years ([206], [207]). We adopt simple models to explain qualitatively the main features of the observation. A quantitative evaluation will involve experiments that are beyond the scope of the thesis. There are two issues in the semiconductor-electrolyte (SE) junction. First is the issue of charge built-up near the interface that will determine the potentials and the charge crossing at the interface that will go from ionic (electronic) to electronic (ionic) environment when it crosses the junction. For the first issue we note that the ZnO used here is predominantly n-type but the nanoparticles (as discussed in Chapter 4) have surface charge and there is depletion layer due to compensation of the electrons by the holes and this depletion layer controls the nature of the visible PL. Following the suggestion of Arutyunyaqn [206], we propose the charge built up as below. This is
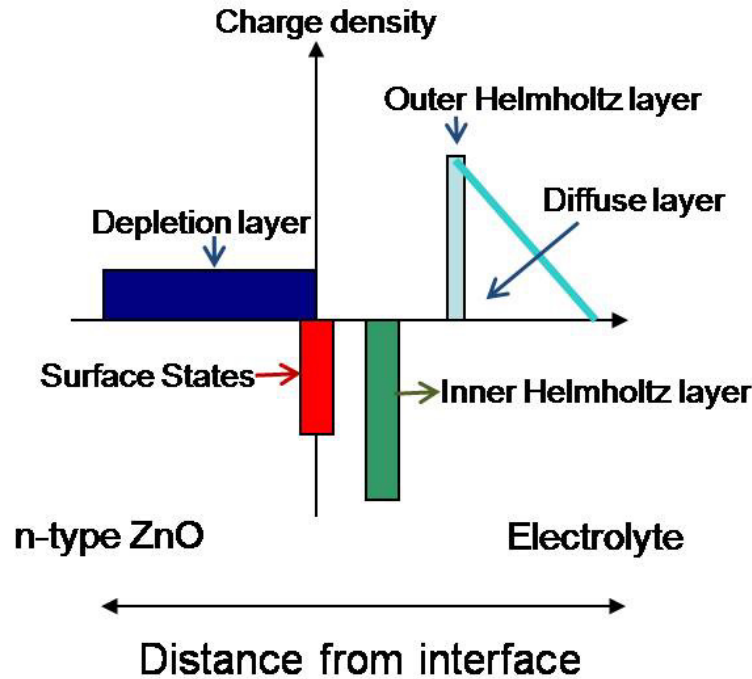
Figure 5.14: The above diagram shows that the charge built-up at the interface will be the dominating factor in determining the potential drops across the junctions. It is generally believed that the Helmholtz layers are thin so that most of the applied bias is applied at the interface.
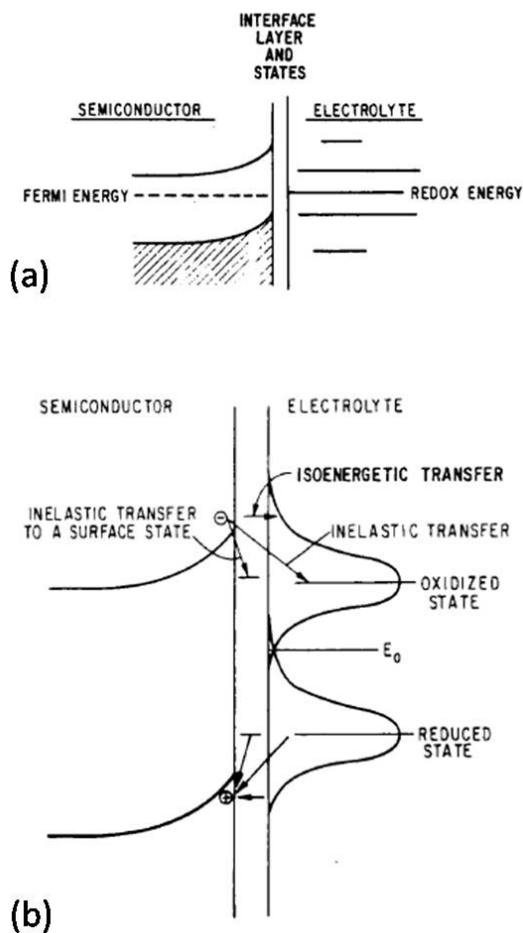
Figure 5.15: (a) Schematic diagram showing relative energy levels to illustrate the difference between semiconductor-electrolyte junctions. (b) Schematic illustration of various electron transfer processes between electrolyte and interface states and semiconductor carriers at the surface of the semiconductor. Figures are reproduced with permission from ref. [207].

the structure of the electric double layer which is generally described by Gouy-Chapman-Stern model (figure 5.14).

The charge transport in the SE junction depends on the basic energy level model. In a typical metal-semiconductor junction (which makes a Schottky junction) the Chemical potential or the Fermi level is aligned. This leads to creation of built in potential and band-bending. The applied voltage creates realignment of the chemical potentials w.r.t. the conduction band. This makes the transport possible with enhanced carrier transport in forward bias condition. Such a picture is not applicable for the junction here primarily due to absence of electronic states in the electrolytes (unlike metals) and one cannot use simple concept of a Schottky junction. Below we reproduce a model of the junction (figure 5.15) due to Wilson [207].

The polymer-electrolyte junction upon application of an appropriate potential between the

electrodes can change the oxidation/reduction condition. The negatively biased polymer electrode is reduced (electron addition) while the other oxidizes (electron removal). In forward bias the current is expected to be carried by the majority carrier (in this case, electrons, ZnO being n-type). In reverse bias (polymer-electrolyte negative, ZnO positive) two situations can arise. One can get electrons crossing into the ZnO from the electrolyte (deposited by anions, ClO_4^-, which collect around the interface since the counter ion Li^+ is pulled to the negatively charged electrode). In addition, in certain range of bias (moderate reverse bias) another process can occur where a majority carrier from ZnO (electron) can cross over to the electrolyte side. When a reduced electrolyte state is at the same energy as the empty states in the semiconductor, i.e., when the states overlap, an electron can transfer to the semiconductor. An electron can transfer from the semiconductor to the electrolyte when an oxidized electrolyte state overlaps the filled states of the semiconductor. This overlap approach has been useful for qualitative discussion of the many combinations of semiconductors and redox couples that have been investigated experimentally. Due to existence of different process the mechanism of charge deposition and transport across the junction is complex.
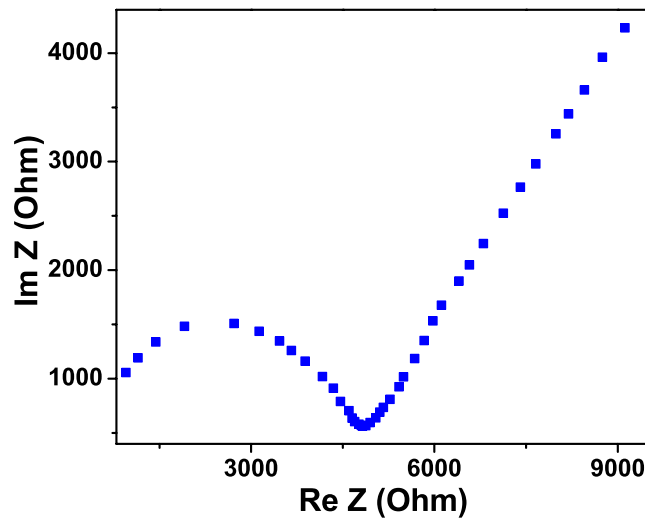
Figure 5.16: Impedance spectroscopy data plotted in cole-cole plot.

It is noted that in recent years ionic-FET has been made in a number of organic devices ([208], [209]). Some of the papers specifically use $PEO/LiClO_4$ as gate electrode. While using polymeric-electrolyte as a gate two things can happen. It can be *charging via the field-effect* (as it occurs in conventional metal-oxide-semiconductor field-effect transistors, MOSFETs) or it can be *electrochemical doping*. The doping can occur if the semiconductor layer permeable to the ions in the polymer electrolyte. If the ions do not penetrate, which is likely the case here, current modulation is achieved by the electrostatic induction of charge carriers in the semiconductor in response to the electric field at the ZnO-electrolyte interface due to formation of the double layer as stated before. In our case, thus the electrolyte is an electrode (can inject charge into or from the ZnO) and also a charge reservoir like a capacitor.

The time scale of the charge dynamics of the junction device is measured from the impedance spectroscopy. The data taken over a frequency range 50 Hz to 5 MHz are shown in figure 5.16 was found to be dominated by the ionic dynamics of the electrolyte which shows similar spectroscopic behavior [210]. In view of this one would expect that a dominant role of the electrolyte is to work also as a dielectric (or charge reservoir) that can control the induced charge on the ZnO.

5.7.2   Voltage control of the PL

One of the principal results that we have is the control of the visible PL by an applied bias. In the previous chapters we have shown how the defect related visible PL can be controlled by the control of the surface charge which in turn controls the band-bending at the surface of the ZnO nanoparticles. We like to propose an explanation in line with the physical picture proposed earlier.

We propose that when negative voltage applied to the electrolyte the Li^+ ions move away from the ZnO-electrolyte interface. This leads to formation of a negatively charged layer on the surface. This induces more positive charge on the ZnO surface leading to more band bending and thus strengthening the emission from the P2 band (see chapter 3, figure 3.8). When a positive voltage is applied to the electrolyte the ZnO-electrolyte interface accumulates the Li^+ ions which induces more negative charge (or reduces the positive charge) in the surface region of ZnO and hence decreases the effect of band bending. This leads to reduction of the PL. We note that the enhancement of the PL occurs in the reverse bias condition when the ZnO is positively biased. This as stated earlier increases the depletion width. In this situation the junction acts like a capacitor. Since there is also a current flowing in the junction, the occupation of the defect sites may be affected. However, it appears that the primary effect of the bias is to redistribute the charges at the junction through the electrolytes.

5.7.3   The dark current

I-V characteristics shown in figure 5.6 have a number of noteworthy features. The dark current itself is an object of interest. The nature of the dark current is completely different in the two bias directions and more so at low bias ($|V|$=1 V). At higher bias particularly at V $\sim$2.5 V the differences in current for the two biases are much less. The I-V curve can thus be split into different bias domains. For bias within $\pm$1 V, it can be seen that the I-V characteristics is qualitatively similar to that of a Schottky diode, where the forward bias current, due to the majority carrier injected from the semiconductor increases exponentially as the bias is increased. Using a simple thermoionic emission model given below,

$$lnI = \frac{q}{kT}\left(\frac{V}{n} - \phi_B\right) + lnABT^2 \tag{5.1}$$

the equivalent barrier potential ϕ_B at the interface arising due to the depletion layer can be obtained. We obtain an estimate of ϕ_B $\sim$0.76 eV with an ideality factor n$\sim$6. The above equation can be fitted down to approximately 0.15 V. There is a clear knee at the data at lower bias. The apparent similarity of the data with the Schottky data can be justified. At low bias the primary effect is readjustment of the redox energy E_0 with E_F by the bias potential. This will induce more negative charge within ZnO in the junction region thus reducing the band

bending much like what happens when one has realignment of the chemical potentials by the applied bias. In the reverse bias the effect is just opposite and the depletion is enhanced.

At higher bias (bias$> \phi_B$), there is an enhancement from what one would expect from the simple exponential rise. This enhancement can come when extra current path opens up on alignment of the filled trap states with the oxidized states of the electrolytes as the chemical potential is shifted on application of the bias. At even higher voltage there is saturation which may be determined by the concentration of ionic charges in the electrolytes. This concentration limited region appears to be the same for both dark and illuminated samples which should be so if the current gets limited by the availability of ions picking carriers at the junctions. In the reverse bias side also we find that that there is a rapid rise in the current at steps as the bias is increased. These enhancements can also come from additional channels opening up when reduced state fill up carriers (minority carriers) to the valence band of ZnO. Eventually this also saturates at higher bias, presumably due to concentration limitations as this also happens at the same magnitude of the bias as the forward bias region.

5.7.4   The current under illumination and the photoresponse

The current both in the reverse as well as the forward bias are enhanced at least by an order or more at low biases by UV illumination. At higher bias where the dark current saturates due to concentration limitation, understandably the current under illumination also saturates. In forward bias, the illumination is expected to create more electrons in the conduction band. This enhances the majority carrier density (hence the photocoductance) and also will reduce the band bending and the barrier due to the band bending. Thus the enhancement of the forward bias current will be of two reasons - photoconductivity as well as lowering of barrier due to accumulation. We note that the enhancement of the current on illumination is not linear and it more or less saturates at illumination intensity of nearly 10 W/cm^2 at higher bias.

In reverse bias, the relative enhancement is more particularly at lower bias. In this range, the enhancement can occur due to two reasons. First, there is a contribution of photoconductivity that will reduce the resistance of the ZnO film and thus will enhance the current. In addition, the photo-generated carrier can actually be collected by the electrodes. The ITO will collect the electron. The hole will cross the junction and will get exchanged with reduced tail of the oxidized states. The band bending due to reverse bias will cause the VB to bend closer to the oxidized states.

The above discussion though qualitative explains most of the observed data. As stated before a quantitative explanation will need more controlled experimentation at the semiconductor electrolyte junction.

5.8   Conclusions

In summary, the device exhibits high gain photoresponse with maximum responsivity of 10 A/W at 1.5 V when illuminated by 345 nm light. The barrier potential created at the ZnO-polymer interface reduces by UV illumination which in turn enhances the current passing through the junction. The total current flowing through the device is determined by the excess carriers generated by UV illumination as well as carrier injected by the application of voltage. However, the response time to the illumination is found to be 10 sec. The device has been fabricated by

a low cost method where use of the polymer electrolyte offers advantages like easier fabrication, mechanical stability and convenient control.

We have also achieved a reversible control over the visible photoluminescence in ZnO nanostructures with the application of electric field through a solid polymer electrolyte. The ZnO-ITO interface has been illuminated by a 345 nm light passing through the ITO glass substrate and the emitted light near 545 nm has been collected in reflection mode. When the solid polymer electrolyte is negatively biased, up to 107 percent enhancement in the visible luminescence has been observed, whereas a complete quenching (87 percent reduction) of the visible emission has been seen when it is positively biased. The sharp NBE emission (near band edge) in the ultraviolet region however has no dependence within the voltage range we are working. An electric double layer forms at the positively charged ZnO and polymer electrolyte interface. Band bending occurs in both directions (upward as well downward) when alternating voltage is applied. Relative occupancy of the defect levels is affected by this band bending which in turn controls the overall intensity of the visible luminescence. Although slow diffusion of ions for the formation of double layers may limit its application at high frequency, the outstanding dc performance and the easy control of the luminescence intensity would make the device attractive for future applications.

Chapter 6

Structural and optical properties of $Zn_{1-x}Mg_xO$ and $Zn_{1-y}Cd_yO$ alloy nanostructures and the issue of phase segregation

6.1 Introduction

One of the interesting features of ZnO is the possibility to tune its band gap by substituting (alloying) bivalent metals like Cd and Mg in place of Zn. For controlled applications, band gap engineering is technologically very important. While Cd is known to reduce the band gap [161], Mg substitution leads to enhancement of band gap [143]. This raises the possibility of band gap engineered heterostructure for optoelectronics applications in the UV range ([144], [142]).

ZnO has Wurtzite structure with lattice constants a=b=3.25 Å and c=5.207 Å. However both MgO and CdO have rock salt structures and the atomic radii of Mg (0.68 Å) and Zn (0.72 Å) are comparable while that of Cd (0.94 Å) is much larger. Therfore, substution of Mg in ZnO is more probable than that of Cd. For instance, ZnMgO alloy can be easily synthsized at temperature below 100^0C by hydrothermal method. On the other hand, synthesis of ZnCdO alloy demands high temperature and the vapour phase methods are generally employed (discussed in chapter 2). Therefore, the synthesis method and the final concentration of the resulting material can be entirely different for production of Mg and Cd substituted ZnO nanostructures. Synthesis of ZnO and its alloy nanostructures [$Zn_{1-x}Mg_xO$ and $Zn_{1-y}Cd_yO$] for optoelectronics applications are generally done through vapor phase deposition with or without catalyst. Routes that have been used to prepare the alloys are Molecular Beam Epitaxy (MBE) ([145], [162]), Vapor liquid solid phase growth [159], Pulsed Laser Deposition (PLD) [146] and Metallo-organic Vapor Phase Epitaxial growth (MOVPE) [147] and remote plasma enhanced metallorganic chemical vapor deposition (RPE-MOCVD) [163]. Recently $Zn_{1-y}Cd_yO$ nanorods have been fabricated by the thermal evaporation of precursors containing Zn and Cd [164]. Materials obtained by the above methods are mostly films or rods. In addition, low temperature ($\leq 100^0C$) solution route has also been used to fabricate aligned nanorods of pure ZnO ([23], [167]). In a recent paper, Mg substituted ZnO ($Zn_{1-x}Mg_xO$) nanorods synthesized by hydrothermal method (100^0C) has been reported [148]. The advantage of the solution route is that it can give high quality

crystalline materials through an energy efficient route that allows wide area growth (e.g., 4-inch Si wafer). Our principal motivation is to explore whether such a low temperature route will allow us to grow well-characterized Mg and Cd substituted nanocrystals of ZnO as an optical material. In the solution route for material synthesis the mixing occurs at the atomic level and the material prepared by this method is close to the thermodynamic equilibrium phase. Production of nanocrystals of Mg and Cd substituted ZnO by vapour phase methods has its limitations because it is expensive and materials obtained are in small quantities. Thus the synthesis of Mg and Cd substituted ZnO nanostructures by hydrothermal method is a very desirable step. Demonstration that one can produce band gap tuned good quality nanocrystals of Cd substituted ZnO by a low temperature solution route opens up the possibility of large scale synthesis of this material.

While investigating the effect of Mg and Cd substitution on the band gap one needs caution. The band gap engineering leads to a tuning of the PL emission energy and also a change of the life time of the emission. In the context of doped ZnO nanocrystals these issues though studied in the past have not been well understood. Also, if the particle size is smaller than 5 nm, the effect of quantum confinement plays a significant role and the band gap becomes a function of the size [151]. While making the alloy, if a strict control of the size is not achieved then two effects (one from quantum confinement, and other due to Mg or Cd substitution) will make comparable contribution. It has been suggested that the effect of confinement and the substitution can be separated out by calculating the size dependence of the excitonic ground state ([152], [153]. In our experiment to avoid complications arising from confinement effects we used nanocrystals of diameter range 10-12 nm. In this range the radius is ≥ 4 times the exitonic Bohr radius. As a result we can cleanly isolate the two effects experimentally.

One of the important issues that limits synthesis of $Zn_{1-x}Mg_xO$ and $Zn_{1-y}Cd_yO$ is the fact that the thermodynamic solubility limit of MgO and CdO in ZnO is ≈ 4 at.% [149] and ≈ 2 at.% [164] respectively. The issue of Mg and Cd incorporation in ZnO in excess of their solubility limit without phase segregation is an important and topical research problem. It has been claimed that using the vapor phase route such as pulsed laser deposition it is possible to incorporate Mg up to ~ 40 at.% [143]. For MOVPE grown films the Mg incorporation has been reported to be ~ 49 at% [147]. For $Zn_{1-x}Mg_xO$ nanorods, grown by solution route, $x \approx 0.25$ has been reported to be achieved [148]. There are reports where Cd concentrations up to 20% [164] and even very high (more than 50%) [176] have been achieved.

In this chapter we would like to explore a very specific question- to what extent one can incorporate Mg and Cd into ZnO nanocrystals without phase segregation using low temperature solution route and the resulting quality of the material as characterized by structural and optical means. The structural and optical properties of Magnesium and Cadmium substituted Zinc Oxide [$Zn_{1-x}Mg_xO$ ($0 < x < 0.2$) of size 10-12 nm and $Zn_{1-y}Cd_yO$ ($0 < y < 0.1$) of size 10-15 nm] synthesized by chemical route are described. Beyond x = 0.2 and y = 0.1 segregation of Mg and Cd rich phase occur respectively. The exact chemical composition has been established by quantitative analysis. Rietveld analysis of the X-ray diffraction (XRD) data confirms the Wurzite structure and a continuous compaction and expansion of the lattice for $Zn_{1-x}Mg_xO$ and $Zn_{1-y}Cd_yO$ nanostructures respectively as x increases. There is an enhancement of the strain in the lattice as the Mg and Cd is substituted. The bandgap gets enhanced (reduced) by Mg (Cd) substitution. One can tune the band gap of ZnO from 3 eV to 4 eV by substitution with Cd (y = 0.065) and Mg (x = 0.17). The nanocrystals show near band edge photo luminescence (PL) at room temperature which shows blue shift (red shift) on Mg (Cd) incorporation.

6.2 Synthesis and compositional analysis

Detailed discussion on synthesis of alloy nanostructures is given in section 2.3 (chapter 2). The structural and microstructural characterization of this nanoparticles so synthesized are given in relevant sections below. However there is one important issue that we bring out here. For all our alloyed samples we have used quantitative chemical composition analysis to establish the level of Mg and Cd incorporation in alloyed structure. We determine the exact chemical composition of the particles using the Inductive Coupled Plasma Atomic Emission Spectroscopy (ICP-AES) technique which shows that the maximum composition of Mg and Cd that we could get into the $Zn_{1-x}Mg_xO$ and $Zn_{1-y}Cd_yO$ nanocrystals correspond to x = 0.17 and y = 0.091 which is comparable to some of the vapor phase synthesized samples [161]. The analysis of the chemical composition by analytical quantitative technique like the ICP-AES is important because it establishes exactly how much Mg and Cd can be incorporated into ZnO. The substitution achieved
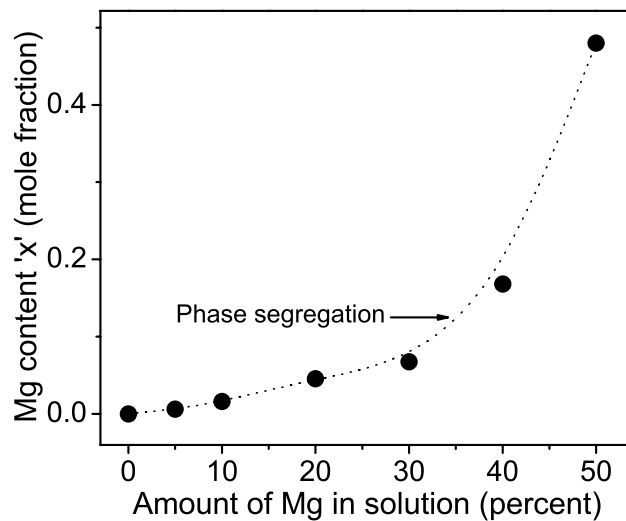
Figure 6.1: Exact concentration x of Mg in $Zn_{1-x}Mg_xO$ nanocrystals determined by ICP-AES vs the molar fraction of Mg acetate $(Mg(CH_3COO)_2.4H_2O)$ in solutions.

in this work is larger than their reported values of equilibrium compositions but much less than what has been reported in some of the vapor phase grown samples where a very high value of Mg and Cd content have been reported ([147], [176]). It appears that the measure of dopant incorporated in a sample is dependent on the analytical technique used. The technique like EDX is surface sensitive being limited by the electron penetration depth and what it reports is essentially the concentration near the surface. Whereas ICP-AES technique is averaged over the bulk and provides the exact compositions of the sample. The high concentration of Cd reported were based on the EDX results [164]. This is expected because of the following reason when there is a possibility of phase segregation as a result of excessive addition of source materials. Due to the segregation of the CdO out from the nanocrystals, there may be a concentration gradient which increases from the interior of the nanocrystals to the surface and the difference in the Cd

concentration seen by the two techniques may reflect this. In figure 6.1 and 6.2 we show the value of exact composition as determined through the ICP-AES analysis vs. the molar fraction of $(Mg(CH_3COO)_2.4H_2O)$ and $(Cd(CH_3COO)_2.4H_2O)$ added in the $(Zn(CH_3COO)_2.2H_2O)$ solution respectively. For samples with concentration above x = 0.17 (Mg content) and y = 0.065 (Cd content) the resulting nanocrystals is not single phase as we will show from the XRD and the TEM data. They show phase separation between two phases viz. wurtzite $Zn_{1-x}Mg_xO$
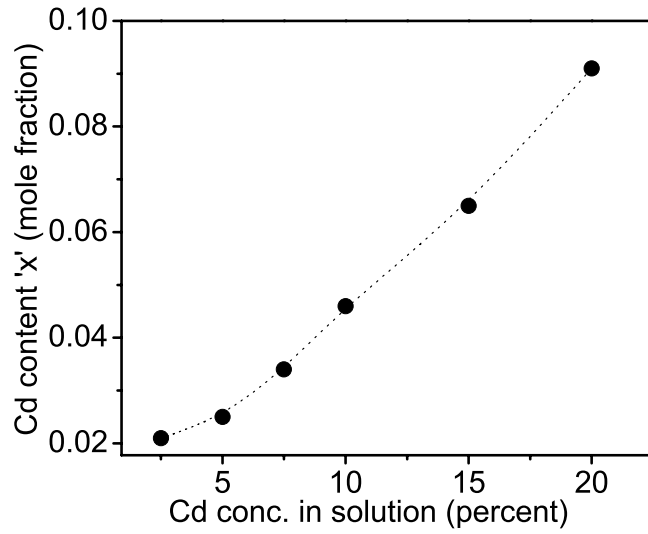
Figure 6.2: The value Cd content y observed by ICPAES analysis against the mixing of various amount of $(Cd(CH_3COO)_2.4H_2O)$ in the $(Zn(CH_3COO)_2.2H_2O)$ solution.

and brucite $Mg(OH)_2$ (this will also be seen clearly from the XRD investigation discussed later) for Mg substitution. Sample with x = 0.52 show a thin layer of $Mg(OH)_2$ on the $Zn_{1-x}Mg_xO$ nanoparticles forming a core-shell structure. In case of Cd substitution two separated phases are wurtzite $Zn_{1-y}Cd_yO$ and rocksalt CdO. The quantitative compositional analysis (irrespective of the technique used) establishes that the Cd incorporation is indeed very low due to the high lattice mismatch and difference in crystal structure of ZnO and CdO. We will see below that the incorporation Cd into ZnO gets limited because phase segregation occurs very early ($y \approx .03$) in the growth process where the $Zn_{1-y}Cd_yO$ nanocrystals physically separate out from the CdO crystals having relatively larger size. Recently it has been established that the doping efficiency is determined by the binding energy of dopant atoms on the individual nanocrystal surface [154]. The binding energy for wurtzite nanocrystals is three times less than that of zinc blend or rocksalt structure on (001) faces. Therefore the low concentration of incorporated Mg and Cd is likely to be a consequence of lower doping efficiency of the wurtzite ZnO nanocrystal surfaces.

6.3 Structural and optical properties of $Zn_{1-x}Mg_xO$ nanocrystals

In this section we show that a low temperature route can be used to make the alloy $Zn_{1-x}Mg_xO$ with x as large as 0.17. Above this composition the MgO segregates. Up to this composition the alloy retains a Wurzite structure and the lattice constants change smoothly as x is varied albeit by a small amount. The phase segregation for $x > 0.20$ has been established by XRD as well as TEM studies. However, even with such low incorporation of Mg there are important and distinct changes in the optical properties of the material. The alloy nanocrystals show an enhanced band gap that reaches $\approx 4.0 \ eV$ for $x = 0.17$ and an appreciable near band edge Photoluminescence (PL) response when excited with UV radiation. The near band edge UV emission occurs at room temperature and the emission shows blue shift as x is increased. The choices of nanocrystals rather than nanorods are two fold. First, working with good quality nanocrystals allows us to use the Rietveld analysis [150] for the x-ray diffraction to get a more quantitative evaluation of lattice constants, which is not possible with aligned rods. Second, ZnO nanocrystals showing good optical properties are basic building blocks for all applications and can often be used directly for many optoelectronic applications. It is like a quantum dot operating in the UV.

In addition to the near band edge emission the ZnO and $Zn_{1-x}Mg_xO$ alloy nanocrystals show considerable emission in the blue-green region at wavelength of $\sim$550 nm. We find that the relative intensity of the green emission increases with the Mg concentration for very low x (upto x = 0.05) and on further increase of the Mg concentration there is a sharp decrease of relative intensity of the green emission eventually leading to a complete quenching of green emission. It is concluded that due to phase segregation (for x>0.20), the formation of the shell of $Mg(OH)_2$ on the ZnO leads to quenching of the green emission. However, this shell formation does not have much effect on the near band edge PL.

6.3.1 Microstructure study by TEM

TEM images of the ZnO (undoped) nanocrystals with a uniform size distribution (average diameter $\sim$10 nm) are shown in figure 6.3. Figure 6.3(a) shows the TEM image of a collection of the particles. The lattice fringes and Fast Fourier Transform (FFT) of the lattice image of a single particle is shown in figure 6.3(b) and 6.3(c) respectively. The FFT confirms the hexagonal symmetry of the particles. The distance between the parallel lattice fringes of the undoped ZnO particle is 2.62Å. The doped particles obtained are well defined crystals. In figure 6.4(a) we show a typical HR-TEM image of an alloy $Zn_{1-x}Mg_xO$ nanoparticle with x=0.17. The distance between the parallel lattice planes is very similar to that of the undoped crystals (2.60Å). Figure 6.4(b) shows the fast fourier transform (FFT) of the lattice image shown in (a) which confirms that the hexagonal symmetry of the ZnO nanocrystals are preserved on Mg substitution. The TEM images clearly establish that the Mg incorporation does not lead to any change in the crystal symmetry and the crystal structure upto about x≈0.17. This is an important observation because MgO has a rock salt structure and for higher concentration of Mg one would expect segregation of phases.

In the following we establish through the TEM study (which will be later elaborated by XRD) that on further addition of Mg there is no incorporation of Mg into the lattice. Instead, there is phase segregation. We observe (presented below) that for higher Mg incorporation there is a clear appearance of XRD peaks due to $Mg(OH)_2$ brucite structure. Figure 6.5 shows the
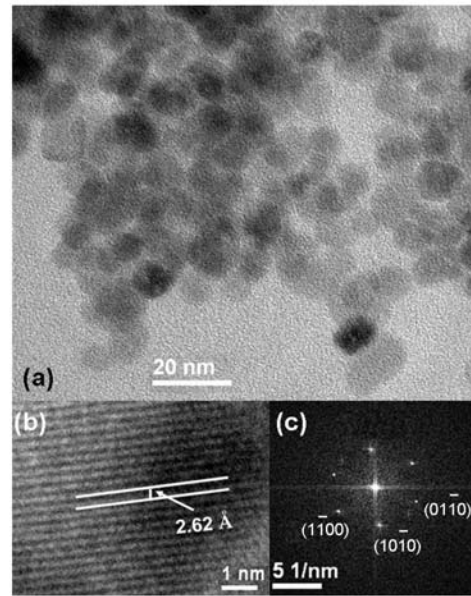
Figure 6.3: (a) TEM image of undoped ZnO nanocrystals. (b) and (c) show the HRTEM image and the SAED of the same sample respectively
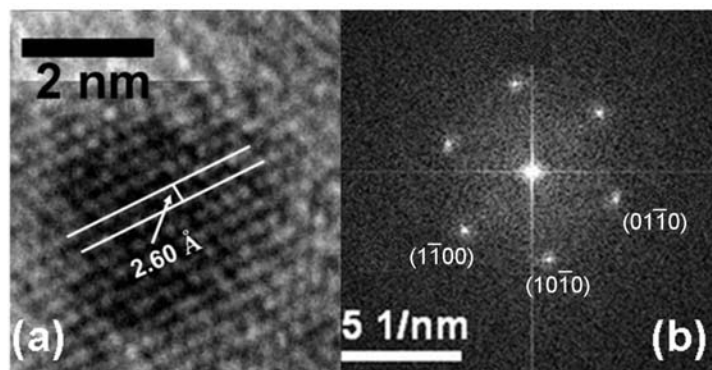
Figure 6.4: (a) and (b) show the HR-TEM image and SAED pattern respectively of the $Zn_{1-x}Mg_xO$ nanocrystals with Mg content x = 0.17.

TEM images of the same sample grown with condition of 55 mole % $(Mg(CH_3COO)_2.4H_2O)$ in the solution ($x = 0.52$) which clearly shows a thin layer of $Mg(OH)_2$ on the $Zn_{1-x}Mg_xO$ core. Upper part of the figure represents a single particle which shows a thin ring around the core. Lower part shows the HRTEM image taken at the junction of the thin layer and the core which clearly establishes the existence of two phases on the two sides of the junction. The left one shows uniformly spaced lattice fringes and two spots on the SAED pattern (left most part, indicated by an arrow) which confirms the existence of single phase. The phase
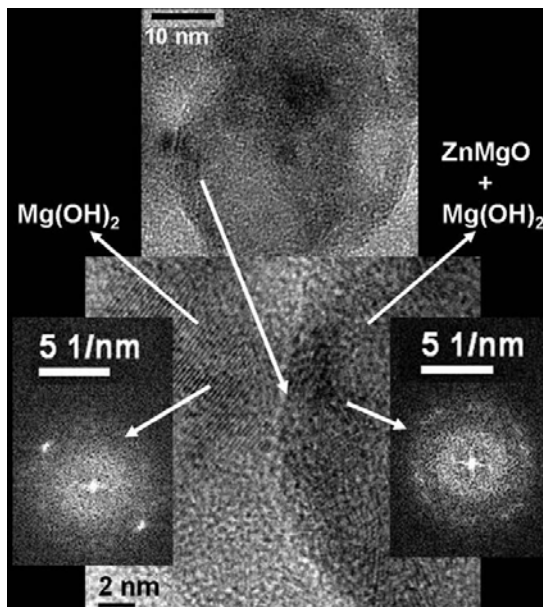
Figure 6.5: TEM image showing core-shell structure of Zn1-xMgxO coated with $Mg(OH)_2$ seen in phase separated nanocrystals. Upper part of the figure shows a thin layer around the core. The lower part represents the lattice image at the interface of the two materials which clearly shows two different arrays of lattice fringes separately for $Mg(OH)_2$ (left) and mixture of $Zn_{1-x}Mg_xO$ and $Mg(OH)_2$ (right).

was identified as $Mg(OH)_2$ by the XRD data as it shows two distinct peaks (corresponding to the spots in the SAED pattern) due to (100) and (110) planes of brucite $Mg(OH)_2$. On the right side of the junction, lattice fringes are overlapped and this indicates mixture of two phases (wurtzite $Zn_{1-x}Mg_xO$ with $Mg(OH)_2$ as cover layer). This fact is also clear from the SAED pattern (right most figure indicated by an arrow) which shows diffused pattern, again indicating a phase mixture. From the XRD data, the core structure of this sample can be easily identifiable as wurtzite $Zn_{1-x}Mg_xO$. To summarize this section we find that Mg can be incorporated upto x = 0.17 in the alloy $Zn_{1-x}Mg_xO$ nanoparticles by low temperature solution method without phase segregation and retaining the Wurzite structure of the parent ZnO system. The resulting nanoparticles (diameter~10-12 nm) are single crystals. Further addition of $(Mg(CH_3COO)_2.4H_2O)$ leads to phase segregation that creates a core of the alloy $Zn_{1-x}Mg_xO$ and a shell of the $Mg(OH)_2$. (Note: The EDX taken in the TEM also allows one to evaluate the Mg concentration in the nanoparticles. A comparison with ICP-AES measurements shows that the concentration determined by EDX alone overestimates x severely. We have used

the ICP-AES results because the method is more standardized with available standards.)

6.3.2   X-ray diffraction results and analysis of the structural data

One of the important issues in the alloy $Zn_{1-x}Mg_xO$ formation is the change in the lattice constant when Mg is incorporated. Although Zn and Mg have very comparable ionic radii (lattice mismatch $\triangle R_{Mg} = 0.09$Å), the crystal structures of MgO and ZnO are different and it is expected that at certain concentration of Mg the simple substitution has to terminate. The alloy formation is thus expected to give a small change in the lattice constants for $Zn_{1-x}Mg_xO$ alloys. As shown in figure 6.6, the observed powder data for $Zn_{1-x}Mg_xO$ can be indexed to
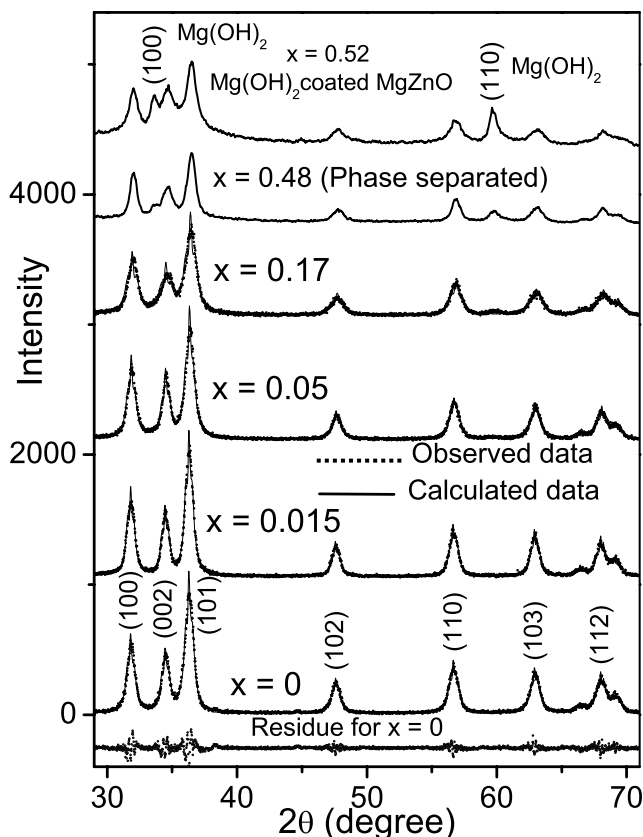
Figure 6.6: XRD data taken on $Zn_{1-x}Mg_xO$ nanocrystals. It shows single phase (wurtzite structure, peaks are indexed) upto $x = 0.17$. Beyond this level phase separation takes place and distinct peaks due to (100) and (110) planes of $Mg(OH)_2$ (indexed in the figure) are observed. The data upto $x = 0.17$ are analyzed by Rietveld method. Observed data (dotted curve) upto $x = 0.17$ are fitted well with the calculated data (solid line). Examples of residues are shown for $x = 0$ at the bottom.

wurtzite structure upto x =0.17. This indicates that single phase $Zn_{1-x}Mg_xO$ nanoparticles form with Mg incorporation. However, for higher Mg content (x>0.17) additional peaks appear in the XRD data. These two peaks are due to (100) and (110) reflections of $Mg(OH)_2$ as indicated in figure 6.6. This indicates phase separation between ZnO and $Mg(OH)_2$. We have
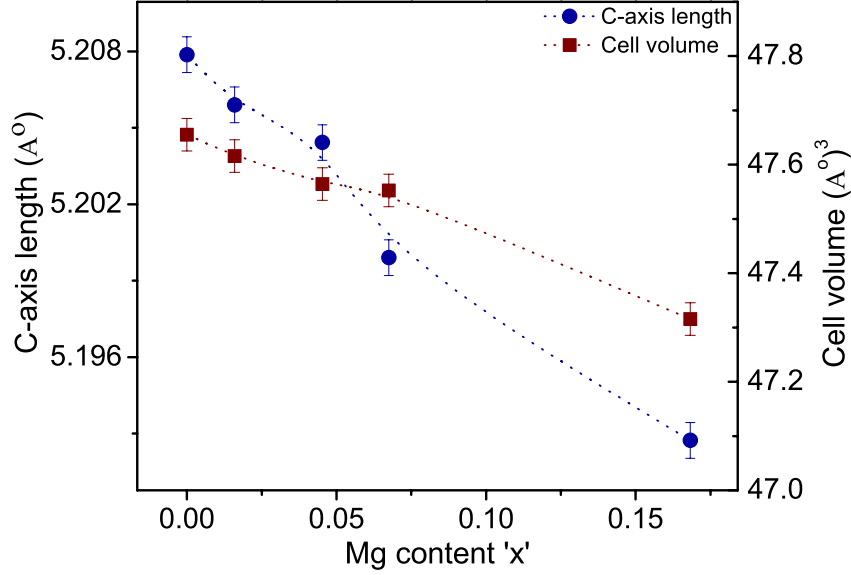
Figure 6.7: Variation of c-axis length and cell volume (extracted from the Rietveld analysis of the XRD data) with the Mg content x.

seen before in the TEM image (figure 6.5) that this sample shows a core-shell structure of a thin layer of $Mg(OH)_2$ on the $Zn_{1-x}Mg_xO$ core. The crystal structures were investigated by analyzing the XRD data (upto x = 0.17) by full profile fitting using Rietveld method [150]. The fit of the data have been shown as a solid line in figure 6.6. In the least square refinement, peak shape was assumed to be Pseudo-voigt. An example of the residue of the fitting is shown in the figure for x = 0 data. The profile fitting to determine the lattice constants assumed that the Mg is on substitutional sites and it occupies these sites randomly. One obtains good fitting with low residue with this assumption. We can thus conclude that the alloy formation does occur with Mg randomly substituting for Zn. The HR-TEM lattice images also corroborate this.

As shown in figure 6.6, the peaks in the powder XRD of the nanocrystals shift to higher angle as x is increased, indicating decrease in the lattice constants of the ZnO due to incorporation of Mg. The lattice constants (a, b, c) and the cell volume V $(=0.866a^2c$ for hexagonal lattice) were determined from the full profile fitting of the observed data. As plotted in figure 6.7 the lattice constants as well as the cell volume decrease monotonously as x is increased. We observed 0.3% change in the c-axis length which is smaller than the approximate decrease in the value of the c-axis lattice constant ($\sim$0.6% for x=0.2) observed in MOVPE grown $Zn_{1-x}Mg_xO$ alloy films [147]. Thus, the lattice constant depends on the method of growth. The Rietveld analysis shows that the lattice constant a $(= b)$ changes by even a smaller amount $\sim$0.15% for the same Mg concentration. The XRD studies show that the main effect of Mg substitution is compaction along the c-axis which in turn leads to a compaction of the unit cell volume.

The XRD data were also used to find the average particle size and microstrain using Williamson-Hall (W-H) analysis using simplified integral breadth method [81] which is discussed in chapter
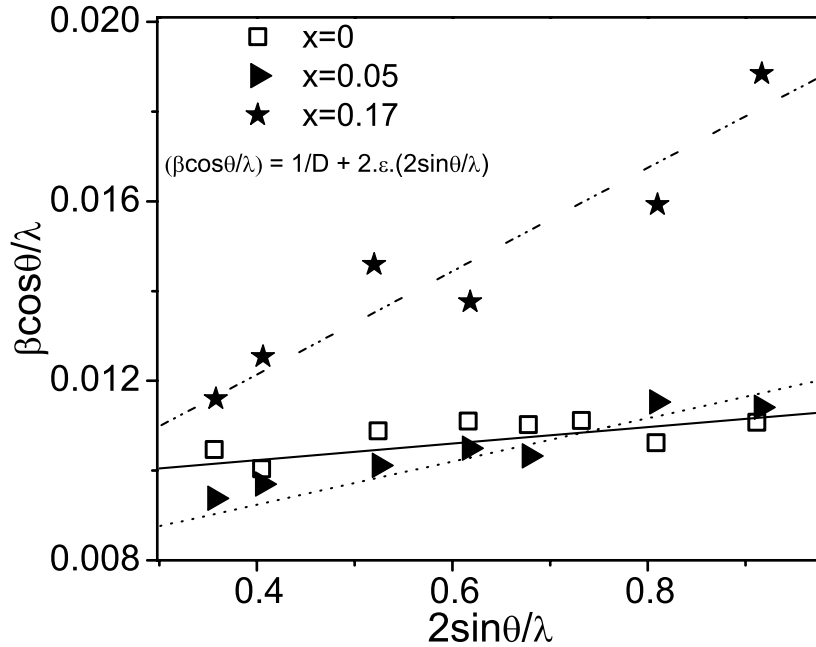
Figure 6.8: Williamson-Hall plot of three representative XRD data shown in figure 6.6. The solid line, dotted line and dashed dotted line are the linear fit of the data points corresponding to the samples undoped ZnO of size ~10 nm, x = 0.05 and x = 0.17 respectively. The average grain sizes and microstrain has been calculated from the y-intercept and slope of the linear fits respectively.

2. The average particle diameter was obtained from this analysis and this matches with that found from the TEM. W-H analysis also allows us to find the microstrain from the slope of the linear fit of the data points [equation 2.8 in chapter 2]. Williamson-Hall plot for three representative samples as indicated on the graph is shown in figure 6.8. The microstrain values calculated by this method were plotted with the Mg content x in figure 6.9. For low x, the microstrain is within the range of $\approx 1 - 5 \times 10^{-3}$ which is similar to that seen in undoped (x=0) nanocrystals. Although there is a gradual increase in microstrain as x increases, for x>0.17 there is a sudden increase in the microstrain value by a large amount. Interestingly this is the value of x for which the phase segregation takes place. The XRD data (along with the TEM data) provides clear evidence for the phase segregation. It therefore appears that the phase segregation is driven by the built in strain on Mg incorporation. To summarize, the extensive analysis of the XRD data shows that Mg can be incorporated in the ZnO forming the random substitutional alloy $Zn_{1-x}Mg_xO$ for x≤0.17. It is important to establish that the material thus formed has the Mg in the substitutional sites. The substitution leads to a compaction of the c-axis lattice constant. However, for higher values of x there is a phase segregation, which is corroborated by TEM results presented in previous subsection.
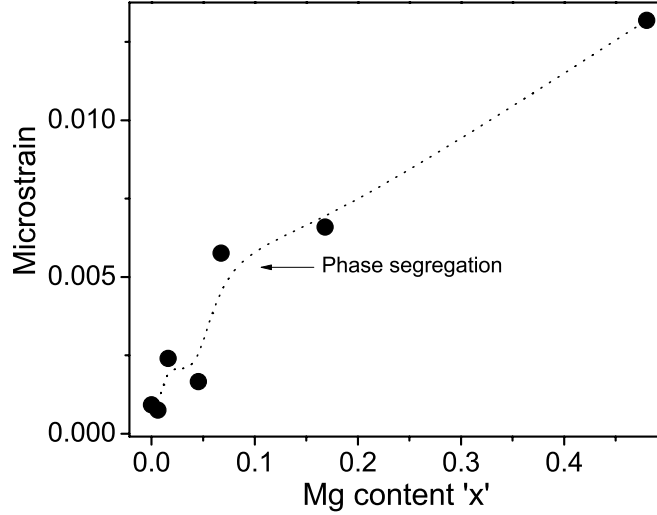
Figure 6.9: Variation of microstrain as obtained from the XRD data with x. The large rise in the microstrain in the region of phase separation can be seen in the graph.

6.3.3 Optical Properties

Investigation of the optical properties of the chemically synthesized alloy $Zn_{1-x}Mg_xO$ nanostructures is a principal motive of the present investigation. The structural studies presented above show the quality of the material grown and also reflect the small yet distinct changes in the crystal lattice that are likely to have an impact on the optical properties.

6.3.3.1 UV-VIS absorption

The room temperature UV-visible absorption spectra of ZnO and the $Zn_{1-x}Mg_xO$ alloy nanocrystals were taken by dispersing them in ethanol. As shown in the figure 6.10(a), a sharp absorption peak appears in the absorption curve due to the large excitons followed by the fundamental absorption. The sharp peak which has been identified as due to excitons and is visible even at room temperatures due to the large exitonic binding energy of ZnO ($\sim$60 meV). The absorption curve shifts to higher energy in the alloy nanocrystals. In the same graph we show the absorption spectra taken at room temperature in a single crystal of ZnO (we refer to this as bulk). Compared to the bulk the fundamental absorption edge is shifted by about 0.25 eV in the nanocrystals (with average diameter$\sim$10 nm). We observe a large and gradual blue shift of the absorption edge on Mg substitution. This is shown in figure 6.10(b) where we plot the shift of the absorption edge energy ($\triangle E_g$) as a function of x for the $Zn_{1-x}Mg_xO$ alloy nanocrystals. Interestingly the E_g shifts to as high as 4 eV on Mg substitution. (As pointed out before it is not possible to have a tight control on the particle size on Mg substitution. The particle sizes may vary by about 2 nm on the average. However, for an average size of 10 nm, such a size variation ($\sim$2nm) can only produce a change in E_g of about 0.05 eV [151]. This is much smaller compared to the change in E_g seen on Mg substitution. For the phase segregated sample (curve
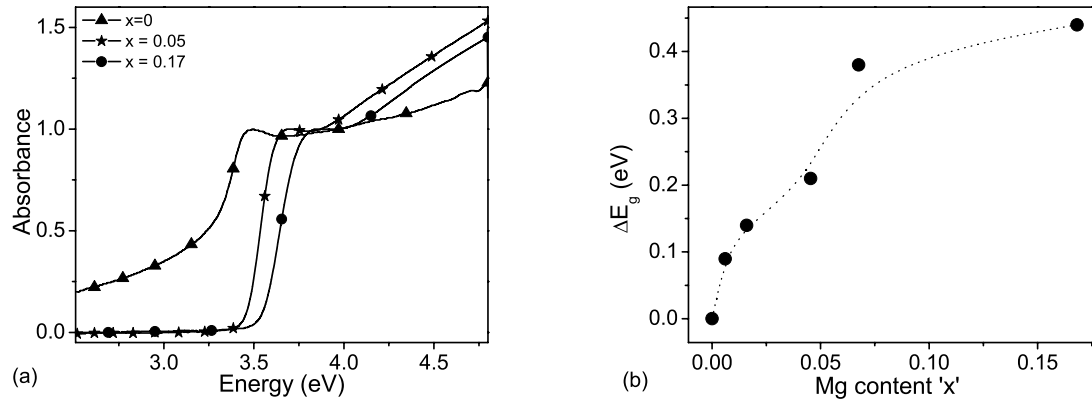
Figure 6.10: (a) Absorption spectra of the $Zn_{1-x}Mg_xO$ nanocrystals for different Mg content. Curve no 5 is for phase segregated sample. (b) shift in the direct band gap values ($\triangle E_g$) of the $Zn_{1-x}Mg_xO$ alloy nanocrystals compared to undoped ZnO nanocrystals.

5 in fig 6.10(a)), no more shift in the band gap value has been observed. Also the excitonic peak disappears from the absorption spectrum.

6.3.3.2   Photoluminescence study

One of the exciting properties of ZnO is its ability to show near band edge Photoluminescence (PL) even at room temperatures when irradiated by radiation with energies somewhat higher than the E_g. At room temperature in addition to the near band edge (NBE) emission a lower energy emission is also seen. The deep level PL has surface related origin and shows dependence on the incorporation of foreign atom like Mg.

In figure 6.11(a) we show the NBE emission obtained from the ZnO and alloy nanocrystals. The PL spectra when analyzed for different peaks showed that it contains two main lines at 347 nm and 377 nm and a weak line at 398 nm. All the samples were excited at 230 nm and have a single peak located in the UV region of the spectra which is due to the excitonic near-band-gap emission. In $Zn_{1-x}Mg_xO$ there is a clear blue shift of the NBE as x is increased. This is shown in figure 6.11(b). For x = 0.17 the blue shift is nearly 99 meV. This is, however, less than the blue shift observed in the band edge from the absorption data (450 meV). The luminescence show a Stokes shift to the lower energy side of the absorption edge which is very common in alloy semiconductors [156]. For instance undoped ZnO (x=0) shows PL peak at 377 nm whereas the E_g occurs at 354 nm. On Mg substitution the PL peak shifts to 365 nm while E_g=312 nm for x = 0.17. The blue shift of NBE emission is because of the doping of Mg in ZnO. Since ZnO is a natural n-type material, the height of the Fermi level increases and will be inside the conduction band due to the incorporation of Mg. The states below the Fermi level in the conduction band being full, the absorption edge shifts to the higher energy [157]. The blue shift of the PL peak with x is also monotonous like the shift in E_g. The NBE emission has details which are not seen in the room temperature spectra. It has been established at least in bulk ZnO by PL investigations at low temperature that the NBE emission actually contains a number of lines that arise from free exciton as well as from exciton bound to impurities. The substitution by

Mg can lead to redistribution of energy among various absorption lines to shift in the NBE, in addition to the blue shift of the PL main line. Importantly these changes on substitution are substantial and they happen even with small amount of substitution (x <0.15).

The NBE UV emission may get a contribution from Raman scattering arising from the phonon modes. To check, whether it has a contribution from the Raman scattering, we varied the excitation frequency and noted the NBE spectra. We find that the line positions mentioned as PL peaks does not shift with the excitation frequency.
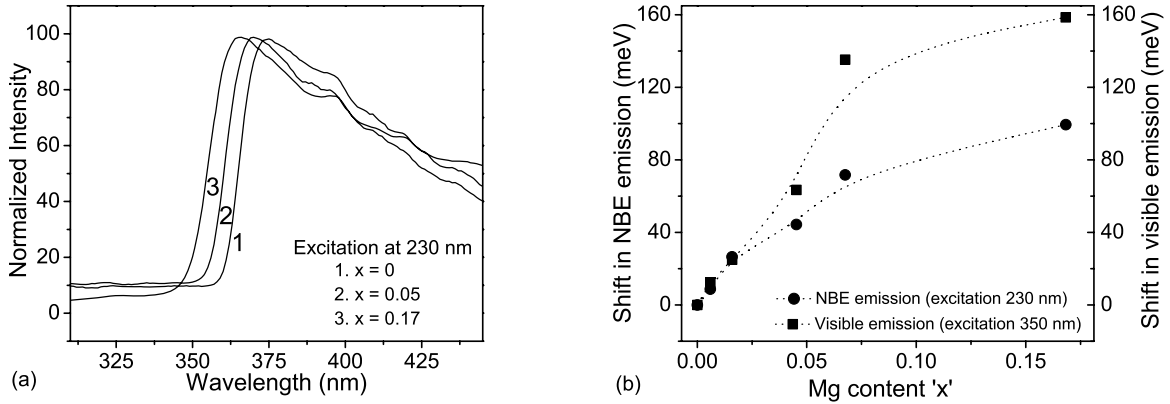
Figure 6.11: (a) The near band edge luminescence in $Zn_{1-x}Mg_xO$ alloy nanocrystals. The PL shows blue shift as the Mg content increases. The visible emission also shifts to the blue side as the Mg content increases. (b) shift in emission energy compared to the undoped sample for both the NBE emission and visible emission as a function of x.

In addition to the near band edge emission, the ZnO and $Zn_{1-x}Mg_xO$ alloy nanoparticles show considerable emission in the blue-green region at wavelength of ∼500-550 nm. This particular emission occurs in almost all samples of ZnO and its origin has been discussed in chapter 3. However the surface defects related origin of this emission is widely accepted [158] and depends on the details of preparation. It can be controlled by size, shape and surrounding liquid environment of the colloidal nanostructures. Here we briefly mention what happens to this emission when Mg substitution occurs. We find that the effect of Mg substitution is two fold. First there is a nonmonotonous dependence of the intensity of the visible emission on x. Second, there is blue shift of the emission peak on Mg substitution. The green emission has a strong and non-monotonous dependence on x. The intensity ratio of the visible to near band edge UV emission increases very rapidly up to x≈ 0.05. An example of the blue-green emission for low x is shown in figure 6.12(a) for x = 0.05. Further increase in the Mg content reduces the intensity ratio between the two lines (figure 6.12(b)). For x >0.2, when the core-shell structure sets in there is complete quenching of the visible emission at 550 nm, whereas the yield of the UV emission remains same. It is likely that the $Mg(OH)_2$ layer on the $Zn_{1-x}Mg_xO$ nanocrystals (revealed by the XRD and the TEM data) quenches the visible emission (∼550 nm) by surface passivation. The quenching of the visible emission on formation of the core-shell structure is a new observation and has the possibility of its utilization in controlled optical properties of ZnO nanocrystals. A detailed investigation of the specific issue of the visible emission from ZnO nanostructure has been provided in chapter 3. Another important effect of Mg substitution is
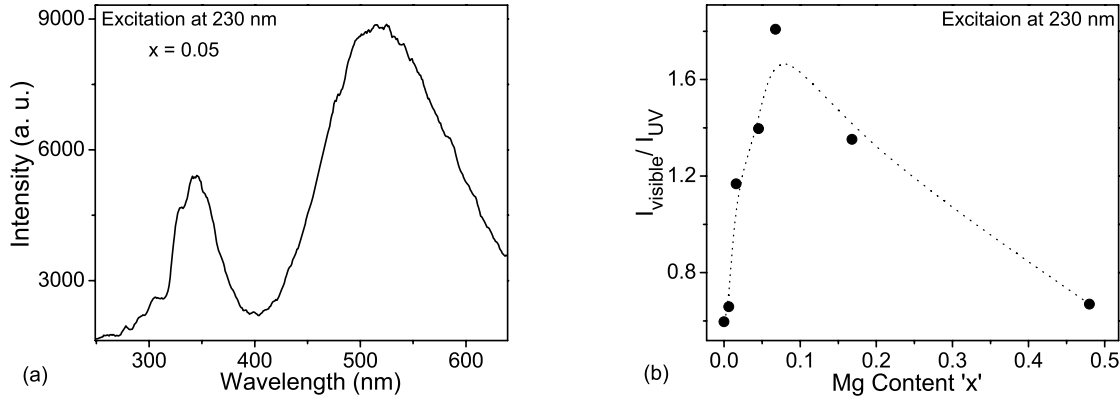
Figure 6.12: (a) An example of the visible emission (550 nm) in doped system with $x = 0.05$. (b) variation of the intensity ratio between the visible and the UV emission as Mg content increases. Plot shows that the intensity of the visible emission increases rapidly as the Mg content increases but falls drastically as soon as the phase segregation starts.

the blue shift in the emission spectra as x increases. As shown in fig. 6.11(b) the visible emission is significantly blue shifted (154 meV) on Mg substitution, ranging from 2.260 eV (550 nm) for $x=0$ to 2.414 eV (514 nm) for $x = 0.17$.

6.4   Structural and optical properties of $Zn_{1-y}Cd_yO$ nanocrystals

The major challenge faced in the solution route synthesis process of $Zn_{1-y}Cd_yO$ is that the CdO is formed at relatively high temperature $(230^0 C)$ which is much higher than the boiling point of most of the solvents generally used for solution synthesis. Also because of different crystal structures of ZnO (wurtzite) and CdO (rock salt), they tend to get phase separated very easily. To overcome these problems, the $Zn_{1-y}Cd_yO$ has been synthesized in an autoclave at high pressure ($\sim 55\ atm.$) capable of increasing the boiling point of solvents like ethanol which allow relatively higher temperature synthesis. At this high temperature and pressure, $Zn_{1-y}Cd_yO$ nanostructures form along with CdO. The nanostructures formed consist of both particles and as well as rods of good crystallinity and optical quality. We show that such nanocrystals have near band edge PL that is red shifted significantly and have relatively large PL decay time ($\sim 10\ ns$) as revealed through time resolved PL measurements. The nanocrystals do not show the defect related green emission often seen in ZnO nanostructers. We could also link the tuning of the band gap and the PL to expansion of the unit cell as a result of the Cd substitution. The full-width at half maximum (FWHM) of the near band edge emission band has been found to be linked to the strain inhomogenity arising from the process of substitution. The Cd substituted ZnO nanostructures ($Zn_{1-y}Cd_yO$ with x upto $\sim$0.09) synthesized by high pressure solution growth method do not exhibit visible luminescence near 550 nm but show blue emission near 400 nm which red shifts when Cd concentration increases. The line width of the PL spectrum is related to the strain inhomogenity and it peaks in the region where the CdO phase separates from the $Zn_{1-y}Cd_yO$ nanostructures. The time resolved photoemission showed a long lived

($\sim$10 ns) component. We propose that the PL behavior of the $Zn_{1-y}Cd_yO$ is dominated by microstrain in the sample with the redshift of the PL linked to the expansion of the unit cell volume on Cd substitution.

6.4.1 Microstructural analysis by TEM

For the purpose of preaparing ZnCdO nanostructures, samples have been prepared in an autoclave. By this method, the nanostructures formed [for low y ($y < 0.03$)] are predominantly spherical shaped nanocrystals. As an example we show in figure 6.13 (a) the particle size distribution of the undoped ZnO sample. The nanostructures are predominantly spherical in shape and the sizes lie within the range of 10-12 nm. This is similar to that found in the synthesis route under normal pressure and at temperature 70^0C [59]. For particles with low values of y, the size distributions are very similar to the undoped nanocrystals. The lattice image (figure 6.13 (b)) confirms the crystalline nature of the sample and the distances between two consecutive lattice fringes (2.41Å) is similar to the interplanar spacing of the (101) set of planes as indicated in the figure.
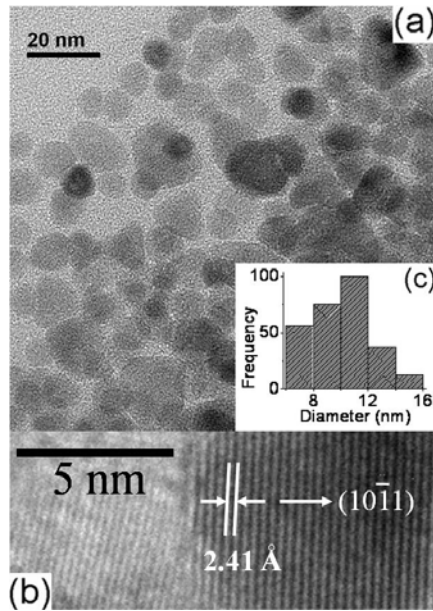
Figure 6.13: (a) The average size distribution and (b) the HR-TEM image of undoped ZnO (y = 0) nanostructures prepared in autoclave under high pressure.

In case of ZnCdO, the spherical shape of the nanostructures no longer persists as soon as significant Cd incorporation starts. This is shown in figure 6.14. For $y > 0.03$, it can be seen that along with spherical nanocrystals one also sees formation of hexagonal nanocrystals as well as the formation of nanorods as marked in the figure. The nanocrystals have typical size from 15-20 nm ($y < 0.03$) to 10 nm for $y > 0.05$. The rods have typical diameter of 10-12 nm and length 20-25 nm. The histogram of the aspect ratio is shown in the inset of figure 6.14. The trend of rod formation persists till higher concentration of Cd and eventually the tendency for rod formation predominates. In figure 6.15 (c) we show the HR-TEM image of a single

rod (formed for y=0.065) which is aligned in the (002) direction. The lattice spacing (2.68Å) matches with the interplanar spacing of the (002) set of planes. As shown in figure 6.15 (d), the FFT (Fast Fourier Transform) of the lattice image confirms that the rods are single crystalline and have only (002) orientation as the growth direction. This preferred orientation also has been confirmed by the XRD data analysis, presented later on. For comparison in figure 6.15 (a) and (b) we show the High Resolution TEM and its FFT of a spherical nanocrystal respectively which shows hexagonal symmetry of the lattice. At higher concentration rods are synthesized in higher proportion but they retain their size and aspect ratio as well as the orientation (002). The single phase nature of the $Zn_{1-y}Cd_yO$ is confirmed by TEM as well as by the XRD data for y≤0.091. There is no further incorporation of Cd in ZnO beyond this value of y. Addition of more Cd salt in the solution leads to formation of more CdO.

We find that the growth of the nanocrystals change characteristics when the Cd is gradually substituted. The two phases in growth with a change at $y \approx 0.03$ is already pointed out. One of the observations about the growth is that when the Cd concentration increases the average size of the nanocrystals grow to about half of the size obtained in the undoped case and there is formation of nanorods with (002) growth direction that predominates near the higher range of Cd concentration. We propose to explain this observation in the following manner. It is known that in solution phase, if the initial nucleation process is fast, the growth generally occurs by such coarsening process as Oswald ripening (OR), which is diffusion limited or through the aggregation by orientation (AO) that leads to ordered growth of nanocrystals with different morphology [181]. The growth of nanorods of ZnO as has been observed by us is likely due to the AO process, which is similar to the growth of TiO_2 nanocrystals from solution [181]. The occurrence of the AO process as an alternate growth process occurs when the diffusion dependent
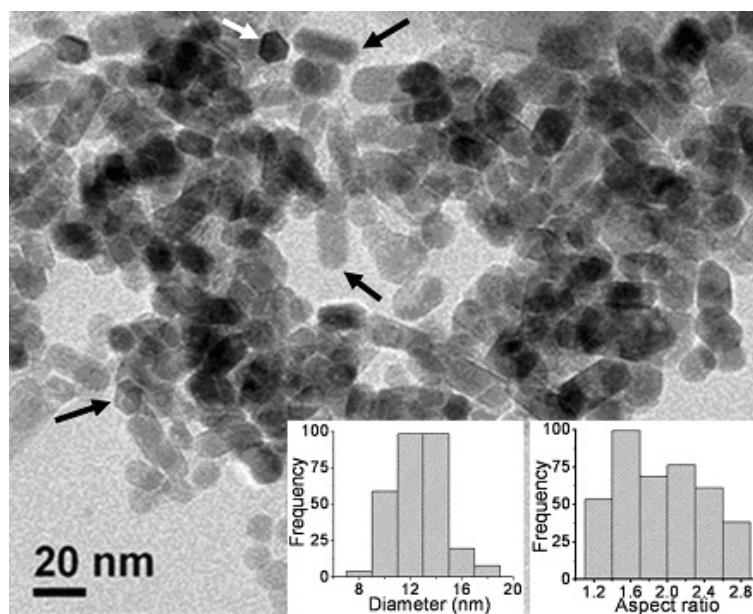
Figure 6.14: Growth of faceted nanocrystals along with hexagonal nanorods of $Zn_{1-y}Cd_yO$ (indicated by arrows) for y>0.03 is shown. The diameter distribution and aspect ratio distribution of the nanorods are depicted in the same figure.
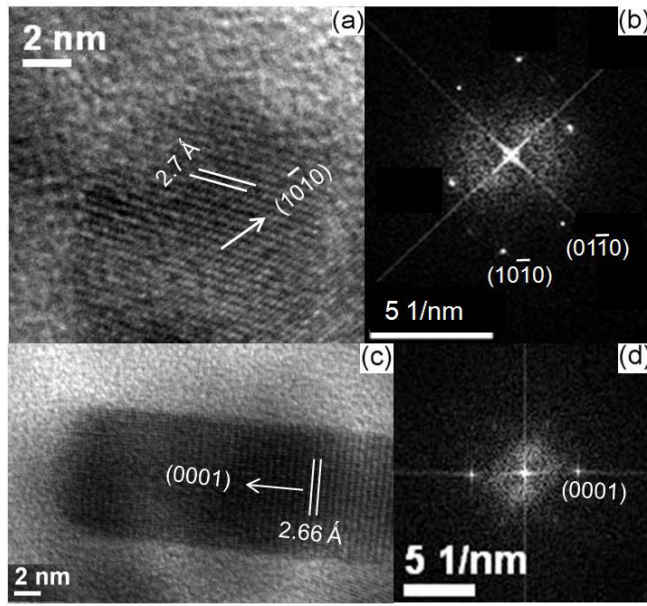
Figure 6.15: High resolution transmission electron microscope of the hexagonal nanoparticle and the nanorod are shown in(a) and (c) respectively. The FFT of the lattice fringes of (a) and (c) are shown in (b) and (d) respectively. The growth direction of the single crystalline nanorods ([002]) can be seen.

process like OR or by direct precipitation from solution gets limited. The size limited growth of nanocrystals on Cd substitution is a manifestation of the reduction of such diffusion dependent pathways. Two processes can limit the diffusion dominated processes. The presence of strain on Cd substitution can limit growth as has been observed in a number of crystal growth processes ([182], [183]). This occurs due to increase of free energy of the strained nanocrystals. Another alternate reason can be the presence of Cd^{++} ions. The incorporation of Cd into ZnO during the growth occurs through absorption of Cd^{++} ions on the surfaces of the growing crystals. It is known that absorption of ions can limit the growth rate in the solution growth process [184]. To summarize this part, the presence of strain and/or adsorption of Cd^{++} ions can limit the growth through diffusion limited process leading to growth by agglomeration by orientation that gives rise to nanorods with (002) orientation.

6.4.2 X-ray diffraction results and analysis of the structural data

We have seen that formation of alloy $Zn_{1-x}Mg_xO$ is reflected by a change in the lattice constant. Although Zn and Mg have very comparable ionic radii (lattice mismatch $\triangle R_{Mg} = 0.09$Å), there is a large lattice mismatch between Zn and Cd ion ($\triangle R_{Cd} = 0.23$Å). So, in $Zn_{1-y}Cd_yO$ there will be appreciable amount of change in lattice constants and phase segregation will appear very quickly compared to that in $Zn_{1-x}Mg_xO$ alloy.

By inspection of the XRD data we can establish the maximum Cd concentration beyond which the phase segregation occurs. We could reach up to to a maximum Cd incorporation of y=0.065 as stated before. The XRD patterns of the $Zn_{1-y}Cd_yO$ alloy nanostructures are shown
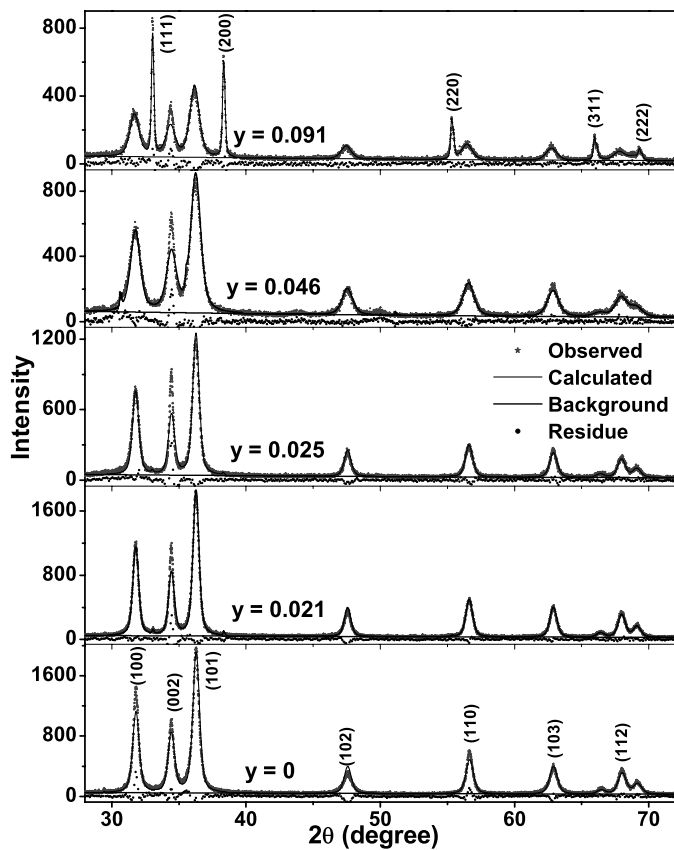
Figure 6.16: The XRD data for single phase wurtzite $Zn_{1-y}Cd_yO$ nanostructures. For $y = 0.091$ the segregated CdO (rock salt structure, peaks are indexed) coexist with $Zn_{1-y}Cd_yO$. The profile fitting of the observed data and the residue has been shown against each curve as indicated in the figure. The gradual increase in the relative intensity of the (002) peak of wurtzite phase can be seen for higher Cd concentration indicating predominance of the [002] aligned nanorods.

in figure 6.16. The nanocrystals have wurtzite structure (peaks are indexed) as that of the parent ZnO (y = 0). The peak positions shift to lower 2θ values due to the Cd incorporation signifying change (increase) in the lattice constant. (Note: We find from the XRD data also that a CdO phase appears at a rather a low level of y = 0.03. However, as mentioned before most of the Cd forms the CdO phase with nanoparticles with average size of $\sim$ 70-80 nm. We have separated
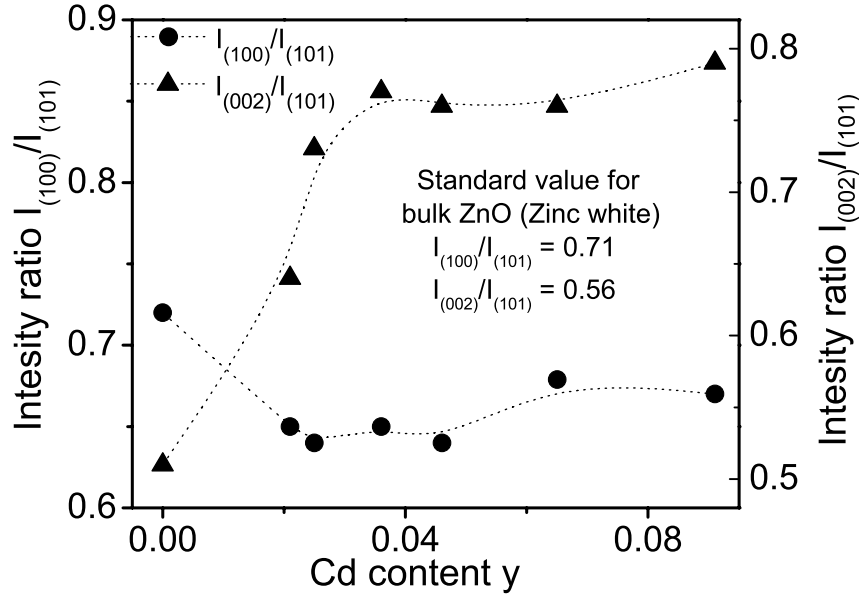
Figure 6.17: The intensity ratios of the Bragg peaks (100) and (002) to the maximum intense peak of the wurtzite structure (101) has been plotted with the Cd content y. The enhanced intensity ratio of (002)/(101) peaks indicates increase in the preferred orientation in (002) direction. In comparison the value of (100)/(101) ratio is mainly unchanged as Cd concentration is changed.

out the CdO particles by centrifuging and the XRD data shown are only from the $Zn_{1-y}Cd_yO$ nanostructures with average size ∼10-20 nm which are single phase.) The XRD data along with the TEM data presented before establish that the high pressure solution route can be used to synthesize nanocrystals of single phase $Zn_{1-y}Cd_yO$ alloy of good crystallinity. The texture growth of rod in the nanostructure synthesis as the Cd content is increased, as seen in the TEM images, is also clearly seen in the XRD data. The relative intensity of the Bragg peak due to (002) planes of the wurtzite structure increases with the increase in Cd content. This fact can be clearly seen from figure. 6.17, where the intensity ratios of the Bragg peaks (100) and (002) with maximum intense peak (101) of the wurtzite phase has been plotted with the increase in Cd content. The important observation is that the intensity ratio (002)/(101) increases sharply up to $y = 0.03$, beyond which it saturates. To establish that the growth occurs preferentially in the [002] direction, we have plotted for comparison the intensity ratios of (100)/(101) peaks which has a more or less constant value. It confirms the increase in the preferred growth of rods aligned in [002] direction as we increase the Cd concentration. The [002] direction is an easy axis of growth for ZnO and most of the nanorod formation in ZnO occurs along this orientation.

The structural analysis of the powdered X ray diffraction data of the $Zn_{1-y}Cd_yO$ nanostructures has been carried out extensively by using Rietveld method [150]. There is yet another important observation that accompanies the process of texturing. The XRD peaks of the wurtzite phase show enhanced full-width at half maximum (FWHM) values for higher Cd con-

tent. We have carried out a Williamson- Hall analysis [81] of the XRD data. The analysis show that the increase in the XRD line width occurs due to an enhancement of the inhomogeneous strain (which we refer to as the microstrain) as well as due to a decrease in the average size of the $Zn_{1-y}Cd_yO$ nanostructures with the increase in Cd content. The enhancement of the microstrain, as seen through the XRD analysis also widens the FWHM of the PL peak as we see later on. Observed increase in microstrain values can be due to the effect of fluctuation in the Cd concentration as previously suggested by Makino et al. [161].

Variation of the lattice constants and crystallite sizes were obtained from Rietveld analysis of the observed XRD data. As the Cd content is increased, the peak positions of the XRD data shift to lower angles due to increase in lattice volume which is caused by the incorporation of Cd^{++} ion having higher ionic radii (0.97Å) in place of the Zn^{++} ion (0.74Å) in the ZnO lattice [24]. The calculated profile matches well with the observed data as shown in Figure 5. The residues of the fitting for all the data are indicated in figure 5. We have noted before (as measured through the HR-TEM observation) that enhanced incorporation of Cd in ZnO also changes the growth morphology. We could find signature of this in the analysis of the XRD data. We find that the average size of the $Zn_{1-y}Cd_yO$ nanostructures observed to be decreased from 15-20 nm (y = 0) to 10 nm for y >.05. Beyond that the size remains constant.

The lattice parameters (c and a axes) extracted by Rietveld analysis show that they increase monotonously as the Cd content is increased. The change is small but it is distinct. In figure 6.18 we show the variation of the unit cell volume ($V=0.866a^2c$), the microstrain as well as the c/a ratio as function of the Cd content. The cell volume increases by nearly 0.8% on Cd substitution. This increase in the unit cell volume on Cd substitution has also been found in films grown by vapor phase [161]. It is interesting to note that the small yet distinct compaction of the lattice does not preserve the c/a ratio. The most of the change occurs in the a-axis which increases by ∼0.3 %, while the c-axis lattice parameter expands only by ∼0.19%. This reduces the c/a ratio. Here we note that the expansion of the unit cell volume on Cd substitution can be thought of as a negative pressure arising from the larger Cd ions. The negative pressure is not hydrostatic and leads to preferential compaction of the a-axis leading to a smaller c/a ratio.

From figure 6.18 it appears that there are two stages in the Cd substitution. The change over occurs at around y∼0.03. Below x=0.03 the nanocrystals are predominantly spherical. In this region the microstrain increases till the CdO separates out which occurs beyond y=0.03. Above y=0.03 when the CdO separates out, the growth leads to nanorod formation that have preferential orientation along [002]. The intensity ratio (002)/(101) shown in figure 6.17 reflects this change of stage at y∼0.03. The intensity ratio saturates beyond y=0.03 indicating preferential growth of (002) oriented nanorods. Figure 6.18 also indicates that beyond y=0.03, the phase separation releases some of the microstrain in the lattice.

The detailed structural investigations presented here established that single crystalline nanocrystals of well characterized structural quality can be synthesized by the high pressure solution route. The structural studies have also established some of the subtle features in growth of Cd substituted nanocrystals, in particular the stages of growth as well as the rod of the textured structure are interesting observation that have not been addressed before. There is a continuous expansion of the unit cell volume on Cd substitution with a small reduction in the c/a ratio for the lattice constants. Below we present the results of the optical studies done on these nanocrystals.
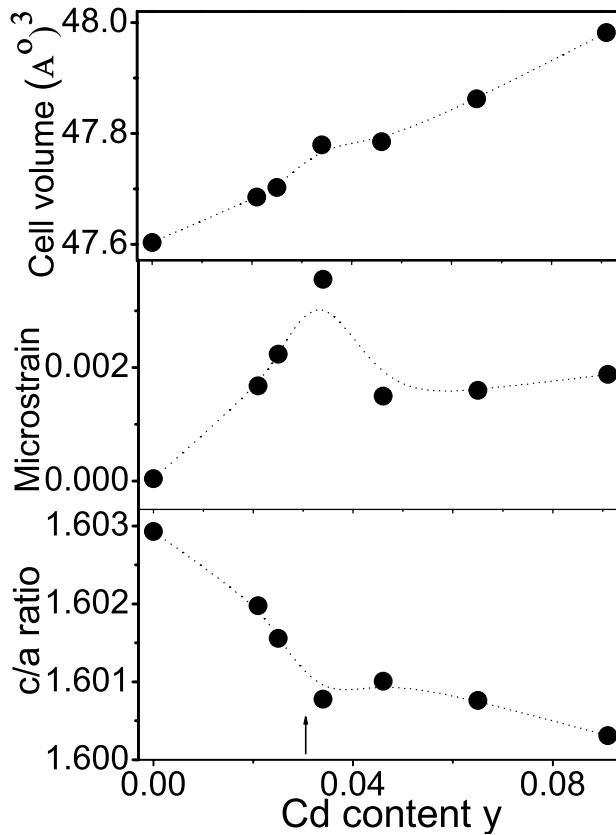
Figure 6.18: Unit cell volume, c/a ratio and the microstrain as a function of y as obtained form analysis of the XRD data. The arrow shows the composition $y=0.03$, where a change in stage of growth seems to be occurring.

6.4.3   Optical Properties

In this section we will investigate the change in the absorption, the Photoluminescence (PL) and also the time resolved PL (TRPL) in $Zn_{1-y}Cd_yO$ nanostructures at room temperature. These measurements allow us to assess the utility of these chemically synthesized materials for application as a band gap engineered optical material.

6.4.3.1   UV-VIS absorption

One of the important effects of Cd incorporation into ZnO is the reduction of its direct band gap value as has been seen in vapor phase synthesized $Zn_{1-y}Cd_yO$ nanostructures. The band gaps of the alloy nanostructures were determined by monitoring the onset of the fundamental absorption edge. As shown in figure 6.19, a sharp peak appears in the absorption spectra of undoped ZnO nanostructures even at room temperature due to the large excitonic binding energy (59 meV) of ZnO. The absorption curves shift to the lower energy for the alloy nanostructures. The absorption edge can be clearly identified from the optical absorption upto $y < 0.03$. Beyond that the absorption edge gets blurred probably due to appearance of large number of
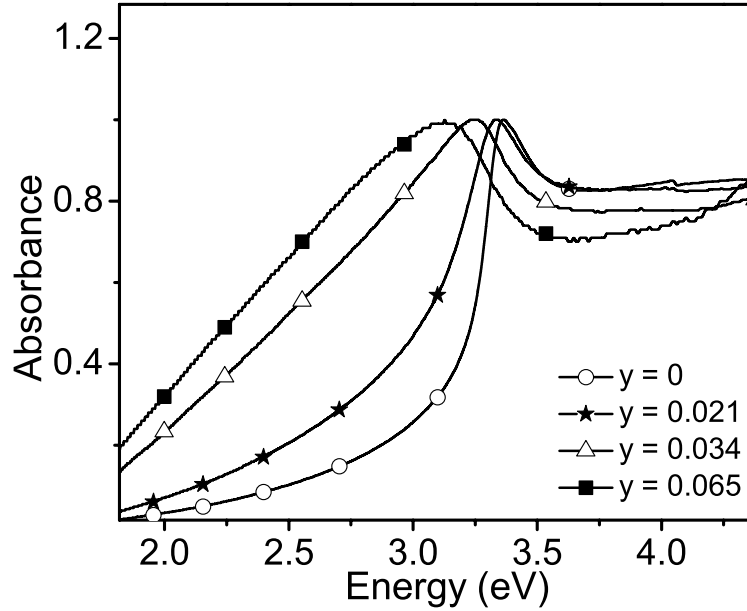
Figure 6.19: Room temperature absorption spectra show shift to the lower energy values indicating reduction in the direct band gap values as a result of Cd incorporation. Broadening of the excitonic peak occurs as soon as Cd incorporation takes place. For $y > 0.03$ determination of the band gap is not possible due to broad nature of the absorption.

disordered induced states within the band gap and partially due to the CdO present along with the $Zn_{1-y}Cd_yO$ nanostructures. The shift in the band edge (for y<0.3) as a function of y are shown in figure 6.21. The direct band gap value of the undoped ZnO nanocrystals ($\sim$10-15 nm) is found to be 3.37 eV which is the fundamental absorption edge of the bulk ZnO. In the size regime we are working, no quantum confinement effect has been observed [151]. One can see a monotonous decrease of the gap with increase of the Cd content. (Note: Although we have observed decrease in the average size of the nanostructures on Cd incorporation, the size is still larger than the size range where quantum confinement effects (diameter < 5nm) can alter the band gap. Even if there is any effect of quantum confinement, this will reduce the extent of red shift.). Thus the limited absorption data can be analyzed to establish that the absorption edge of the chemically synthesized $Zn_{1-y}Cd_yO$ nanostructures also can be red shifted clearly as in the vapor phase grown materials and the shifts are comparable [161].

6.4.3.2   Photoluminescence study of $Zn_{1-y}Cd_yO$ alloy nanostructures

A clearer signature of the reduction in band gap energy of ZnO nanostructures on Cd substitution can be seen from the photoluminescence data. The photoluminescence (PL) spectra of pure ZnO and $Zn_{1-y}Cd_yO$ nanostructures have been measured with an excitation of 325 nm. The emission spectra following the 325 nm is shown in figure 6.20. The undoped ZnO nanostructures show

sharp emission in the UV region (E_1) at 371 nm (3.345 eV). The emission at 371 nm has been established due to exciton recombination [13]. A broad and weak emission (E_2) is also observed at 389 nm (3.189 eV), the exact nature of which has not been identified but it arises also from excitons those are bound to defects [177]. (Note: In most nanocrystals and quantum dots of ZnO the emission at room temperature occurs at around 3.25-3.35 eV. While in bulk single crystals at room temperature the UV emission at ∼3.3 eV is attributed to free exciton. The UV emission in nanocrystals and quantum dots are due to acceptor or donor bound excitons that can arise from lattice defects ([179], [180]).)

The $Zn_{1-y}Cd_yO$ nanostructures show E_1 as in the case of undoped ZnO and there is no significant shift in the position of the component E_1 on Cd substitution. However, the relative contribution of this line to the total emission reduces significantly. The main change occurs in the broad peak E_2 which show gradual red shift as well as enhanced intensity due to the incorporation of Cd. The gradual red shift of emission energy of E_2 with Cd content is shown in figure 6.21. For the highest Cd content (y = 0.091) E_2 occurs at 417 nm (2.976 eV) which is 213 meV red shifted from the undoped ZnO. In figure 6.21 we also show the intensity ratio of the two peaks (E_2/E_1) as a function of y. The figure shows the shift in the intensity as the alloying takes place. However, after the first stage of growth ($y \sim 0.03$) the ratio saturates. Substantial change in the PL characteristics can be seen in the line width of the E_2 band. The full width at half maximum (FWHM) of the E_2 line changes as the Cd concentration increases (see figure 6.22). It can be seen that the dependence is not monotonous. It first increases with y reaching a maximum at $y \sim 0.04$-.045 and then decreases again. For the line E_1, the FWHM is more or less constant but it shows a shallow peak near the composition range where FWHM of the line E_2 also shows a peak. We note here that the line width appears to have a relation to the micostrain whose variation with y is shown in figure 6.18. The microstrain reaches a maximum for $y \sim 0.03$-0.04. Later on we discuss this issue elaborately.

It is important to note here that we do not see any green-yellow emission in the range ∼450-550 nm which has been generally seen in a number of nanoparticles of ZnO [93]. The green emission is typically taken as a signature of defects (like oxygen vacancy) and highly sensitive to the surface condition which in turn depends on the way the nanostructures have been prepared [178]. Undoped ZnO nanostructures of spherical morphology (size <15 nm) prepared in ambient pressure show intense yellow emission near ∼550 nm (figure 1.5). As discussed in chapter 2 and 3, the nanostructures prepared under high pressure within autoclaves show different morphologies like spherical, rods and hexagonal platelets depending on the precursor concentrations and growth time. The visible emission from these nanostructures also bears the signature of their shape and size (discussed in chapter 3). The spherical particles (size <10 nm) synthesized under high pressure for short duration show emission near 550 nm (~ 2.2 eV) whereas the cylindrical nanorods of diameter ∼25 nm is dominated by the 500 nm (~ 2.5 eV) emission band (figure 3.4 in chapter 3). The spherical nanoparticles in this study are synthesized via high pressure route for three hours and has average size ∼12 nm. In addition to that due to high pressure synthesis agglomeration takes place and effective surface to volume ratio of the nanoparticles decreases. Since the surface to volume ratio is a measure of the visible emission intensity (discussed in chapter 3), the nanoparticles considered here do not show any visible emission around ∼ 550 nm, although the spherical nanoparticles of similar size range prepared in ambient pressure show significant yellow emission. The yellow emission from nanospheres (size <20 nm) prepared under high pressure route can be recovered by reducing the agglomeration after sonication for longer time. The green emission (∼500 nm) on the other hand has different origin and can be seen for
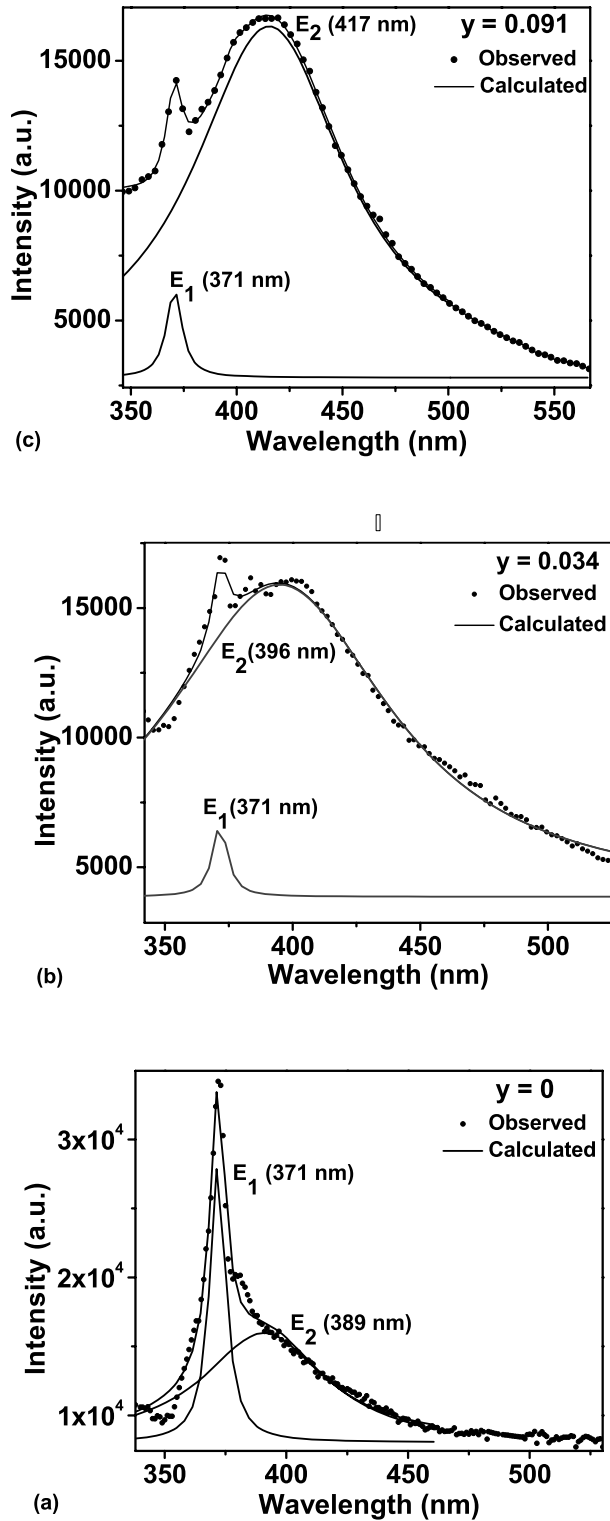
Figure 6.20: The room temperature emission spectra for $y = 0$, $y = 0.034$ and $y = 0.091$ are shown in Fig (a), (b), and (c) respectively. The E_2 emission band of $Zn_{1-y}Cd_yO$ nanostructures show red shift due to the incorporation of Cd as indicated in the figure.
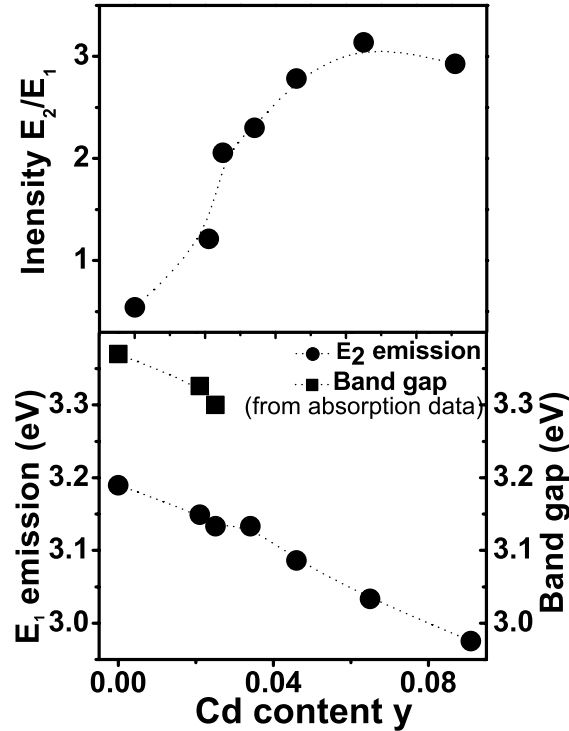
Figure 6.21: The variation of the emission energy of E_2 band and the direct band gap values as a function of y. The variation of the relative intensity of the E_2 and E_1 lines are also shown in the same figure.

relatively bigger particles like nanorods of diameter ∼25 nm (chapter 3). The absence of this visible emission is consistent even after the Cd substitution takes place.

    Time Resolved Photoluminescence: We have taken time resolved photoluminescence (TRPL) data on the nanocrystals of $Zn_{1-y}Cd_yO$. The representative data taken on three compositions are shown in figure 6.23. The TRPL data have been taken on the line E_2 after excitation at 299 nm. The lifetime decay curves have been resolved into three components by deconvolution fitting of the data with the relation:

$$I(t) = \Sigma_{i=1}^3 A_i exp(-t/\tau_i) \tag{6.1}$$

    The parameters A_i (i=1,2,3) which give the weight of the components and the decay time constants τ_i (i=1,2,3) of the transients are shown in table 6.1. The first observation that we make is that there is actually an increase in all the decay time constants on Cd substitution. The natural decay time of free excitons in ZnO is rather small and in the range of 1 ns. The decay times observed here are larger suggesting that the emission mainly involves bound exciton. The
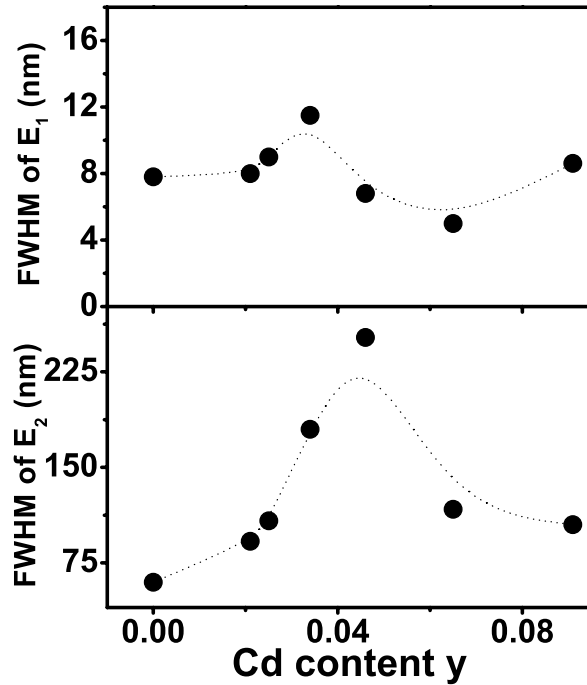
Figure 6.22: Variation of the line width of the E_1 and the E_2 emission lines (Full width at half maximum) as a function of y.

change in the decay time constant on Cd substitution is different for the three components. It is marginal for the longest time constant τ_3 ($\sim$ 10%), noticeable for the intermediate time constant τ_2 ($\sim$ 25%) and substantial for the shortest time constant τ_1 which changes from around 260 ps to a more than 500 ps. We find that the maximum decay occurs through process that has the longest decay time constant τ_3 ($\sim$ 9-10 ns) which has a relative weight of nearly 50% and there is a very little change in its weight on alloying.

6.4.3.3   Discussions

The synthesis of $Zn_{1-y}Cd_yO$ alloy nanostructures by chemical method is a challenging task given the differences in the crystal structures of ZnO and CdO and the large difference in the ionic radii. It has been established that incorporation of Cd up to y$\simeq$0.08 is a possibility. The small amount of incorporation however, had a very large impact on the optical properties. In this section we bring them together. First point that we note is that the absorption edge redshifts. In the next section we re-look into this issue with the help of structural modelling. The second important point is that the near band edge emission not only shows a redshift but it is likely that the exciton binding dynamics is changed. These samples also show lack of visible emission. This however, is linked to the method of preparation (high pressure synthesis within autoclave)
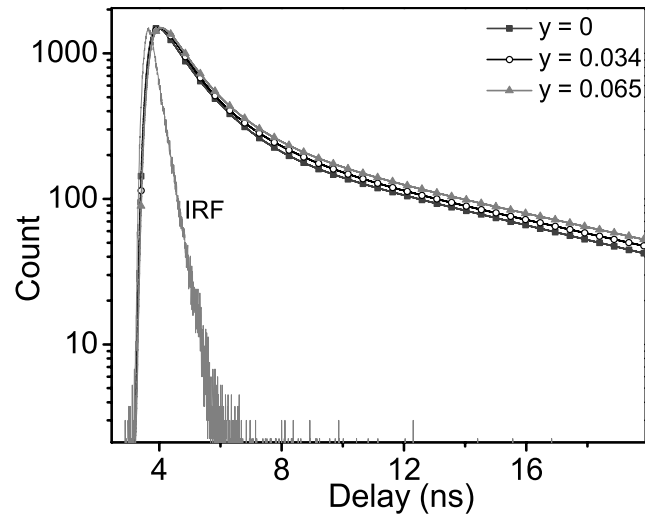
Figure 6.23: Time resolved decay curves of the PL for three different values of y as indicated on the graph.

Table 6.1: Decay constants

Samples	τ_1 (ps)	τ_2 (ps)	τ_3 (ps)	A_1 (%)	A_2 (%)	A_3 (%)
y=0	266	1203	8594	10	38	52
y=0.034	532	1555	9355	19	29	52
y=0.065	544	1482	9375	16	30	54
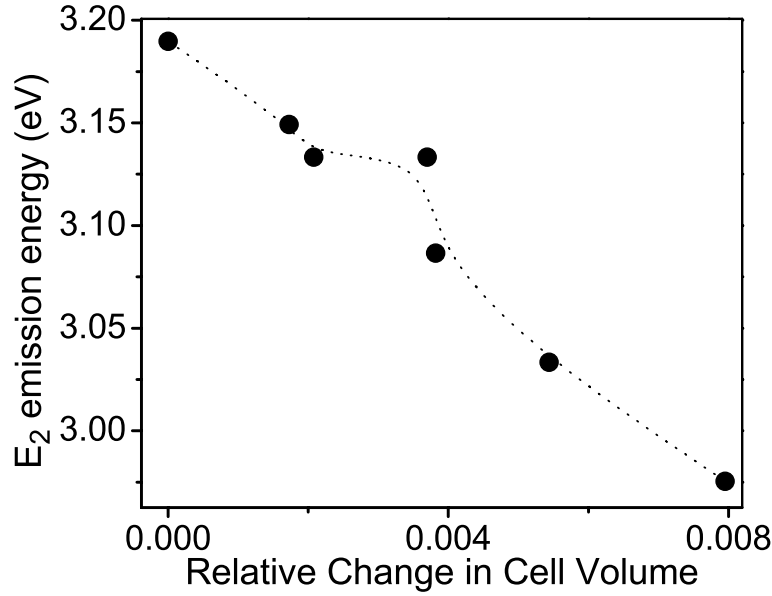
Figure 6.24: Variation of the E_2 emission line as a function of the unit cell volume as determined from the XRD data.

rather than Cd alloying. Below we discuss the change in NBE emission and its likely cause.

The effects of the Cd substitution are clearly apparent on the PL properties. The main effect is indeed on the emission line E_2. The line red shifts and broadens (as revealed through the enhancement of the FWHM). This red shift is substantial and is similar to that found in the vapor phase grown samples. The position of the line E_2 appears to be tagged to the red-shift of the band edge with the Stokes shift (redshift of the emission from its absorption edge) nearly remaining constant on Cd substitution. (Note: The data on band edge shift is limited to $y < 0.03$). In ZnO crystals it has been shown that a hydrostatic pressure can blue shift the band gap [185]. In films of wide band gap semiconductors like ZnO grown on substrates with lattice constant mismatch, the PL is shifted by the in-plane strain arising due to the mismatch [186]. It has been shown that in films with compressive strain, the PL is blue shifted while tensile strain leads to red shift. We propose that the red shift of the PL in $Zn_{1-y}Cd_yO$ nanostructures, which is a consequence of the red shift of the band edge, arises due to the strain produced by the Cd substitution. The Cd substitution that leads to an expansion of the unit cell can be interpreted as a *negative* pressure producing similar effect as a tensile strain in a film. It is proposed that the *negative* lattice pressure produced by the Cd substitution is the cause of the red shift seen in the PL. We plot in figure 6.24 the red shift of PL line (E_2) as a function of the unit cell size. One can see the smooth variation of the PL line with the unit cell volume.

The line width of the main PL line as measured by the FWHM has a severe sensitivity to the inhomogeneous lattice strain (micro strain) that develops during the process of Cd substitution. As can be seen from figure 6.18, the microstrain reaches a maximum for $y \approx 0.03$-0.04. This is the region where the segregation of the CdO occurs and this phase separation actually reduces

the microstrain somewhat. The FWHM of the PL reflects this variation of the microstrain and reaches a shallow maximum for $y \approx$0.04-0.05 (see figure 6.22). A similar trend, although much weaker is seen for the FWHM of the line E_1 also suggesting that the broadening of the PL line is predominantly due to the strain homogeneity arising due to the Cd substitution.

The dependence of the position of the PL line on the cell volume as well as the line width of the PL line on microstrain strongly suggests a link between the emission process and the strain. It has been seen in a number of random substitution alloy semiconductor ($e.g.$, CdS_xSe_{1-x}) [187] that the disorder due to random substitution can lead to smearing of the band edge absorption as well as broadening of the PL line. Its origin is thought to be fluctuations (static) in the band-gap due to random fluctuations in compositions. In addition, the strain field can also lead to exciton localization [188]. The large absorption in the $Zn_{1-y}Cd_yO$ nanostructures in the subbandgap region suggests presence of disorder induced states from the random substitution. It is likely that the microstrain seen in the Cd substituted samples arise from the randomness of the substitution process. The Cd substitution sites can provide the excitonic binding sites. This type of strain induced localization can trap the exciton and can lead to large PL decay time as has been seen in this investigation.

6.5 Modelling of band gap variation in $Zn_{1-x}Mg_xO$ and $Zn_{1-y}Cd_yO$ alloys

In this section we try to understand the phenomena of band gap variation in the alloy nanostructures of ZnO. In ref. [160], a complete first principle study on the electronic structure of $Zn_{1-x}Mg_xO$ and $Zn_{1-y}Cd_yO$ clusters is presented. The change in the band gap (or HOMO-LUMO gap) in pristine $(ZnO)_n$ with size variation and its alloy such as $(ZnMgO)_n$ and $(ZnCdO)_n$ ($1 \leq n \leq 12$) clusters for different doping concentration has been observed. Although the size of the alloyed cluster is almost 10 times less than the nanocrystals size considered experimentally, the variation in the HOMO-LUMO gap of doped $(ZnO)_{12}$ clusters show similar qualitative trend as the size induced variation of the band gap in larger nanostructures. Also, as the size of the cluster is increased, the change in the HOMO-LUMO gap seems to converge to a definite trend with alloying concentration.

The 12-molecule ZnO cluster are relatively more stable than other small clusters. The undoped $(ZnO)_{12}$ cluster is almost spherical in shape and resembles almost fullerene structure [figure 6.25(a)]. The exact fullerene structure, however, consists of hexagonal and pentagonal units, whereas this $(ZnO)_{12}$ structure consists of units of rhombus and hexagons. The total cohesive binding energy of $(ZnO)_{12}$ cluster is 75.89 eV and its HOMO-LUMO gap is 2.33 eV. The substitutional doping of $(ZnO)_{12}$ cluster, that is, replacing Zn atom(s) by dopant atom(s) has been carried out. Figure 6.25(b) shows the structures of $(Zn_{12-n}Mg_n)O_{12}$ clusters doped by five Mg atoms. The largest ZnO bond length in an undoped $(ZnO)_{12}$ cluster is 1.97 Å. The inclusion of Mg atoms reduces the average bond length as Mg-O bond lengths vary only between 1.90 and 1.94 Å. This observation suggests greater stability to the Mg-doped cluster compared to an undoped ZnO cluster. The structures of $(Zn_{12-n}Cd_n)O_{12}$ clusters doped with five Cd atoms is shown in figure 6.25(c). The Cd-O bond lengths in these clusters vary between 2.10 and 2.18 Å, thus making the clusters relatively less stable.

Figure 6.26(a) shows the variation of binding energy of the clusters with increasing concentration of dopant atoms. The total binding energy of these doped clusters increases with
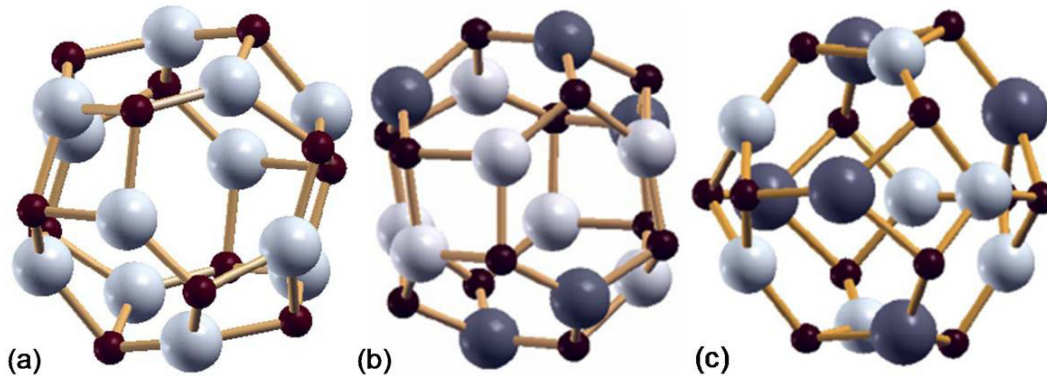
Figure 6.25: (a) $(ZnO)_n$ clusters for n=12; large light (gray) spheres represent Zn atoms and smaller dark (red) spheres the O atoms. (b) Structures of Mg-doped $(ZnO)_{12}$ clusters; lightly shaded large spheres represent Mg atoms, white large spheres represent Zn atoms, and smaller black spheres represent O atoms. (c) Structures of Cd-doped $(ZnO)_{12}$ cluster, lightly shaded spheres represent Zn atoms, small dark spheres represent O, and large dark spheres represent Cd.
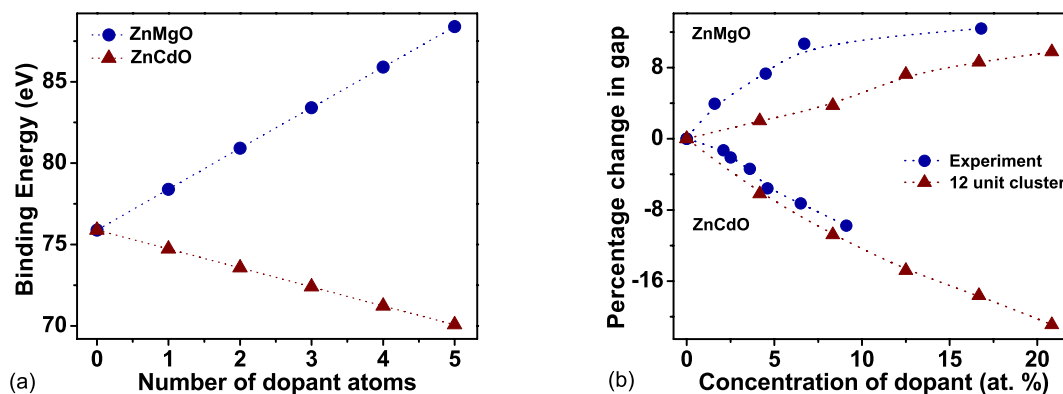
Figure 6.26: (a) Variation of the binding energy with Mg and Cd doping. (b) Variation in energy gaps of $(ZnO)_{12}$ by Mg and Cd atoms. Energy gap variation in cluster is compared with experimental data on doped ZnO nanostructures.

increasing concentration of Mg, whereas it decreases with increasing Cd concentration. This means that doping with Mg increases the stability of the clusters, whereas doping with Cd decreases stability. This is an important observation that connects with the following experimental facts: (i) low doping efficiency of Cd compared to Mg and (ii) increase in photoluminescence peak width of $Zn_{1-y}Cd_yO$. The lower stability of $Zn_{1-y}Cd_yO$ clusters gives rise to fluctuations in the Cd content of the material as well as overall lower Cd incorporation into ZnO.

The experimental variation in band gap in nanostructure and theoretically obtained HOMO-LUMO gap in $(ZnO)_{12}$ clusters with increasing concentration of Mg and Cd are compared in
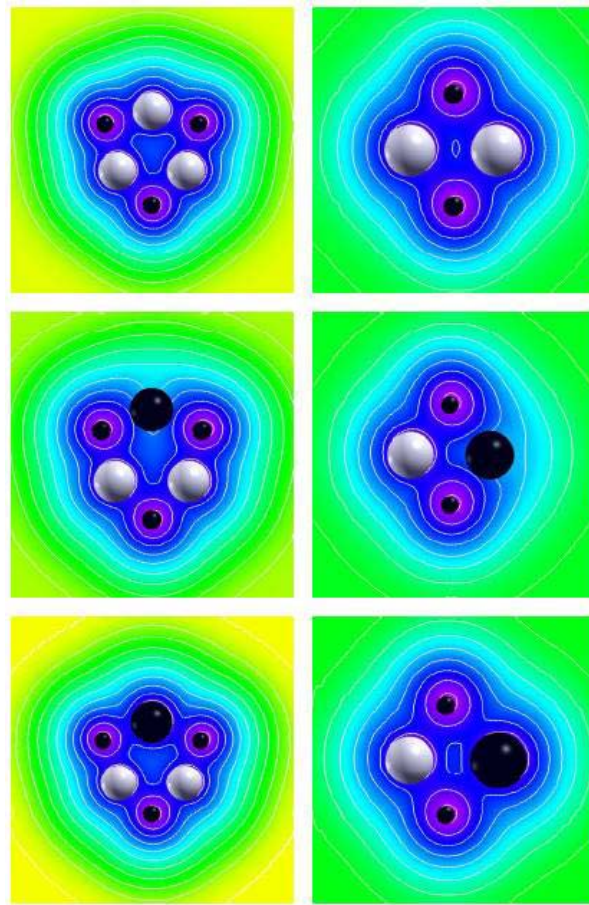
Figure 6.27: Charge densities of (top) pristine ZnO, (middle) Mg-doped ZnO, and (bottom) Cd-doped ZnO for the (left) $(ZnO)_3$ ring and (right) the $(ZnO)_2$ ring. Small black spheres represent O atoms, large white spheres represent Zn, and large black spheres are either Mg (middle) or Cd (bottom) atoms.

figure 6.26(b). The value corresponding to zero percentage of dopant atom refers to the value of undoped ZnO structure. The HOMO-LUMO gap increases with increasing concentration of Mg and decreases with increasing concentration of Cd. A cluster with a larger HOMO-LUMO gap is more stable and vice versa. Therefore, the fact that the increase in Mg concentration increases the HOMO-LUMO gap and the increase in Cd concentration decreases HOMO-LUMO gap is consistent with stability character shown by binding energy result.

Now we try to analyze the effect of alloying on the bonding charge density within the cluster and its consequent effect on the HOMO-LUMO gap. Let us look at the cluster $(ZnO)_{12}$ and the two clusters $Mg_5Zn_7O_{12}$ and $Cd_5Zn_7O_{12}$ (figure 6.25). All the three clusters are constructed out of six membered and four-membered rings. Let us look at the charge densities on planes through one of these rings. These are shown in figure 6.27. The figure shows the Zn^{2+}, Mg^{2+}, and Cd^{2+} ions sitting in the sea of valence electron cloud. As compared to the pristine ZnO cluster, wherever a Mg^{2+} ion sits, the charge density is pushed away from it towards the Zn^{2+}
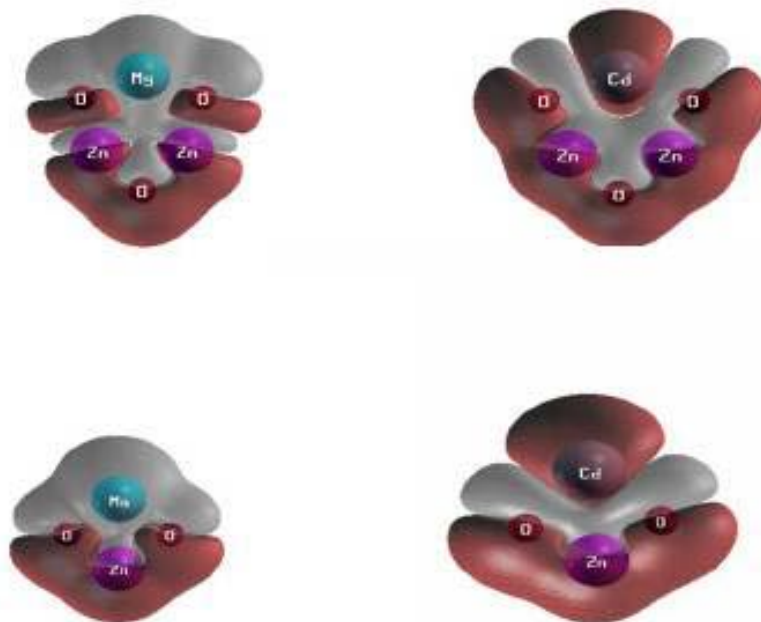
Figure 6.28: Difference in charge densities (left) between Mg-doped ZnO and pristine ZnO and (right) Cd-doped ZnO and pristine ZnO. The light gray shaded areas are of negative difference (charge depleted) and the black (red) areas of positive difference (charge accumulation).

ions. The reverse is true wherever a Cd^{2+} sits. This ion appears to pull the electronic charge cloud towards it. The relative shift of the charge density for the two ions (Mg^{2+} and Cd^{2+}) is thus believed to be linked to the shift in the HOMO-LUMO gap on alloying. Both the substitutions are isoelectronic and change in the structure is also not substantial. Thus such effects as change/shift in electronic density around ions are important factors. This is much better seen from the charge density difference map between the doped and pristine clusters as shown in figure 6.28.

To understand the fact, we first note that the geometric structure of the atoms is not important, since the same phenomenon is apparent in both the four-membered and the six-membered rings. Figure 6.28 indicates that the electronegativity difference between Mg, Zn, Cd and O decreases as we go from Mg to Cd. The XO (X=Mg, Zn, or Cd) bonds are partially ionic and partially covalent. If we relate the ionicity of the XO bond to the electronegativity difference between X and O, then MgO should be the most ionic and CdO the least with ZnO in the middle. We can argue that this is so because the $3s$ energy level in Mg, $4s$ in Zn, and $5s$ in Cd decrease in this order. Consequently, the energy difference between these s levels and the O $2p$ level is smallest in CdO and increases for ZnO and largest in MgO. Thus, ionicity is lowest in CdO, larger in ZnO, and largest in CdO. This is now consistent with larger band gaps for $Zn_{1-x}Mg_xO$ and smaller ones for $Zn_{1-y}Cd_yO$ in the spirit of the ionicity theory of Phillips [54]. This doping dependence of bond strength is also reflected in the fact that while the Zn-Zn distance in the pristine $(ZnO)_{12}$ is 2.60 Å on a six-membered ring, it reduces to 2.54 Å in the Mg-doped cluster. This is a sign of strengthened bonding between Zn atoms and in a simple

tight binding description leads to a larger overlap between tight binding basis orbitals. For the Cd-doped cluster, this distance enlarges to 2.64 Å indicating weakened bonding between Zn atoms and lower overlap between tight-binding basis orbitals. These local distortions should have their signature in Raman experiments and have a profound influence on the behavior of these clusters. In this simple bond by bond picture, there is a correlation between the gap and bonding energy.

6.6   Conclusion

In summary, $Zn_{1-x}Mg_xO$ and $Zn_{1-y}Cd_yO$ nanocrystals (with average size $\sim$10-15 nm) are synthesized by using a low temperature solution growth method (growth temperature $60-75^0C$) and a high pressure solution route in an autoclave respectively. The crystal structure analysis (based on the XRD data) and the TEM-diffraction pattern show that the $Zn_{1-x}Mg_xO$ and $Zn_{1-y}Cd_yO$ nanocrystals have wurtzite structure as that of ZnO, upto a certain concentration (below $x = 0.17$ and $y = 0.09$). Beyond that phase segregation occurs. After phase segregation, for Mg doping the excess $Mg(OH)_2$ forms a layer on the nanocrystals, which quenches the visible emission. In case of Cd doping, the CdO (size $\sim$70-80 nm) segregates and remains in the solution. The composition as checked by the ICP-AES shows that EDX composition analysis (as is generally done in doped ZnO films) may overestimate the actual Mg or Cd incorporation. Room temperature spectra reveals that Mg substitution leads to enhancement of the fundamental absorption edge from 3.55 eV to 3.99 eV and Cd substitution reduces the same below 3 eV. The variation in band gap due to alloying by Mg and Cd has been explained on the basis of their ionicity by first principle electronic structure calculation of the alloy ZnO clusters. The near band edge emission shifts from 3.3 eV to 3.4 eV for Mg content (x) as little as 0.17. For Cd substitution the near band edge emission shows redshift as the Cd content increases. We find a close link of the strain to the PL properties where the microstrain broadens the PL line width. The time resolved photoemission showed a long lived ($\sim$10 ns) component. We suggest that the long life time arise from exciton localization due to disorder created by the random strain field.

Chapter 7

Concluding remarks on this thesis

7.1 A summary of the work done

In this thesis we intended to investigate the structural and optical properties of colloidal ZnO and its alloy nanostructures. ZnO is a very useful material and nanostructures of ZnO has attracted enormous attention over the last decade. New structures have been fabricated and some unique properties have been explored. In this thesis we have focused on the ZnO based colloidal nanostructures which was not investigated in detail in the past. First we have synthesized various kinds of pure ZnO and ZnO based alloy nanostructues following low temperature solution routes which have been standardized in this thesis. These nanostructures have been characterized by various complimentary techniques and a detailed structural analysis has been performed. The well characterized nanostructures are then used for studying their optical properties. We have mainly focused on the intense visible luminescence from the ZnO nanostructures. We observed that the shape of the nanostructures change from spherical to rod and hexagonal platelet like morphology beyond the size limit of $\sim$20 nm which severely affects the visible emission. The effect of size reduction on the optical properties of ZnO nanostructures having different morphologies has been studied. The intensity of the visible emission has been controlled by dispersing the nanoparticles in different ionic environments. Also a reversible control of this visible emission is demonstrated in a simple ZnO based device by the application of electric field. The nanostructured ZnO film of the same device exhibits high gain photoresponse which is promising for application in the area of UV detection and photovoltaics. Another important aspect that we covered in this thesis is tailoring of the properties of pure ZnO nanostructures by alloying which was not addressed earlier. $Zn_{1-x}Mg_xO$ and $Zn_{1-y}Cd_yO$ ternary alloy nanostructures have been fabricated by novel low temperature solution routes. The band gap of ZnO nanostructures is varied from 3-4 eV. Change in structural and optical properties of ZnO nanostructures due to alloying by Mg and Cd has been investigated.

In chapter 1, we have discussed some basic properties of ZnO with emphasis on its optical properties and documented a brief review of previous investigations on ZnO. Also the major aspects of this thesis discussed in the subsequent chapters have been summarized.

In Chapter 2, the synthesis schemes of the various kind of nanostructures have been described. A good control over the nanostructures size and morphology have been achieved. A high pressure solution route has been prescribed for synthesizing nanostructures of different morphology. Site specific growth of single crystal and aligned nanorods of ZnO is possible on a substrate by using

a seed layer in a low cost solution method. We studied the effect of various growth parameters (such as seeding density, microstructure of the seed layer) as well as the growth time on the growth and alignment of the nanorods. In this thesis we have demonstrated that the density of the nanorod array is closely related to their alignment as well as the preferred orientation which can be controlled by varying the aerial density of the seed particles. In this chapter we have also supplied a brief description of the frequently used experimental techniques and methods of analysis.

ZnO nanostructures prepared by chemical method undergo a shape transition as the size increases beyond 20 nm. Nanostructures in the size range $5-15$ nm are mostly spherical whereas beyond 20 nm flat faces arise leading to hexagonal platelet and rod like morphologies. In chapter 3, we have discussed the evidences of this shape transition and its effect on the optical properties of the nanostructures. Mainly, precursor concentrations and growth time were found responsible for the change in morphology and size of the nanostructures. This shape transition can be visualized from the TEM images and can be understood in terms of the relaxation of microstrain determined from the X-ray data as the flat faces arises for relatively bigger particles. Effect of these shape transition on the optical properties of the nanostructures have been studied. It has been observed that the spectral components of the defect related visible emission from the nanostructures shifts to higher energy as the shape changes from spherical to rod like morphology. Our observations provide additional support of the fact that visible emission from ZnO nanostructures originates from the charged oxygen vacancies residing at the surface.

In chapter 4 we describe that the visible photoluminescence from ZnO nanoparticles can be controlled by changing the ionic or polar nature of the medium in which the nanoparticles are dispersed. We find that the presence of sufficient amount of electrolyte can even quench the emission. An explanation is proposed based on the surface charge of the ZnO nanoparticles, which controls the band bending in the depletion layer at the surface. The band bending in turn, decides the predominant nature of the visible emission. The explanation is validated by establishing a direct correlation between the visible emission and the zeta potential.

Chapter 5 deals with the fabrication and performance of a simple ZnO based optoelectronic device by the use of solid polymer electrolyte for making contact on nanocrystalline ZnO. The nanocrystalline ZnO film can be deposited by simple and cost effective techniques like spin coating or drop coating and offers large collection area for the incident optical radiation. The fabricated device shows high gain photo-response when irradiated by UV light.

The device has also been used to demonstrate the phenomenon of electrophotoluminescence in nanostructured ZnO film. We have achieved a reversible control over the visible photoluminescence in ZnO nanostructures with the application of electric field through solid polymer electrolyte. The combination of ZnO on top of ITO provides a suitable spectral range for excitation and luminescence measurement of the device.

In chapter 6, we discuss the structural and optical properties of $Zn_{1-x}Mg_xO$ (0<x<0.2) and $Zn_{1-y}Cd_yO$ (0<y<0.1) ternary alloy nanostructures of size ~10-15 nm, suspended in a liquid medium. A challenging problem of synthesizing $Zn_{1-y}Cd_yO$ nanostructures by a low temperature solution method has been solved. The band gap of the ZnO nanostructures has been varied from 3-3.9 eV by isovalent substitution of Mg and Cd into ZnO lattice. The chemical compositions of the doped material have been determined accurately. The change in structural and optical properties on alloying has been investigated in depth using various complementary techniques like XRD, TEM, ICPAES, Absorption, Photoluminescence and Raman Spectroscopy.

7.2 Summary of main results

7.2.1 Growth of ZnO and its alloy nanostructures of different size and morphology

We have synthesized pure ZnO nanostructures of different morphologies (spherical, cylindrical rod and hexagonal platelet) in the size range of 4-80 nm by dissociation of the precursor $Zn(CH_3COO)_2.2H_2O$ in a basic medium. Below 20 nm, nanostructures were found to exhibit spherical morphology. Beyond that size limit hexagonal platelet and rod like morphologies dominate. The low cost method that we use is scalable for production of large quantity materials. Compact and aligned ZnO nanorod arrays (dia ∼50-200 nm) have been grown on a glass substrate with varying seed particle density. The suspension of ZnO nanoparticles (size ∼15 nm) of various concentrations are used as seed layer for the growth of nanorod arrays via self assembly of ZnO from solution. We find that the growth, aerial density and alignment of the nanorods depend on the density of seed particles which can be controlled. It is observed that there is a critical density of the seed particles at which nanorod arrays show maximum preferred orientation along [002] direction. The minimum and maximum radius of the aligned nanorods synthesized by this method lie in the range 50-220 nm which depends on the seeding density and time of growth. These nanorods have a bandgap of 3.3 eV as in the case of bulk crystals and show emission in the UV region of the spectrum (∼400 nm) due to excitonic recombination.

7.2.2 Shape transition in ZnO nanostructures and its effect on blue-green photoluminescence

We find that ZnO nanostructures synthesized by a chemical route undergo a shape transition at ∼20 nm from spherical to hexagonal morphology thereby changing the spectral components of the blue-green emission. Spherically shaped nanocrystals (size range 11-18 nm) show emission in the range of 555-564 nm and the emission shifts to the longer wavelength as the size increases. On the other hand, rods and hexagonal platelets (size range 20-85 nm), which are the equilibrium morphology after the shape transition, show an emission near 465-500 nm which shifts to shorter wavelength as the size increases. The shape transition also leads to relaxation of microstrain in the system. Our analysis shows that the visible emission originates from a defect layer on the nanostructure surface which is affected by the shape transition. The change in the spectral component of the blue-green emission on change of shape has been explained as arising from band bending due to a depletion layer in smaller spherical particles which is absent in the larger particles with flat faces.

7.2.3 Ionic environment control of visible photoluminescence from ZnO nanostructures

Photoluminescence properties of the spherical particles [dominated by 550 nm (2.2 eV) band] and the cylindrical nanorods [showing emission around 500 nm (2.5 eV)] have been investigated by dispersing them in various ionic environment such as electrolyte solution in ethanol and water. As the concentration of the electrolyte ($LiClO_4$ in ethanol and NaCl in water) increases, the intensity of visible emission from both the nanostructures reduces and finally almost complete quenching is achieved. Maximum 70% decrease in the intensity is obtained for 1M $LiClO_4$ concentration. The positions of the spectral components show a small but gradual shift on

increasing the electrolyte concentration. Reduction in integrated intensity due to the change in relative strength of the spectral components is directly linked with the surface charge of the nanoparticles characterized by zeta potential measurement.

7.2.4   High gain photoresponse and electrophotoluminescence in thin film of ZnO nanostructures

We have fabricated a simple ZnO based device which shows high gain photoresponse and displays reversible change in the luminescence intensity of ZnO nanoparticles by application of electric field. A film of ZnO nanoparticles (size $\sim$10-15 nm) has been deposited on top of a conducting ITO layer supported by a glass substrate. A gel of PEO and $LiClO_4$ is deposited on the ZnO layer at room temperature. The device thus fabricated exhibits high gain photoresponse when illuminated by a 345 nm light passing through the transparent (above 325 nm) ITO glass substrate. Maximum photo-responsivity of 10 A/W at 1.5 V is detected when illuminated by 345 nm light. The barrier potential created at the ZnO-polymer interface reduces by UV illumination which in turn enhances the current passing through the junction. The total current flowing through the device is determined by the excess carriers generated by UV illumination as well as carrier injected by the application of voltage.

The visible luminescence from ZnO nanostructures sandwiched between ITO film and PEO/$LiClO_4$ solid electrolyte as described above can be controlled by the application of a few volts ($<$5V). The excitation light is allowed to pass through the ITO-glass substrate side which illuminates the ZnO-ITO interface and the PL spectrum (peaked at 545 nm) has been collected in reflection mode. In principle for excitation any broad-band UV source that has component in the wavelength range of 320-375 nm can be used. When the PEO/$LiClO_4$ is negatively biased, up to 107 percent enhancement in the visible luminescence has been observed whereas a complete quenching (87 percent reduction) of the visible emission has been seen when the PEO/$LiClO_4$ is positively biased. The applied voltage thus allows for nearly 100% modulation. However the sharp near band edge emission around 400 nm, has no dependence on the applied voltages ($<$5 V). The response time of the luminescence output to the applied voltage lies within the range of 20 - 30 sec.

7.2.5   Structural and optical properties of $Zn_{1-x}Mg_xO$ and $Zn_{1-y}Cd_yO$ ternary alloy nanostructures

$Zn_{1-x}Mg_xO$ and $Zn_{1-y}Cd_yO$ nanocrystals (with average size $\sim$10-15 nm) are synthesized by using a low temperature solution growth method. The alloy nanocrystals retain the parent wurtzite structure, up to a certain concentration of Mg and Cd ($x <$0.17 and $y <$0.09). Beyond that phase segregation occurs. While fabricating $Zn_{1-x}Mg_xO$ alloy, after phase segregation, the excess $Mg(OH)_2$ forms a layer on the alloy nanocrystals, which quenches the visible emission. In case of Cd incorporation, the CdO phase (size $\sim$70-80 nm) segregates out and remains suspended in the solution. The chemical composition as checked by the ICP-AES shows that EDX composition analysis (as is generally done in doped ZnO films) may overestimate the actual Mg or Cd incorporation. Mg substitution leads to enhancement of the fundamental absorption edge from 3.55 eV to 3.99 eV and Cd substitution reduces the same below 3 eV. The variation in band gap due to alloying by Mg and Cd has been explained on the basis of their ionicity by first principle electronic structure calculation of the alloy ZnO clusters. The near band edge emission

shifts from 3.3 eV to 3.4eV for Mg content (x) as little as 0.17. For Cd substitution the near band edge emission shows redshift as the Cd content increases. We find a close link of the strain to the PL properties where the microstrain broadens the PL line width.

7.3   Main deficiencies of this work

The investigations have been performed on ZnO nanocrystals obtained as colloidal solution. Collection of nanomaterials of size less than 10 nm in powdered form for structural studies is difficult. Further, powdered materials are of polycrystalline nature, therefore the results obtained are not crystal direction specific.

The smallest size of the nanocrystals we could achieve is 4 nm, which is higher than the excitonic Bohr radius of ZnO ($\sim$1.4 nm). Therefore the quantum confinement effect seen in our samples is weak and the study of quantum size effect on the optical properties remains partly incomplete.

Almost all the measurements have been carried out at room temperature. For identifications of defects in ZnO and to understand the nature of the visible emission, low or high temperature study of the emission properties is required.

The optoelectronic device we have fabricated suffers from many technical difficulties. By deposition techniques like spin coating or drop coating it is difficult to obtain smooth thin film of equal area repeatatively. Further, thin nanocrystalline ZnO film is porous. Therefore, metal contacts on nanostructured ZnO thin film may result short circuit condition. To overcome this shortcoming we have been compelled to work on a rather thick film ($> 1~\mu m$) of ZnO nanostructures specially when the PEO/$LiClO_4$ has not been used as top layer. It is also found difficult to obtain a thin polymer layer on ZnO film.

7.4   Future scope of the work

Temperature dependent study of the optical and structural properties on the systems presented in this thesis will be an useful extension of this work. Investigation on systems with even lower particle size ($<$4 nm) will be interesting. Modelling of many important effects observed in this thesis work viz., shape transition, ionic environment control of photoluminescence, electrophoto-luminescence and photoresponse has immense importance. ZnO nanoparticles can be applied as biosensor by utilizing the idea of ionic environment control of visible luminescence. The device performance can be improved by employing advanced lithographic technique and vapour phase deposition for making contacts. The principle of our device can be used for general application in the field of UV detection and photovoltaics.

Appendix A

Size determination by time dependent absorption measurement of the sedimenting particles

This appendix describes a simple method of size determination for the colloidal nanoparticles. The as grown samples can be easily tested by this method for a rough idea of their size before being characterized by TEM. Due to easier accessibility of the UV-VISIBLE spectrometer compared to TEM, we devised an indirect method for particle determination using absorption measurements instead of taking the actual image. Determination of particle size from the peak position at the onset of absorption spectra is very common. One has to follow the procedure prescribed by Brus to connect the particle size with the absorption peak position [96]. In this method, nanoparticles in ethanol solution were allowed to sediment and time dependent absorption measurements were performed to obtain the change in particle concentration with time. As the particles are acted on by two opposing forces: the downward force due to gravity and the upward viscous force, they soon attain a terminal velocity. This information has been used in obtaining a formula for the change in particle density with time as described in the next section.

A.1   Derivation of the basic formula

We consider N number of particles dispersed in a liquid at the initial time. The liquid containing the particles occupy a volume $LA\ cm^3$ where A is the cross-sectional area and L is the height of the liquid.

According to Stoke's law, each particle of radius r experiences an upward viscous drag given by

$$F_U = 6\pi\eta rv \tag{A.1}$$

where η is the coefficient of viscosity of the fluid, r is the radius of the particle and v is its terminal velocity.

Also due to gravity, downward force on each particle is

$$F_D = mg = \frac{4}{3}\pi r^3(\rho - \sigma)g \tag{A.2}$$

where ρ and σ are the densities of the particle and the fluid respectively. In equilibrium, the upward and downward forces are balanced and the particles attain a terminal velocity. Balancing the two forces,

$$6\pi\eta r v = \frac{4}{3}\pi r^3(\rho - \sigma)g \tag{A.3}$$

$$\implies v = \frac{2r^2(\rho - \sigma)g}{9\eta} \tag{A.4}$$

Let us now focus our attention on a single particle moving downwards with the terminal velocity given in (A.4). If the particle is at a height x, the time taken by it to reach the bottom of the container, i.e. precipitate is x/v. Assuming uniform distribution of the particles initially, as there are equal number of particles at height L as well as zero height, the average time taken by all the particles is $L/2v$. Hence, the rate of change of the number of particles in solution is

$$\frac{dN(t)}{dt} = -\frac{2vN(t)}{L}$$
$$= -\frac{4r^2(\rho - \sigma)gN}{9\eta L} \tag{A.5}$$

However in reality, all the particles do not have the same radius r. A Gaussian distribution is assumed for the particles. We now make use of the property of the Gaussian distribution that if μ is the mean and σ_s is the standard deviation, then 99.9% of the function values lie between the radii values $\mu - 3.29\sigma_s$ and $\mu + 3.29\sigma_s$. Thus, in actual case, the rate of change of the number of particles is

$$\frac{dN(t)}{dt} = -\frac{4(\rho - \sigma)gN}{9\eta L\sigma_s\sqrt{2\pi}} \int_{\mu-3.29\sigma_s}^{\mu+3.29\sigma_s} r^2 e^{-(r-\mu)^2/2\sigma_s^2} dr \tag{A.6}$$

The above integral can be integrated as

$$I = \int_{\mu-3.29\sigma_s}^{\mu+3.29\sigma_s} r^2 e^{-(r-\mu)^2/2\sigma_s^2} dr$$
$$= 2\sigma_s^3 \int_0^{3.29} z^2 e^{-z^2/2} dz + 2\sigma_s\mu^2 \int_0^{3.29} e^{-z^2/2} dz \tag{A.7}$$

and obtaining the values of the above error integrals numerically, the integral is expressed in terms of the mean and standard deviation as $2.47476\sigma_s^3 + 2.50412\mu^2\sigma_s$. Finally the rate equation becomes

$$\frac{dN(t)}{dt} = -\frac{4(\rho - \sigma)gN}{9\eta L\sigma_s\sqrt{2\pi}}(2.47476\sigma_s^3 + 2.50412\mu^2\sigma_s) \tag{A.8}$$

Solving the rate equation, we obtain the number of dispersed particles in solution in terms of the initial number of particles $N(0)$ as

$$N(t) = N(0)exp\left[-\frac{4(\rho - \sigma)gN}{9\eta L\sqrt{2\pi}}(2.47476\sigma_s^2 + 2.50412\mu^2)t\right] \tag{A.9}$$

Applying logarithm to both sides, we obtain

$$ln\ N(t) = ln\ N(0) - \frac{4(\rho - \sigma)gN}{9\eta L\sqrt{2\pi}}(2.47476\sigma_s^2 + 2.50412\mu^2)t \tag{A.10}$$
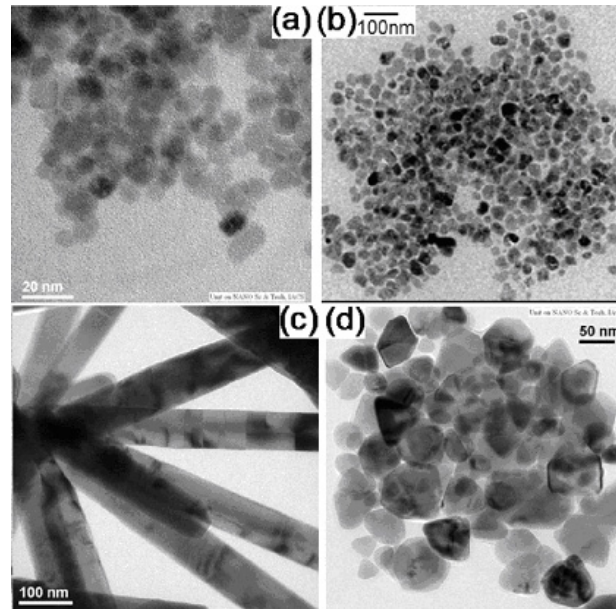
Figure A.1: TEM images of ZnO nanostructures having different average sizes namely a)9 nm, b)15 nm, c)100 nm and d)60 nm respectively.
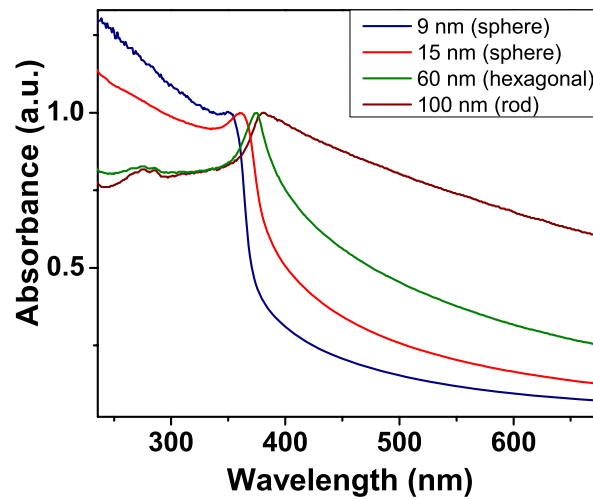
Figure A.2: Absorption spectra of ZnO nanostructures dispersed in ethanol with different sizes as indicated on the graph.
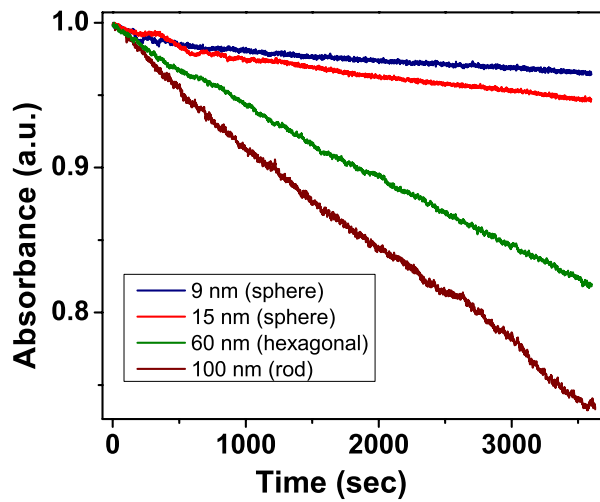
Figure A.3: Time dependent absorbance of sedimenting ZnO nanostructures dispersed in ethanol with different sizes as indicated on the graph.
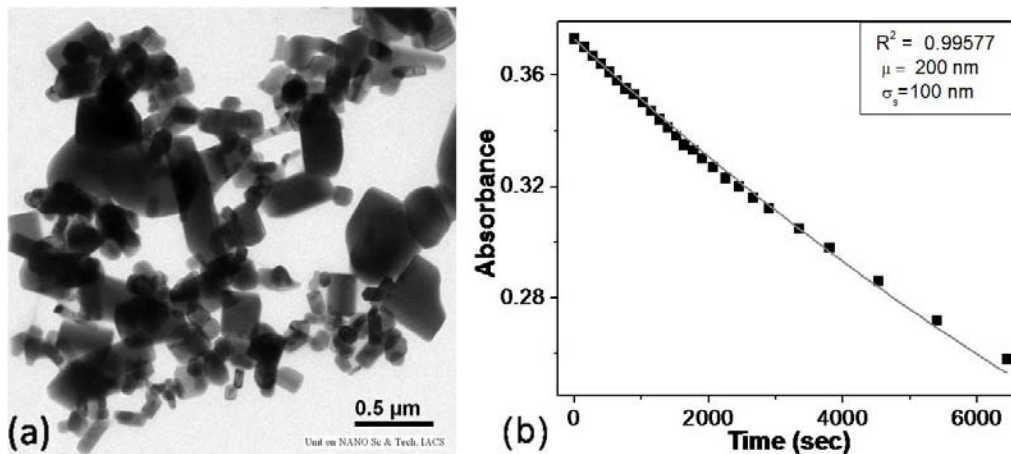
Figure A.4: (a) TEM image of the commercial ZnO powder shows a wide distribution in its size and shape. (b) Time dependent absorbance of sedimenting particles shown in (a) is fitted using the equation A.10

A.2 Results

In figure A.1, we show the TEM images of the investigated nanostructures having different sizes: a)9 nm, b)15 nm, c)100 nm and d)60 nm respectively. The absorption spectra of these colloidal nanoparticles have been plotted in figure A.2. The peak position at the onset of the absorption spectrum shifts towards higher wavelength as the size increases. Particle sizes calculated by applying the Brus equation agrees well with that obtained from the TEM images [96].

A similar trend is observed in the time dependent absorbance of the nanoparticles of different sizes. As observed from figure A.3, the slope of the absorbance vs. time graph increases with particle size. If properly callibrated, by observing the time dependent absorbance, the particle size of an unknown sample can be obtained. Finally, equation A.10 has been employed for fitting the time dependent absorbance data for the commercial ZnO powder with a wide size distribution as shown in figure A.4a).

For a liquid column of height $L = 4cm$, density of particles (ZnO) $\rho = 5.67gm/cc$, density of fluid (ethanol)$\rho = 0.789gm/cc$, acceleration due to gravity $g = 981cm/s^2$ and coefficient of viscosity of the fluid $\eta = 1.2 \times 10^{-3}N.s.m^{-2}$, we perform the time dependent absorption measurement using a UV-VIS spectrometer. Since the absorbance is equal to the product of the concentration of the particles in the fluid c, the length of the fluid column through which light travels x and the extinction coefficient λ, and we also have the formula $N(t) = N(0)exp(-\lambda x t)$, the absorbance is proportional to the logarithm of the number of particles in the given volume at that instant (as the length of the fluid column x and the extinction coefficient λ remains same at all times and the concentration c is proportional to the number of particles $N(t)$). So, the time dependent absorbance of the sedimenting particles can be fitted with the equation A.10 with the initial absorbance being its value measured at t=0. The fitting (A.4b)) gives a mean size of $\mu = 200nm$ and a standard deviation of $\sigma_s = 100nm$.

Though the above method is applicable for particles of larger sizes (> 100 nm), for smaller particles, the effects of random Brownian motion, particle correlations and confinement leading to diffusion becomes very important and the above method loses its applicability. In order to understand the time-evolution of a given initial state towards sedimentation-diffusion equilibrium, the interplay of direct and (solvent-mediated) hydrodynamic interactions between the particles need to be analyzed. A more detailed analysis involving dynamical density functional theory (DDFT) and Brownian dynamics computer simulation is more appropriate in that case [203].

Appendix B

Probing defects in ZnO nanostrucures by Positron Annihilation Spectroscopy and origin of the visible photoluminescence

B.1   Introduction

In chapter 3 and chapter 4, we have seen that ZnO nanostructures show a broad visible photoluminescence (PL) in the blue-yellow region (470-570 nm) which is linked to defects in ZnO [77]. Majority of the researchers believe that this visible emission originates from defects such as Oxygen vacancy which are located near the surface region ([89], [58]). The emission energy as well as the intensity of the visible photoluminescence not only depends on the size, but is also related to the morphology of the nanostructures. For example, ZnO nanostructures synthesized by chemical route undergo a shape transition at $\sim$ 20 nm which changes the spectral components of the blue- yellow emission. In particular, spherical ZnO nanoparticles of sizes less than 20 nm show broad visible photoluminescence around 550 nm ($\sim$2.2 eV) but the nanorods (of diameter $>$ 20 nm and length $\sim$ 100-150 nm) show a peak around 500 nm ($\sim$2.5 eV) [93]. Both these emissions show very systematic dependence on the surface to volume ratio which confirms the surface related origin of this emission. The change in the spectral component of the blue green emission on change of shape has been explained as arising from band bending due to depletion layer in smaller spherical particles which is absent in the larger particles with flat faces. We have also encountered the phenomenon that emission energies and relative intensity of the spectral components depends upon the ionic nature of the environment, ie the surface charge of the nanotructures plays a crucial role in detemining the nature of the visible luminescence.

In the subsequent sections we will discuss that the change in visible photoluminescence on the change in size (and shape) has a close correlation with the size induced change in the positron trapping rate which is directly proportional to the defect concentration. Our analysis on the positron annihilation lifetime data reveals that there is more than one type of defects present in the synthesized nanostructures. The positron trapping rates are calculated assuming a three state trapping model in which positron may annihilate with Zn vacancy, triple junction and free delocalized electrons. The trapping rates initially increases with the decrease in size for rods

135

and hexagonal platelets of size above 20 nm. But in the size range below 23 nm trapping rates decrease as we reduce the size up to 5 nm. Thus there is a non-monotonous dependence of trapping rates on size around a critical size of 20 nm when morphology changes from spherical to hexagonal shape. While increase of the trapping rate on size reduction is expected due to accumulation of more defects at the surface, the initial dependence of the trapping rate on the size (for diameter <20 nm) is anomalous. To resolve this anomaly we propose a defect arrangement for ZnO nanocrystals in which positive charge received at the surface due to the presence of oxygen vacancy creates an energy barrier for the positrons. Higher energy barrier for smaller spherical particles confine positrons within the defect free core region and is responsible for sudden reduction in positron trapping rate and S-parameter when the morphology changes from spherical to faceted (size <20 nm). This shape transition is reflected by a sudden rise of the S-parameter and leads to relaxation of microstrain in the system by creation of enhanced low momentum positron annihilation sites like voids. By using two complimentary techniques viz. Photoluminescence (PL) and Positron Annihilation Spectroscopy, it is seen that nanostructure surface is a likely site for the positively charged oxygen vacancies which is responsible for both the green and yellow emissions.

B.2 Sample preparation and experimental techniques

The controlled ZnO nanostructures (with wurtzite crystal structure) have been synthesized by acetate route described in detail in chapter 2. Unlike in chapter 3 where all the samples were prepared under high pressure, the smaller samples considered here (<15 nm) were prepared under ambient pressure as described in chapter 2. The larger samples (size >20 nm) are similar to that considered in chapter 3 and prepared in an autoclave under 54 atm. pressure at $230^{o}C$ as described in chapter 2 (Table 2.1). Two groups of samples have been investigated. Gr-I samples with spherical morphology (size < 20nm) are synthesized under ambient pressure. Gr-II samples, having hexagonal and rod like shape with size >20 nm were synthesized in the autoclave.

For positron annihilation study, a 12 μCi 22Na activity deposited and sealed within two aluminium foils was used as the positron source. The PALS (Positron Annihilation Lifetime Spectroscopy) system was a standard fast-fast coincidence set-up using two identical 1-inch tapered off BaF_2 scintillator detectors fitted with XP2020Q photomultiplier tubes. The time resolution obtained using 60Co source with 22Na gates was 298 ps. A total of more than 1 million counts were recorded for each lifetime spectra. All the spectra were analyzed using PATFIT 88 [99], after proper background and source corrections. Each lifetime spectra were deconvoluted into three exponentially decaying lifetime components and a Gaussian resolution function to obtain the best fit. Several data were retaken and reanalyzed to monitor the stability of the spectrometer and reproducibility of the results. The DBPAS spectra were recorded using a single HPGe detector with energy resolution of 1.8 keV for gamma rays from ^{137}Cs standard source [98]. Each spectrum was acquired for two hours, which corresponded to more than 1 million counts under the annihilation peak.

Representative transmission electron microscope (TEM) images of the samples are shown in figure B.1. We find that the samples with sizes below ∼20 nm have a spherical shape [figure B.1 (a), (b) and (c)]. However, for size >20nm there is a shape transition and these samples show mostly hexagonal facets and some of them show rod like morphologies [figure B.1 (d), (e) and (f)]. The details of the sample has been listed in table B.1. The crystal structures

and size of all the samples have been analyzed by X-ray diffraction technique which confirms wurtzite symmetry of the synthesized nanostructures. The size determined by TEM and XRD analysis (listed in table B.1) agrees well within the range of ± 2 nm for particle size below 15 nm. The root mean square (rms) distribution in size (d) of the samples can be quantified as $\triangle d_{rms}/d \approx 10\%$ for d<20 nm and $\triangle d_{rms}/d \approx 20\%$ for d >20 nm.

Table B.1: Size and morphology of ZnO nanostructures

Identification		Morphology	Size by TEM (nm)	Size by XRD (nm)	E_{NBE} (eV)
I	(i)	Spherical	4	5	3.45
	(ii)	Spherical	10	10	3.35
	(iii)	Spherical	15	15	3.34
II	(iv)	Rod diameter	24	23	3.33
	(v)	Hexagonal platelet	55	44	3.28
	(vi)	Rods and square pillars	100	85	3.27
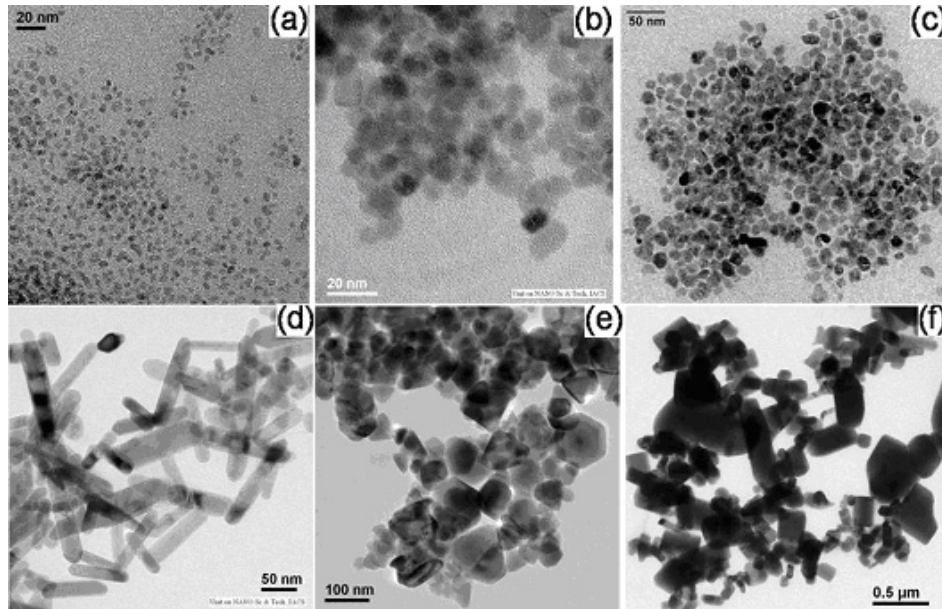
Figure B.1: TEM images Gr-I [a), b), c)] and Gr-II [d), e), f)]samples.

B.3   Positron Annihilation Spectroscopy study

Positrons diffusing through matter may be captured in special trapping sites. These trapping centers are crystal imperfections, e.g. vacancies and dislocations. The wave function of a positron captured in such a defect is localized until it annihilates with an electron of the immediate surrounding into γ-rays. Since the local electron density and the electron momentum distribution are changed with respect to the defect-free crystal, the annihilation radiation can be utilized to obtain information on the localization site. Hence, the character and the concentration of the trapping centers, i.e. lattice defects, can be investigated by positrons. As has been mentioned in the previous section, the lifetime or the time dependent positron decay spectra were deconvoluted into three components. In a nanocrystalline material with grain size smaller than the positron diffusion length (100-200 nm in a solid), the mechanism of positron annihilation is qualitatively different from that in bulk crystals. Grain boundaries being rich in defects, act as strong trapping centers for positrons and all positrons get trapped in the vicinity of grain boundaries leading to a case called saturated trapping. In case of saturated trapping, the shortest lifetime τ_1 with corresponding percentage intensity I_1 may be attributed to the annihilation events at the structural defects in the grain interfaces. So, positron lifetime spectra of nanocrystalline materials generally do not have any contribution from the electrons residing inside the grains and provide information regarding the annihilation at grain boundaries only. But in certain cases when the defect density at the grain surfaces is not that large, a fraction of positrons may cross more than one grain-surface and annihilate with free electrons inside a grain. The intermediate lifetime τ_2 with corresponding intensity I_2 has been assigned to trapping of positrons in nano-voids at the intersection of three or more grain boundaries (e.g. triple junction) and the longer lifetime τ_3 with a very small intensity $I_3 < 2\%$, has been attributed to the pick-off annihilation of ortho-positronium formed in larger free volumes. These free volumes most likely appear because of the pores present in the pellets of the powdered sample and are not related to the sample property. Hence, the variation of τ_3 and I_3 has not been discussed in the present case. Moreover, owing to its low intensity, the effect of τ_3 has not been included in the trapping model analysis.

A two-state trapping model, which assumes the presence of only one kind of vacancy type defect, can be applied to reveal some important facts about the annihilation mechanism of positrons ([104], [105]). In case of two-state trapping model the two lifetimes τ_1 and τ_2 are related by the following equations:

$$\tau_1^{-1} = \tau_f^{-1} + K \tag{B.1}$$

$$I_2 = 1 - I_1 = \frac{K}{K + \lambda_f - \lambda_d} \tag{B.2}$$

where, τ_f is the lifetime corresponding to annihilation of positrons with delocalized electrons at a defect free region in a grain. The annihilation rate at the defect site is given by $\lambda_d = 1/\tau_d$, where $\tau_d = \tau_2$ (defect related lifetime of positrons). K is the trapping rate and $\lambda_f = 1/\tau_f$ is the annihilation rate of positrons at the defect free sites. The trapping rate K is proportional to the concentration C_d of positron traps (K $= \mu C_d$). The value of λ_f is taken as $1/158$ $(picosec)^{-1}$. The trapping rate was calculated for different grain sizes using equation B.2 with the experimentally obtained value of τ_2 and I_2, and the value of τ_1 according to the two-sate trapping model (τ_1^{TM}) has been calculated using the K values in eqnuation B.1. Figure B.2 shows the comparison

of the experimental lifetime τ_1 with that calculated using the two-state trapping model. The mismatch between the two values readily suggests that a two-state trapping model is not valid which further indicates the presence of more than one type of defects. A consistently larger value of τ_1 than that of τ_1^{TM} for all the samples suggests the presence of a defect related lifetime close to τ_f, which is difficult to resolve by a numerical fitting.

Chen et al (ref. [106]) have reported that in ZnO, zinc vacancy (V_{Zn}) is the dominant defect which can be sensed by positrons, as they appear in negative and neutral charge states. The reported lifetime of positrons in Zn monovacancies is about 237 ps. So, the shortest lifetime τ_1 may be assumed to be a mixed state of positrons annihilating with free electrons in defect-free regions and zinc monovacancies. So, if we assume that n_f is the fraction of positrons annihilating in the defect free regions and n_v is the fraction of positrons annihilating in the zinc vacancy site with a lifetime τ_v, then the experimentally obtained value of τ_1 can be expressed as,

$$\tau_1 = n_f\tau_f + n_\nu\tau_\nu \tag{B.3}$$

Figures B.3 and B.4 gives the variation of the lifetime components and the corresponding intensities respectively as a function of grain size. The value of τ_1 was initially seen to increase with reduction in grain size from 80 nm to 23 nm. This increase in τ_1 is quite obvious as the contribution of trapping at the zinc monovacancies in the interfaces increases due to the increase in the interface area with size reduction leading to an increase in n_v. Hence, from equation B.3, it follows that τ_1 will increase. A further reduction in the grain size should have increased the value of τ_1. But surprisingly, the value of τ_1 was seen to decrease for samples having average grain size smaller than 23 nm. The only plausible explanation is that the fraction n_f increases for these samples. The reason behind the increase in n_f may be explained as a result of reduction in the increasing contribution from the annihilation events at the zinc vacancies. However,
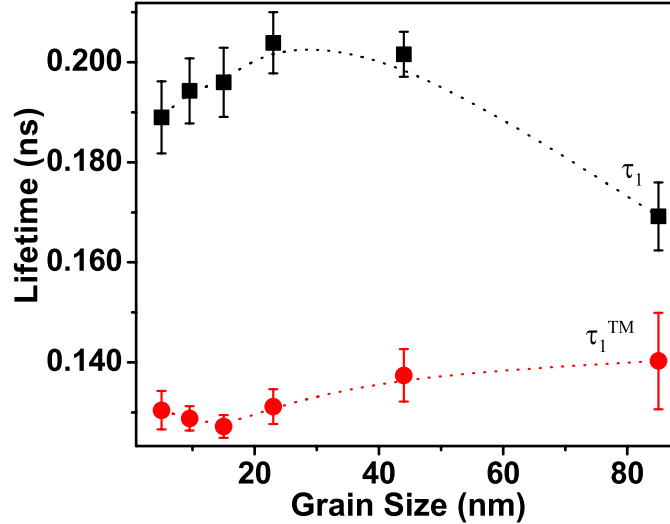
Figure B.2: Measured lifetime is compared with the calculated lifetime considering a two state trapping model.

the variation of I_1 in figure B.4 cannot explain the variation of zinc monovacancies at the grain boundaries since I_1 contains contribution from free annihilation of positrons also and moreover the value of I_1 depends on the value of I_3 and I_2. The variation of defect concentration with grain sizes can be observed from the trapping rates since the trapping rates are directly depen-
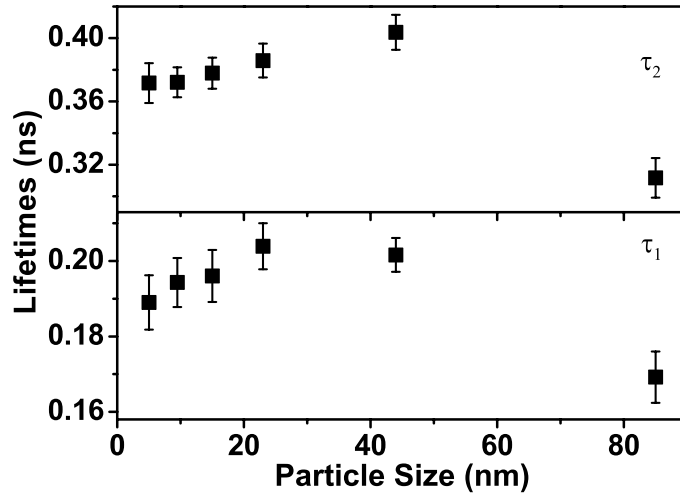
Figure B.3: Measured lifetime plotted as a function of particle size.
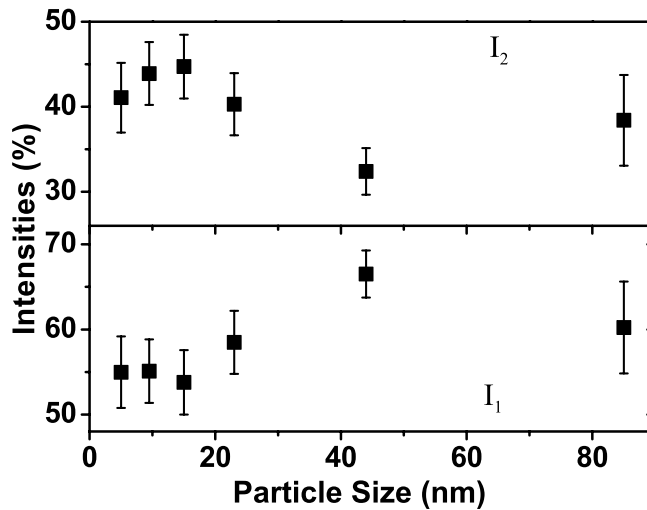
Figure B.4: Intensities I_1 and I_2 corresponding to the lifetime components τ_1 and τ_2.

dent on the concentration of defects. A three-state trapping model can be applied to calculate the trapping rates at these defects. This model assumes that the shortest lifetime τ_1 is an admixture of positron lifetime τ_{D1} in monovacancies and τ_f, whereas τ_2 (which is equal to τ_{D2} in the present trapping model) is the correctly resolved lifetime component. The trapping rates k_1 and k_2 in both the defects were calculated using the following equations,

$$k_1 = \frac{\tau_1(\lambda_B - I_2\lambda_{D2}) - I_1}{\tau_{D1} - \tau_1} \tag{B.4}$$

$$k_2 = \frac{I_2}{I_1}(\lambda_B - \lambda_{D2} + k_1) \tag{B.5}$$

where the annihilation rates are $\lambda_B = \tau_B^{-1}$ and $\lambda_{D2} = \tau_2^{-1}$. The lifetime τ_B is taken as 158 ps and τ_{D1} as 237 ps. Figure B.5 represents the variation of the trapping rates as a function of grain size. Both the trapping rates k_1 and k_2 were seen to decrease for grain sizes lower than 23 nm. Also the value of I_2 was also seen to decrease with grain size smaller than 23 nm. All these observations support the fact that the contribution from the annihilation events at the grain boundaries is reducing as the grain sizes become smaller than 23 nm. From the above discussion it has been found that for the samples with average grain sizes lower than 23 nm the contribution from the free annihilation events increases at the cost of reduced annihilation events of the trapped positrons. This anomalous behavior can be explained on the basis of size and morphology dependent visible emission energy from ZnO nanostructures.
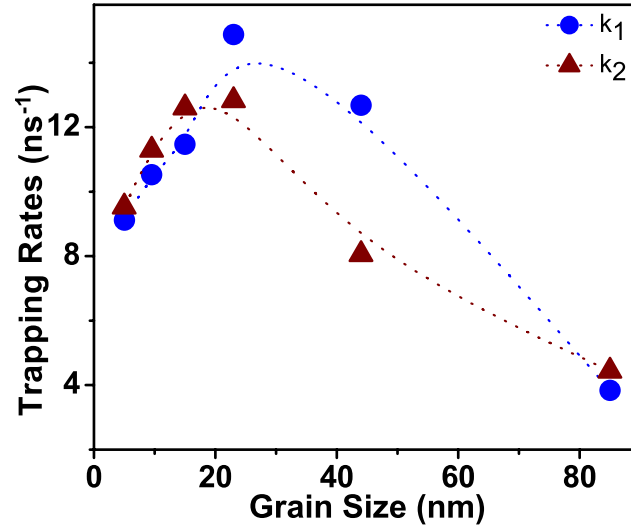
Figure B.5: Positron trapping rates calculated by three state trapping model.

B.4   Correlation between Photoluminescence and PAS origin of visible photoluminescence in ZnO

As described in chapter 3, the two groups of samples considered have bluegreen emissions in the range 470 nm-570 nm which show a distinct nonmonotonous shift in the emission energies as the particle shape changes. As already demonstrated, the broad emission in the blue-green region is composed of two broad lines [shown as dotted line in figure 3.4 for sample (vii)] which are marked as P1 and P2. This two peak fitting procedure adopted in this manuscript has a physical significance as far as the visible emission from ZnO is concerned. Role of the oxygen vacancy behind the broad visible emission was predicted earlier[[88], [89]]. It was also suggested that the singly ionized oxygen vacancy is responsible for the green emission in ZnO which results from the recombination of a photogenerated hole with the singly ionized charge state of this defect [88]. It is seen that free-carrier depletion at the particle surface, and its effect on the ionization state of the oxygen vacancy, can strongly impact the green emission intensity [89]. Consequently the singly and doubly charged oxygen vacancies are found to be responsible for the green (500 nm) and yellow (550 nm) emissions. The two peak fitting method is applied to find out the relative contribution of these two emissions depending upon the relative occupancy of the two charge states of the oxygen vacancy [87]. Furthermore all the synthesized nanostructures in our study are oxygen deficient. The weight ratio of O and Zn in stoichiometric ZnO should be 20% and 80 % respectively. But the weight ratio of oxygen determined from the average value of EDX data taken over different locations of the sample lies within the range 5.3 % to 10 % for the samples in our study. The spherical sample of size 10 nm shows highest oxygen deficiency (Oxygen 5.3 % and Zn 94.7%). The hexagonal platelets of size 55 nm contains 10 % oxygen and 90 % Zn. Therefore, charged oxygen vacancies (V_o^{++} and V_o^{+}) are responsible for the broad visible luminescence which will be supported later by further evidences. V_o^{++} and V_o^{+} were found responsible for emission near 2.2 eV (yellow band P2) and 2.5 eV (green band P1) respectively [93]. The spectral content or the relative weight of two lines of the blue-green band is determined by the relative occupancy of these charged oxygen vacancies. We find that the change in shape brings about a sharp change in the relative contribution of the two lines. P2 line is dominant in Gr-I samples (size ranging from 5-15 nm) having spherical morphology. As faceting starts appearing for nanostructures greater than 20 nm (Gr-II samples), intensity of P2 line gradually reduces and P1 emerges as the dominant emission band. This can be seen in chapter 3, figure 3.5 (upper panel) where we show the variation of the intensity ratio of the two lines (I_{P2}/I_{P1}). The shape change suppresses the P2 emission and changes sharply the energy of emission of both the bands. Therefore, Gr-I spherical particles (smaller than 20 nm) and Gr-II hexagonal and rod like structure (size>20 nm) are preferentially occupied by doubly charged oxygen vacancies (V_o^{++}) and the singly charged oxygen vacancy (V_o^{+}) respectively. So the spherical particles receive more positive charge than the rods and hexagonal platelets. This fact has been confirmed by the Zeta potential measurement discussed in chapter 4. Both the samples receive positive charges due to the presence of charged oxygen vacancies and spherical particles have higher positive charge (Zeta potential value is 18 mV) compared to the rods (Zeta potential value 8 mV). But the oxygen vacancies (V_O) are invisible to positrons in the sense that positrons are not trapped in these defects since positron binding energy to neutral oxygen vacancy V_O is only 0.04 eV (for V_{Zn} the positron binding energy is 0.39 eV). Positive charge to the oxygen vacancies rules out the possibilities to trap a positively charged positron and the zinc vacancies present in the sample surface are responsible for the trapping of positrons. Therefore

the positive charge at the sample surface creates a potential barrier for the positrons and the height of this barrier is higher in case of spherical particles than the rods and hexagonal platelets (figure B.6). As a result, the positrons, which have initially got higher energies, manage to enter a grain but cannot escape after losing its energy through various inelastic collision processes. However a fraction of positrons still gets trapped at the zinc vacancies as can be seen from the difference in the τ_1 and τ_{TM}. As a result of increased number of positrons getting trapped inside the grain the chances of their annihilation with free electrons in the defect free regions increases thereby increasing the fraction n_f for small spherical particles. So, τ_1 for these samples decreases. Therefore for samples with grain sizes between 80 nm to 23 nm, the zinc vacancies at the grain boundaries participate substantially to trap positrons because the trapping rate increases as we decrease the size. But for the samples with average grain sizes below 23 nm the positive surface charge suddenly increases. This increase in the barrier height confines positrons within the bulk core of a nanocrystal which contains fewer defects (zinc vacancies) than the surface. So the trapping rate decreases for small spherical particles of sizes < 23 nm. Interestingly this is the size regime where shape transition associated with sudden change in the surface charge has been observed (chapter 3) which is reflected by anomalous nature of the positron trapping rate, positron lifetimes, visible emission intensities and its spectral components.
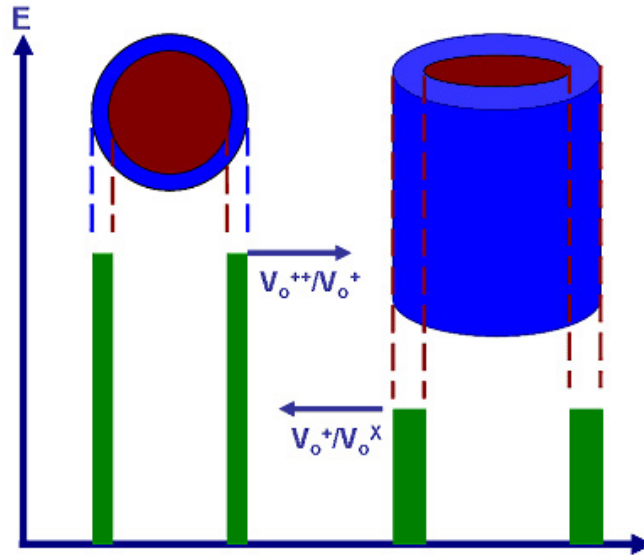
Figure B.6: Spherical particles offer higher barrier for positrons confined in the core region than rods and hexagonal platelets.

The S-parameter obtained from the DBPAS spectra can be accounted as a verification of the above proposed model. It is a measure of the fraction of positron annihilating with electrons of relatively lower momentum than the core electrons. It is expected that the S parameter corresponding to the positron annihilating in the defective surface layer (where relative number of low electron density sites such as voids is high) is higher than that in the delocalized bulk state. The S-parameter is defined as the ratio of the counts integrated under a central region spreading over ± 0.8 KeV around the 511 KeV annihilation line [shaded area in figure B.7] to
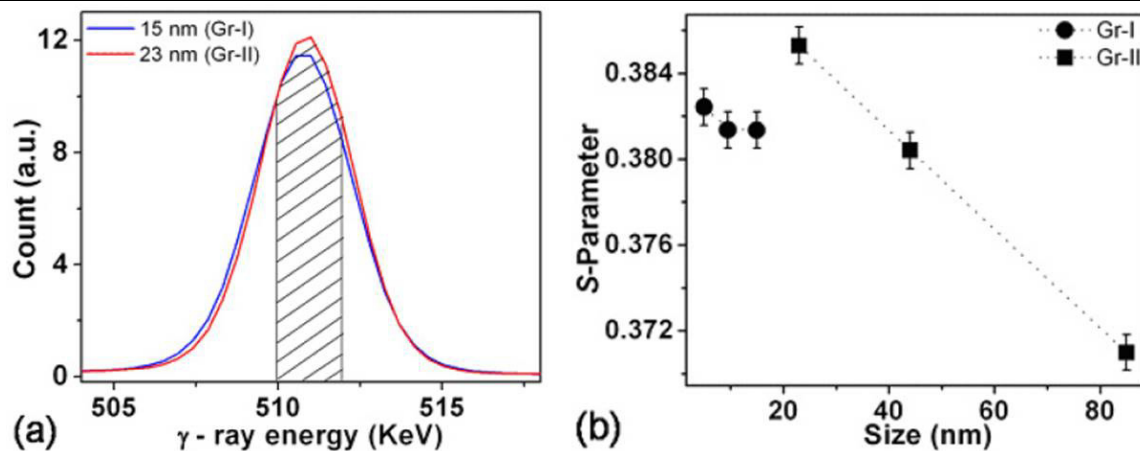
Figure B.7: DBPAS spectra and S- parameter.

the counts under the full spectrum.

$$S - Parameter \ = \ \frac{Integrated\ count\ under\ central\ shaded\ region\ (figure\ B.7)}{Total\ count} \quad (B.6)$$

In figure B.7 (a) we show two representative line profiles for Gr-I (15 nm) and Gr-II (23 nm) samples, obtained from DBPAS. The enhancement in the S-parameter value at the size where the shape transition occurs can be interpreted as creation of low electron density sites like voids due to strain relaxation in the structure on shape change (discussed in chapter 3). In figure B.7 (b), we plot the S-parameter as a function of size of the nanostructures.

For samples with grain sizes between 80 nm to 23 nm, the zinc vacancies at the grain boundaries participate substantially to trap positrons. The effect of grain boundary increases as we decrease the size, thereby increasing the S-parameter (grain sizes from 80nm to 23 nm). However, positively charged oxygen vacancies create a potential barrier at the grain surfaces for the positrons. And the barrier height is higher for smaller particles due to the increased positive charge states of oxygen vacancy. So the positrons predominately annihilate within the defect free bulk core for small spherical particles and a distinct reduction in the S-parameter values can be observed at the size where the shape transition occurs. The S-parameter for the smaller spherical particles remains almost constant because the positrons are annihilating with the free electrons inside the grain and no more sensing the defects (zinc vacancy) residing at the surface. Sudden rise in the S-parameter is seen for rods of bigger sizes when positron starts sensing defects (Zn vacancy) at the grain surfaces.

Appendix C

Phonon dynamics of $Zn_{1-x}Mg_xO$ and $Zn_{1-y}Cd_yO$ alloy nanostructures and their phase segregation

Phonon dynamics in $Zn_{1-x}Mg_xO$ and $Zn_{1-y}Cd_yO$ alloy nanostructures using non-resonant Raman and Fourier Transformed Infrared Spectroscopy (FTIR) has been studied. The experiments were carried out on $Zn_{1-x}Mg_xO$ ($0 \leq x \leq 0.07$) and $Zn_{1-y}Cd_yO$ ($0 \leq y \leq 0.03$) alloy nanostructures of sizes $\sim$10 nm synthesized by chemical route. A brief description of the samples considered in this study is listed in table C.1. Substitution by Mg makes the unit cell compact while Cd substitution leads to unit cell expansion. On alloying, both $A_1(\text{LO})$ and $E_1(\text{LO})$ mode of wurtzite Zn(Mg,Cd)O nanostructures show blue shift for $Zn_{1-x}Mg_xO$ and red shift for $Zn_{1-y}Cd_yO$ alloy nanostructures. Significant shift has been observed in $E_1(\text{LO})$ mode for $Zn_{1-x}Mg_xO$ (73 cm^{-1} for $x = 0.07$) and $Zn_{1-y}Cd_yO$ (17 cm^{-1} for $y = 0.03$). The IR bands also show blue (red) shift on alloying with Mg (Cd). However, on progressive alloying one can detect phase segregation (due to presence of interstitial Mg and Cd ions) in the alloy nanostructures for relatively higher Mg and Cd concentrations. This is confirmed by the gradual absence of the characteristic IR bands of wurtzite ZnO near 400-600 cm^{-1} as well as by X-Ray and TEM studies.

Table C.1: Size, morphology and chemical compositions of the nanostructures investigated

Samples		Morphology	Average size(nm)
ZnO	Bulk	Square pillar or rod	100
$Zn_{1-x}Mg_xO$	X=0	Spherical	10
	X=0.02	Spherical	13
	X=0.07	Spherical	12
	X=0.40	Spherical	14
$Zn_{1-y}Cd_yO$	Y=0.02	Spherical and rods	11
	Y=0.03	Spherical and rods	12

C.1   Raman study on ZnO and the effect of alloying

Group theory predicts that near the centre of the Brillouin zone, there is an A_1 branch, a doubly degenerate E_1 branch, two doubly degenerate E_2 branches, and two B branches of ZnO with C_{6V} symmetry. The A_1 and E_1 branches are both Raman and infrared active; the E_2 branches are Raman-active only, while the B branches are inactive [197]. The room temperature non-resonant Raman spectra of polycrystalline ZnO having orientation in all directions exhibits all the characteristic Raman peaks as shown in figure C.1 (a) for commercially available ZnO powder of particle size >100 nm. In table C.2, the major peaks in the samples have been assigned along with the frequencies of the characteristic Raman active modes for commercially available polycrystalline ZnO which matches well with the earlier results ([190], [191]). Since the measurement was carried out on compacted pellets, the orientations of the nanocrystallites are random. As a result, although a few prominent peaks are clearly observable, some are not that prominent and some of them are even missing. As for example, E_1 (TO) modes strongly appear for $Zn_{1-x}Mg_xO$ (with x = 0.02) and $Zn_{1-y}Cd_yO$ (y=0.02 and 0.03) samples, while the A_1 (TO) mode appears clearly in case of bulk ZnO powder and the lower Cd content sample. In
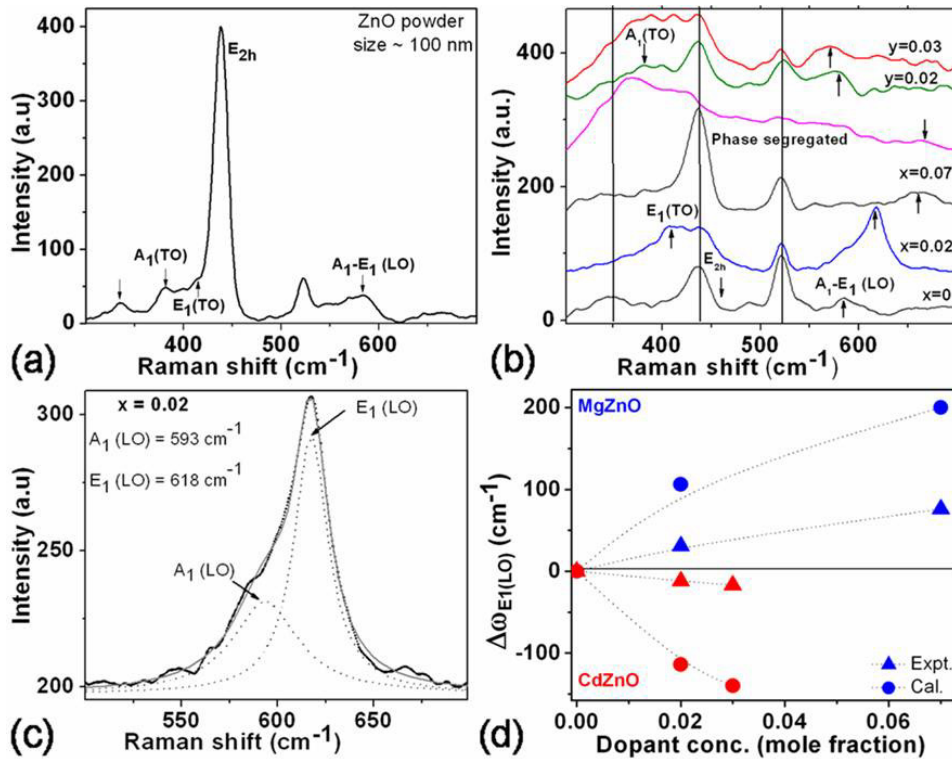
Figure C.1: Non-resonant Raman spectra of (a) Bulk ZnO powder (b) series of $Zn_{1-x}Mg_xO$ and $Zn_{1-y}Cd_yO$ alloy nanostructures. Assigned Raman modes are indicated on the graph. A sharp peak at 521 cm^{-1} originates from the glass substrate (c) The LO mode of $Zn_{1-x}Mg_xO$ (x = 0.02) nanostructures is fitted by two Gaussians to resolve A_1 (LO) and E_1 (LO) modes of ZnO. Observed and calculated shift in the E_1 (LO) mode with Mg and Cd concentration is plotted in (d).

Table C.2: Assignments of characteristic Raman modes for bulk ZnO powder

Symmetry character	Bulk ZnO (our work)	Ref.15
E_2(high)	438	437
A_1(TO)	381	380
E_1(TO)	409	407
A_1(LO)	571	574
E_1(LO)	583	583
Multiphonon processes	335	334

addition a broad peak is observed in the pure ZnO nanoparticles at 335 cm^{-1} which is attributed to second order Raman processes.

C.2 Effect of alloying

As indicated in the above discussion, the wurtzite structure has two symmetry types of Raman active LO modes viz A_1 (LO) and E_1 (LO) which arise depending on the experimental geometry. In crystallites of tilted orientation (as in powders), the two LO modes are expected to interact and create a single mode of a mixed $A_1 - E_1$ symmetry known as the quasi-LO mode [198]. Previous studies concerning the phonon modes of wurtzite $Zn_{1-x}Mg_xO$ thin films and powders showed that the E_1(LO) frequency of the film exhibited a significant blue shift while the A_1(LO) frequency was unaffected by the increasing Mg concentration ([192],[198]). In this work, the mixed $A_1 - E_1$ mode has been resolved into two separates modes viz. A_1 (LO) and E_1 (LO) by Gaussian fitting as demonstrated in figure C.1 (c) for $Zn_{1-x}Mg_xO$ sample with x = 0.02. We have observed a shift in both A_1 (LO) and E_1 (LO) modes due to alloying of ZnO by Mg and Cd [figure C.1(b)]. Also the broad peak appearing in the low frequency region due to multi-phonon processes becomes broader for alloy nanostructures. Interestingly, the frequency of E_2 (high) mode remains unaffected by the alloying which is not clearly mentioned in the previous reports ([192],[198]). Another very important issue in alloying of ZnO is the phase segregation. As can be seen from the XRD data (figure 6.6 and figure 6.16, chapter 6), if more than 40 wt.% of magnesium acetate and 20 wt.% of cadmium acetate are added to the zinc acetate, phase segregation occurs with $Mg(OH)_2$ and CdO coexisting with $Zn_{1-x}Mg_xO$ and $Zn_{1-y}Cd_yO$ phases respectively. Raman spectra also shows the effect of phase segregation in the case of $Zn_{1-x}Mg_xO$ (x >0.17) sample as indicated in figure C.1(b). Characteristic Raman modes are averaged out due to the lack of long range order and the Raman signal partly bears the signature of an amorphous material. Although the $Zn_{1-y}Cd_yO$ alloy nanostructures do not show phase segregation up to y = 0.03 (determined by XRD results), the broad Raman spectrum in the low frequency region indicates disorder in the sample.

The lattices of semiconductors can be perturbed by the addition of foreign atoms or by the application of stress. These perturbations change the force constant and mass matrices of the lattice vibrations. Hence a detailed knowledge of the lattice dynamics of semiconductors

Table C.3: Selected Raman modes of ZnO and its alloy nanostructures

	E_2 (high) (cm^{-1})	$A_1(LO)$ (cm^{-1})	$E_1(LO)$ (cm^{-1})	Shift in $E_1(LO)$ (Expt.) (cm^{-1})	Shift in $E_1(LO)$ (Cal.) (cm^{-1})	Multiphonon peaks (cm^{-1})	$A_1(TO)$ (cm^{-1})
ZnO bulk	438	571	583	–	–	535	381
$x=0$	437	579	587	–	–	346	381
$x=0.02$	437	593	618	31	106	355	388
$x=0.07$	437	651	663	76	200	346	382
$y=0.02$	437	564	575	12	114	–	–
$y=0.03$	436	556	569	17	140	–	–

is essential in treating their common perturbations. In case of isoelectronic substitution of Mg and Cd into ZnO lattice, one can assume that the mass defect (M) and the volume change resulting from the difference in atomic radii (R) of the impurity and the host atoms is uniformly distributed over all the atoms of the crystal. The only predicted effect is a frequency shift induced by the perturbation such as mass defect and volume change [199]. These perturbations eventually depend on the concentration of the impurities. Also we have came across that the mass defect ($\triangle M$) and difference in radii ($\triangle R$) are -41.085 and -0.09Å respectively for Mg substitution and that of 47.02 and 0.23Å for Cd substitution. The negative (+ve) sign applied in the difference values for Mg (Cd) substitution implies that the Mg (Cd) atom is lighter (heavier) and smaller (bigger) in diameter than the Zn atom and leads to compaction (expansion) of lattice. Therefore a particular Raman mode shifts to higher (lower) frequency side as a result of Mg (Cd) incorporation. Because of the alloying, the E_1 (LO) mode shows blue shift up to 73 cm^{-1} (for x = 0.07) and red shift up to 17 cm^{-1} (for y = 0.03) for $Zn_{1-x}Mg_xO$ and $Zn_{1-y}Cd_yO$ alloy nanostructures respectively [figure C.1 (d) and table C.3].

As we have seen, these chemically synthesized alloy nanostructures show phase segregation after a certain concentration of the impurities. Generally, the other alternative alloying process results in the nearly random spatial distribution of the intermixing atomic species. This randomness removes the translational symmetry of the crystal, so that Raman spectra from semiconductor alloys might be expected to be similar to the Raman spectra from amorphous semiconductors, which are roughly proportional to the density of phonon states. This is reflected in the broad peak observed in the low frequency region (300-400 cm^{-1}) for the alloy nanostructures. The broadening is more prominent in case of $Zn_{1-y}Cd_yO$ alloy nanosructures because the atomic radii mismatch is higher in case of Zn and Cd (0.23 Å) compared to that of Zn and Mg (0.09 Å) as mentioned earlier in this section. So, the substitution of Cd into ZnO lattice is difficult and intermixing of two atomic species is highly probable. However, alloying is in general a much gentler perturbation than amorphization, as seen from the X-ray diffraction studies of our samples which clearly indicates the existence of a remaining order and a well defined average lattice constant.
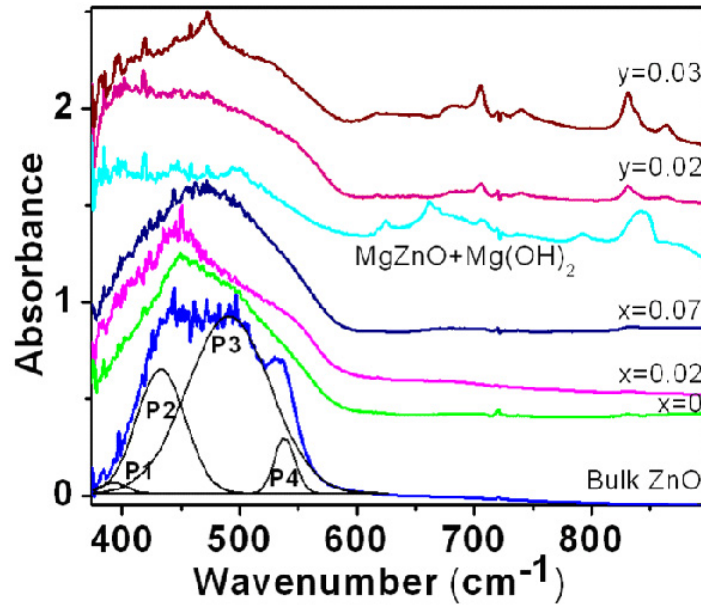
Figure C.2: The FTIR spectra of $Zn_{1-x}Mg_xO$ and $Zn_{1-y}Cd_yO$ and phase segregated MgZnO alloy as indicated on the graph.

C.3   Fourier Transform Infrared Spectroscopy (FTIR) study

In order to provide an additional support to the observation made by Raman spectroscopy, the infrared transmission spectra of ZnO and its alloy nanoparticles embedded in KBr powder media, have been measured in the wavelength range 375 to 4000 cm^{-1} (which is much higher than the particle diameter ∼10 nm). The IR active optical phonon modes of ZnO appear within the range of 300-600 cm^{-1} (see figure C.2) whereas the higher wave number peaks correspond to vibration modes of various impurities such as hydroxyl, carboxylate or alkane present in the sample [202]. In this work, within the displayed frequency range, phase segregated ZnMgO and ZnCdO alloy nanostructures show two impurity bands near 600-1000 cm^{-1} due to C-OH bond. The sources of these impurities are the organic precursors employed in the synthesis process and they reside on the surface of nanoparticles resulting in the gradual vanishing of the impurity peaks for bigger particles.

As mentioned earlier, only A_1 and E_1 modes of ZnO are IR active. Investigation done by the polarized light on $Zn_{0.8}Mg_{0.2}O$ thin film gives rise to four distinct vibration modes, such as A_1(TO), E_1(TO), A_1(LO) and E_1(LO) at 384 cm^{-1}, 417 cm^{-1}, 505 cm^{-1} and 586 cm^{-1} respectively ([200], [193]). Due to peak broadening, distinct nature of the IR absorption bands disappear for nanostructures of size ∼10 nm adopted in this work. IR bands in the range of 375 cm^{-1}-600 cm^{-1} is fitted by four Gaussians as indicated by $P1$, $P2$, $P3$ and $P4$ in figure C.3 and assigned as ω_{TO1}, ω_{TO2}, ω_{LO1}, ω_{LO2} respectively (Table C.4). Undoped ZnO and $Zn_{1-x}Mg_xO$ alloy nanostructures do not show ω_{LO2} mode in the range of 530-540 cm^{-1}. Although the IR bands of undoped ZnO nanostructures in this work do not match exactly with the previous report, a systematic variation in the vibration modes for $Zn_{1-x}Mg_xO$ and $Zn_{1-y}Cd_yO$ alloy nanostructures is found. As shown in figure C.3, all the IR modes shift to the blue and red
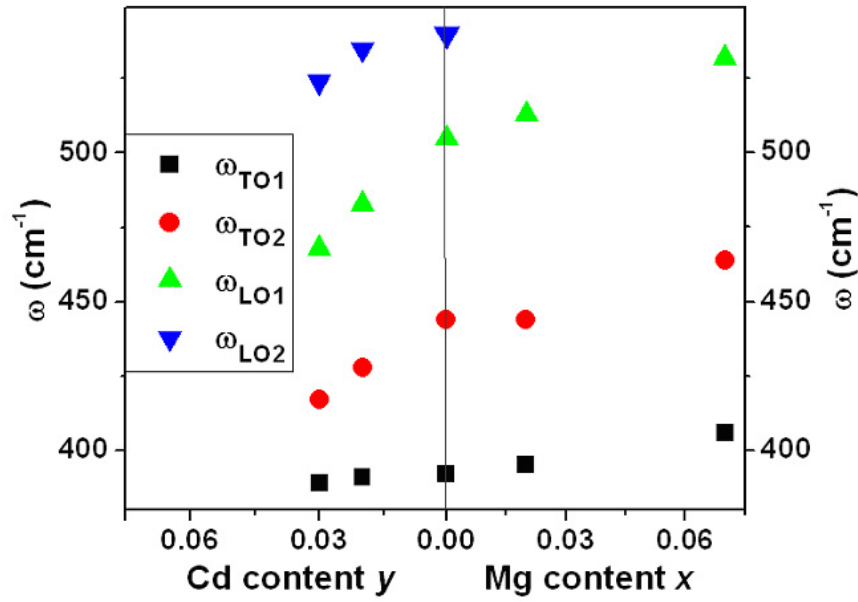
Figure C.3: The shift in the vibration modes of $Zn_{1-x}Mg_xO$ and $Zn_{1-y}Cd_yO$ alloy as indicated on the graph.

Table C.4: IR active vibration modes for ZnO and its alloy nanostructures

Samples	ω_{TO1} (cm^{-1})	ω_{TO2} (cm^{-1})	ω_{LO1} (cm^{-1})	ω_{LO2} (cm^{-1})
Bulk Zno	393	435	493	540
X=0	392	444	505	–
X=0.02	395	444	513	–
X=0.07	406	464	532	–
Y=0.02	391	428	483	535
Y=0.03	389	417	468	524

side of the spectrum for $Zn_{1-x}Mg_xO$ and $Zn_{1-y}Cd_yO$ alloys respectively. It should be noted that similar to the Raman spectra, FTIR spectra also carries the signature of phase segregation. Progressive alloying ultimately leads to phase segregation which results in a flat FTIR spectrum in the range of 300 -600 cm^{-1}.

C.4   Conclusions

An analysis of the optical phonon modes in polycrystalline ZnO and Zn(Mg,Cd)O alloy nanostructures have been documented. On alloying, both A_1 (LO) and E_1 (LO) mode of wurtzite Zn(Mg,Cd)O nanostructures show blue shift for $Zn_{1-x}Mg_xO$ and red shift for $Zn_{1-y}Cd_yO$ alloy nanostructures. Significant shift has been observed in E_1(LO) mode for $Zn_{1-x}Mg_xO$ (73

cm^{-1} for $x = 0.07$) and $Zn_{1-y}Cd_yO$ (17 cm^{-1} for $y = 0.03$). Phase segregation in the alloy nanostructures is confirmed by the absence of the characteristic IR bands of wurtzite ZnO near 400-600 cm^{-1}, which shift towards higher and lower wavenumbers for $Zn_{1-x}Mg_xO$ (x = 0.07) and $Zn_{1-y}Cd_yO$ ($y = 0.03$) alloy nanostructures respectively.

Bibliography

[1] U Ozgur, Y I Alivov, C Liu, A. Teke, M A Reshchikov, S Dogan, V Avrutin, S-J Cho and H Morko 2005 *J. Appl. Phys.* **98** 041301.

[2] D G Thomas 1960 *Journal of Physics and Chemistry of Solids* **15** 86.

[3] D .M. Bagnall, Y. F Chen, Z Zhu and T. Yao 1997 *Appl. Phys. Lett.* **70** 2230.

[4] Z. K. Tang, G. K. L. Wong, P. Yu, M. Kawasaki, A. Ohtomo, H. Koinuma, and Y. Segawa 1998 *Appl. Phys. Lett.* **72** 3270.

[5] S. J. Pearton *et al.* 2003 *J. Appl. Phys.* **93** 1.

[6] D. G. Thomas 1960 *J. Phys. Chem. Solids* **15** 86.

[7] E. Tomzig and H. Helbig 1976 *J. Lumin.* **14** 403.

[8] J. J. Hopfield 1960 *J. Phys. Chem. Solids* **15** 97.

[9] D. C. Reynolds, C. W. Litton, and T. C. Collins 1965 *Phys. Rev.* **140** A1726.

[10] D. C. Reynolds and T. C. Collins 1969 *Phys. Rev.* **185** 1099.

[11] D. C. Reynolds, D. C. Look, B. Jogai, C. W. Litton, T. C. Collins, W. Harsch and G. Cantwell 1998 *Phys. Rev. B* **57** 12151.

[12] D. C. Reynolds, D. C. Look and B. Jogai 2001 *J. Appl. Phys.* **89** 6189.

[13] B. K. Meyer *et al.* 2004 *phys. stat. sol. (b)* **241** 231.

[14] Bingqiang Cao, Weiping Cai and Haibo Zeng 2006 *Appl. Phys. Lett.* **88** 161101.

[15] E. G. Bylander 1978 *J. Appl. Phys.* **49** 1188.

[16] S. B. Zhang, S. H. Wei, and A. Zunger 2001 *Phys. Rev. B* **63** 075205.

[17] L. S. Vlasenko and G. D. Watkins 2005 *Phys. Rev. B* **71** 125201.

[18] F. H. Leiter, H. R. Alves, A. Hofstaetter, D. M. Hofmann, and B. K. Meyer 2001 *Phys. Status Solidi B* **226** R4.

[19] Sun X W, Yu S F, Xu C X, Yuen C, Chen B J and Li S 2003 *Jpn. J. Appl. Phys.* **42** L1229.

[20] Minami T 2005 *Semicond. Sci. Technol.* **20** S35.

[21] Ding G Q, Zheng M J, Xu W L and Shen W Z 2005 *Nanotechnology* **16** 1285.

[22] Kind H, Yan H Q, Messer B, Law M and Yang P D 2002 *Adv. Mater.* **14** 158.

[23] Pacholski C, Kornowski A and Weller H 2002 *Angew. Chem. Int. Ed.* **41** 1188.

[24] Kim J H, Andeen D and Lange F F 2006 *Adv. Mater.* **18** 2453.

[25] Dorfman A, Kumar N and Hahm J 2006 *Adv. Mater.* **18** 2685.

[26] N Kumar, A Dorfman and J-i Hahm 2006 *Nanotechnology* **17** 2875.

[27] Jang E S, Won J H, Hwang S J and Choy J H 2006 *Adv. Mater.* **18** 3309.

[28] Lee C J, Lee T J, Lyu S C, Zhang Y, Ruh H and Lee H J 2002 *Appl. Phys. Lett.* **81** 3648.

[29] Banerjee D, Jo S H and Ren Z F 2004 *Adv. Mater.* **16** 2028.

[30] Ramgir N S, Mulla I S, Vijayamohanan K, Late D J, Bhise A B, More M A and Joag D S 2006 *Appl. Phys. Lett.* **88** 042107.

[31] Wang Xudong, Zhou J, Lao C, Song J, Xu N and Wang Z L 2007 *Adv. Mater.* **19** 1627.

[32] Greene L E, Law M, Goldberger J, Kim F, Johnson J C, Zhang Y, Saykally R J and Yang P 2003 *Angew. Chem. Int. Ed.* **42** 3031.

[33] H Eiji, F Shinobu, K Toshio and I Hiroaki 2004 *Journal of sol-gel science and technology* bf 29 71.

[34] P Uthirakumar, B. Karunagaran, S. Nagarajan, E-K Suh and C-H Hong 2007 *Journal of Crystal Growth* **304** 150.

[35] Q Ahsanulhaq, A Umar and Y B Hahn 2007 *Nanotechnology* **18** 115603.

[36] Ranjani Viswanatha, Heinz Amenitsch and D. D. Sarma 2007 *J. Am. Chem. Soc.* **129** 4470.

[37] Y Sun, G M Fuge, N A Fox, D J Riley and M N R Ashfold 2005 *Adv. Mater.* **17** 2477.

[38] Y Chen,M Kim, G Lian,M B Johnson and X Peng 2005 *J. Am. Chem. Soc.* **127** 13331.

[39] T Zhang, W Dong, M K-Brewer, S Konar, R N Njabon and Z R Tian 2006 128 *J. Am. Chem. Soc.* **128** 10960.

[40] M Yin,Y Gu,I L Kuskovsky, T Andelman, Y Zhu, G F Neumark and S OBrien 2004 *J. Am. Chem. Soc.* **126** 6206.

[41] Y. R. Ryua, T. S. Lee, J. A. Lubguban, A. B. Corman, H. W. White, J. H. Leem, M. S. Han, Y. S. Park, C. J. Youn and W. J. Kim 2006 *Appl. Phys. Lett.* **88** 052103.

[42] J. M. Khoshman, D. C. Ingram and M. E. Kordesch 2008 *Appl. Phys. Lett.* **92** 091902.

[43] Ma T, Guo M, Zhang M, Zhang Y and Wang X 2007 *Nanotechnology* **18** 035605.

[44] Park J, Choi H H, Siebein K and Singh R K 2003 *J. Cryst. Growth* **258** 342.

[45] Zhang Y S, Wang L S, Liu X H, Yan Y J, Chen C Q and Zhu J 2005 *J. Phys. Chem. B* **109** 13091.

[46] Li S Y, Lin P, Lee C Y, Ho M S and Tseng T Y 2004 *J. Nanosci. Nanotechnol.* **4** 968.

[47] Kumar S, Gupta V and Sreenivas K 2005 *Nanotechnology* **16** 1167.

[48] Kim T Y, Kim J Y, Lee S H, Shim H W, Lee S H, Suh E K and Nahm K S 2004 Synth. Met. **144** 61.

[49] Hirate T, Sasaki S, Li W C, Miyashita H, Kimpara T and Satoh T 2005 Thin Solid Films **487** 35.

[50] Chander R and Raychaudhuri A K 2006 *J. Mater. Sci.* **41** 3623.

[51] Chen D R, Jiao X L and Cheng G 1999 *Solid State Commun.* **113** 363.

[52] Lu C H and Yeh C H 2000 *Ceram. Int.* **26** 351.

[53] K. Jacobi 1983 *Surface Science* **132** l.

[54] J C Phillips 1970 *Reviews of Modern Physics* **42** 317.

[55] C R A Catlowt and AM Stoneham 1983 *J. Phys. C: Solid State Phys.* **16** 4321.

[56] Cao M H, Guo C X, Qi Y J, Hu C W and Wang E B 2004 *J.Nanosci. Nanotechnol.* **4** 829.

[57] Guo M, Diao P and Cai S 2005 *J. Solid State Chem.* **178** 1864.

[58] Shalish I, Temkin H and Narayanamurti V 2004 *Phys. Rev. B* **69** 245401.

[59] M Ghosh and A K Raychaudhuri 2006 *J. Appl. Phys.* **100** 034315.

[60] M Ghosh and A K Raychaudhuri 2007 *Nanotechnology* **18** 115618.

[61] Garcia S P and Semancik S 2007 *Chem. Mater.* **19** 4016.

[62] Vayssieres L, Keis K, Hagfeldt A and Lindquist S-E 2001 *Chem. Mater.* **13** 4395.

[63] Travnikov V V, Freiberg A and Savikhin S F 1990 *J. Lumines.* **47** 107.

[64] T Kenji, F Hiroshi, O Naoki and H Hajime 2004 *Thin Solid Fils* **486** 42.

[65] O Naoki, T Kenji, H Shunichi, S Isao, F Hiroshi, H Hajime 2007 *J. Electrochem. Soc.* 154 D82.

[66] H Zheng, X L Du, Q Luo, J F Jia, C Z Gu and Q K Xue 2007 *Thin Solid Film* 515 3967.

[67] P-S Xu, Y-M Sun, C-S Shi, F-Q Xu, H-B Pan 2001 *Chinese Phys. Lett.* **88** 1252.

[68] F A Selim, M H Weber, D Solodovnikov, K G Lynn 2007 *Phys. Rev. Lett.* **99** 085502.

[69] Zhi Gen Yu, Ping Wu, Hao Gong 2006 *Appl. Phys. Lett.* **88** 132114.

[70] X Wang, Y M Lu, D Z Shen, Z Z Zhang, B H Li, B Yao, J Y Zhang, D X Zhao, X W Fan and Z K Tang 2007 *Semicond. Sci. Technol.* **22** 65.

[71] Jianguo Lu, Qunian Liang, Yinzhu Zhang, Zhizhen Ye and Shizuo Fujita 2007 *J. Phys. D: Appl. Phys.* 40 3177.

[72] N S Pesika, Z Hu, K J Stebe and P C Searson 2002 *J. Phys. Chem. B* **106** 6985.

[73] Djurisic A B *et al* 2007 *Nanotechnology* **18** 095702.

[74] Heo Y W, Norton D P and Pearton S J 2005 *J. Appl. Phys.* **98** 073502.

[75] van Dijken A, Makkinje J and Meijerink A 2001 *J. Lumin.* **92** 323.

[76] Ong H C and Du G T 2004 *J. Cryst. Growth* **265** 471.

[77] Tam K H et al 2006 *J. Phys. Chem. B* **110** 20865.

[78] Li Y, Paul W M, Lei Y and Tom B S 2007 *Nanotechnology* **18** 215602.

[79] Xiong G, Pal U and Serrano J G 2007 *J. Appl. Phys.* **101** 024317.

[80] Cao H L, Qian X F, Gong Q, Du W M, Ma X D and Zhu Z K 2006 *Nanotechnology* **17** 3632.

[81] Williamson G K and Hall W H 1953 *Acta Metall.* **1** 22.

[82] Herring C 1951 *Phys. Rev.* **82** 87.

[83] Jun Y-W, Choi J-S and Cheon J 2006 *Angew. Chem. Int. Edn* **45** 3414.

[84] Gao P X and Wang Z L 2005 *J. Appl. Phys.* **97** 044304.

[85] Tersoff J and Tromp R M 1993 *Phys. Rev. Lett.* **70** 2782.

[86] Goldfarb I 2007 *Surf. Sci.* **601** 2756.

[87] Ye J D et al 2005 *Appl. Phys. A* **81** 759.

[88] van Dijken A, Meulenkamp E A, Vanmaekelbergh D and Meijerink A 2000 *J. Phys. Chem. B* **104** 1715.

[89] Vanheusden K, Seager C H, WarrenW L, Tallant D R and Voigt J A 1996 *Appl. Phys. Lett.* **68** 403.

[90] van Dijken A, Meulenkamp E A, Vanmaekelbergh D and Meijerink A 2000 *J. Lumin.* **8789** 454.

[91] Qu F and Morais P C 1999 *J. Chem. Phys.* **111** 8588.

[92] Seager C H and Castner T G 1978 *J. Appl. Phys.* **49** 3879.

[93] M Ghosh and A K Raychaudhuri 2008 *Nanotechnology* **19** 445704.

[94] M Ghosh and A K Raychaudhuri 2008 *Appl. Phys. Lett.* **93** 123113.

[95] M Ghosh and A K Raychaudhuri 2008 *Bull. Mater. Sci.* **31** 283.

[96] L E Brus 1984 *J. Chem. Phys.* **80** 4403.

[97] Slow Positron Beam Technique for Solids and Surfaces, edited by G. Brauer and W. Anwand 2002 *Appl. Surf. Sci.* **194** 1.

[98] Kirkegaard P and Eldrup M 1972 *Comput. Phys. Commun.* **3** 240.

[99] Chaudhuri S K, Goswami K, Ghugre S S and Das D 2007 *J. Phys. Condens. Matter* **19** 216206.

[100] Thakur V, Shrivastava S B and Rathore M K 2004 *Nanotechnology* **15** 467.

[101] Stephan W. H. Eijt, Anton (TOM) Van Veen, Henk Schut, Peter E. Mijnarends, Art B. Denison, Bernardo Barbiellini and Arun Bansil 2006 *Nature Materials* **5** 23.

[102] G. Brauer, W. Anwand and W. Skorupa 2006 *Phys. Rev. B* **74** 045208.

[103] Y. Nagai, M. Hasegawa, Z. Tang, A. Hempel, K. Yubuta, T. Shimamura, Y. Kawazoe and F. Kano 2000 *Phys. Rev. B* **61** 6574.

[104] S.K. Chaudhuri, S. Mukherjee, P.V. Rajesh, S.S. Ghugre, D. Das 2005 *Physica B* **362** 249.

[105] R.N. West 1973 *Adv. Phys.* **22** 263.

[106] A. Uedono, T. Koida, A. Tsukazaki, M. Kawasaki, Z. Q. Chen, SF. Chichibu and H. Koinuma 2003 *J. Appl. Phys.* **93** 2481.

[107] Lin B, Fu Z and Jia Y 2001 *Appl. Phys. Lett.* **79** 943.

[108] A and Van de Walle C G 2006 *J. Cryst. Growth* **287** 58.

[109] Zhao J L, Zhang W, Li X M, Feng J W and Shi X 2006 *J. Phys.: Condens. Matter* **18** 1495.

[110] Kohan A F, Ceder G, Morgan D and van de Walle C G 2000 *Phys. Rev. B* **61** 15109.

[111] Oba F, Nishitani S R, Isotani S, Adachi H and Tanaka I 2001 *J. Appl. Phys.* **90** 824.

[112] Hsu N E, Hung W K and Chen Y F 2004 *J. Appl. Phys.* **96** 4671.

[113] Lauer R B 1973 *J. Phys. Chem. Solids* **34** 249.

[114] Djurisic A B, Leung Y H, TamK H, Ding L, GeWK, Chen H Y and Gwo S 2006 *Appl. Phys. Lett.* **88** 103107.

[115] Greene L E, Law M, Goldberger J, Kim F, Johnson J C, Zhang Y, Saykally R J and Yang P 2003 *Angew. Chem. Int. Edn* **42** 3031.

[116] Li D, Leung Y H, Djurisic A B, Liu Z T, Xie M H, Shi S L, Xu S J and Chan W K 2004 *Appl. Phys. Lett.* **85** 1601.

[117] Zhou H, Alves H, Hofmann D M, Kriegseis W, Meyer B K, Kaczmarczyk G and Hoffmann A 2002 *Appl. Phys. Lett.* **80** 210.

[118] Kwok W M, Leung Y H, Djurisic A B, Chan W K and Phillips D L 2005 *Appl. Phys. Lett.* **87** 093108.

[119] Cross R B M, De Souza M M and Sankara Narayanan E M 2005 *Nanotechnology* **16** 2188.

[120] Studenikin S A, Golego N and Cocivera M 1998 *J. Appl. Phys.* **84** 2287.

[121] Gomi M, Oohira N, Ozaki K and Koyano M 2003 Japan. *J. Appl. Phys.* **42** 481.

[122] Fan H J, Scholz R, Kolb F M, Zacharias M, Gosele U, Heyroth F, Eisenschmidt C, Hempel T and Christen J 2004 *Appl. Phys. A* **79** 1895.

[123] K. Vanheusden,W. L. Warren, C. H. Seager, D. R. Tallant, J. A. Voigt and B. E. Gnade 1996 *J. of Appl. Phys.* **79** 7983.

[124] Konrad Colbow 1965 *Physical Review* **139** A274.

[125] H Shimotani, H Asanuma, A Tsukazaki, A Ohtomo, M Kawasaki and Y Iwasa 2007 *Appl. Phys. Lett.* **91** 082106.

[126] P Chen, X Ma and D Yang 2007 *Appl. Phys. Lett.* **89** 111112.

[127] Xiangyang Ma, Peiliang Chen, Dongsheng Li, Yuanyuan Zhang, and Deren Yang 2007 *Appl. Phys. Lett.* **91** 021105.

[128] P J Daniel, R F Schwarz, M E Lasser and L W Hershinger 1958 *Physical Review* **111** 1240.

[129] Marcus C. Newton, Steven Firth, and Paul A. Warburton 2008 *IEEE Transaction on Nanotechnology* **7** No. 1.

[130] W. I. Park, Gyu-Chul Yi, J.-W. Kim and S.-M. Park 2003 *Appl. Phys. Lett.* **82** 4358.

[131] Jiping Cheng, Ming Fu, Yunjin Zhang, and Ruyan Guo 2007 *Mater. Res. Soc. Symp. Proc.* **957** 0957-K01-07.

[132] H. Shen, M. Wraback, C. R. Gorla, S. Liang, N. Emanetoglu, Y. Liu, and Y. Lu *Materials Research Society* F99W11.16

[133] M. Nakano, A. Tsukazaki, R. Y. Gunji, K. Ueno, A. Ohtomo, and T. Fukumura M. Kawasaki 2007 *Applied Physics Letter* **91** 142113.

[134] H Endo, M Sugibuchi, K Takahashi, S Goto, S Sugimura, K Hane, Y Kashiwaba 2007 *Appl. Phys. Lett.* **90** 121906.

[135] T Shirakawa, T Umeda, Y Hashimoto, A Fujii and K Yoshino 2004 *J. Phys. D: Appl. Phys.* **37** 847.

[136] C Lu, Q Fu, S Huang and J Liu 2004 *Nano Lett.* **4** 623

[137] G P. Siddons, D Merchin, J H Back, J K Jeong and M Shim 2004 *Nano Lett.* **4** 927.

[138] A Das, A. K. Sood, A. Govindaraj, A. M Saitta, M Lazzeri, F Mauri and C. N. R Rao 2007 *Phys. Rev. Lett.* **99** 136803.

[139] H Shimotani, H Asanuma, A Tsukazaki, A Ohtomo, M Kawasaki and Y Iwasa 2007 *Appl. Phys. Lett.* **91** 082106.

[140] S. Liang , H. Sheng, Y. Liu, Z. Huo, Y. Lu, and H. Shen 2001 *J. Cryst. Growth* **225** 110.

[141] D. Basak, G. Amin, B. Mallik, G.K. Paul, and S.K. Sen 2003 *J. Cryst. Growth* **256** 73.

[142] W. I. Park, G. C. Yi, M. Y. Kim and S. J. Pennycook 2003 *Adv. Mater* **15** 526.

[143] A. Ohtomo, M. Kawasaki, T. Koida, K. Masubuchi, H. Koinuma, Y. Sakurai, Y. Yoshida, T. Ysuda, and Y. Segawa 1998 *Appl. Phys. Lett.* **72** 2466.

[144] H. Cao, Y. G. Zhao, H. C. Ong, S. T. Ho, J. Y. Dai, J. Y. Wu, and R. P. H. Chang 1998 *Appl. Phys. Lett.* **73** 3656.

[145] A. K. Sharma, J. Narayan, J. F. Muth, C. W. Tang, C. Jin, A. Kvit, R. M. Kolbas, and O. W. Holland 1999 *Appl. Phys. Lett.* **75** 3327.

[146] M. Lorenz, E. M. Kaidashev, A. Rahm, Th. Nobis, J. Lenzner, G. Wagner, D. Spemann, H. Hochmuth, and M. Grundmann 2005 *Appl. Phys. Lett.* **86** 143113.

[147] W. I. Park, Gyu-Chul Yi, and H.M. Jang 2001 *Appl. Phys. Lett.* **79** 2022.

[148] Chia Ying Lee, Tseung Yuen Tseng, Seu Yi Li and Pang Lin 2005 *Nanotechnology* **16** 1105.

[149] Segnit E R and Holland A E 1965 *J. Am. Ceram. Soc.* **48** 412.

[150] H.M. Rietveld 1969 *J. Apl. Cryst.* **2** 65.

[151] Ranjani Viswanatha, Sameer Sapra, B. Satpati, P. V. Satyam, B. N. Devb and D. D. Sarma 2004 *J. of Mater Chem.* **14** 661.

[152] Vladimir A. Fonoberov, and Alexander A. Balandin 2004 *Phys. Rev. B* **70** 195410.

[153] Vladimir A. Fonoberov, and Alexander A. Balandin 2004 *Appl. Phys. Lett.* **85** 5971.

[154] Steven C. Erwin1, Lijun Zu, Michael I. Haftel, Alexander L. Efros, Thomas A. Kennedy1 and David J. Norris 2005 *Nature* **436** 91.

[155] R. D. Shannon1976 *Acta Crystallogr., Sect. A: Cryst. Phys., Diffr., Theor. Gen. Crystallogr.* **32** 145.

[156] R. W. Martin, P. G. Middleton, K. P. O Donnell, and W. Vander stricht 1999 *Appl. Phys. Lett.* **74** 263.

[157] E. Burstein 1954 *Phys. Rev.* **93** 632.

[158] Nick S. Norberg and Daniel R. Gamelin 2005 *J. Phys. Chem. B.* **109** 20810.

[159] M Schirra, A Reiser, G M Prinz, R Schneider, R Sauer and K Thonke, MRS Proceeding, 0957-K03-07.

[160] Manoj K. Yadav, Manoranjan Ghosh, Ranjit Biswas, Arup K. Raychaudhuri, and Abhijit Mookerjee 2007 *Phys. Rev. B* **76** 195450.

[161] T. Makino, Y. Segawa, M. Kawasaki, A. Ohtomo, R. Shiroki, K. Tamura, T. Yasuda and H. Koinuma 2001 *Appl. Phys. Lett.* **78** 1237.

[162] Keiichiro Sakurai, Takeshi Kubo, Daisuke Kajita, Tetsuhiro Tanabe, Hidemi Takasu, Shizuo Fujita and Shigeo Fujita 2000 *Jpn. J. Appl. Phys.* **39** L1146-L1148.

[163] Satoshi Shigemori, Atsushi Nakamura, Junji Ishhara, Toru Aoki and Jiro Temmyo 2004 *Jpn. J. Appl. Phys.* **43** L1088-L1090.

[164] F. Z. Wang, Z. Z. Ye, D. W. Ma, L. P. Zhu, F. Zhuge and H. P. He 2005 *Appl. Phys. Lett.* **87** 143101.

[165] Zhong Lin Wang 2004 *J. Phys.: Condens. Matter* **16** R829-R858.

[166] Fen Xu, Zhong-Yong Yuan, Gao-Hui Du, Tie-Zhen Ren 2006 *Nanotechnology* **17** 588.

[167] H Q Le, S J Chua, K P Loh, E A Fitzgerald and Y W Koh 2006 *Nanotechnology* **17** 483.

[168] Feng Li, Yong Ding, Puxian Gao, Xinquan Xin, and Zhong L. Wang 2004 *Angew. Chem.* **116** 5350.

[169] C X. Xu, A Wei, X W Sun and Z L Dong 2006 *J. of Phys. D: Applied Physics* **39** 1690.

[170] JEOL Ltd. 1-2, Musashino 3-chome Akishima, Tokyo 196-8558, Japan

[171] PANalytical B.V., Lelyweg 1, 7602EA ALMELO, The Netherlands

[172] Shimadzu Scientific Instruments, 7102 Riverwood Drive, Columbia, MD21046, USA

[173] HORIBA Jobin Yvon, 3880 Park Avenue, Edison, NJ08820-3012, USA

[174] Edinburgh Instruments Ltd., 2 Bain Square, Kirkton Campus, Livingston, EH547DQ UK

[175] J. Zuniga-Perez, V. Munoz-Sanjose, M. Lorentz, G. Benndorf, S. Heitsh, D. Spemann, and M. Grundmann 2006 *J. of Appl. Phys.* **99** 023514.

[176] A.V. Osinsky *et al.* 2006 *Mater. Res. Soc. Symp. Proc.* **892** FF18-01-EE09-01.1.

[177] F.Z. Wang, H.P.He, Z.Z. Ye, and L.P. Zhu 2005 *Journal of Applied Physics* **98** 084301.

[178] D. C. Reynolds, D. C. Look, and B. Jogai 2001 *J. of Appl. Phys.* **89** 6189.

[179] R. L. Weiher, and W. C. Tait 1968 *Phys. Rev.* **166** 791.

[180] Vladimir A Fonoberov, Khan A Alim and Alexander A. Balandin 2006 *Phys. Rev. B* **73** 165317.

[181] Benjamin Gillbert, Hengzhong Zhang, Feng Huang, Michael P. Finnegan, Glenn A. Waychunas and Jillian F. Banfield 2003 *Geochem. Trans.* **4** 20.

[182] D. E. Jesson, G Chen, K. M. Chen, and S. J. PEnnycook 1998 *Phys. Rev. Lett.* **80** 5156.

[183] Michael J. Aziz, Paul C. Sabin, and Guo-Quan Lu 1991 *Phys. Rev. B* **44** 9812.

[184] Gerko Oskam, Zeshan Hu, R. Lee Penn, Noshir Pesika, and Peter C. Searson 2002 *Phys. Rev. E* **66** 011403.

[185] W. Shan, W. Walukiewicz, J. W. Ager, III, K. M. Yu, Y. Zhang, S. S. Mao, R. Kling, C. Kirchner and A. Waag 2005 *Appl. Phys. Lett.* **86** 153117.

[186] R. Ghosh, D. Basak, and S. Fujihara 2004 *J. of Appl. Phys* **96** 2689.

[187] E. Cohen and M. D. Sturge 1982 *Phys. Rev. B* **25** 3828.

[188] J. A. Kash, Arza Ron, E. Cohen 1983 *Phys. Rev. B* **28** 6147.

[189] Sun X W, Yu S F, Xu C X, Yuen C, Chen B J, and Li S 2003 *Jpn. J. Appl. Phys. Part 2* **42** L1229.

[190] Alim K A, Fonoberov V A, Shamsa M, and Balandin A A 2005 *J. Appl. Phys* **97** 124313.

[191] Cheng H M, Hsu H C, Tseng Y K, Lin L J, and Hsieh W F 2005 *J. Phys. Chem. B* **109** 8749.

[192] Bergman L, Morrison J L, Chen X B, Huso J and Hoeck H 2006 *Appl. Phys. Lett.* **88** 023103.

[193] Bundesmann C, Rahm A, Lorenz M, Grundman M and Schubert M 2006 *J. Appl. Phys.* **99** 113504.

[194] Kumar S, Gupta V and Sreenivas K 2005 *Nanotechnology* **16** 1167.

[195] Kim T Y, Kim J Y, Lee S H, Shim H W, Lee S H, Suh E K and Nahm K S 2004 *Synth. Met.* **144** 61.

[196] Bandyopadhyay A K, Dilawar N, Vijayakumar A, Varandani D and D. Singh 1998 *Bull. Mater. Sci.* **21** 433.

[197] Damen T C, Porto S P S and Tell B 1966 *Phys. Rev.* **142** 570.

[198] Huso J, Morrison L, Hoeck H, Casey E, Bergman L, Pounds T D and Norton M G 2007 *Appl. Phys. Lett.* **91** 111906.

[199] Weber W H and Merlin R, Raman Scattering in Material Science *Springer* 2000, **ISBN 3540672230**.

[200] Bundesmann C, Schubert M, Spemann D, Butz T, Lorenz M, Kaidashev E. M, Grundmann M, Ashkenov N, Neumann H and Wagner G 2002 *Appl. Phys. Lett.* **81** 2376.

[201] Decremps F, Porres J P, Saitta A M, Chervin J C and Polian A 2002 *Phys. Rev. B* **65** 092101.

[202] Kwon Y J, Kim K H , Lim C S and Shim K B 2002 *Journal of Ceramic Processing Research.* **3** 146.

[203] C P Royall, J Dzubiella, M Schmidt, A v Blaaderen 2007 *Phys. Rev. Lett.* **98** 188304.

[204] A S. Dhoot, J D. Yuen, M Heeney, I McCulloch, D Moses, and A J. Heeger 2006 *PNAS* **103** 18834.

[205] B. Natesan, N. K. Karan, and R. S. Katiyar 2006 *Phys. Rev. E* **74** 042801.

[206] V.M. Arutyunyaqn 1989 *Soviet Phys. Uspeshki* **32** 521.

[207] R.H. Wilson 1980 *Critical Reviews in Solid State and Materials Sciences* **10** 1.

[208] M J. Panzer and C. D Frisbie 2007 *J. Am. Chem. Soc.* **129** 6599.

[209] J D. Yuen, A S. Dhoot, E B. Namdas, N E. Coates, M Heeney, I McCulloch, D Moses and A J. Heeger 2007 *J. Am. Chem. Soc.* **129** 14367.

[210] P Basak, O Parkash and P. R. Chatterji 2001 *Journal of Macromolecular Science, Part A* **38** 399.